

ABSTRACT

NOSBISCH, JAMIE. Modeling Polarization of the PLC/PKC Signaling Pathway in Fibroblast Chemotaxis. (Under the direction of Dr. Jason Haugh).

Cell movement directed by external gradients of soluble chemicals (chemotaxis) is critical for a number of physiological processes, including the immune response, wound healing, and development. Over the past two decades, a number of mathematical models have been proposed to explain how signaling pathways sense external gradients and polarize to bias the migration of a cell; however, most of these models are based on theoretical concepts, whereas models cast in terms of defined molecules and mechanisms are much less common. In this work, a mechanistic, reaction-diffusion model was developed to analyze the phospholipase C (PLC)/protein kinase C (PKC) signaling pathway, which was recently shown to be essential for PDGF gradient sensing in mesenchymal cells such as skin fibroblasts. Our goal was to identify mechanisms that can amplify this intracellular signaling pathway in shallow external gradients of chemoattractant.

Novel insights from this model include the mechanism of substrate-buffering by myristoylated alanine-rich C kinase substrate (MARCKS). We show that phosphorylation of MARCKS by membrane-localized PKC constitutes a positive feedback that is sufficient for local pathway amplification at the leading edge, while the release of MARCKS and its subsequent diffusion and dephosphorylation in the cytosol also serves to suppress the pathway at the rear of the cell. By itself, this mechanism only weakly amplifies signaling in a shallow PDGF gradient, but it synergizes with two additional feedback loops involving the lipid, phosphatidic acid (PA), for substantial signal amplification at shallow gradients and a more robust response to changes in PDGF gradient conditions. An analysis of these feedbacks implicated a critical role for DAG

kinases and the PA-producing enzyme, phospholipase D, in controlling the lipid metabolism and thus polarization of the PLC/PKC pathway.

PLC γ 1, the specific isozyme of PLC involved in the PLC/PKC signaling pathway in fibroblasts, is basally autoinhibited, and recent work detailing the structure of the full-length enzyme elucidated a more detailed mechanism for its activation. To better understand the kinetics of this process, we developed a rule-based model to investigate how domain interactions and reaction rates affect PLC γ 1 activation. Our model was able to reproduce the increased levels of activity associated with known activating mutations of PLC γ 1 while also predicting faster kinetics for mutations affecting the autoinhibition and slower kinetics for mutations affecting the rate of membrane binding. A combined model of PLC γ 1 activation and PLC/PKC polarization predicted these activating mutations would also diminish the polarization of the pathway in response to shallow gradients of chemoattractants. Based on an analysis of the PLC γ 1 activation model, a modified feedback loop involving PA was formulated in the combined model, and that mechanism was found to synergize with MARCKS for polarization of the PLC/PKC pathway.

These models offer a framework for a mechanistic understanding of PLC/PKC signaling in gradient sensing, the kinetics of PLC γ 1 activation, and how perturbations to PLC γ 1 activation affect the polarization of the PLC/PKC pathway. Testable predictions made by these models can be used to guide further study of signal transduction affecting chemotaxis of fibroblast cells. Given the role chemotaxis plays in cancer cell metastasis and considering the diseases and cancers linked to dysfunction of the PLC and PKC enzymes, further study of this signaling pathway will continue to be of vital importance.

© Copyright 2020 by Jamie Nosbisch

All Rights Reserved

Modeling Polarization of the PLC/PKC Signaling Pathway in Fibroblast Chemotaxis

by
Jamie Nosbisch

A dissertation submitted to the Graduate Faculty of
North Carolina State University
in partial fulfillment of the
requirements for the degree of
Doctor of Philosophy

Biomathematics

Raleigh, North Carolina
2020

APPROVED BY:

Dr. Jason Haugh
Committee Chair

Dr. Julio Monti Belmonte

Dr. Kevin Flores

Dr. Emily Griffith

DEDICATION

To my parents for always providing me with unconditional love and support enabling me to do whatever I put my mind to, and to my twin sister who has always been there for me, even before I was born.

BIOGRAPHY

Jamie Nosbisch grew up in northern Minnesota and went to the University of Minnesota Duluth for her undergraduate studies. Unable to decide which STEM field she liked best, she ended up getting two Bachelor of Science degrees in Biochemistry and Cell and Molecular Biology with a minor in Mathematics. After getting involved in undergraduate research in the lab of Dr. Erin Sheets, she decided to continue doing research after her graduation and enrolled in the Biomathematics program at North Carolina State University. While there, she joined the lab of Dr. Jason Haugh and started working on a multiscale modeling project to study wound healing. This project helped solidify her scientific interests, and now she plans on pursuing a career that combines her biological curiosity and quantitative skills with her passion for improving human health.

ACKNOWLEDGMENTS

I would like to start by acknowledging my advisor, Dr. Jason Haugh. Without his expert guidance, endless knowledge, and unwavering support, I would not be receiving this degree. I would like to thank the past and present members of the Haugh lab and our collaborators in the labs of Dr. Jim Bear and Dr. Tim Elston at the University of North Carolina at Chapel Hill who have taught me so much and have always been willing to help. I would also like to thank my committee members Dr. Julio Belmonte, Dr. Kevin Flores, and Dr. Emily Griffith for their support through this process.

I would like to acknowledge Dr. Alun Lloyd, the Biomathematics Program Director, who would check in with me and make sure I was staying on track while also doing so much for the program and my fellow graduate students. I would like to thank Dr. Kelly as well as Dr. Haugh for their work with the GAANN Fellowship that supported three years of my graduate research work. As part of this fellowship, I also participated in supervised teaching experiences and would like to thank Dr. Goller and Dr. Chen for their guidance in the High-Throughput Discovery course. I would also like to thank my BioLunch faculty advisor, Dr. Reeves, who helped me and the other coordinators organize a really interesting seminar series.

I would like to acknowledge my family for providing me with everything I needed to succeed. I am so fortunate to have the best parents and sister in the world, without whom I would not be here. I would also like to thank my friends Anna, Emma, Marcella, Mary, Meredith, Natalie, Rachael, and Sadie. All of you made graduate school fun, and I am so grateful for your support over these past few years and well into the future. Lastly, I would like to thank my boyfriend, Richard, whose love, support, and ability to make me laugh made me happy even when things got tough.

TABLE OF CONTENTS

LIST OF TABLES	viii
LIST OF FIGURES	ix
Chapter 1: Introduction to the PLC/PKC Signaling Pathway and Fibroblast Chemotaxis	
Chemotaxis	1
1.1 Chemotaxis: Cell Migration Directed by a Chemical Gradient.....	2
1.2 PLC/PKC Signaling Pathway	5
1.3 Mathematical Modeling of Chemotactic Gradient Sensing.....	10
1.4 Mechanistic Modeling of PLC/PKC Signaling in Fibroblast Chemotaxis	12
1.5 Overview of Dissertation	14
1.6 References.....	16
Chapter 2: A Reaction-Diffusion Model Explains Amplification of the PLC/PKC Pathway in Fibroblast Chemotaxis	
Pathway in Fibroblast Chemotaxis	21
2.1 Introduction.....	22
2.2 Materials and Methods.....	24
2.2.1 Basic model description	24
2.2.2 Modeling MARCKS-membrane interactions	26
2.2.3 Modeling implementation.....	28
2.3 Results.....	29
2.3.1 Regulation of MARCKS by PKC is sufficient to amplify the PLC/PKC pathway	29
2.3.2 Differential buffering of PIP2 by MARCKS as a distinct mode of gradient amplification	33
2.3.3 Regulation of MARCKS synergizes with other feedback mechanisms to enhance amplification of the PLC/PKC pathway	38
2.3.4 The coupling of MARCKS and PKC feedbacks yields oscillations in certain regions of parameter space.....	43
2.4 Discussion	46
2.5 Acknowledgments.....	49
2.6 References.....	50
Chapter 3: Mechanistic Models of PLC/PKC Signaling Implicate Phosphatidic Acid as a Key Amplifier of Chemotactic Gradient Sensing	
a Key Amplifier of Chemotactic Gradient Sensing	55
3.1 Introduction.....	56
3.2 Results.....	58
3.2.1 New models of the PLC/PKC pathway based on putative feedback mechanisms in the literature	58
3.2.2 Stabilization of PLC recruitment by phosphatidic acid (PFL 1), combined with neutralization of MARCKS by PKC, promotes sensitive and robust gradient sensing	60
3.2.3 Analysis of the mechanisms driving PLC/PKC polarization.....	64
3.2.4 Subtle asymmetry in cell morphology polarizes the PLC/PKC network with PFL 1 and influences external gradient sensing	67

3.2.5 The model predicts a critical role of DAG kinases affecting the responsiveness of the gradient sensing network through PFL 1	69
3.2.6 PKC-mediated activation of PLD (PFL 2) confers less responsiveness than PFL 1, but the two feedbacks synergize in the polarization of PLC/PKC signaling	73
3.2.7 Thresholds for chemotactic migration matching those of DAG/PKC polarization yield efficient collective invasion and chemotactic wavelets in simulations of wound invasion	75
3.3 Discussion	78
3.3.1 Novel ways that lipid signaling might enhance chemotactic gradient sensing, corroborated by modeling	78
3.3.2 Robustness and reversibility of polarization	79
3.3.3 Testable hypotheses guided by the models	80
3.3.4 Limitations of the models	82
3.4 Materials and Methods	83
3.4.1 Models of PLC/PKC signaling	83
3.4.2 Implementation of PLC/PKC models	85
3.4.3 Wound healing model	86
3.5 Acknowledgments	88
3.6 References	89
Chapter 4: A Structure-Based Model of PLCγ1 Activation	95
4.1 Introduction	96
4.2 Materials and Methods	98
4.2.1 Rule-based model of PLC γ 1 activation	98
4.2.2 Implementation of the rule-based model	103
4.2.3 Combining the PLC γ 1 activation model with the PLC/PKC polarization model	103
4.3 Results	104
4.3.1 A structure-based model of PLC γ 1 activation	104
4.3.2 Tyr783 phosphorylation helps relieve autoinhibition leading to PLC γ 1 activation	107
4.3.3 The parameter k_{act} increases the lifetime of active PLC γ 1 at the membrane	110
4.3.4 Activating mutations and their effect on the kinetics of PLC γ 1 activation	111
4.3.5 A modified version of PFL 1 can amplify the signaling pathway in a combined model of PLC γ 1 activation and PLC/PKC polarization	114
4.4 Discussion	118
4.5 Acknowledgments	122
4.6 References	123
Chapter 5: Summary and Future Directions	125
5.1 Summary of Work and Important Insights	126
5.2 Future Modeling and Experimental Work	128
5.3 Outlook	132

5.4 References	133
Appendices	136
Appendix A	137
A.1 Modeling Details for Chapter 2	138
A.1.1 Reaction-diffusion model: general considerations.....	138
A.1.2 Molecular diffusivities	139
A.1.3 Reaction dynamics	140
A.1.4 Production rates for the PLC/PKC pathway	141
A.1.5 Rate laws for the PLC/PKC pathway.....	143
A.1.6 Specification of adjustable parameters	146
A.1.7 Scaling analysis of MARCKS phosphorylation, diffusion, and dephosphorylation.....	148
A.2 References	150
Appendix B	151
B.1 Modeling Details for Chapter 3.....	152
B.1.1 General forms of the differential equations and boundary conditions	152
B.1.2 Molecular diffusivities and initial concentrations	152
B.1.3 Production rates	154
B.1.4 Rate law expressions	156
B.1.5 Specification of rate parameters	159
B.1.6 Steady state analysis of DAG and PA levels (no PFL 2)	160
B.2 References	163
Appendix C	164
C.1 VCell Math Description Code for PLC γ 1 Activation Model	165
C.2 VCell Math Description Code for Combined PLC γ 1 Activation Model and PLC/PKC Polarization Model.....	175

LIST OF TABLES

Table 4.1	Brief reaction rule description with base case values for the associated rate constants.	100
Table A.1	List of model species, their diffusivities, and their initial concentrations / densities.	139
Table A.2	Reaction rate expressions describing the PLC/PKC pathway. Note that free PIP ₂ concentration, p , is calculated based on the variables p_T and m_T , assuming pseudo-equilibrium of PIP ₂ -MARCKS interactions.	146
Table B.1	List of model species, their diffusivities, and their initial concentrations / densities.	153
Table B.2	Reaction rate expressions.	158

LIST OF FIGURES

- Figure 1.1 Directed migration cues for mesenchymal cells. (A) Diagram illustrating the diverse types of directional cues that mesenchymal cells respond to. Of note is the hybrid cue where chemotactic cues (e.g., growth factors) are bound to ECM scaffolds. (B) During cutaneous wound healing, fibroblasts (prototypical mesenchymal cells) respond to both PDGF (chemotaxis) and ECM cues (haptotaxis/durotaxis). (C) Likewise, mesenchymal tumor cells emerging from primary tumors sense multiple directional cues. Reprinted from Current Opinion in Cell Biology, 30, James E Bear and Jason M Haugh, Directed migration of mesenchymal cells: where signaling and the cytoskeleton meet, 74-82, Copyright (2014), with permission from Elsevier.3
- Figure 1.2 Mesenchymal vs. amoeboid motility and chemotaxis. The illustrations and table compare the structural and dynamic features of mesenchymal migration to those of amoeboid cells such as neutrophils and lymphocytes. Reprinted from Current Opinion in Cell Biology, 30, James E Bear and Jason M Haugh, Directed migration of mesenchymal cells: where signaling and the cytoskeleton meet, 74-82, Copyright (2014), with permission from Elsevier.5
- Figure 1.3 Signal transduction pathways controlling myosin contractility and lamellipodial actin assembly. Work on chemotaxis has focused almost exclusively on F-actin polymerization mediated by the Arp2/3 complex; however, new data suggests an essential role of Myosin II regulation through the PLC γ /DAG/PKC α pathway. Figure by Jason Haugh and used with permission.7
- Figure 1.4 Quantitative chemotaxis assay reveals a critical role for PLC/PKC signaling. (A) The microfluidic chamber has been adapted to present PDGF gradients of varying steepnesses. (B) Wind-rose plots show that the depletion of PLC and PKA by siRNAs block PDGF chemotaxis. (C) GFP-tagged tandem CI probe, imaged by TIRF, is preferentially localized in protrusions oriented towards the PDGF gradient (0°). Figure adapted from (23) by Jason Haugh and used with permission.9
- Figure 2.1 Reaction-diffusion model of the PLC/PKC pathway. (A) Schematic of the pathway describing interactions among signaling proteins (PLC, PKC, and MARCKS) and plasma membrane lipids (PIP₂ and DAG). Dashed arrows with circles at the end signify catalysis of the indicated transition. (B) Heat map plotting the density of free PIP₂ (p) as a function of the density of membrane-bound MARCKS (m_T) and of the density of total PIP₂ (p_T). A shift from the initial condition may be interpreted as changes in PLC-mediated PIP₂ hydrolysis and/or PKC activation, as indicated. (C) The fractions of membrane-bound MARCKS with i molecules of PIP₂ bound (m_i/m_T) are plotted as a function of the density of free PIP₂ (p).25

Figure 2.2	Reaction network of the PLC/PKC pathway constructed in Virtual Cell. Green spheres represent the model species. Yellow squares represent the reaction nodes, black solid arrows represent species transformations, and dashed arrows signify catalysis.	28
Figure 2.3	Regulation of MARCKS by PKC is sufficient to amplify the PLC/PKC pathway. Simulations were done for a steep PDGF gradient (67% relative gradient) with midpoint [PDGF] = 0.03 nM, introduced at time = 1200 s. (A) Kinetics of active PKC (c^*) in the absence of MARCKS. (B) Surface plot of the steady-state front/back ratio of active PKC (c^*) as a function of MARCKS phosphorylation (k_{pm}) and dephosphorylation (k_{dpM}) rate constants. (C) Optimal MARCKS phosphorylation rate constant ($dots$) for each value of the MARCKS dephosphorylation rate constant. The line shows the best fit of the log-transformed variables. (D) Kinetics of active PKC (c^*) for the base parameter set with $k_{pm} = 1 \mu\text{m}^{-2} \text{s}^{-1}$ and $k_{dpM} = 1 \text{s}^{-1}$ (see also Fig. 2.4).	31
Figure 2.4	Kinetics of all species for the simulation represented in Fig. 2.3D.....	32
Figure 2.5	Differential buffering of PIP ₂ by MARCKS as a distinct mode of gradient amplification. These results pertain to the simulation with base parameters and a steep PDGF gradient, as in Figs. 2.3D and 2.4, comparing steady-state levels at the front and back of the simulated cell and the initial levels. (A) Heat map of free PIP ₂ (p) as a function total PIP ₂ (p_T) and total membrane-bound MARCKS (m_T), as introduced in Fig. 2.1B. Circles show how the PDGF gradient shifts the steady state at the front and rear of the simulated cell. (B–D) Bar plots of free and bound PIP ₂ levels in the presence and absence of MARCKS (B), membrane-bound MARCKS with various numbers of PIP ₂ bound (C), and cytosolic MARCKS (unphosphorylated, M , and phosphorylated, M_p) (D).....	34
Figure 2.6	Pathway amplification is affected by MARCKS mobility in the cytosol. These results pertain to the simulation with base parameters and a steep PDGF gradient, but with the cytosolic diffusion coefficients for unphosphorylated MARCKS (D_M) and phosphorylated MARCKS (D_{Mp}) varied. The base values are $D_M = D_{Mp} = 32 \mu\text{m}^2/\text{s}$. The heat map plots the front/back ratio of active PKC as a function of those parameters.	36
Figure 2.7	Geometry effects in 3D simulations. 3D geometries with (A) and without (B) a filopod-like protrusion are shown. In both cases, the nucleus is a sphere, radius 4 μm , with membrane surface given by the following equation. The rest of the cell has a ‘fried egg’ shape, with a radius of 20 μm at $z = 0$, except for the geometry in A, which has a thin, finger like protrusion projecting in positive x direction. The plasma membrane surface is given by the following equation for negative z and bounded also by the $z = 0$ plane. $H(x)$ is the Heaviside step function. The dimensions of the filopod in A are $d = 0.2 \mu\text{m}$, $L_{fil} = 5 \mu\text{m}$ ($L_{fil} = 0$ in B). Kinetics of active PKC (c^*) at the front and back of the geometry with	

	filopod (C) and without filopod (D) for a PDGF relative gradient of 67% and midpoint [PDGF] = 0.03 nM.	37
Figure 2.8	Kinetics of active PKC (c^*) with or without MARCKS for a PDGF gradient with relative steepness 10% and midpoint [PDGF] = 0.03 nM.	39
Figure 2.9	Regulation of MARCKS synergizes with other feedback mechanisms to enhance amplification of the PLC/PKC pathway. (A) Cutout of the pathway schematic depicting the addition of intermolecular PKC autophosphorylation as an additional positive feedback. (B) Surface plot of the steady-state front/back ratio of active PKC (c^*) as a function of intramolecular (k_{pc1}) and intermolecular (k_{pc2}) PKC phosphorylation rate constants for the steep (67%) PDGF gradient. (C and D) Characterization of the system with PKC feedback ($k_{pc1} = 0.01 \text{ s}^{-1}$ and $k_{pc2} = 1 \mu\text{m}^{-2} \text{ s}^{-1}$). Comparison of the kinetics of active PKC (c^*) and distribution of free PIP ₂ with MARCKS, and the kinetics of active PKC without MARCKS, for steep (67% (C)) and shallow (10% (D)) PDGF gradients with midpoint [PDGF] = 0.03 nM, introduced at time = 1200 s. The lighter circles on the heat maps are for the base parameter set without PKC feedback; black circles are for the parameter set with PKC feedback included.	41
Figure 2.10	Parameter sweeps for intramolecular (k_{pc1}) and intermolecular (k_{pc2}) phosphorylation rates in the absence of MARCKS.	42
Figure 2.11	Geometry effects with both positive feedbacks in a shallow gradient. 3D geometries with (A) and without (B) a filopod-like protrusion are shown, identical to those shown in Fig. 2.7. Kinetics of active PKC (c^*) at the front and back of the geometry with filopod (C) and without filopod (D) for the model with both MARCKS and PKC feedbacks and for a shallow PDGF gradient with 10% relative steepness and midpoint [PDGF] = 0.03 nM.	43
Figure 2.12	The PLC/PKC pathway with multiple feedbacks is capable of oscillations. Kinetics of active PKC (c^*) at the front and back of the simulated cell for PDGF gradients of varying relative steepness as indicated and midpoint [PDGF] = 0.03 nM, introduced at time = 1200 s. Deviations from the base parameter values are $k_{pm} = 0.03 \mu\text{m}^{-2} \text{ s}^{-1}$, $k_{dpM} = 0.01 \text{ s}^{-1}$, $k_{pc1} = 0.01 \text{ s}^{-1}$, and $k_{pc2} = 1 \mu\text{m}^{-2} \text{ s}^{-1}$	44
Figure 2.13	Kinetics of all species for the simulation represented in Fig. 2.12 with 67% relative gradient.	45
Figure 2.14	Expanded view of oscillating species from Fig. 2.13. The dotted vertical line allows comparisons across species.	46
Figure 3.1	Model of the PLC/PKC network including phosphatidic acid (PA). (A) Model schematic depicting the interactions and reactions among signaling proteins and plasma membrane lipids. Dashed lines ending in a filled circle indicate that the species enhances the associated process. The reactions and interactions shown in	

	red are associated with the generation and influence of PA in positive feedback loops (PFLs) labeled (1) and (2). (B) Base model geometry and orientation of the receptor occupancy gradient, which is linear in the direction of the cell's long axis, x . (C) Plots illustrating the linear profile of active receptor density imposed across the 40 μm length of the cell for varying values of $rfrac$ (relative midpoint density) and $rsteep$ (relative steepness, expressed here as a percentage difference across the cell).	59
Figure 3.2	Gradient amplification by PFL 1 combined with regulation of MARCKS. (A) The concentration of active PKC molecules at the front (red circle) and back (blue circle) of the cell are plotted as a function of the mean fractional occupancy of receptors, $rfrac$, for varying values of gradient steepness. When the simulations produced oscillations, the maxima (upward-pointing triangles) and minima (downward-pointing triangles) of the oscillations are plotted; the front and back are still denoted by shades of red and blue, respectively. The simulation achieving steady state with the maximum front/back ratio is denoted by the dashed vertical line. For these simulations, the direction of the gradient was reversed after 20,000 s. If the active PKC pattern failed to reverse in response, the simulation is marked with an asterisk. (B) Table showing the maximum front/back ratio for each gradient steepness in simulations run with PFL1 and either with or without MARCKS protein.	61
Figure 3.3	Time courses of all model species for Fig. 3.2A, 10% steepness and $rfrac = 0.1$. ..	62
Figure 3.4	Transition from oscillations to stable pattern as $rfrac$ is increased (10% steepness).....	63
Figure 3.5	Analysis of the mechanisms driving PLC/PKC polarization. (A) Sensitivity of the results in Fig. 3.2A, 10% gradient steepness, to the indicated fold-changes in MARCKS (M and M_p) cytosolic diffusivities (1 = base case). (B) Sensitivity of the results in Fig. 3.2A, 10% gradient steepness, to the indicated fold-changes in total PIP_2 and membrane-associated MARCKS (p_T and m_T) membrane diffusivities (1 = base case). (C) Plot of the d - and e -nullclines (<i>Appendix B</i>) evaluated at the front and back of the cell for the base-case parameters as in Fig. 3.2A, with 10% gradient steepness and $rfrac = 0.1$	65
Figure 3.6	Phase plots for different $rfrac$ values. These correspond to the simulations analyzed in Fig. 3.2A with 10% gradient steepness. The plot with $rfrac = 0.1$ is the same as in Fig. 3.5A. When $rfrac = 0.0278$, DAG is low at both the front and back of the cell; with $rfrac = 0.278$, DAG is high at both the front and back of the cell.	66
Figure 3.7	Subtle asymmetry in cell morphology causes spontaneous polarization of the proposed PLC/PKC network and influences external gradient sensing. (A) Comparison of the symmetric cell geometry versus the asymmetric cell geometry. (B) Results for the asymmetric geometry with uniform receptor	

occupancy (0% gradient steepness) show spontaneous polarization of the system for a particular range of receptor occupancy values. Symbols have the same meanings as in Fig. 3.2A. (C) Sensitivity of the results in B to the indicated fold-changes in MARCKS (M and M_p) cytosolic diffusivities (1 = base case). (D) Table showing the maximum front/back active PKC ratio for each gradient steepness indicated using the asymmetric geometry. Consistent with the rest of the paper, the front and back of the cell refer to the ends with the highest and lowest receptor activation, respectively. For the front-end blunted simulations where the ratio is less than 1 (internal gradient opposite the external gradient), the inverse of the ratio is indicated. 68

Figure 3.8 Systematic variation of kinetic parameters (no PFL 2). 70

Figure 3.9 Variation of PA/DAG ratio modulates the sensitivity and dose response of the pathway. (A) The final steady-state concentration of PA (d_p) is plotted versus the concentration of DAG (d) at the front of the cell for each simulation presented in Fig. 3.2. These points fall along the line predicted by the equation shown, for which net diffusion of lipids is assumed to be slow. (B) Relative to the parameter set associated with Fig. 3.2, the parameter k_{DAGK} was taken at 0.3 or 3 times its base value, at 10% gradient steepness. Colors and symbols have the same meanings as in Fig. 3.2A. The maximum front/back ratio is shown underneath the symbols. (C) Bar plots comparing the DAG and PA steady-state concentrations at the front and back of the cell for 1x and 3x k_{DAGK} simulations, with 10% steepness and $rfrac = 0.1$. (D) Same as B, but with 3% gradient steepness. For B-D, the direction of the gradient was reversed after 20,000 s. If the active PKC pattern failed to reverse in response, the simulation is marked with an asterisk. (E) The parameter scaling factor refers to the fold-change by which the parameters k_{DAGK} , k_{PAP} , $k_{basal,dp}$, and K_{PA} were decreased, while the parameter $k_{off,c}$ was divided by the scaling factor to increase its value. These parameter changes increase DAG and PA levels at the front of the cell systematically, while maintaining approximately the same PA/DAG ratio and comparable effects of PA and DAG on PFL 1 and PKC recruitment, respectively. 72

Figure 3.10 PFL 2 confers less responsiveness than PFL 1, but the two can synergize in the polarization of PLC/PKC signaling. The simulations shown are all at a 10% gradient of receptor occupancy. All colors, symbols, and values have the same meanings as in previous figures. (A) PFL 2 and MARCKS regulation but no PFL 1. For PFL 2, the parameters K_{PLD} and $\gamma V_{synth,dp}$ are set at 1 and 1, respectively. (B) PFL 1 and PFL 2 but no MARCKS. The parameters K_{PLD} and $\gamma V_{synth,dp}$ are set at 0.1 and 10, respectively. (C) All three feedbacks are included, and K_{PLD} and $\gamma V_{synth,dp}$ are set as in B. For all of these simulations, the direction of the gradient was reversed after 20,000 s. If the active PKC pattern failed to reverse in response, the simulation is marked with an asterisk. 74

Figure 3.11	Variation of key parameters with PFL 2 included in the system. The parameters targeted were k_{DAGK} , which affects the conversion of DAG to PA; K_{PA} , which Affects the PA-PLC affinity in PFL 1; and K_{PLD} , which affects the sensitivity of PFL 2 to active PKC. Each parameter was decreased to 0.3X and increased to 3X. Each plot shows active PKC density vs. $rfrac$ for 10% gradient steepness, as in Fig. 3.10.	75
Figure 3.12	Simulation of wound invasion with chemotactic switching based on DAG/PKC polarization. (A) Depiction of individual cells in the hybrid simulation, in which the concentration of PDGF is modeled as a continuum. The cells are initially seeded in the adjacent dermis; position along the vertical dimension is for visualization only. As time elapses, the cells invade and populate the clot region through a combination of directed migration and proliferation. (B) Depth of penetration into the wound at $t = 10$ days for random migration only or with chemotaxis allowed (mean \pm s.d., $n = 10$ simulations each). (C) Spatial profiles of cell densities (randomly or chemotactically migrating) and dimensionless PDGF concentration. (D) Zoomed-in view of the cell density and PDGF concentration profiles for 1 mm length of the clot region, showing chemotactic wavelets.	77
Figure 3.13	Plot of Eq. 3.4. For each cell i in the simulation, its mean receptor activation r_i and the difference in receptor activation across its length Δr_i were calculated. Cells with receptor activation states above the curve engaged in chemotaxis, whereas those with states below the curve engaged in random migration only.....	88
Figure 4.1	Model schematic of the full reaction network generated by the BioNetGen modeling engine in VCell showing 17 different species and 53 reactions. Cytosolic species are in blue, species bound to the RTK are in yellow, and active species are in red. The space between the solid blue line and dotted blue represent species that are bound to the membrane via the core but are not bound to the RTK.	99
Figure 4.2	A molecular depiction of the reaction rules described in Table 4.1. All domains and states shown in yellow represent features of the reaction rule that were purposely specified. The sites in gray mean that domain can be in any state and bound or unbound when the rule is applied.	102
Figure 4.3	Illustration of PLC γ 1 activation. (A) Cartoon depicting the steps of PLC γ 1 activation. Shown is the regulatory and catalytic regions of the PLC γ 1 enzyme oriented in the N-terminal to C-terminal direction. The catalytic core separated into an X and Y box are shown in green with the regulatory X-Y linker region containing the nSH2 and cSH2 domains on top. The dimerized and activated RTK is shown in the membrane with a phosphotyrosine site shown. (B) Molecular depiction of the canonical pathway for PLC γ 1 activation in the model with the reaction rates shown for each step. (C) Cartoon showing the two-step inactivation process for PLC γ 1.....	106

- Figure 4.4 Dose-response dynamics for Tyr783 phosphorylation. (A) The fraction of active PLC γ 1 is plotted as a function of the initial receptor concentration while the parameter K_p was varied. The legend for this plot corresponds to the same line color and symbols used in plots for B and C. Plots where the Tyr783 phosphorylation rate (B) and dephosphorylation rate (C) were varied for $K_p = 10$ and $K_p = 100$ 109
- Figure 4.5 Decay of active species once PLC γ 1 can no longer leave the cytosol. Time courses for (A) k_{phos} and (B) k_{act} showing the decay of active PLC γ 1 species once the rates k_{on_nSH2} and k_{act} were set to zero at 5000 s preventing any PLC γ 1 from leaving the cytosol. The second plot shows the same time course on a log scale for the fraction of active PLC γ 1. The third plot shows the half-life for decay, calculated as the time it takes for the fraction of active PLC γ 1 to reach half its steady-state concentration. 111
- Figure 4.6 The effects of activation mutations on the kinetics of PLC γ 1 activation. (A) Cartoon depicting the effects of K_c mutations on the location of the cSH2 relative to the core. (B) Cartoon depicting the effects of K_a mutations on the ability of the uninhibited enzyme to bind the membrane. Time course plotting the saturation of the fraction of active PLC γ 1 when the (C) K_c parameters and (D) K_a parameters were varied with the wild-type case shown in black. The table shows the half-life for saturation, calculated as the time it takes for the fraction of active PLC γ 1 to reach half its steady-state concentration. 113
- Figure 4.7 The effects of activation mutations on the kinetics of PLC γ 1 activation ($K_p = 10$). Time course plotting the saturation of the fraction of active PLC γ 1 when the (A) K_c parameters and (B) K_a parameters were varied with the wild-type case shown in black. The table shows the half-life for saturation, calculated as the time it takes for the fraction of active PLC γ 1 to reach half its steady-state concentration. 114
- Figure 4.8 Gradient amplification by PFL 1* combined with the regulation of MARCKS in a combined model of PLC γ 1 activation and PLC/PKC polarization. (A) The concentration of active PKC molecules at the front (red circle) and back (blue circle) of the cell are plotted as a function of the mean fractional occupancy of receptors, rfrac, for varying values of gradient steepness. When the simulations produced oscillations, the maxima (upward-pointing triangles) and minima (downward-pointing triangles) of the oscillations are plotted; the front and back are still denoted by shades of red and blue, respectively. The simulation achieving steady state with the maximum front/back ratio is denoted by the dashed vertical line and its time course is plotted in (B)..... 116
- Figure 4.9 The effect of parameter variations on the sensitivity of the pathway. (A) Relative to the base case parameter set associated with the PLC/PKC polarization model, the parameter k_{DAGK} was taken at 0.3 or 3 times its base value. Colors and symbols have the same meanings as in Figure 4.8. The

maximum front/back ratio is shown underneath the symbols. (B) Bar plots comparing the DAG and PA steady-state concentrations at the front and back of the cell for 1x and 3x k_{DAGK} simulations, with $rfrac = 0.077$. (C) PFL 2 is added to PFL 1* and MARCKS and the parameters K_{PLD} and $\gamma V_{synth,dp}$ are set at 0.1 and 10, respectively. (D) The parameters $k_{unbind,c}$ and k_{inact} are taken at 10x and 0.1x their base case values listed in Table 4.1. 118

Figure 5.1 Substitutions of PLC- γ 1 found in cancers activate the enzyme. (a) Position (n = 26) and frequency of substitutions (red spheres) in PLC- γ 1 for a cohort of 370 patients with adult T cell leukemia/lymphoma. (b) Mutations from (a) mapped onto the structure of PLC- γ 1. (c) Basal phospholipase activity of mutant forms of PLC- γ 1 in cells. Data represent the mean \pm SEM of triplicate samples from a single experiment representative of three independent experiments. *Inset* shows mutant forms of PLC- γ 1 with the lowest relative basal activity. Immunoblots of cell lysates are presented in the same order as the bar graph. Reprinted from eLife 2019;8:e51700 DOI: 10.7554/eLife.51700, Hajicek et al. Structural basis for the activation of PLC- γ isozymes by phosphorylation and cancer-associated mutations, Copyright (2019) Hajicek et al. This article is distributed under the terms of the Creative Commons Attribution 4.0 International License (creativecommons.org/licenses/by/4.0/), which permits unrestricted use and redistribution. 130

CHAPTER 1

Introduction to the PLC/PKC Signaling Pathway and Fibroblast Chemotaxis

1.1 Chemotaxis: Cell Migration Directed by a Chemical Gradient

Directed cell migration, or cell migration biased by external spatial cues, is important for a number of physiological phenomena including embryogenesis, angiogenesis, cancer metastasis, and wound healing (1). During these events, cells migrate toward a target by sensing gradients of surface-bound immobilized ligands (haptotaxis), mechanical stiffness (durotaxis), an electric field (galvanotaxis), soluble chemical cues (chemotaxis), or a combination of the above (Fig. 1.1A). The focus of this work is on chemotaxis which is the process by which cells direct their migration based on an external gradient of soluble, chemical cues called chemoattractants (2).

Many cell types chemotax, but the phenotypic characteristics of their motility may look considerably different based on whether they fall under the category of amoeboid (e.g. leukocytes) or mesenchymal (e.g. fibroblasts). One example of a biological process where both forms of motility come into play is wound healing (Fig. 1.1B). Within hours of wounding, inflammation sets in, which relies on rapid migration of amoeboid cells like neutrophils and macrophages. These cells respond to gradients of chemokines that elicit rapid wound invasion. Once there, these cells are responsible for phagocytosing cellular debris and bacteria and for producing growth factors and cytokines (3, 4). Thereafter, the proliferative phase of wound healing ensues. During this phase, fibroblast cells respond to gradients of growth factors, in particular platelet-derived growth factor (PDGF), by proliferating and migrating to the wound site. Relative to the immune response, fibroblast invasion is a much slower process, evolving over the course of days to weeks following wounding. Once in the wound, fibroblasts specialize in the secretion and deposition of ECM, and they eventually differentiate into myofibroblasts that actively contract ECM to close the wound (4, 5). While amoeboid and mesenchymal motility phenotypes are considered distinct modes of cell migration, cells can switch phenotypes along

this continuum. As a prominent example, metastatic cancer cells undergo an epithelial-to-mesenchymal transition, accompanied by their net emigration from the primary tumor (Fig 1.1C)

(6).

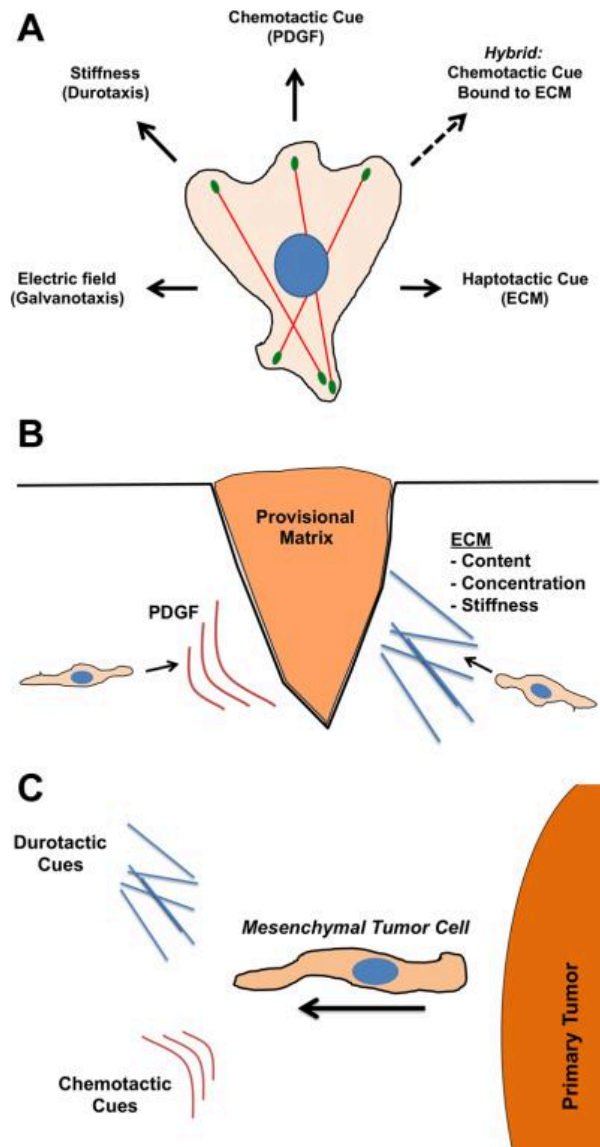


Figure 1.1 Directed migration cues for mesenchymal cells. (A) Diagram illustrating the diverse types of directional cues that mesenchymal cells respond to. Of note is the hybrid cue where chemotactic cues (e.g., growth factors) are bound to ECM scaffolds. (B) During cutaneous wound healing, fibroblasts (prototypical mesenchymal cells) respond to both PDGF (chemotaxis) and ECM cues (haptotaxis/durotaxis). (C) Likewise, mesenchymal tumor cells emerging from primary tumors sense multiple directional cues. Reprinted from *Current Opinion in Cell Biology*, 30, James E Bear and Jason M Haugh, Directed migration of mesenchymal cells: where signaling and the cytoskeleton meet, 74-82, Copyright (2014), with permission from Elsevier.

Certain characteristics differentiate amoeboid motility from mesenchymal motility, as summarized in Figure 1.2. Amoeboid migration can be thought of as a “path-finding” mode of migration. These cells readily deform, modifying their shape to squeeze through pores they encounter in the extracellular matrix (ECM) by extending pseudopods or blebs (7, 8). To maintain a fast migration speed ($\sim 10 \mu\text{m}/\text{min}$), their adhesion to the ECM is relatively weak, and they rely on having a strongly polarized actin cytoskeleton to promote efficient migration (9). Amoeboid cells tend to have a rounded shape with a well-defined leading edge composed of branched actin. Amoeboid cells also have a structure at the rear of the cell called a uropod, which is where Myosin II motor activity is responsible for a contractile, squeezing force that promotes forward protrusion and the release of adhesions from the ECM (10). The importance of these properties of amoeboid migration are readily apparent in light of the innate immune response, which requires that leukocytes like neutrophils and macrophages quickly and efficiently migrate through tissue, intercepting invading pathogens and thus preventing injury and disease (11).

In contrast to “path-finding” amoeboid motility, mesenchymal cells exhibit “path-generating” migration. Mesenchymal cells use strong, adhesive connections to crawl through the ECM. Rather than trying to squeeze through pores, these cells must apply proteolytic activity of matrix metalloproteinases to degrade the ECM in their path, causing them to move much slower than amoeboid cells ($< 1 \mu\text{m}/\text{min}$) (9). Unlike the strong polarization seen in amoeboid cells, mesenchymal cells are only weakly polarized and use multiple competing protrusions called lamellipodia for forward migration (12, 13). Mesenchymal cells do not form Myosin II-containing uropods; instead, Myosin II is found throughout the cell and is associated with bundled actin stress fibers that associate with adhesions to generate the necessary traction forces for motility (14). These migration properties lend themselves to the biological role of

mesenchymal cells like fibroblasts whose primary function is producing ECM in connective tissue (15).

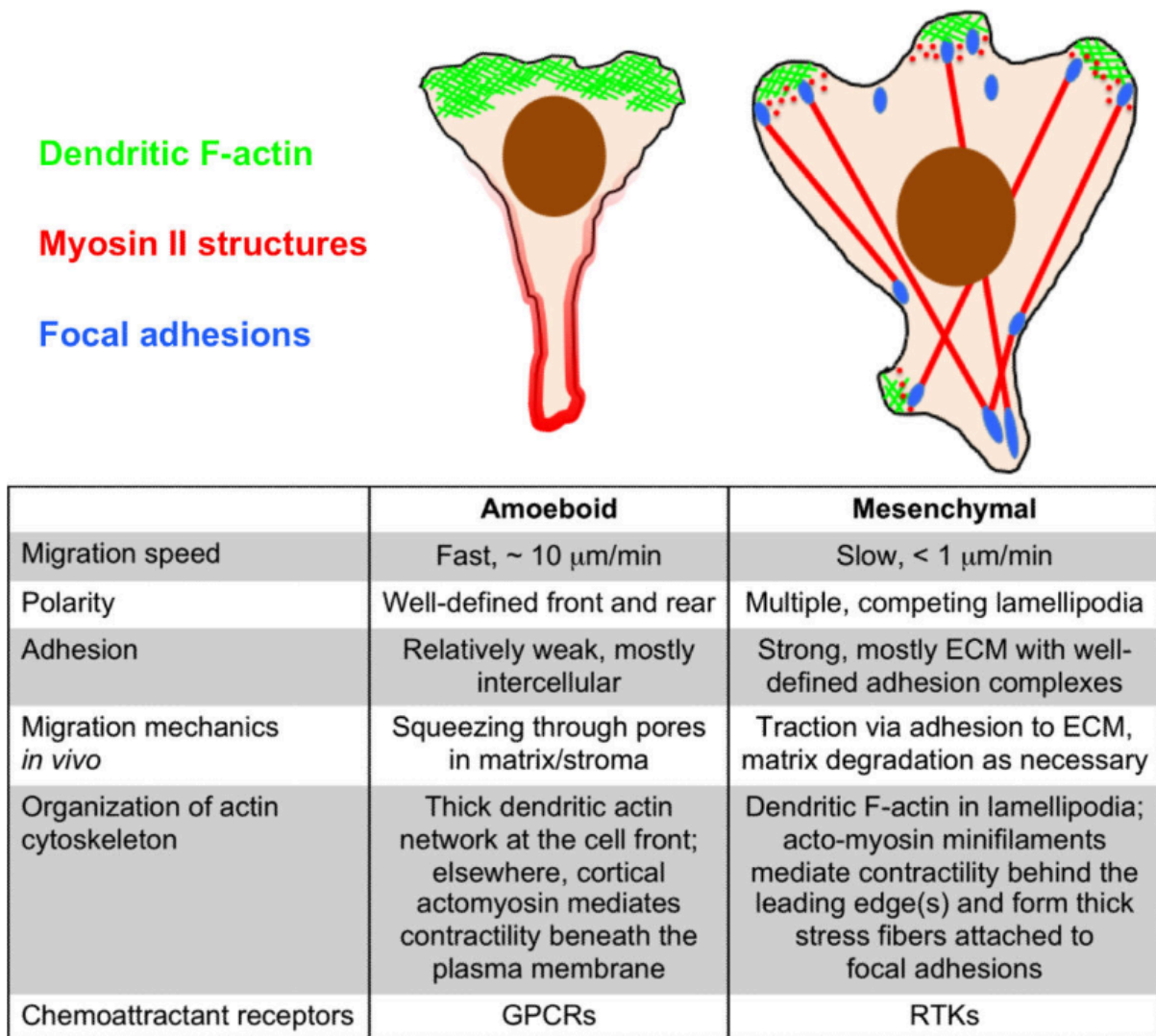


Figure 1.2 Mesenchymal vs. amoeboid motility and chemotaxis. The illustrations and table compare the structural and dynamic features of mesenchymal migration to those of amoeboid cells such as neutrophils and lymphocytes. Reprinted from Current Opinion in Cell Biology, 30, James E Bear and Jason M Haugh, Directed migration of mesenchymal cells: where signaling and the cytoskeleton meet, 74-82, Copyright (2014), with permission from Elsevier.

1.2 PLC/PKC Signaling Pathway

Despite distinct differences in the mechanics of chemotaxis between amoeboid and mesenchymal cells, the signal transduction pathway responsible for gradient sensing was thought

to function similarly in both cell types. While amoeboid cells use receptors of the G protein-coupled receptor (GPCR) class and mesenchymal cells use receptors of the receptor tyrosine kinase (RTK) class, both receptors recruit and activate specific isoforms of the phosphoinositide 3-kinase (PI3K) enzyme (2). These PI3K isoforms catalyze the conversion of the lipid phosphatidylinositol bisphosphate (PIP₂) into phosphatidylinositol trisphosphate (PIP₃). Biased receptor activation by the external gradient of chemoattract leads to biased PI3K activation which causes PIP₃ accumulation at the membrane of the leading edge in cooperation with other feedback loops (16). Several pathways link PI3K activation and PIP₃ production to the activation of guanine-nucleotide exchange factors (GEFs) which in turn activate the GTPases Rac and Cdc42 (17, 18). The lipids PIP₂ and PIP₃ along with Rac and Cdc42 aid in the recruitment and activation of the WAVE and WASP proteins which stimulate the activity of the Arp2/3 complex. The Arp2/3 complex nucleates new branched actin filaments which leads to localized actin polymerization and protrusion. Together with the mutual antagonism provided by RhoA activation of Myosin at the rear, the conceptual model posits that cells polarize and migrate in the direction of the gradient (19, 20).

While this signaling pathway (Fig 1.3) is important for the regulation of motility and polarity in many cell types, chemotaxis assays have shown that the GTPases Rac and Cdc42 as well as the Arp2/3 complex are not essential for the directional response of fibroblast cells toward PDGF (21, 22). In the study by Monypenny et al. 2009, siRNAs were used to inhibit the expression of Cdc42 and Rac1 in mouse embryonic fibroblasts. These Cdc42- and Rac1-deficient cells displayed aberrant morphology, including cell elongation and rounding as well as the loss of lamellipodia, and an analysis of the trajectories of these cells showed that their migration speed was greatly reduced; however, these cells were still capable of sensing and

migrating toward a gradient of PDGF. In the study by Wu et al. 2012, a stable cell line of fibroblasts that were depleted of the Arp2/3 complex also showed aberrant morphology without dendritic F-actin or lamellipodia; but again, when these cells were placed in chemotaxis chambers, they responded normally to gradients of PDGF. These studies suggested that the PI3K/GTPase/WAVE/Arp2/3 signaling pathway culminating in localized branched actin assembly and protrusion structures are necessary for efficient motility of fibroblasts but are not required for sensing external gradients of chemoattractants.

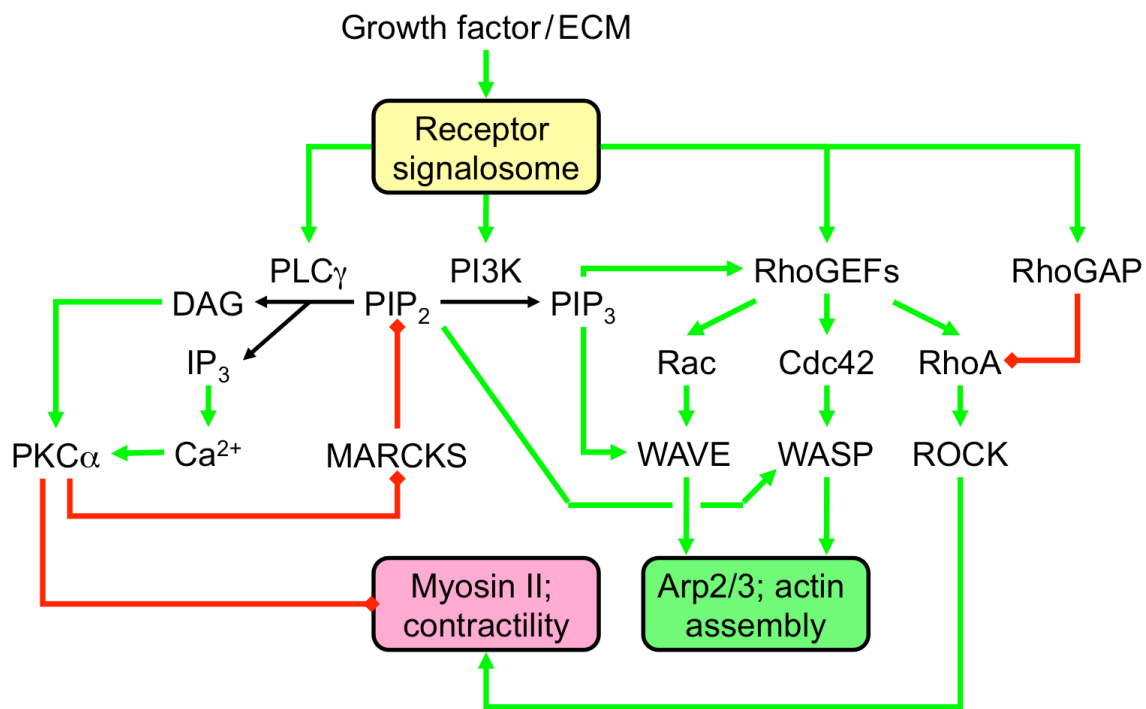


Figure 1.3 Signal transduction pathways controlling myosin contractility and lamellipodial actin assembly. Work on chemotaxis has focused almost exclusively on F-actin polymerization mediated by the Arp2/3 complex; however, new data suggests an essential role of Myosin II regulation through the PLC γ /DAG/PKC α pathway. Figure by Jason Haugh and used with permission.

To identify the requirements for mesenchymal chemotaxis, Asokan et al. conducted chemotaxis experiments using a microfluidic chamber designed to maintain gradients of

chemoattractants for multiple hours while also allowing direct observation of the cells (23). The cells' centroid positions were tracked over time, so information about migration speed, persistence, and directionality could be extracted (Fig 1.4A). These experiments showed that Myosin IIA, PLC γ , and PKC α are essential for chemotaxis. The results of these chemotaxis experiments were plotted as wind-rose (radial) histograms, in which each leaflet represents the count frequency of cells migrating in the corresponding angle bin. For these histograms, traveling toward 0° is representative of traveling in the direction of the PDGF gradient. Figure 1.4B shows that fibroblast cells depleted of the enzymes PLC γ 1 or PKC α lost their ability to chemotax towards a gradient of PDGF. This is quantified (24) in terms of the FMI, or forward migration index, which is used to quantify directionality. For the control, the FMI value of 0.42 indicates positive chemotaxis. For the knockdowns of PLC γ 1 and PKC α , the FMI values less than ~0.1 indicate that chemotaxis was not distinguishable from random migration (23).

In addition to establishing the requirement of the Myosin IIA isoform and the enzymes PLC γ and PKC α , localized diacylglycerol (DAG) production by PLC γ was also shown to be required for mesenchymal chemotaxis. To visualize the intracellular distribution of DAG, the tandem C1 domain fragment of the PKC δ enzyme was tagged with GFP, and its translocation to the plasma membrane was monitored by total internal reflection fluorescence (TIRF) microscopy to visualize the accumulation of DAG. Cells expressing this biosensor consistently showed significant enrichment of DAG at the leading edge when chemotaxing to gradients of PDGF (Fig. 1.4C).

These results implicated a new signaling pathway responsible for gradient sensing in mesenchymal cells. To summarize: activated receptors recruit activate PLC γ ; the biased activation of PLC γ results in production of a localized gradient of DAG, which recruits and

mediates activation of PKC α . Active PKC α phosphorylates and inactivates Myosin IIA, and this mechanical asymmetry biases directional migration (Fig. 1.3) (23).

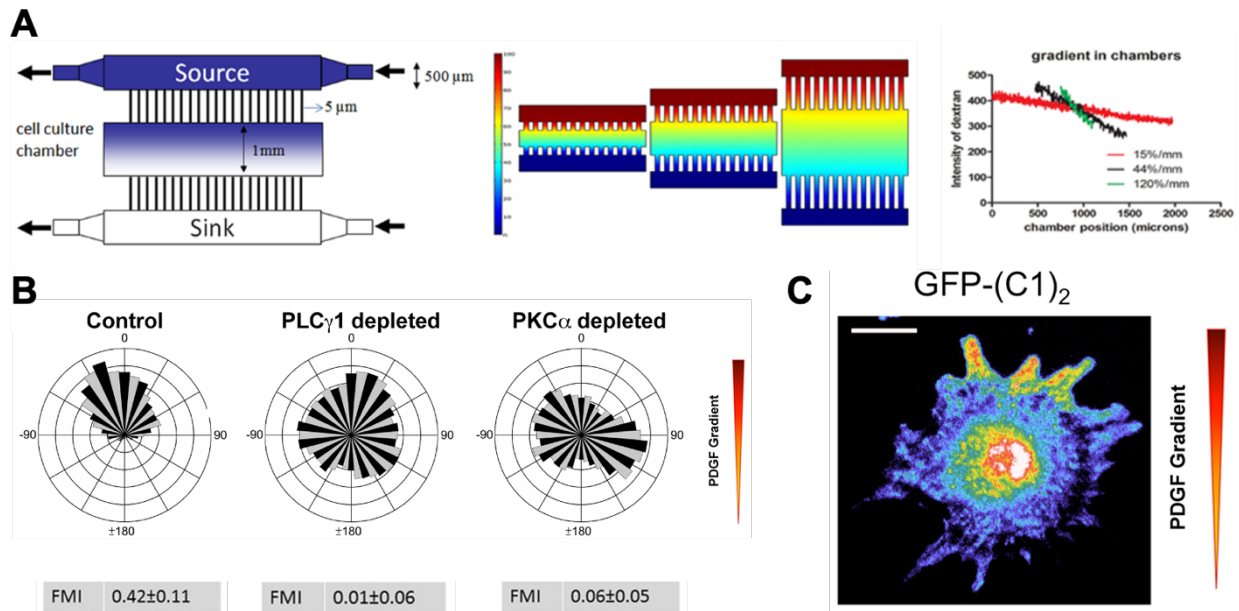


Figure 1.4 Quantitative chemotaxis assay reveals a critical role for PLC/PKC signaling. (A) The microfluidic chamber has been adapted to present PDGF gradients of varying steepnesses. (B) Wind-rose plots show that the depletion of PLC and PKA by siRNAs block PDGF chemotaxis. (C) GFP-tagged tandem CI probe, imaged by TIRF, is preferentially localized in protrusions oriented towards the PDGF gradient (0°). Figure adapted from (23) by Jason Haugh and used with permission.

While these experiments were able to elucidate the pathway responsible for gradient sensing in mesenchymal cells, a critical research question remains. Namely, it is not yet clear how the cells interpret a shallow external gradient of chemoattractant to execute a robust chemotactic response, at the level of the necessary structural and mechanical changes to the cytoskeleton. Addressing that question, using mathematical modeling, is the primary focus of this thesis.

1.3 Mathematical Modeling of Chemotactic Gradient Sensing

Over the past two decades, a number of mathematical models have been proposed to explain the gradient sensing and polarization aspects of chemotaxis. Gradient sensing describes the cell's ability to sense external gradients of chemoattractants and convert that receptor occupancy information across the membrane into an amplified, intracellular response while polarization describes the changes in the cell's cytoskeleton and morphology generated by the asymmetric redistribution of multiple proteins and lipids (25-27). In general, these models offer variations on three different principles such as Turing-type diffusive instabilities, wave-based propagation, and most commonly, local excitation and global inhibition mechanisms (28).

In reaction-diffusion systems, Turing patterns arise when the steady state of the system becomes destabilized by diffusion-driven instability. This instability causes minor fluctuations in a species concentration to become amplified at different rates until the fluctuation with the highest growth rate becomes fixed (29). In the context of polarization, a simple activator-inhibitor model can display Turing pattern formation if the inhibitor has a much larger diffusivity than the activator (30). Meinhardt and Gierer built on this idea with their proposed local self-activation and lateral inhibition model in which the activator is autocatalytic and locally enhances the signal by positive feedback. The inhibitor, which is also activated by the activator, provides a much more diffuse negative feedback, and coupled together, will produce a stable signaling pattern (31). Similar to the Turing instability model, is the wave-pinning (WP) model proposed by Mori et al. 2008 which also relies on an activator-inactivator pair, unequal diffusivities, and positive feedback on the activator. In addition, the WP model requires conservation of the active and inactive species and that the inhibitor is depleted as activation

takes place. These conditions lead to the formation of a decelerating wave front which eventually becomes stationary, or pinned, leading to stable pattern formation (32).

The last category relies on localized excitation and global inhibition (LEGI) while also incorporating a response term that is controlled by the difference between those two processes. Upon stimulation by a gradient, both the excitation and inhibition processes are activated; however, the excitation reacts faster than the inhibition causing the response. In time, the response will undergo adaptation and all three processes will reach a steady state. The excitation profile will mimic the graded receptor occupancy across the cell while the inhibitor profile is proportional to the mean level of receptor occupancy and is uniform across the cell. As a result, the excitation exceeds the inhibition at the front of the cell, but as the level of receptor occupancy decreases toward the back of the cell, the inhibitor will eventually exceed the excitation. This leads to a persistent response at the front of the cell with a limited response at the rear of the cell (33, 34). Variations on this model include the two-component LEGI model which introduces an additional species that allows for two LEGI mechanisms to happen in parallel leading to amplification of the external gradient, something the original LEGI model cannot do (35). A balanced inactivation model has also been proposed to explain the clearly distinct front and rear regions that form in polarized cells. This variation incorporates a new species that antagonizes the response leading to a more switch-like behavior in response to the external gradient (36). Positive feedback loops triggered by the response involving autocatalysis, substrate delivery or depletion, as well as inhibition of degradation have all been proposed as additions to the LEGI model to better explain features of polarization during chemotaxis (26).

In addition to the large collection of theoretical work that has been done describing possible mechanisms for gradient sensing and polarization, a number of biochemistry-based,

mechanistic models have also been explored. Based on experiments in *Dictyostelium discoideum* that suggested the phosphoinositides PIP₂ and PIP₃ may be the source of signal amplification in the gradient sensing pathway (37), Narang et al. 2001 proposed a model describing the kinetics of the phosphoinositide cycle and how a localized increase in the pool of PIP₂ can be generated by positive feedback on the PIP₂-producing enzyme PI4P5K (phosphatidylinositol-4-phosphate 5-kinase) at the membrane while global inhibition is happening through a substrate-depletion mechanism caused by the formation of inositol triphosphate during PIP₂ hydrolysis (38). Building on this model, was the model by Levchenko and Iglesias 2002 which introduces the GPCR-activated enzyme PI3K as a local activator for PIP₃ production and PTEN (phosphatase and tensin homolog) as the global inhibitor due to its 3' lipid phosphatase activity (39). In a model describing gradient sensing and polarization in neutrophils, Onsum and Rao 2007 include the Rho GTPases Ras and RhoA to link the PI3K/PTEN pathway with F-actin polymerization at the front of the cell and myosin contractility at the rear (40). Schneider and Haugh 2005 developed a model that showed experimental results of PIP₃-mediated PDGF gradient sensing in fibroblast cells could be quantitatively reproduced by a model that does not contain feedback amplification or inhibition mechanisms, including only receptor activation dynamics and PI3K exchange from a common cytosolic pool (41).

1.4 Mechanistic Modeling of PLC/PKC Signaling in Fibroblast Chemotaxis

While new models of chemotaxis continue to be proposed, a “unified” model that captures all the features of chemotactic cells does not exist. Given the diversity of cell-biological contexts and experimental evidence, it seems misguided to think that any one model will be able to explain the chemotactic behaviors of all cell types, much less their molecular requirements

and mechanisms. With the ideas embodied by the previously cited models in mind, but asserting a more mechanistic emphasis, we formulated and analyzed models to investigate signal amplification of the PLC/PKC pathway. Based on the experimental results described above, we knew the key species and features that this model needed to include, namely, the PDGF receptor, the PLC and PKC enzymes, and the lipid intermediate, DAG. In our model, active PDGF receptors at the plasma membrane recruit the PLC enzyme from the cytosol to form active PLC at the membrane. Active PLC hydrolyzes PIP_2 , leaving the lipid product DAG, which recruits PKC from the cytosol and forms active PKC. The experimental results from the chemotaxis assays suggested active PKC phosphorylates and inactivates Myosin IIA which links this signal transduction pathway to changes in the actomyosin cytoskeleton and consequently the cell's motility.

From this basic description of the biology and consideration of putative feedback mechanisms in the literature, and based on fundamentals of chemical reaction engineering, we composed partial differential equations describing the intracellular diffusion and transformations (formation of complexes and biochemical reactions) of the molecular species in their various states. With with the appropriate diffusion constants, initial conditions, and boundary conditions, this reaction system was implemented in the Virtual Cell (VCell) software environment (42). A two-dimensional cell geometry maintaining the approximate surface area to volume ratio of a migrating fibroblast was used for simulations, with the steepness and midpoint concentration of PDGF was varied across the length of the cell. With this model, we were able to link the external PDGF gradient conditions to the activation of PKC. Based on this fundamental structure, we searched the literature for sources of feedback or other mechanisms of regulation that could be added to this model to amplify the pathway and polarize the DAG and PKC signaling. As a first

step, we considered the influence of the myristoylated alanine-rich C kinase substrate (MARCKS) protein, specifically its ability to buffer PIP_2 (43-45). We then went on to consider other putative feedback mechanisms reported in the literature (46-49), with the lipid intermediate phosphatidic acid proving to be a key molecular player. The influence of at least two feedbacks is necessary for polarization of PLC/PKC signaling elicited by shallow chemoattractant gradients. Finally, we refined our modeling to consider the regulation of the $\text{PLC}\gamma 1$ enzyme, at the level of its domain structure. By developing this mechanistic model, we also created an explicit framework to guide future experimental verification of our proposed feedback mechanisms and other model predictions.

1.5 Overview of Dissertation

In the remainder of this dissertation, mechanisms for signal amplification of the PLC/PKC pathway are proposed and analyzed to assess their role in polarizing the intracellular signaling pathway in response to gradients of PDGF. Chapter 2 describes the formulation of the reaction-diffusion model and investigates the role of MARCKS in signal amplification of the PLC/PKC pathway. Our results show that the regulation of MARCKS by active PKC is able to amplify the pathway at sufficiently steep gradients. To our knowledge, the buffering ability of PIP_2 by MARCKS is novel in its method of action for signal amplification.

In Chapter 3, we build on the results of Chapter 2 and introduce a new lipid species, phosphatidic acid (PA), as part of two feedback mechanisms. Our results indicate that these feedback loops can synergize with the regulation of MARCKS for substantial signal amplification at shallow gradients (10%) and create a more robust response to changes in PDGF gradient conditions. An analysis of parameter variations also indicated a critical role for DAG

kinases in controlling the lipid metabolism and thus polarization of the PLC/PKC pathway.

Chapter 3 also includes results gained from a one-dimensional, agent-based model of wound invasion developed by Dr. Anisur Rahman, in which the PDGF gradient evolves as a continuum while fibroblasts are treated as motile line segments. Based on the characterization of the PLC/PKC polarization model, thresholds for polarization based on PDGF gradient conditions were applied to the motility of the fibroblasts, such that only cells that are experiencing the PDGF gradient conditions necessary for polarization exhibit chemotactic motility.

Chapter 4 describes the development of a rule-based model using BioNetGen to study the activation dynamics of the PLC γ 1 isozyme. Our results highlight how variations in a particular reaction rate lead to increased lifetime of PLC γ 1 at the membrane corresponding to a proposed method of feedback investigated in Chapter 3. This detailed model of PLC γ 1 activation is also combined with the PLC/PKC polarization model and mutations affecting the activation of PLC γ 1 are assessed on their ability to polarize the PLC/PKC pathway.

Chapter 5 concludes the dissertation describing the insights from this work and the outlook for future areas of study of PLC/PKC signaling. Given the role chemotaxis plays in cancer cell metastasis, and considering numerous diseases implicated by aberrant activation of PLC (50-52) and PKC (53-55), further study of this signaling pathway will continue to be of vital importance.

1.6 References

1. Lara Rodriguez L, Schneider IC. Directed cell migration in multi-cue environments. *Integrative Biology (Cambridge)*. 2013 Oct 21;;5(11):136-1323.
2. Bear JE, Haugh JM. Directed migration of mesenchymal cells: where signaling and the cytoskeleton meet. *Current Opinion in Cell Biology*. 2014;30:74-82.
3. Eming SA, Martin P, Tomic-Canic M. Wound repair and regeneration: Mechanisms, signaling, and translation. *Science Translational Medicine*. 2014 Dec 3;;6(265):265sr6.
4. Werner S, Grose R. Regulation of wound healing by growth factors and cytokines. *Physiological Reviews*. 2003 Jul 1;;83(3):835-70.
5. Singer AJ, Clark RAF. Cutaneous wound healing. *New England Journal of Medicine*. 1999 Sept 2;;341(10):738-46.
6. Thiery JP. Epithelial–mesenchymal transitions in tumour progression. *Nature Reviews. Cancer*. 2002;2(6):442-54.
7. Lämmermann T, Bader BL, Monkley SJ, Worbs T, Wedlich-Söldner R, Hirsch K, et al. Rapid leukocyte migration by integrin-independent flowing and squeezing. *Nature (London)*. 2008;453(7191):51-5.
8. Talkenberger K, Cavalcanti-Adam EA, Voss-Böhme A, Deutsch A. Amoeboid-mesenchymal migration plasticity promotes invasion only in complex heterogeneous microenvironments. *Scientific Reports*. 2017;7(1):9237-12.
9. Friedl P, Wolf K. Plasticity of cell migration: a multiscale tuning model. *The Journal of Cell Biology*. 2010;188(1):11-9.
10. Hind L, Vincent WB, Huttenlocher A. Leading from the back: The role of the uropod in neutrophil polarization and migration. *Developmental Cell*. 2016;38(2):161-9.
11. Chaplin DD. Overview of the immune response. *Journal of Allergy and Clinical Immunology*. 2010;125(2):S3-S23.
12. Petrie RJ, Doyle AD, Yamada KM. Random versus directionally persistent cell migration. *Nature Reviews. Molecular Cell Biology*. 2009;10(8):538-49.
13. Erik S Welf, Shoeb Ahmed, Heath E Johnson, Adam T Melvin, Jason M Haugh. Migrating fibroblasts reorient directionality by a metastable, PI3K-dependent mechanism. *The Journal of Cell Biology*. 2012 Apr 2;;197(1):105-14.
14. Burridge K, Guilluy C. Focal adhesions, stress fibers and mechanical tension. *Experimental Cell Research*. 2016;343(1):14-20.

15. Kendall RT, Feghali-Bostwick CA. Fibroblasts in fibrosis: novel roles and mediators. *Frontiers in Pharmacology*. 2014;5:123.
16. Srinivasan S, Wang F, Glavas S, Ott A, Hofmann F, Aktories K, et al. Rac and Cdc42 play distinct roles in regulating PI(3,4,5)P₃ and polarity during neutrophil chemotaxis. *The Journal of Cell Biology*. 2003;160(3):375-85.
17. Welch HCE, Coadwell WJ, Stephens LR, Hawkins PT. Phosphoinositide 3-kinase-dependent activation of Rac. *FEBS Letters*. 2003;546(1):93-7.
18. Rohatgi R, Ho HY, Kirschner MW. Mechanism of N-WASP activation by CDC42 and phosphatidylinositol 4, 5-bisphosphate. *The Journal of Cell Biology*. 2000 Sep 18;150(6):1299-310.
19. Rotty JD, Wu C, Bear JE. New insights into the regulation and cellular functions of the ARP2/3 complex. *Nature Reviews. Molecular Cell Biology*. 2012;14(1):7-12.
20. Lebensohn AM, Kirschner MW. Activation of the WAVE complex by coincident signals controls actin assembly. *Molecular Cell*. 2009;36(3):512-24.
21. Monypenny J, Zicha D, Higashida C, Ocegueda-Yanez F, Narumiya S, Watanabe N. Cdc42 and Rac family GTPases regulate mode and speed but not direction of primary fibroblast migration during platelet-derived growth factor-dependent chemotaxis. *Molecular and Cellular Biology*. 2009;29(10):2730-47.
22. Wu C, Asokan S, Berginski M, Haynes E, Sharpless N, Griffith J, et al. Arp2/3 is critical for lamellipodia and response to extracellular matrix cues but is dispensable for chemotaxis. *Cell*. 2012 Mar 2;148(5):973-87.
23. Asokan S, Johnson H, Rahman A, King S, Rotty J, Lebedeva I, et al. Mesenchymal chemotaxis requires selective inactivation of Myosin II at the leading edge via a noncanonical PLC γ /PKC α pathway. *Developmental Cell*. 2014 Dec 22;31(6):747-60.
24. Arrieumerlou C, Meyer T. A local coupling model and compass parameter for eukaryotic chemotaxis. *Developmental Cell*. 2005;8(2):215-27.
25. Iglesias PA, Levchenko A. Modeling the cell's guidance system. *Sci Signal*. 2002 -09-03 00:00:00;2002(148).
26. Iglesias PA, Devreotes PN. Navigating through models of chemotaxis. *Current Opinion in Cell Biology*. 2008 February 1;20(1):35-40.
27. Devreotes P, Janetopoulos C. Eukaryotic chemotaxis: Distinctions between directional sensing and polarization. *The Journal of Biological Chemistry*. 2003;278(23):20445-8.

28. Jilkine A, Edelstein-Keshet L. A comparison of mathematical models for polarization of single eukaryotic cells in response to guided cues. *PLoS Computational Biology*. 2011 Apr 1;7(4):e1001121.
29. Landge AN, Jordan BM, Diego X, Müller P. Pattern formation mechanisms of self-organizing reaction-diffusion systems. *Developmental Biology*. 2020 Apr 1;460(1):2-11.
30. Gierer A, Meinhardt H. A theory of biological pattern formation. *Kybernetik*. 1972 Dec;12(1):30.
31. Meinhardt H, Gierer A. Pattern formation by local self-activation and lateral inhibition. *BioEssays : news and reviews in molecular, cellular and developmental biology*. 2000 Aug;22(8):753-60.
32. Mori Y, Jilkine A, Edelstein-Keshet L. Wave-pinning and cell polarity from a bistable reaction-diffusion system. *Biophysical Journal*. 2008;94(9):3684-97.
33. Kutscher B, Devreotes P, Iglesias PA. Local excitation, global inhibition mechanism for gradient sensing: An interactive applet. *Science Signaling*. 2004 Feb 10;2004(219):pl3.
34. Janetopoulos C, Firtel RA. Directional sensing during chemotaxis. *FEBS Letters*. 2008;582(14):2075-85.
35. Ma L, Janetopoulos C, Yang L, Devreotes PN, Iglesias PA. Two complementary, local excitation, global inhibition mechanisms acting in parallel can explain the chemoattractant-induced regulation of PI(3,4,5)P₃ response in Dictyostelium cells. *Biophysical Journal*. 2004 Dec;87(6):3764-74.
36. Levine H, Kessler DA, Rappel W. Directional sensing in eukaryotic chemotaxis: A balanced inactivation model. *Proceedings of the National Academy of Sciences - PNAS*. 2006 Jun 27;103(26):9761.
37. Parent CA, Devreotes PN. A cell's sense of direction. *Science*. 1999 Apr 30;284(5415):765-70.
38. Narang A, Subramanian KK, Lauffenburger DA. A mathematical model for chemoattractant gradient sensing based on receptor-regulated membrane phospholipid signaling dynamics. *Annals of Biomedical Engineering*. 2001 Jan 1;29(8):677-91.
39. Levchenko A, Iglesias PA. Models of eukaryotic gradient sensing: Application to chemotaxis of amoebae and neutrophils. *Biophysical Journal*. 2002;82(1):50-63.
40. Onsum M, Rao CV. A mathematical model for neutrophil gradient sensing and polarization. *PLoS Computational Biology*. 2007 Mar 16;3(3):e36.

41. Schneider IC, Haugh JM. Quantitative elucidation of a distinct spatial gradient-sensing mechanism in fibroblasts. *The Journal of Cell Biology*. 2005 December 5;;171(5):883-92.
42. Cowan AE, Moraru II, Schaff JC, Slepchenko BM, Loew LM. Spatial modeling of cell signaling networks. In: *Methods in Cell Biology*. United States: Elsevier Science & Technology; 2012. p. 195-221.
43. Michael Glaser, Stephen Wanaski, Carolyn A. Buser, Valentina Boguslavsky, Wahid Rashidzada, Andrew Morris, et al. Myristoylated alanine-rich C kinase substrate (MARCKS) produces reversible inhibition of phospholipase C by sequestering phosphatidylinositol 4,5-bisphosphate in lateral domains. *Journal of Biological Chemistry*. 1996 Oct 18;;271(42):26187-93.
44. McLaughlin S, Wang J, Gambhir A, Murray D. PIP2 and proteins: Interactions, organization, and information flow. *Annual Review of Biophysics and Biomolecular Structure*. 2002 Jun;31(1):151-75.
45. Wang J, Gambhir A, Hangyás-Mihályiné G, Murray D, Golebiewska U, McLaughlin S. Lateral sequestration of phosphatidylinositol 4,5-bisphosphate by the basic effector domain of myristoylated alanine-rich C kinase substrate is due to nonspecific electrostatic interactions. *The Journal of Biological Chemistry*. 2002;277(37):34401-12.
46. Jones GA, Carpenter G. The regulation of phospholipase C- γ 1 by phosphatidic acid. *J Biol Chem*. 1993 10/05;;268(28):20845-50.
47. H Eldar, P Ben-Av, U S Schmidt, E Livneh, M Liscovitch. Up-regulation of phospholipase D activity induced by overexpression of protein kinase C- α . Studies in intact Swiss/3T3 cells and in detergent-solubilized membranes in vitro. *Journal of Biological Chemistry*. 1993 Jun 15;;268(17):12560-4.
48. Y H Lee, H S Kim, J K Pai, S H Ryu, P G Suh. Activation of phospholipase D induced by platelet-derived growth factor is dependent upon the level of phospholipase C- γ 1. *Journal of Biological Chemistry*. 1994 Oct 28;;269(43):26842-7.
49. Henage LG, Exton JH, Brown HA. Kinetic analysis of a mammalian phospholipase D: allosteric modulation by monomeric GTPases, protein kinase C, and polyphosphoinositides. *The Journal of biological chemistry*. 2006 Feb 10;;281(6):3408-17.
50. Hajicek N, Keith NC, Siraliev-Perez E, Temple BR, Huang W, Zhang Q, et al. Structural basis for the activation of PLC- γ isozymes by phosphorylation and cancer-associated mutations. *eLife*. 2019;8(2019).
51. Liu Y, Bunney TD, Khosa S, Macé K, Beckenbauer K, Askwith T, et al. Structural insights and activating mutations in diverse pathologies define mechanisms of deregulation for phospholipase C gamma enzymes. *EBioMedicine*. 2020;51:102607.

52. Koss H, Bunney TD, Behjati S, Katan M. Dysfunction of phospholipase C γ in immune disorders and cancer. *Trends in Biochemical Sciences*. 2014;39(12):603-11.
53. Konopatskaya O, Poole AW. Protein kinase C α : disease regulator and therapeutic target. *Trends in Pharmacological Sciences*. 2009;31(1):8-14.
54. Kang J. Protein kinase C (PKC) isozymes and cancer. *New Journal of Science*. 2014 May 4;2014:1-36.
55. Garg R, Benedetti LG, Abera MB, Wang H, Abba M, Kazanietz MG. Protein kinase C and cancer: what we know and what we do not. *Oncogene*. 2013;33(45):5225-37.

CHAPTER 2

A Reaction-Diffusion Model Explains Amplification of the PLC/PKC Pathway in Fibroblast Chemotaxis

Adapted from: Mohan K, Nosbisch JL, Elston TC, Bear JE, Haugh JM. A reaction-diffusion model explains amplification of the PLC/PKC pathway in fibroblast chemotaxis. *Biophysical Journal*. 2017. July 11;113(1):185–94. 10.1016/j.bpj.2017.05.035

2.1 Introduction

Chemotaxis, or cell migration directed by spatial gradients of soluble chemicals (chemoattractants), is a primary means of organizing cell movements in and between tissues. Whereas chemotaxis of fast-moving amoeboid cells (e.g., leukocytes and *Dictyostelium discoideum*) has been extensively studied for decades (1,2), chemotaxis of slow-moving mesenchymal cells (e.g., fibroblasts and metastatic cancer cells) is far less well understood (3). Fibroblast chemotaxis, elicited by platelet-derived growth factor (PDGF) and other chemoattractants, is considered a rate-limiting step in physiological processes that include embryonic development and invasion of the fibrin clot during the proliferative phase of wound healing (4–8). With regard to the latter, failure to coordinate and regulate the movements and functions of fibroblasts and other cell types results in aberrant wound repair, with either insufficient or excessive matrix production leading to chronic ulcers or fibrosis, respectively (9).

Chemotaxis and other forms of directed cell migration are controlled by a network of intracellular signaling pathways that modulate the dynamics of the actin cytoskeleton (2,3). In the prevailing conceptual model of amoeboid chemotaxis, gradient sensing and biased movement are linked through receptor-mediated activation of phosphoinositide 3-kinase (PI3K) and/or the small GTPases Rac and Cdc42, which in turn activate nucleation-promoting factors that position the Arp2/3 complex at the plasma membrane and thus promote F-actin polymerization by dendritic branching of actin filaments with growing barbed ends (10–13). This chemotactic “compass” is amplified by positive feedback within the signaling circuit at the front of the cell and mutual antagonism with active RhoA at the cell rear, and thus it biases Arp2/3-mediated membrane protrusion toward the external chemoattractant gradient (14). Numerous mathematical models have been proposed to explore these specific concepts and the biochemical pathways

involved (reviewed in (15–17)). These models offer variations of principles such as Turing instability (or diffusion-driven instability) (18–21), local excitation/ global inhibition (22,23), and wave propagation (24).

Although this view of chemotactic gradient sensing and response parsimoniously explains the extensive evidence gathered for amoeboid cells, it is reasonable to question whether or not it applies to chemotaxis of weakly polarized, mesenchymal cells. In fibroblasts, signaling through PI3K, Rac, and Cdc42 is localized in leading-edge protrusions (lamellipodia) (25–27), and this circuit is clearly important for efficient migration and the cell-shape dynamics associated with fibroblast turning (28–30); however, studies have also indicated that all of these signaling activities are dispensable for fibroblast chemotaxis to PDGF (27,31). Even more compelling, fibroblasts with Arp2/3 complex depleted or conditionally knocked out lack dendritic F-actin and lamellipodia and show greatly reduced migration speed, as expected, yet they still chemotax toward PDGF (32,33). Forced to reevaluate which signaling pathways and mechanisms of cytoskeletal regulation are essential for fibroblast chemotaxis, we recently showed that PDGF receptor-mediated activation of the phospholipase C (PLC)/protein kinase C (PKC) pathway, and PKC α -mediated regulation of myosin IIA motor activity, are required (33). This pathway is well-suited for the control of mesenchymal chemotaxis, given the distribution of myosin IIA and its role in reining in leading-edge protrusion in mesenchymal cells (3,34). PKC α is activated through its binding to the lipid second messenger diacylglycerol (DAG), which is formed from hydrolysis of phosphatidylinositol (4,5)-bisphosphate (PIP₂) by PLC (35,36). Strikingly, in fibroblasts exposed to a shallow PDGF gradient, we found that the density of DAG in the plasma membrane is focally enriched at the up- gradient leading edge and much lower elsewhere (33), suggesting an internal amplification mechanism that has yet to be explored.

In this work, we have developed and analyzed a mechanistic, reaction-diffusion model of the PLC/PKC signaling pathway activated in a PDGF gradient. The model includes the major proteins (PDGF receptor, PLC, and PKC) and lipids (PIP₂ and DAG) in the central pathway, as well as the abundant protein myristoylated alanine-rich C kinase substrate (MARCKS), a buffer of PIP₂ that is neutralized by PKC-mediated phosphorylation (37–39). This mechanism has been implicated in fibroblast chemotaxis (40) and constitutes a positive feedback loop that is sufficient for local amplification of DAG and active PKC in our model; however, by itself it fails to explain the focal enrichment of DAG in a shallow PDGF gradient. To remedy this, we show that MARCKS regulation can synergize with other putative feedbacks, which are similarly limited in their capacity to enhance amplification. We expect that the model presented here will serve as a framework for linking molecular-scale understanding of PDGF gradient sensing to collective fibroblast migration during wound invasion and as a guide for the design of live-cell imaging experiments.

2.2 Materials and Methods

2.2.1 Basic model description

Our model consists of partial differential equations and associated boundary and initial conditions, which describe receptor-mediated activation of the PLC/PKC pathway (Fig. 2.1A). A complete description of the model equations and parameter values is provided in *Appendix A*. Model species, their diffusivity values, and initial conditions are listed in Table A.1; model rate equations and the corresponding base-case values of rate constants are listed in Table A.2.

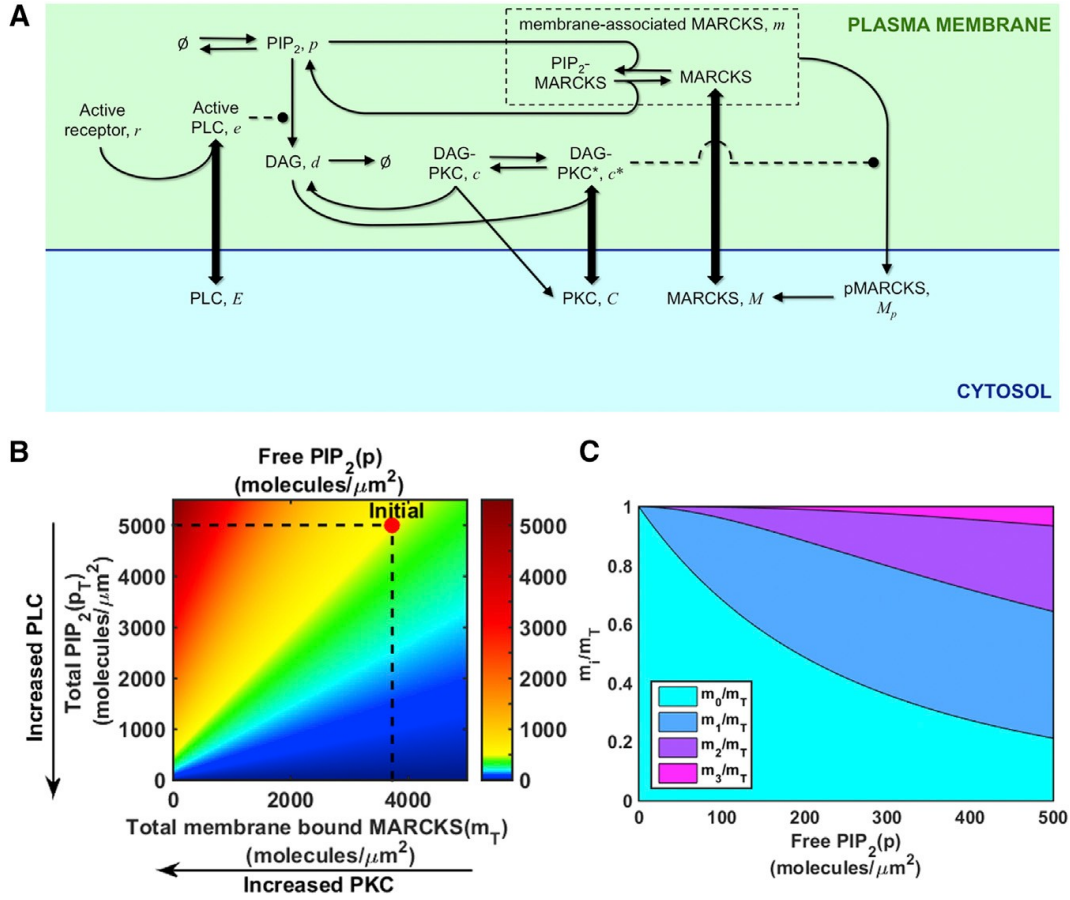


Figure 2.1 Reaction-diffusion model of the PLC/PKC pathway. (A) Schematic of the pathway describing interactions among signaling proteins (PLC, PKC, and MARCKS) and plasma membrane lipids (PIP₂ and DAG). Dashed arrows with circles at the end signify catalysis of the indicated transition. (B) Heat map plotting the density of free PIP₂ (p) as a function of the density of membrane-bound MARCKS (m_T) and of the density of total PIP₂ (p_T). A shift from the initial condition may be interpreted as changes in PLC-mediated PIP₂ hydrolysis and/or PKC activation, as indicated. (C) The fractions of membrane-bound MARCKS with i molecules of PIP₂ bound (m_i/m_T) are plotted as a function of the density of free PIP₂ (p).

The extracellular ligand, PDGF, is recognized by PDGF receptors on the cell surface, resulting in receptor binding and dimerization that results in formation of active receptor complexes, as modeled previously (41,42). Active receptors recruit inactive PLC enzyme (E) from the cytosol to form active PLC at the membrane (e). Active PLC hydrolyzes PIP₂ (free-density p). In the absence of PDGF, the density of PIP₂ is maintained through basal synthesis and

turnover. PIP_2 hydrolysis by PLC generates the lipid second messenger, DAG (d). DAG is consumed by a pseudo-first-order reaction that represents the action of DAG kinases and the subsequent metabolism of phosphatidic acid (43). DAG recruits catalytically competent but inactive PKC (C) from the cytosol by reversible binding of the tandem C1 domain of PKCs, forming active PKC (c^*) at the membrane (35). Membrane-bound PKC is sensitive to dephosphorylation, and so the active PKC is converted to an inactive, membrane-bound form (c); this species is either autophosphorylated to regenerate active PKC (35) or it dissociates to join the cytosolic pool. In addition to the central PLC/PKC pathway described thus far, the model incorporates the regulatory protein MARCKS. MARCKS is an abundant substrate of PKC that is present in both cytosolic and membrane-bound forms (39). The unphosphorylated, cytosolic form (M) inserts into the plasma membrane via its myristoyl group and interacts with PIP_2 via its effector domain; the latter is a high-avidity, electrostatic interaction, and thus, MARCKS sequesters a substantial fraction of the intracellular PIP_2 (37,44). The membrane-bound forms of MARCKS are phosphorylated by active PKC, causing loss of affinity for the plasma membrane and liberation of PIP_2 ; the phosphorylated form of MARCKS (M_p) is cytosolic (38). MARCKS is dephosphorylated in the cytosol to complete the cycle.

2.2.2 Modeling MARCKS-membrane interactions

To model the binding of unphosphorylated MARCKS with the membrane, we assume that the reversible insertion of the myristoyl lipid is rate-limiting, whereas the interactions with PIP_2 at the membrane are in quasi-equilibrium. MARCKS can interact with multiple PIP_2 molecules, which explains the cooperativity of binding (44,45); for simplicity, we model the polybasic motif of MARCKS as three equivalent binding sites for PIP_2 . Therefore, defining m_i as

the density of membrane-bound MARCKS with i molecules of PIP₂ bound, p as the density of free PIP₂, and K_{PIP_2} as the single-site equilibrium constant,

$$m_i = \left(\frac{4-i}{i} \right) K_{PIP_2} p m_{i-1}, \quad (2.1)$$

and taking m_T as the sum of m_i , we obtain

$$m_T = m_0 (1 + K_{PIP_2} p)^3. \quad (2.2)$$

From Eqs. 2.1 and 2.2, the density of PIP₂ molecules bound to MARCKS is calculated, and hence the density of total PIP₂, p_T , is related to p as follows:

$$p_T = p + \left(\frac{3K_{PIP_2}p}{1 + K_{PIP_2}p} \right) m_T \quad (2.3)$$

Equation 2.3 is rearranged as a quadratic and solved for p (*Appendix A*).

In our simulations, we assume an initial total PIP₂ density (p_T) of 5000 molecules/ μm^2 , which corresponds to a concentration of $\sim 10 \mu M$ on a whole-cell volume basis (39). Given the proposed role of MARCKS as a PIP₂ buffer, we assume that 90% of the PIP₂ is sequestered by MARCKS in resting cells; i.e., the initial free PIP₂ density, p , was 500 molecules/ μm^2 . The total cellular concentration of MARCKS has been estimated at $\sim 10 \mu M$, similar to the abundance of PIP₂ (39). MARCKS is predominantly membrane-localized in resting cells, and so we assume that 90% is membrane-associated initially. This sets the initial value of M at 1 μm , and, based on the assumed geometry of the cell, the initial value of m_T was set at 3727 molecules/ μm^2 . These considerations and Eq. 2.3 determined the value of K_{PIP_2} . With this parameter fixed, the relationship expressed in Eq. 2.3 is used to calculate the density of free PIP₂, which is available to be hydrolyzed by PLC, from computed values of p_T and m_T . This relationship is shown as a heat map, with the initial condition labeled as a point (Fig. 2.1B). Changes elicited by PDGF stimulation, namely, the activation of PLC and PKC, can be viewed as a shift in the coordinates

on this map. Another outcome is that PLC-mediated reduction in free PIP_2 affects the occupancy of membrane-associated MARCKS, which is calculated directly from Eqs. 2.1 and 2.2. As shown for the value of K_{PIP_2} assumed in our model, a decrease in free PIP_2 density results in lower avidity of MARCKS binding and thus progressively fewer PIP_2 molecules bound per molecule of MARCKS at the membrane (Fig. 2.1C).

2.2.3 Model implementation

The PLC/PKC model is implemented in Virtual Cell (<http://www.vcell.org>), a computational environment for modeling and simulation in cell biology (46). The Biomodel and primary simulations are publicly available in Virtual Cell under user name jnosbis, Biomodel name Mohan chemotaxis 2017. The reaction network as defined in the Virtual Cell interface is shown in Fig. 2.2.

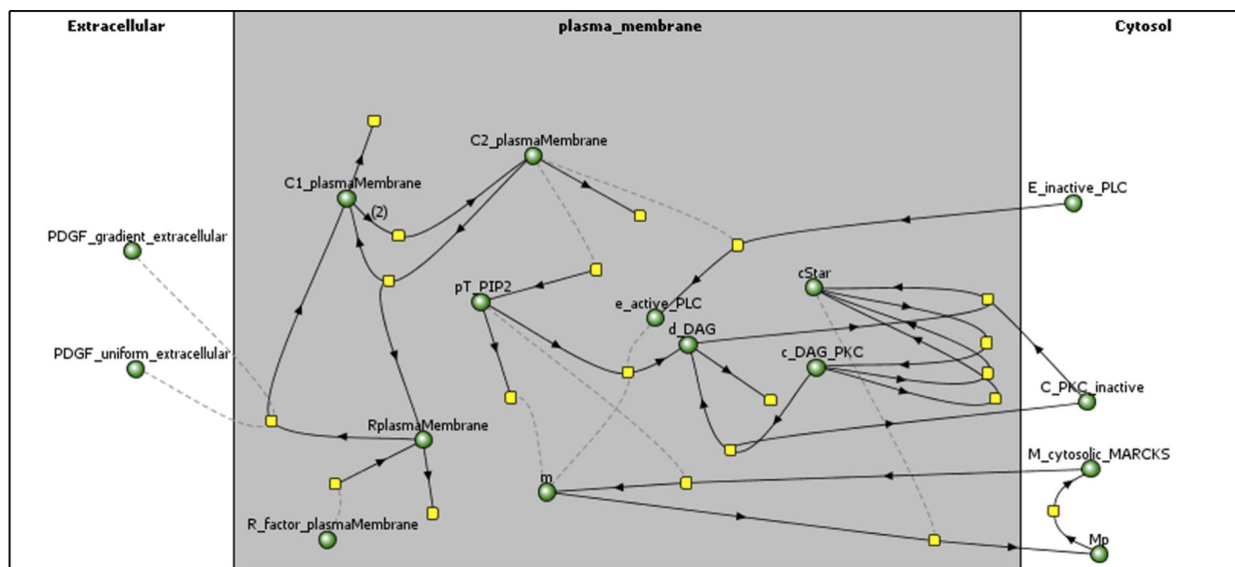


Figure 2.2 Reaction network of the PLC/PKC pathway constructed in Virtual Cell. Green spheres represent the model species. Yellow squares represent the reaction nodes, black solid arrows represent species transformations, and dashed arrows signify catalysis.

The base geometry used in our two-dimensional simulations is an ellipse with a major axis length of $40\ \mu\text{m}$ and minor axis length of $1.8\ \mu\text{m}$; these dimensions yield a head-to-tail length and a cytosolic volume/membrane area ratio that are typical of a migrating fibroblast. Virtual Cell uses a finite-volume method to numerically solve the reaction-diffusion equations, and the Fully-Implicit Finite Volume (variable time step) solver was used, with voxel dimensions of $\Delta x = \Delta y = 0.2\ \mu\text{m}$ and a maximum time step of $0.05\ \text{s}$. We confirmed that a fourfold change of the spatial resolution did not markedly change the results. The initial conditions were chosen such that the system is stationary in the absence of PDGF, after which a linear PDGF gradient is applied parallel to the long axis of the domain. Simulations were run for sufficiently long (nominally, $2 \times 10^4\ \text{s}$) to ensure a steady state.

2.3 Results

2.3.1 Regulation of MARCKS by PKC is sufficient to amplify the PLC/PKC pathway

To the extent that phosphorylation of MARCKS by PKC liberates the PLC substrate PIP_2 , this process constitutes a positive feedback loop, which might amplify the intracellular gradients of DAG and active PKC. To explore this possibility, we simulated an idealized scenario using our model: the response to a PDGF gradient with subsaturating midpoint concentration ($0.03\ \text{nM}$) and a drastic relative steepness of 67% (i.e., 0.02 and $0.04\ \text{nM}$ at the cell's extrema). The twofold ratio of PDGF concentrations results in a 3.65-fold ratio of receptor activation at steady state, owing to the sensitivity of receptor dimerization (41). In the analyses that follow, we use the steady-state, front/ back ratio of active PKC density as a metric to assess pathway amplification.

In the absence of MARCKS regulation or any other feedback in the PLC/PKC pathway, it is intuitive that amplification relative to the gradient of receptor activation is not possible. The saturability of the protein-protein and protein-lipid interactions involved and the depletion of PIP_2 by PLC-catalyzed hydrolysis only diminish the ratio of PKC activation relative to that of receptor activation. Accordingly, in the absence of MARCKS in our base-case model, the steady-state PKC activation ratio is 2.71 (Fig. 2.3A). To identify the effect of MARCKS on the PLC/PKC pathway, we reasoned that the rate constants describing MARCKS phosphorylation (k_{pm}) and dephosphorylation (k_{dpM}) characterize the putative feedback loop. We systematically varied these parameters and found that MARCKS regulation is sufficient to enhance the steady-state PKC activation ratio, achieving values as high as 9.19 for the idealized PDGF gradient (Fig. 2.3B), with a similar ratio of free DAG densities (10.5). Maximal amplification requires an optimal balance of phosphorylation and dephosphorylation and a sufficiently high MARCKS dephosphorylation rate; the optimal value of k_{pm} is approximately proportional to the square root of the k_{dpM} value (Fig. 2.3C), consistent with a scaling analysis (*Appendix A*). We comment on this relationship further in the next section.

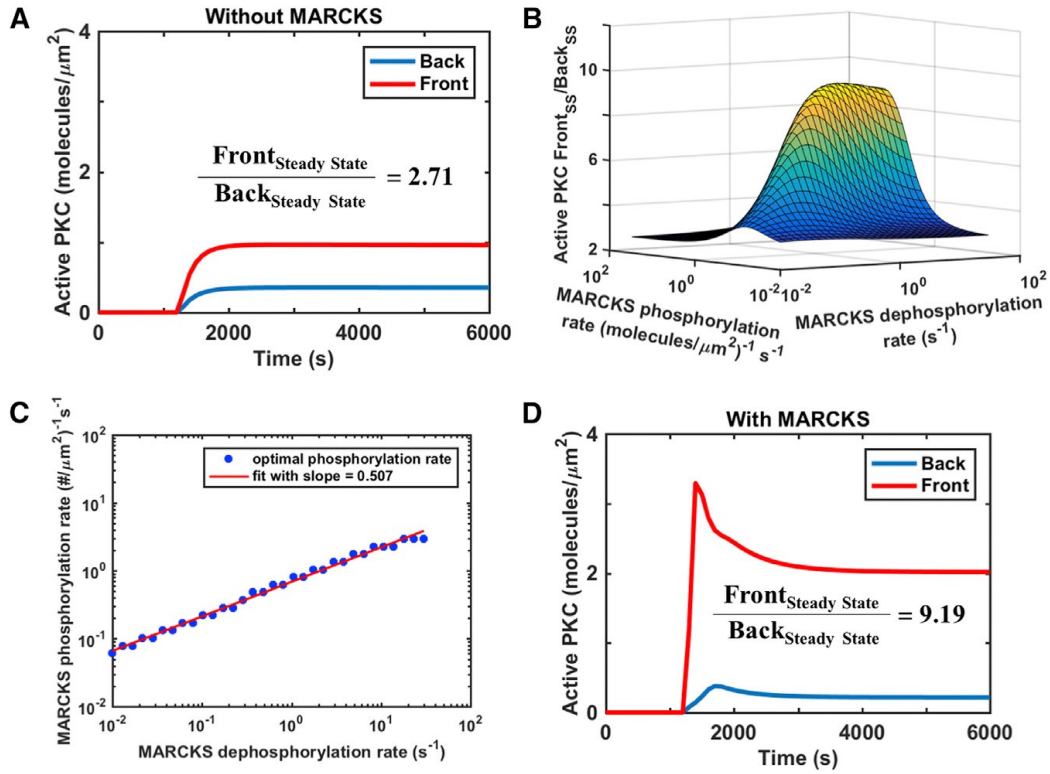


Figure 2.3 Regulation of MARCKS by PKC is sufficient to amplify the PLC/PKC pathway. Simulations were done for a steep PDGF gradient (67% relative gradient) with midpoint $[\text{PDGF}] = 0.03 \text{ nM}$, introduced at time = 1200 s. (A) Kinetics of active PKC (c^*) in the absence of MARCKS. (B) Surface plot of the steady-state front/back ratio of active PKC (c^*) as a function of MARCKS phosphorylation (k_{pm}) and dephosphorylation (k_{dpM}) rate constants. (C) Optimal MARCKS phosphorylation rate constant (dots) for each value of the MARCKS dephosphorylation rate constant. The line shows the best fit of the log-transformed variables. (D) Kinetics of active PKC (c^*) for the base parameter set with $k_{\text{pm}} = 1 \mu\text{m}^{-2} \text{ s}^{-1}$ and $k_{\text{dpM}} = 1 \text{ s}^{-1}$ (see also Fig. 2.4).

Considering the space of parameter values shown in Fig. 2.3B, we show additional results for the parameter set with k_{pm} and k_{dpM} equal to 1 in their respective units; this parameter set yields a PKC activation ratio close to the maximum. The kinetics of the active PKC species at the front and rear of the cell are shown (Fig. 2.3D) and may be compared to the “MARCKS null” case considered in Fig. 2.3A. With MARCKS, the kinetics of active PKC at both ends of the cell show an overshoot and partial adaptation, which is attributed to the rapid liberation and hydrolysis of PIP_2 , followed by slower depletion of the total pool of PIP_2 as the steady state is

approached (Fig. 2.3D). Without MARCKS, there is no sequestered PIP_2 , and DAG accumulation mirrors the depletion of PIP_2 ; consequently, the rapid initial phase of PIP_2 hydrolysis is absent (Fig. 2.3A). Regarding the simulation represented in Fig. 2.3D, the kinetics of the other model species are shown in Fig. 2.4; the spatiotemporal dynamics of MARCKS are particularly interesting and are discussed in the next section. We conclude that the influence of MARCKS constitutes a PKC-mediated feedback loop that is sufficient to amplify an intracellular gradient of PLC/PKC signaling in cells exposed to a steep PDGF gradient.

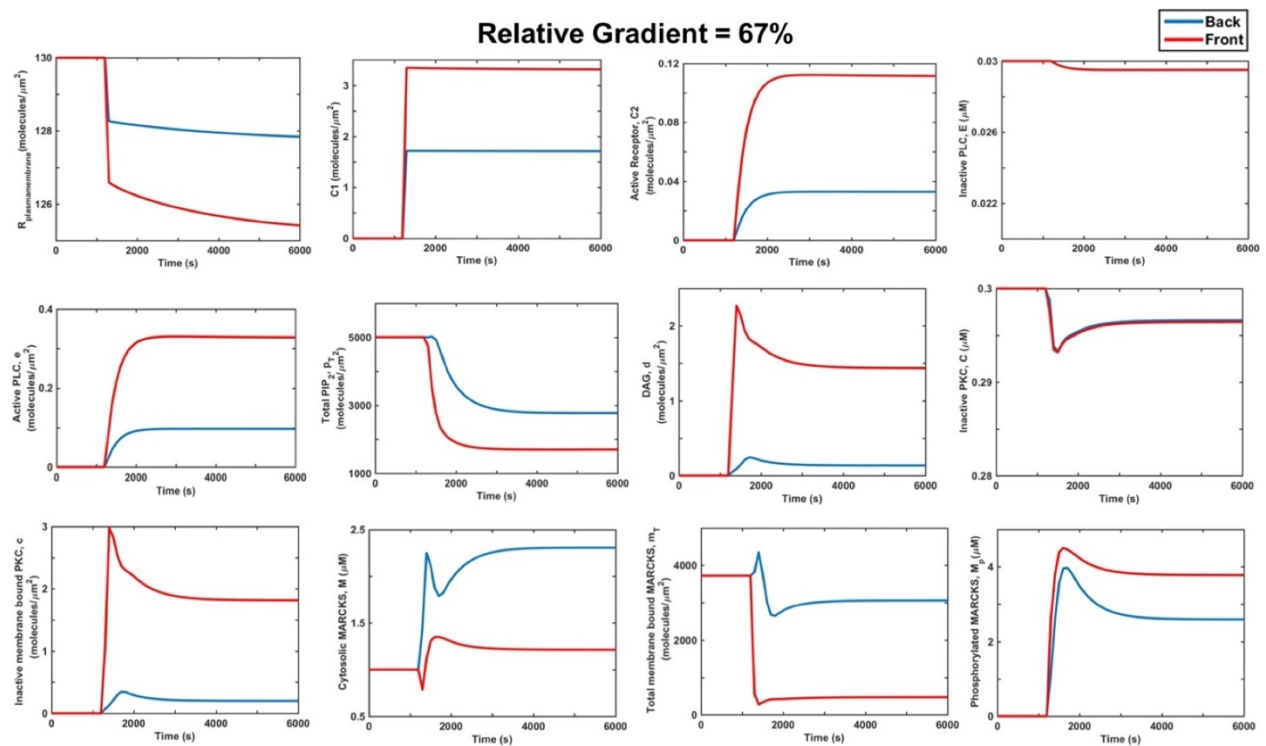


Figure 2.4 Kinetics of all species for the simulation represented in Fig. 2.3D.

2.3.2 Differential buffering of PIP₂ by MARCKS as a distinct mode of gradient amplification

To explore the mechanism by which regulation of MARCKS results in amplification of the PLC/PKC pathway, we plot the changes in free PIP₂ density at the front and back of the cell in terms of the total PIP₂ and total membrane-bound MARCKS densities for the same parameter set as in Figs. 2.3D and 2.4 (Fig. 2.5A). Receptor-mediated activation of PLC reduces the total PIP₂ level, whereas activation of PKC tends to reduce the membrane-associated MARCKS. We also plot the initial and steady-state levels of PIP₂ (bound to MARCKS and free), membrane-bound MARCKS with various stoichiometries of PIP₂ occupancy (m_i), and cytosolic MARCKS (M , M_p) at the front and back of the cell (Fig. 2.5, B–D). With PKC-mediated MARCKS regulation, the level of free PIP₂ is higher at the front of the cell, despite a lower total PIP₂ density there compared to the back (Fig. 2.5, A and B). Accordingly, there is far less membrane-bound MARCKS at the front, although the MARCKS there is more avidly bound (Fig. 2.5, A and C). Thus, the increase in PKC activity at the front compared to the back leads to differential buffering of PIP₂ by MARCKS.

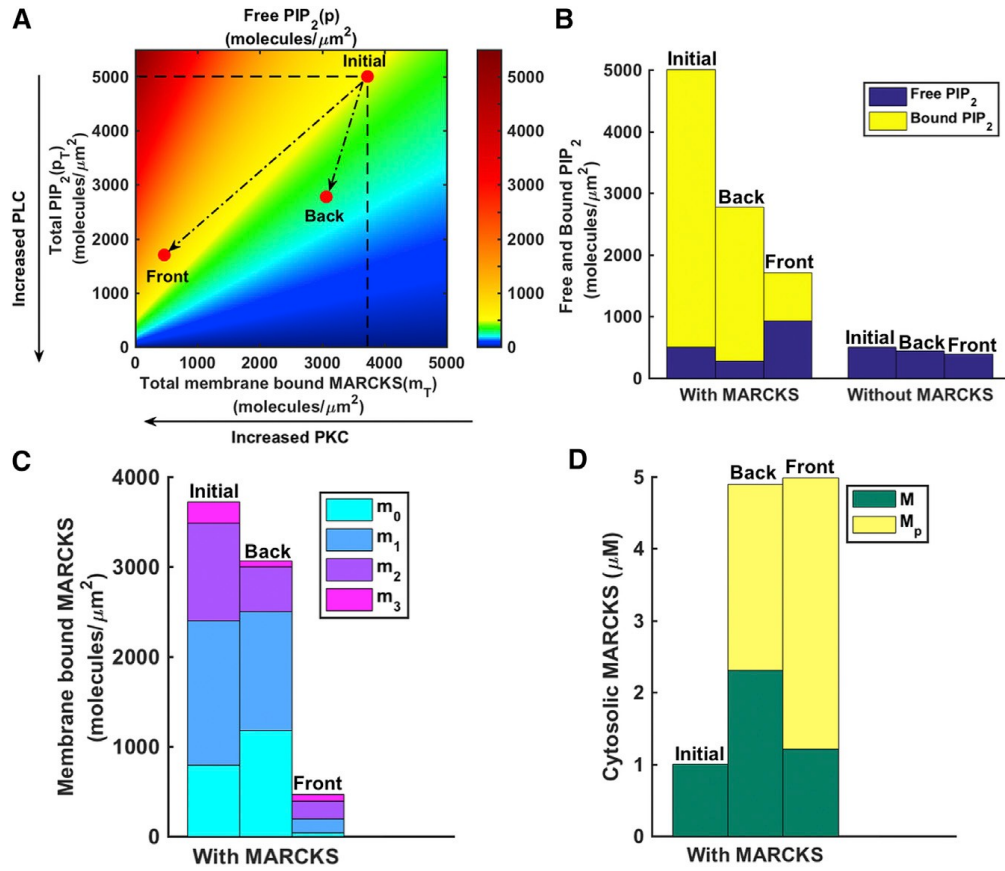


Figure 2.5 Differential buffering of PIP₂ by MARCKS as a distinct mode of gradient amplification. These results pertain to the simulation with base parameters and a steep PDGF gradient, as in Figs. 2.3D and 2.4, comparing steady-state levels at the front and back of the simulated cell and the initial levels. (A) Heat map of free PIP₂ (p) as a function total PIP₂ (p_T) and total membrane-bound MARCKS (m_T), as introduced in Fig. 2.1B. Circles show how the PDGF gradient shifts the steady state at the front and rear of the simulated cell. (B–D) Bar plots of free and bound PIP₂ levels in the presence and absence of MARCKS (B), membrane-bound MARCKS with various numbers of PIP₂ bound (C), and cytosolic MARCKS (unphosphorylated, M , and phosphorylated, M_p) (D).

MARCKS phosphorylation is accompanied by an increase in the overall concentration of MARCKS in the cytosol. Interestingly, the subsequent dephosphorylation of MARCKS yields a higher concentration of unphosphorylated MARCKS (M) able to bind PIP₂, especially at the back of the cell (Fig. 2.5D), with complex kinetics (Fig. 2.4). The concentration of M spikes rapidly, and membrane-bound MARCKS initially increases at the back; these responses quickly

adapt as PIP₂ decays, followed by a second, slow phase that is attributed to cytosolic diffusion. The increase in unphosphorylated MARCKS ameliorates the reduction in MARCKS binding caused by depletion of free PIP₂, more so at the back of the cell, and thus, the differential buffering between the front and back is enhanced.

The scenario described above is that of a long-range inhibition by MARCKS. Consistent with this notion, the scaling relationship presented in Fig. 2.3C was interpreted as a trade-off between maintaining both substantial MARCKS phosphorylation at the front of the cell and a gradient of unphosphorylated MARCKS in the cytosol. If so, then the PKC activation ratio ought to be sensitive to parameters that affect the diffusion of MARCKS (diffusivities and dimensions/geometry of the simulated domain). A reduction in diffusivity might hypothetically reflect transient interaction(s) with less mobile entities, for example, which could differ according to the phosphorylation status of MARCKS. In accord with the concept of long-range inhibition, reducing the diffusivities of both phospho- and unphosphorylated MARCKS from their base value of 32 $\mu\text{m}^2/\text{s}$ tempers the PKC activation ratio (Fig. 2.6). A systematic variation of the two diffusivities further shows that a slightly higher PKC activation ratio can be achieved if the diffusivity of phospho-MARCKS modestly exceeds that of unphosphorylated MARCKS (Fig. 2.6). The mobility difference allows phosphorylated MARCKS to diffuse more rapidly from where it was released from the membrane. Molecular diffusion links time- and lengthscales, and therefore, the geometry of the simulated domain is expected to matter as well. Consistent with a simplified analysis of such a system (47), we found that the thinning of the cell's height near the leading edge, and especially the formation of thin protrusions such as filopodia, enhances PKC phosphorylation of MARCKS there (Fig. 2.7).

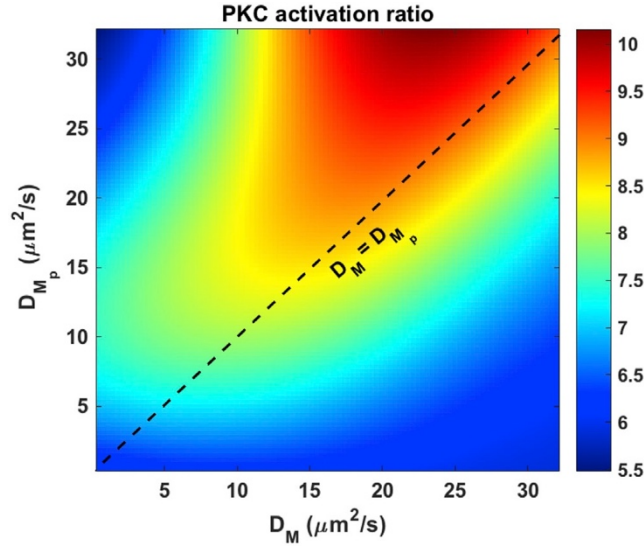


Figure 2.6 Pathway amplification is affected by MARCKS mobility in the cytosol. These results pertain to the simulation with base parameters and a steep PDGF gradient, but with the cytosolic diffusion coefficients for unphosphorylated MARCKS (D_M) and phosphorylated MARCKS (D_{Mp}) varied. The base values are $D_M = D_{Mp} = 32 \mu\text{m}^2/\text{s}$. The heat map plots the front/back ratio of active PKC as a function of those parameters.

To summarize this section, MARCKS sequesters a large pool of PIP_2 that can be made available to PLC, locally and rapidly, upon MARCKS phosphorylation by PKC. Moreover, MARCKS phosphorylation causes its release from the plasma membrane and distribution of the protein throughout the cytosol; once dephosphorylated, MARCKS can rebind the membrane, further diminishing PIP_2 availability wherever PKC activity is low. In our model, these effects combine to differentially buffer PIP_2 at the front and back of the cell relative to an external gradient of chemoattractant.

Relative Gradient = 67%

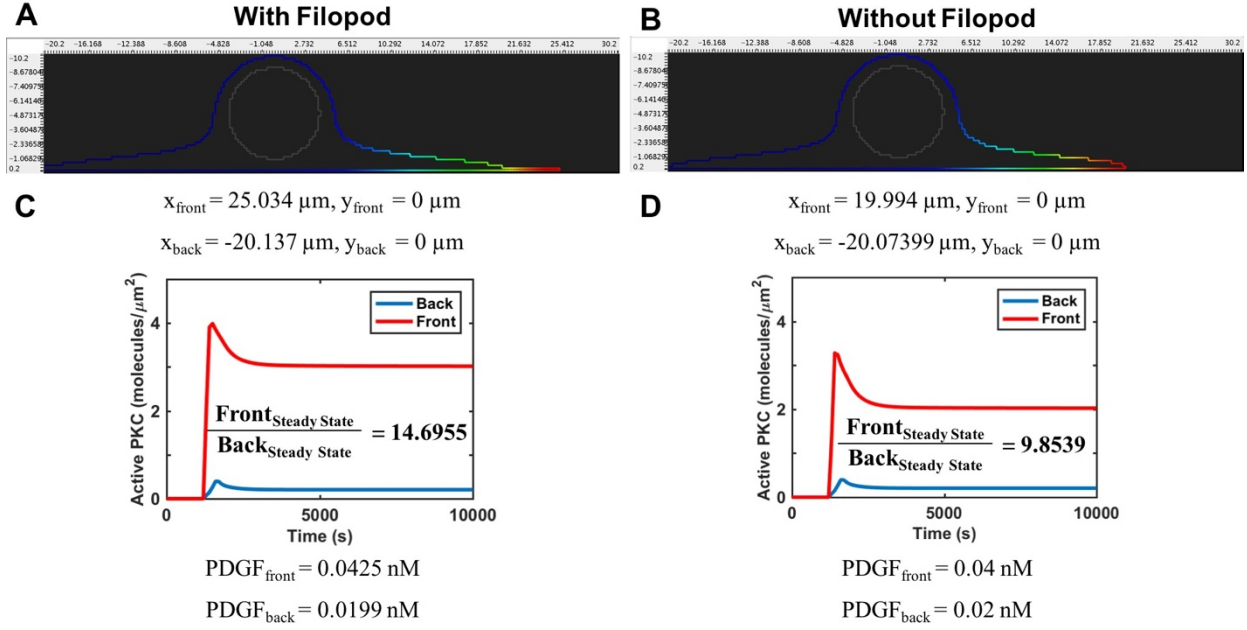


Figure 2.7 Geometry effects in 3D simulations. 3D geometries with (A) and without (B) a filopod-like protrusion are shown. In both cases, the nucleus is a sphere, radius $4 \mu\text{m}$, with membrane surface given by

$$x^2 + y^2 + (z + 5)^2 = 4^2$$

The rest of the cell has a ‘fried egg’ shape, with a radius of $20 \mu\text{m}$ at $z = 0$, except for the geometry in A, which has a thin, finger like protrusion projecting in positive x direction. The plasma membrane surface is given by

$$\left\{ \frac{\left(\frac{1}{20 + L_{fil}H(x)} \right)^2 + \left(\frac{1}{20} \right)^2 \left[\left(\frac{2y}{d_{fil}} \right)^6 + \left(-\frac{z}{d_{fil}} \right)^6 \right]}{\left[1 + \left(-\frac{z}{2.66} \right)^3 \right] \left[1 + \left(\frac{2y}{d_{fil}} \right)^6 + \left(-\frac{z}{d_{fil}} \right)^6 \right]} \right\} (x^2 + y^2 + z^2) + \frac{\left(\frac{1}{5} \right)^2 [x^2 + y^2 + (5 + z)^2] \left(-\frac{z}{2.66} \right)^3}{1 + \left(-\frac{z}{2.66} \right)^3} = 1$$

for negative z and bounded also by the $z = 0$ plane. $H(x)$ is the Heaviside step function. The dimensions of the filopod in A are $d = 0.2 \mu\text{m}$, $L_{fil} = 5 \mu\text{m}$ ($L_{fil} = 0$ in B). Kinetics of active PKC (c^*) at the front and back of the geometry with filopod (C) and without filopod (D) for a PDGF relative gradient of 67% and midpoint [PDGF] = 0.03 nM .

2.3.3 Regulation of MARCKS synergizes with other feedback mechanisms to enhance amplification of the PLC/PKC pathway

In the model calculations shown thus far, we assumed a steep PDGF gradient. Although responses to PDGF gradients of that magnitude have been studied in micropipette experiments (42), we sought to assess the possibility of substantial pathway amplification in response to a shallower PDGF gradient (10% relative steepness). This is important, because the recent observations of polarized DAG densities were made in microfluidic devices with PDGF gradients of comparable steepness (33). A PDGF gradient of $\sim 10\%$ relative steepness is also consistent with model simulations of dermal wound invasion; such gradients are realistically achievable if fibroblasts collectively consume PDGF via receptor-mediated endocytosis and lysosomal degradation (48). Under this gradient condition, and applying the same base-case parameters as in Figs. 2.3 and 2.5, the PLC/PKC pathway is amplified, but modestly so (the PKC activation ratio is 1.5) and thus inconsistent with experiments (Fig. 2.8); variation of the MARCKS phosphorylation and dephosphorylation rate constants, as in Fig. 2.3B, did not affect this conclusion. This result suggests that other mechanisms are needed to explain the observed amplification of the pathway in a shallow gradient. Although various positive feedback loops might be considered plausible, we chose to focus on a mechanistically simple one at the level of PKC activation.

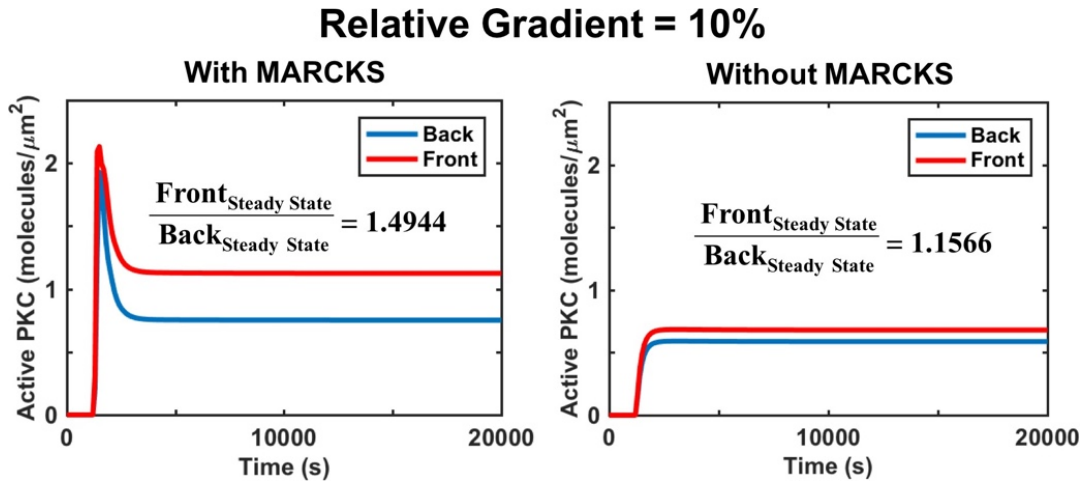


Figure 2.8 Kinetics of active PKC (c^*) with or without MARCKS for a PDGF gradient with relative steepness 10% and midpoint [PDGF] = 0.03 nM.

During the process by which PKC is primed for activation, it is autophosphorylated; however, upon DAG-mediated recruitment and activation, PKC is susceptible to dephosphorylation, leading to termination of the activation cycle (35). Here, in addition to the intramolecular phosphorylation reaction shown in Fig. 2.1A, we propose that phosphorylation of PKC might also be maintained via an intermolecular, autocatalytic reaction between active and inactive PKC molecules associated with DAG at the membrane (Fig. 2.9A). For the same steep PDGF gradient and MARCKS parameters used in Figs. 2.3D and 2.5, we assessed the PKC activation ratio between the front and back of the cell with various combinations of intra- (k_{pc1}) and intermolecular (k_{pc2}) PKC phosphorylation rate constants (Fig. 2.9B). We found a region of the parameter space where the PKC activation ratio is dramatically amplified and selected a parameter set ($k_{\text{pc1}} = 0.01 \text{ s}^{-1}$ and $k_{\text{pc2}} = 1 \mu\text{m}^2 \text{ s}^{-1}$) from this region for further study. In response to the steep PDGF gradient, the high PKC activation ratio (~ 90 -fold; the corresponding ratio of free DAG densities is ~ 16 -fold) is achieved because the PKC activity at the back of the cell is maintained at a low level; analysis of free PIP_2 densities at the front and back shows an even

greater contrast in MARCKS regulation, with MARCKS binding at the back of the cell actually increasing in response to the gradient (Fig. 2.9C). In the absence of MARCKS, the autocatalytic PKC phosphorylation mechanism is sufficient for pathway amplification, but to a far lower extent than when the two feedbacks work in concert (Fig. 2.9C; parameter sweeps for k_{pc1} and k_{pc2} are shown in Fig. 2.10). More critically, any feedback involving PKC only also fails to explain the experimentally observed amplification at the level of DAG.

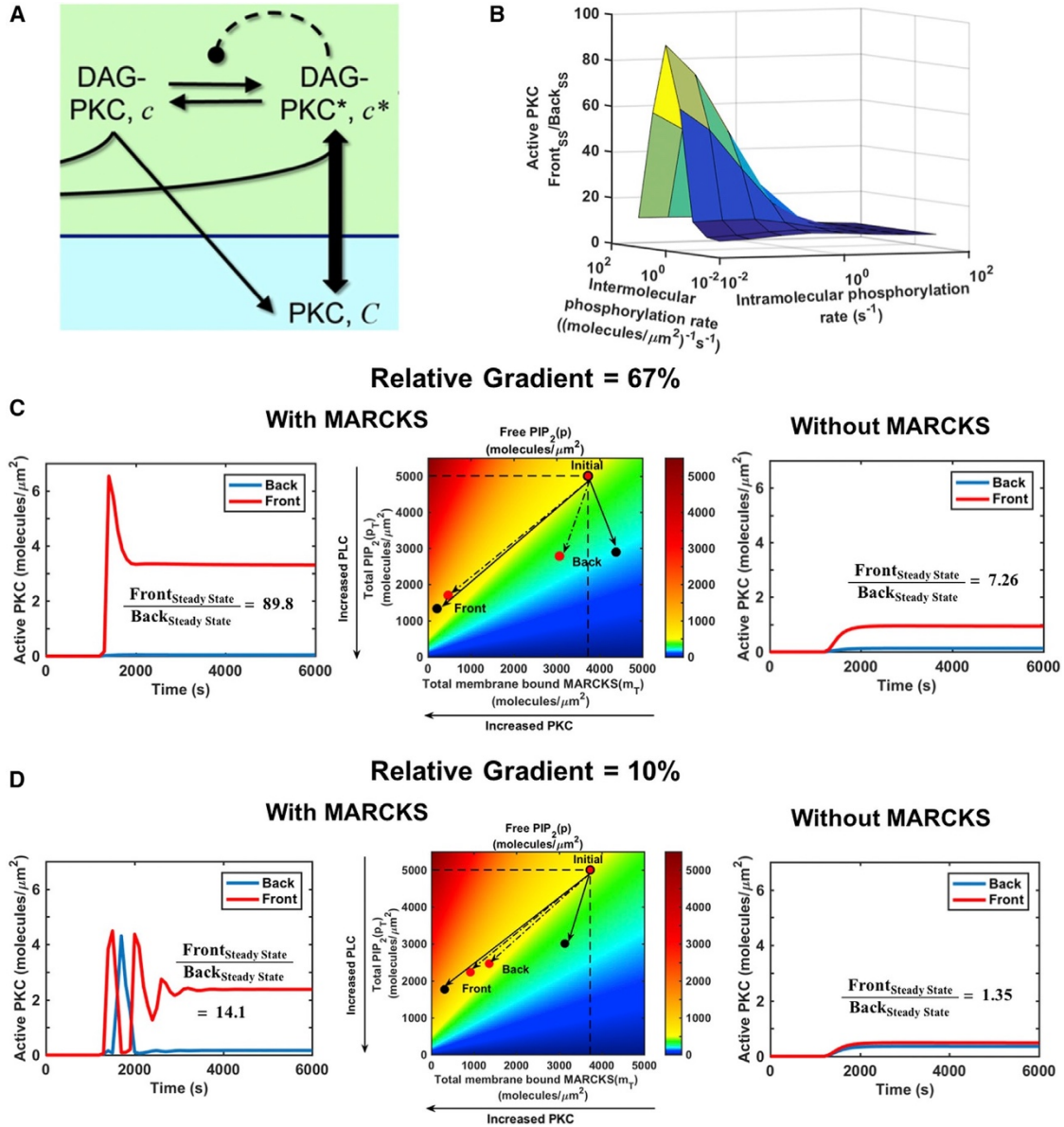


Figure 2.9 Regulation of MARCKS synergizes with other feedback mechanisms to enhance amplification of the PLC/PKC pathway. (A) Cutout of the pathway schematic depicting the addition of intermolecular PKC autophosphorylation as an additional positive feedback. (B) Surface plot of the steady-state front/back ratio of active PKC (c^*) as a function of intramolecular (k_{pc1}) and intermolecular (k_{pc2}) PKC phosphorylation rate constants for the steep (67%) PDGF gradient. (C and D) Characterization of the system with PKC feedback ($k_{pc1} = 0.01 \text{ s}^{-1}$ and $k_{pc2} = 1 \mu\text{m}^{-2} \text{ s}^{-1}$). Comparison of the kinetics of active PKC (c^*) and distribution of free PIP_2 with MARCKS, and the kinetics of active PKC without MARCKS, for steep (67% (C)) and shallow (10% (D)) PDGF gradients with midpoint $[\text{PDGF}] = 0.03 \text{ nM}$, introduced at time = 1200 s. The lighter circles on the heat maps are for the base parameter set without PKC feedback; black circles are for the parameter set with PKC feedback included.

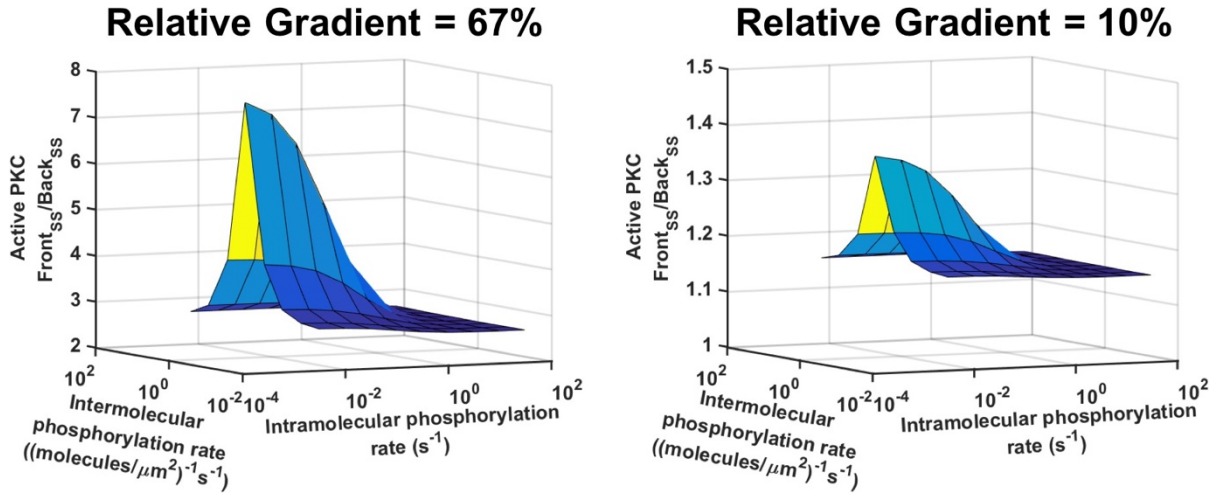


Figure 2.10 Parameter sweeps for intramolecular (k_{pc1}) and intermolecular (k_{pc2}) phosphorylation rates in the absence of MARCKS.

Turning to the shallow PDGF gradient (10% relative steepness), we assessed the amplification of the pathway with both feedbacks in place. Unlike the MARCKS-only case (Fig. 2.8), the addition of intermolecular PKC feedback resulted in a substantial PKC activation ratio (~ 14 -fold, or ~ 28 -fold for the most favorable geometry described in the previous section) by enhancing the differential regulation of MARCKS (Figs. 2.9D and 2.11). Indeed, in the absence of MARCKS, but with PKC feedback, the pathway is not significantly amplified in response to the shallow gradient (Fig. 2.9D). Taken together, these results suggest that although regulation of MARCKS is sufficient for some measure of pathway amplification, it can also synergize with other feedbacks to achieve greater amplification, which is necessary to explain the pathway response to a shallow PDGF gradient.

Relative Gradient = 10%

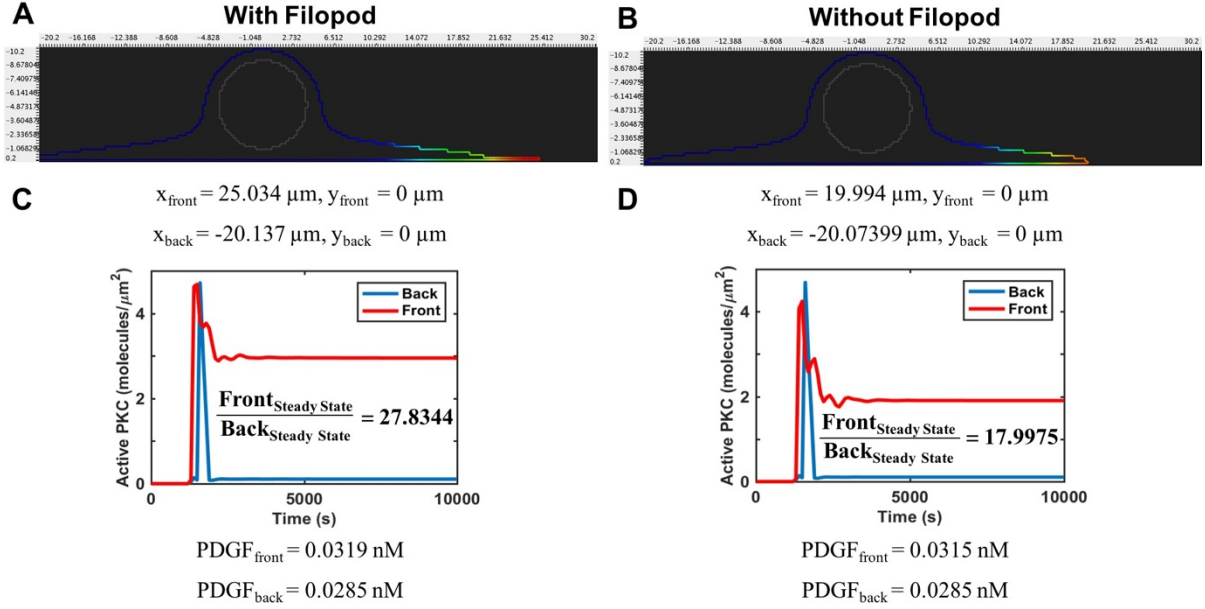


Figure 2.11 Geometry effects with both positive feedbacks in a shallow gradient. 3D geometries with (A) and without (B) a filopod-like protrusion are shown, identical to those shown in Fig. 2.7. Kinetics of active PKC (c^*) at the front and back of the geometry with filopod (C) and without filopod (D) for the model with both MARCKS and PKC feedbacks and for a shallow PDGF gradient with 10% relative steepness and midpoint [PDGF] = 0.03 nM.

2.3.4 The coupling of MARCKS and PKC feedbacks yields oscillations in certain regions of parameter space

The initial transient kinetics (damped oscillations) seen in (Fig. 2.9D) suggest that the system is on the cusp of instability under those conditions. To explore the potential for other nonlinear behaviors in the two-feedback system, we kept the same values of k_{pc1} and k_{pc2} from Fig. 2.9, C and D, and varied the rate constants of MARCKS phosphorylation and dephosphorylation. For a particular region of this parameter space, for example, $k_{\text{pm}} = 0.03 \mu\text{m}^2 \text{s}^{-1}$, $k_{\text{dpM}} = 0.01 \text{s}^{-1}$, we found that the kinetics of active PKC oscillate at the front and back of the simulated domain in response to PDGF stimulation (Fig. 2.12).

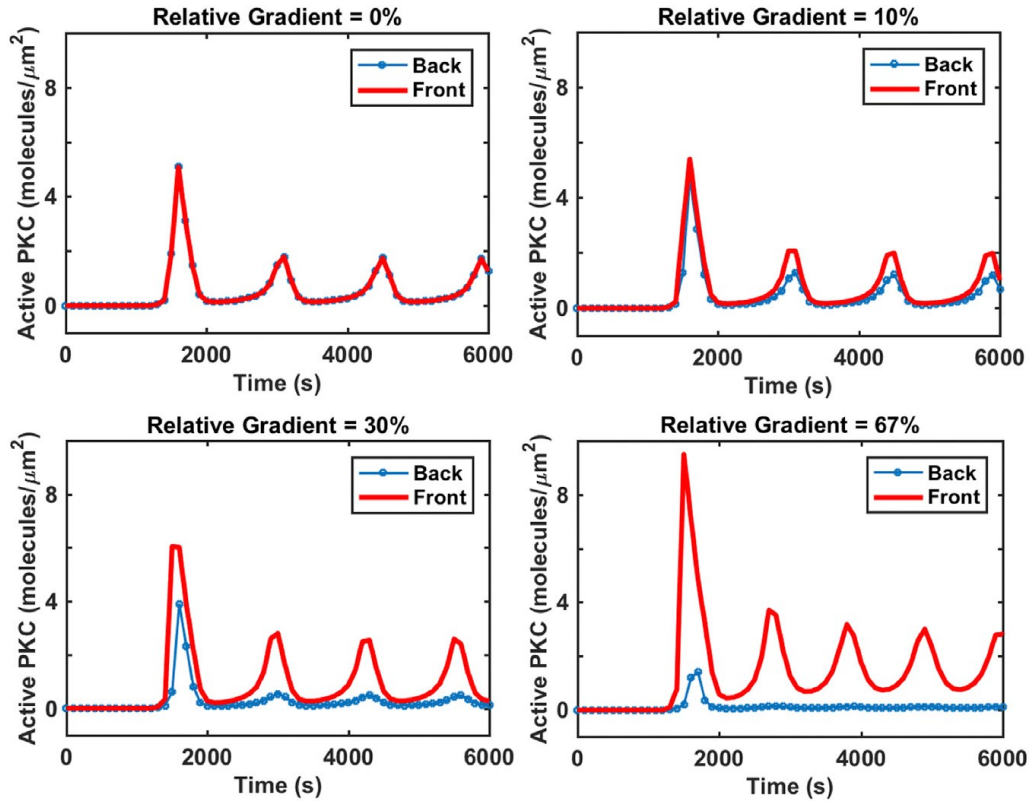


Figure 2.12 The PLC/PKC pathway with multiple feedbacks is capable of oscillations. Kinetics of active PKC (c^*) at the front and back of the simulated cell for PDGF gradients of varying relative steepness as indicated and midpoint [PDGF] = 0.03 nM, introduced at time = 1200 s. Deviations from the base parameter values are $k_{pm} = 0.03 \mu\text{m}^{-2} \text{s}^{-1}$, $k_{dpM} = 0.01 \text{s}^{-1}$, $k_{pc1} = 0.01 \text{s}^{-1}$, and $k_{pc2} = 1 \mu\text{m}^{-2} \text{s}^{-1}$.

The kinetics of all model species for the 67% PDGF gradient simulation are shown in Fig. 2.13. A closer look at the kinetics reveals a cycle in which activation of PKC at the front of the cell increases, fueled by the two positive feedbacks, with corresponding increases in MARCKS phosphorylation and depletion of membrane-bound MARCKS at the cell front; this is followed by dephosphorylation of MARCKS, net diffusion of unphosphorylated MARCKS from back to front, and restoration of MARCKS-PIP₂ binding at the front (Fig. 2.14). The latter process acts as a negative feedback of sorts, with a spatial character. We conclude that the

PLC/PKC pathway model, with the amplification mechanisms presented in this article, is a substrate-depletion/diffusion oscillator in certain regions of parameter space.

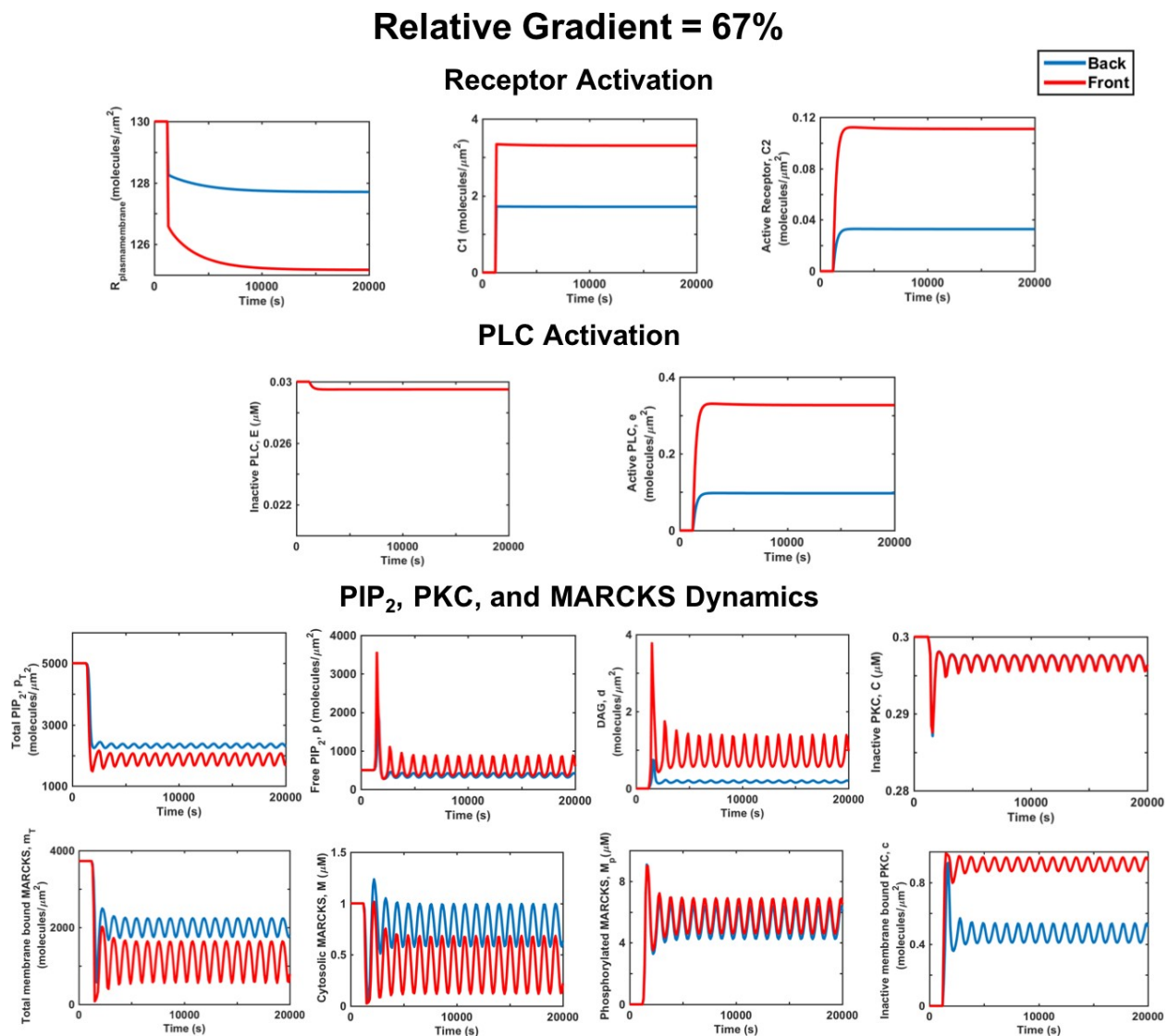


Figure 2.13 Kinetics of all species for the simulation represented in Fig. 2.12 with 67% relative gradient.

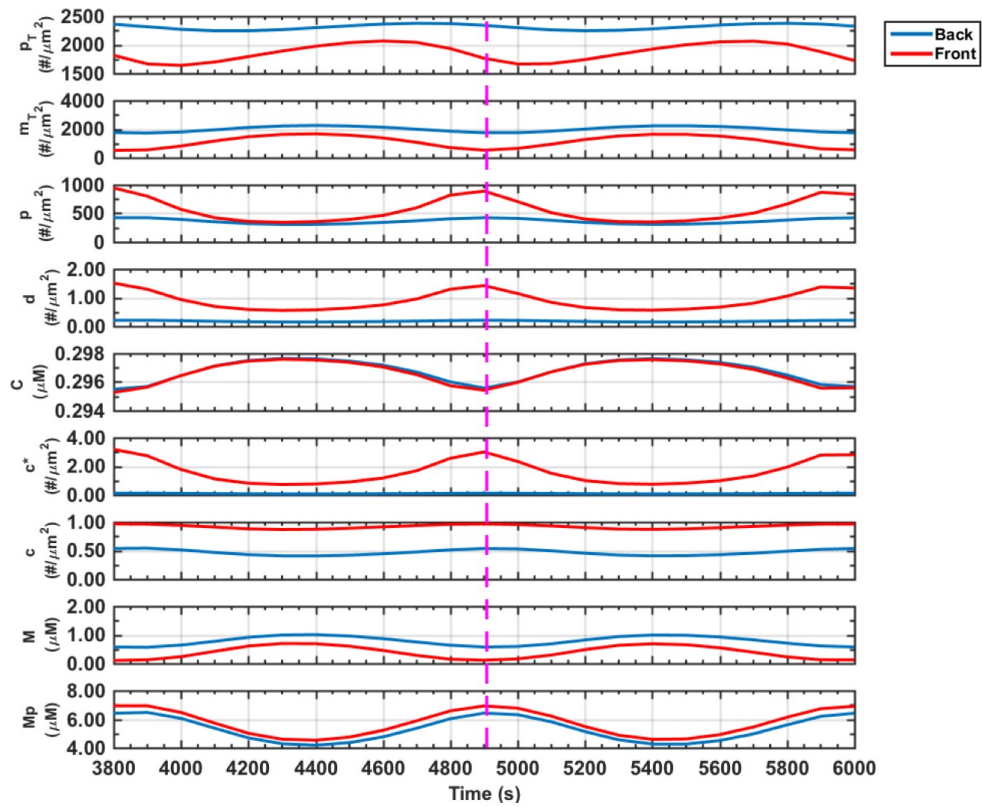


Figure 2.14 Expanded view of oscillating species from Fig. 2.13. The dotted vertical line allows comparisons across species.

2.4 Discussion

The mathematical model offered here is the first, to our knowledge, to describe gradient sensing through the PLC/PKC signaling pathway, which is required for fibroblast chemotaxis to PDGF. This pathway achieves asymmetric force generation via local inactivation of myosin II rather than by activation of Arp2/3 complex (32,33). In particular, we evaluated the regulation of MARCKS as a newly described positive feedback loop capable of amplifying PLC/PKC signaling. Positive feedback or other sources of ultrasensitivity are necessary for the amplification, because saturability of molecular interactions and enzymatic depletion of substrates generally diminish the sensitivity of the input-output relationship. Additional positive feedback in the pathway synergizes with MARCKS regulation and yields high amplification in

both steep and shallow gradients of PDGF, although this combination renders the steady state unstable in certain regions of parameter space.

The proposed feedback circuit shares certain qualitative features with hypothetical local excitation/global inhibition mechanisms (16), with localized PLC/DAG/PKC signaling and a more global distribution of MARCKS via fast diffusion of its phosphorylated form in the cytosol. However, since the model presented here is based on molecular mechanisms reported in the literature, its topology is distinct from previous theoretical models in certain intriguing ways. For one, the inhibitor MARCKS regulates substrate (PIP_2) supply and thus not only suppresses signaling at the cell rear, but neutralization of this negative regulator (49) is also an important part of the local amplification mechanism. Also, the capacity of the mechanism to supply PIP_2 is directly coupled to the flux of phospho-MARCKS into the cytosol. The global inhibition aspect is more complex than envisioned in other models, because it depends on the balance of MARCKS phosphorylation and dephosphorylation kinetics, along with MARCKS diffusion and its rate of membrane association. Last, and arguably most important, MARCKS is a buffer: it regulates the supply of PIP_2 by sequestering it, and as such, it does not alter the steady-state density of PIP_2 under perfectly mixed conditions (if the steady state is stable). The influence of such a buffer, the mobility of which is regulated, is a new concept in the study of gradient sensing.

In its membrane-bound state, MARCKS cross-links and anchors actin filaments (50), but it remains unclear how this function influences leading-edge dynamics. Moreover, the availability of PIP_2 potentially influences both the PLC/PKC pathway and PI3K signaling (51); though the latter is not required for fibroblast chemotaxis, it certainly affects the efficiency of fibroblast movement and turning behavior (27,30). We also recently showed that PI3K signaling

is enriched in filopodia (52), consistent with geometry-dependent regulation of MARCKS predicted by our model (Fig. 2.7). A more complete yet complex model of fibroblast motility would incorporate PI3K and small GTPase signaling and the coordinated regulation of the actin cytoskeleton via myosin II and Arp2/3 complex. The influence of PLC signaling on cofilin-mediated actin severing (53), which has been examined using a quantitative model (54), could also be integrated in a more comprehensive framework, along with aspects of phosphoinositide dynamics modeled previously (55,56). Extension to other chemotactic cell types might also be considered; however, although PKC and MARCKS have been implicated in chemotaxis of, e.g., neutrophils (57-60), one can only speculate now whether or not the PLC/PKC pathway is amplified, or about its role relative to other signaling pathways in other cell types.

The model presented here describes regulation of MARCKS combined with a simple feedback at the level of PKC, because the MARCKS feedback alone does not sufficiently amplify DAG production in a shallow PDGF gradient. Although the introduction of the second, putative feedback successfully showed how MARCKS regulation might synergize with other sources of nonlinearity, experiments and additional modeling will need to be carried out to identify and characterize them. Another aspect that will need to be addressed, both in experiments and models, is the robustness/fragility of the gradient-sensing circuit. DAG localization in fibroblasts responding to PDGF gradients with varied midpoint concentration and steepness remains to be characterized; comparison to such measurements will be critical if revisions or refinements of this model are to be meaningfully undertaken.

2.5 Acknowledgments

This work was supported by National Institutes of Health grant U01-EB018816. The Virtual Cell is supported by National Institutes of Health grant P41 GM103313 from the National Institute for General Medical Sciences.

2.6 References

1. Insall R.H. Understanding eukaryotic chemotaxis: a pseudopod-centered view. *Nat. Rev. Mol. Cell Biol.* 2010;11:453–458.
2. Artemenko Y., Lampert T.J., Devreotes P.N. Moving towards a paradigm: common mechanisms of chemotactic signaling in *Dictyostelium* and mammalian leukocytes. *Cell. Mol. Life Sci.* 2014;71:3711–3747.
3. Bear J.E., Haugh J.M. Directed migration of mesenchymal cells: where signaling and the cytoskeleton meet. *Curr. Opin. Cell Biol.* 2014;30:74–82.
4. Singer A.J., Clark R.A.F. Cutaneous wound healing. *N. Engl. J. Med.* 1999;341:738–746.
5. Martin P. Wound healing—aiming for perfect skin regeneration. *Science.* 1997;276:75–81.
6. Werner S., Grose R. Regulation of wound healing by growth factors and cytokines. *Physiol. Rev.* 2003;83:835–870.
7. McClain S.A., Simon M., Clark R.A.F. Mesenchymal cell activation is the rate-limiting step of granulation tissue induction. *Am. J. Pathol.* 1996;149:1257–1270.
8. Andrae J., Gallini R., Betsholtz C. Role of platelet-derived growth factors in physiology and medicine. *Genes Dev.* 2008;22:1276–1312.
9. Diegelmann R.F., Evans M.C. Wound healing: an overview of acute, fibrotic and delayed healing. *Front. Biosci.* 2004;9:283–289.
10. Ridley A.J., Schwartz M.A., Horwitz A.R. Cell migration: integrating signals from front to back. *Science.* 2003;302:1704–1709.
11. Wu C.Y., Lin M.W., Chen C.L. The role of phosphoinositide-regulated actin reorganization in chemotaxis and cell migration. *Br. J. Pharmacol.* 2014;171:5541–5554.
12. Welch C.M., Elliott H., Hahn K.M. Imaging the coordination of multiple signalling activities in living cells. *Nat. Rev. Mol. Cell Biol.* 2011;12:749–756.
13. Rotty J.D., Wu C., Bear J.E. New insights into the regulation and cellular functions of the ARP2/3 complex. *Nat. Rev. Mol. Cell Biol.* 2013;14:7–12.
14. Xu J., Wang F., Bourne H.R. Divergent signals and cytoskeletal assemblies regulate self-organizing polarity in neutrophils. *Cell.* 2003;114:201–214.
15. Jilkine A., Edelstein-Keshet L. A comparison of mathematical models for polarization of single eukaryotic cells in response to guided cues. *PLoS Comput. Biol.* 2011;7:e1001121.

16. Iglesias P.A., Devreotes P.N. Navigating through models of chemotaxis. *Curr. Opin. Cell Biol.* 2008;20:35–40.
17. Welf E.S., Haugh J.M. Signaling pathways that control cell migration: models and analysis. *Wiley Interdiscip. Rev. Syst. Biol. Med.* 2011;3:231–240.
18. Meinhardt H. Orientation of chemotactic cells and growth cones: models and mechanisms. *J. Cell Sci.* 1999;112:2867–2874.
19. Subramanian K.K., Narang A. A mechanistic model for eukaryotic gradient sensing: spontaneous and induced phosphoinositide polarization. *J. Theor. Biol.* 2004;231:49–67.
20. Otsuji M., Ishihara S., Kuroda S. A mass conserved reaction-diffusion system captures properties of cell polarity. *PLoS Comput. Biol.* 2007;3:e108.
21. Goryachev A.B., Pokhilko A.V. Dynamics of Cdc42 network embodies a Turing-type mechanism of yeast cell polarity. *FEBS Lett.* 2008;582:1437–1443.
22. Levchenko A., Iglesias P.A. Models of eukaryotic gradient sensing: application to chemotaxis of amoebae and neutrophils. *Biophys. J.* 2002;82:50–63.
23. Shi C., Huang C.H., Iglesias P.A. Interaction of motility, directional sensing, and polarity modules recreates the behaviors of chemotaxing cells. *PLoS Comput. Biol.* 2013;9:e1003122.
24. Mori Y., Jilkin A., Edelstein-Keshet L. Wave-pinning and cell polarity from a bistable reaction-diffusion system. *Biophys. J.* 2008;94:3684–3697.
25. Kraynov V.S., Chamberlain C., Hahn K.M. Localized Rac activation dynamics visualized in living cells. *Science.* 2000;290:333–337.
26. Weiger M.C., Ahmed S., Haugh J.M. Directional persistence of cell migration coincides with stability of asymmetric intracellular signaling. *Biophys. J.* 2010;98:67–75.
27. Melvin A.T., Welf E.S., Haugh J.M. In chemotaxing fibroblasts, both high-fidelity and weakly biased cell movements track the localization of PI3K signaling. *Biophys. J.* 2011;100:1893–1901.
28. Pankov R., Endo Y., Yamada K.M. A Rac switch regulates random versus directionally persistent cell migration. *J. Cell Biol.* 2005;170:793–802.
29. Wu Y.I., Frey D., Hahn K.M. A genetically encoded photoactivatable Rac controls the motility of living cells. *Nature.* 2009;461:104–108.
30. Welf E.S., Ahmed S., Haugh J.M. Migrating fibroblasts reorient directionality by a metastable, PI3K-dependent mechanism. *J. Cell Biol.* 2012;197:105–114.

31. Monypenny J., Zicha D., Watanabe N. Cdc42 and Rac family GTPases regulate mode and speed but not direction of primary fibroblast migration during platelet-derived growth factor-dependent chemotaxis. *Mol. Cell. Biol.* 2009;29:2730–2747.
32. Wu C., Asokan S.B., Bear J.E. Arp2/3 is critical for lamellipodia and response to extracellular matrix cues but is dispensable for chemotaxis. *Cell.* 2012;148:973–987.
33. Asokan S.B., Johnson H.E., Bear J.E. Mesenchymal chemotaxis requires selective inactivation of myosin II at the leading edge via a noncanonical PLC γ /PKC α pathway. *Dev. Cell.* 2014;31:747–760.
34. Vicente-Manzanares M., Ma X., Horwitz A.R. Non-muscle myosin II takes center stage in cell adhesion and migration. *Nat. Rev. Mol. Cell Biol.* 2009;10:778–790.
35. Newton A.C. Regulation of the ABC kinases by phosphorylation: protein kinase C as a paradigm. *Biochem. J.* 2003;370:361–371.
36. Kadamur G., Ross E.M. Mammalian phospholipase C. *Annu. Rev. Physiol.* 2013;75:127–154.
37. Glaser M., Wanaski S., McLaughlin S. Myristoylated alanine-rich C kinase substrate (MARCKS) produces reversible inhibition of phospholipase C by sequestering phosphatidylinositol 4,5-bisphosphate in lateral domains. *J. Biol. Chem.* 1996;271:26187–26193.
38. Seykora J.T., Myat M.M., Aderem A. Molecular determinants of the myristoyl-electrostatic switch of MARCKS. *J. Biol. Chem.* 1996;271:18797–18802.
39. McLaughlin S., Wang J., Murray D. PIP₂ and proteins: interactions, organization, and information flow. *Annu. Rev. Biophys. Biomol. Struct.* 2002;31:151–175.
40. Ott L.E., Sung E.J., Jones S.L. Fibroblast migration is regulated by myristoylated alanine-rich C-kinase substrate (MARCKS) protein. *PLoS One.* 2013;8:e66512.
41. Park C.S., Schneider I.C., Haugh J.M. Kinetic analysis of platelet-derived growth factor receptor/phosphoinositide 3-kinase/Akt signaling in fibroblasts. *J. Biol. Chem.* 2003;278:37064–37072.
42. Schneider I.C., Haugh J.M. Quantitative elucidation of a distinct spatial gradient-sensing mechanism in fibroblasts. *J. Cell Biol.* 2005;171:883–892.
43. Mérida I., Avila-Flores A., Merino E. Diacylglycerol kinases: at the hub of cell signalling. *Biochem. J.* 2008;409:1–18.

44. Gambhir A., Hangyás-Mihályiné G., McLaughlin S. Electrostatic sequestration of PIP₂ on phospholipid membranes by basic/aromatic regions of proteins. *Biophys. J.* 2004;86:2188–2207.
45. Wang J., Gambhir A., Murray D. A computational model for the electrostatic sequestration of PI(4,5)P₂ by membrane-adsorbed basic peptides. *Biophys. J.* 2004;86:1969–1986.
46. Cowan A.E., Moraru I.I., Loew L.M. Spatial modeling of cell signaling networks. *Methods Cell Biol.* 2012;110:195–221.
47. Haugh J.M. Membrane-binding/modification model of signaling protein activation and analysis of its control by cell morphology. *Biophys. J.* 2007;92:L93–L95.
48. Haugh J.M. Deterministic model of dermal wound invasion incorporating receptor-mediated signal transduction and spatial gradient sensing. *Biophys. J.* 2006;90:2297–2308.
49. Rahman A., Haugh J.M. Deactivation of a negative regulator: a distinct signal transduction mechanism, pronounced in Akt signaling. *Biophys. J.* 2014;107:L29–L32.
50. Aderem A. Signal transduction and the actin cytoskeleton: the roles of MARCKS and profilin. *Trends Biochem. Sci.* 1992;17:438–443.
51. Ziemba B.P., Burke J.E., Falke J.J. Regulation of PI3K by PKC and MARCKS: single-molecule analysis of a reconstituted signaling pathway. *Biophys. J.* 2016;110:1811–1825.
52. Johnson H.E., King S.J., Haugh J.M. F-actin bundles direct the initiation and orientation of lamellipodia through adhesion-based signaling. *J. Cell Biol.* 2015;208:443–455.
53. Mouneimne G., DesMarais V., Condeelis J. Spatial and temporal control of cofilin activity is required for directional sensing during chemotaxis. *Curr. Biol.* 2006;16:2193–2205.
54. Tania N., Condeelis J., Edelstein-Keshet L. Modeling the synergy of cofilin and Arp2/3 in lamellipodial protrusive activity. *Biophys. J.* 2013;105:1946–1955.
55. Haugh J.M., Wells A., Lauffenburger D.A. Mathematical modeling of epidermal growth factor receptor signaling through the phospholipase C pathway: mechanistic insights and predictions for molecular interventions. *Biotechnol. Bioeng.* 2000;70:225–238.
56. Xu C., Watras J., Loew L.M. Kinetic analysis of receptor-activated phosphoinositide turnover. *J. Cell Biol.* 2003;161:779–791.
57. Eckert R.E., Neuder L.E., Jones S.L. Myristoylated alanine-rich C-kinase substrate (MARCKS) protein regulation of human neutrophil migration. *Am. J. Respir. Cell Mol. Biol.* 2010;42:586–594.

58. Tang W., Zhang Y., Wu D. A PLC β /PI3K γ -GSK3 signaling pathway regulates cofilin phosphatase slingshot2 and neutrophil polarization and chemotaxis. *Dev. Cell.* 2011;21:1038–1050.
59. Xu X., Gera N., Jin T. GPCR-mediated PLC $\beta\gamma$ /PKC β /PKD signaling pathway regulates the cofilin phosphatase slingshot 2 in neutrophil chemotaxis. *Mol. Biol. Cell.* 2015;26:874–886.
60. Sheats M.K., Sung E.J., Jones S.L. In vitro neutrophil migration requires protein kinase C-delta (δ -PKC)-mediated myristoylated alanine-rich C-kinase substrate (MARCKS) phosphorylation. *Inflammation.* 2015;38:1126–1141.

CHAPTER 3

Mechanistic Models of PLC/PKC Signaling Implicate Phosphatidic Acid as a Key Amplifier of Chemotactic Gradient Sensing

Adapted from: Nosbisch JL, Rahman A, Mohan K, Elston TC, Bear JE, Haugh JM. Mechanistic models of PLC/PKC signaling implicate phosphatidic acid as a key amplifier of chemotactic gradient sensing. PLoS Comput Biol. 2020 Apr; 16(4): e1007708.

3.1 Introduction

Chemotaxis, the bias of cell movement towards soluble chemical cues (chemoattractants), is critical for embryonic development, angiogenesis, the immune response, and wound healing in metazoans (1). Fibroblasts, the cells directly responsible for regenerating wounded tissue, respond chemotactically to platelet-derived growth factor (PDGF) as a cue to invade the wound; this proliferative phase of wound healing typically unfolds over the course of several days (2–5). Chemoattractant ligands such as PDGF bind to cognate receptors on the cell surface, and in eukaryotic cells this signal is sensed spatially, relying on a gradient of receptor occupancy and activation. The activated receptors interface with a network of intracellular signaling pathways that modulate the dynamics of the cytoskeleton and thus cell motility. This modulation can be achieved by spatially varying the rate of F-actin polymerization or the mechanical influence of Myosin II contractility (6,7). In fibroblasts exposed to a steady PDGF gradient, many of the prominent signaling pathways that enhance the rate of F-actin polymerization have been found to be dispensable for chemotaxis (8–10), whereas regulation of Myosin IIA by phospholipase C (PLC)/protein kinase (PKC) signaling, a well-studied pathway activated by many receptors, is essential (11). Another key finding in that study was that diacylglycerol (DAG), the lipid product of PLC that activates most PKC isoforms, is sharply concentrated in the fibroblasts' protrusions (lamellipodia) exposed to the highest concentration of PDGF (11). Given that the external gradients in such experiments are characteristically shallow (typically, $\sim 5\%$ across a cell's length), the PLC/PKC signaling circuit must be locally amplified to explain the observed polarization of DAG production. What are the biochemical and biophysical mechanisms that cause the pathway to polarize?

To partially address this question, a reaction-diffusion model of the PLC/PKC signaling pathway identified phosphorylation of myristoylated alanine-rich C kinase substrate (MARCKS) by PKC, which increases the availability of the PLC substrate (PIP₂) (12–15), as a positive feedback loop (PFL); this mechanism is sufficient for polarization in response to an abnormally steep external gradient (16). By itself, however, the MARCKS feedback was unable to polarize signaling in response to shallow external gradients ($\leq 10\%$), and the system lacked robustness to modest changes in the midpoint concentration of chemoattractant. In this work, we address these issues through formulation of more mechanistic, partial differential equation models of the PLC/PKC pathway. These models consider two additional PFLs supported by literature evidence and thus introduce a key molecular player: phosphatidic acid (PA), a lipid intermediate in the metabolism of DAG.

PA is recognized as a signaling molecule affecting a number of cellular functions including cell growth and proliferation, vesicular trafficking, and cytoskeletal rearrangement (17,18). In the present models, we include reactions by which PA is produced by phosphorylation of DAG by DAG kinases or from hydrolysis of phosphatidylcholine by phospholipase D (PLD) (19–22). Feedback loops incorporating PA were added to the model based on published evidence that: 1) PA binds PLC γ and increases the rate of PIP₂ hydrolysis in vitro (23); and 2) active PKC can enhance the activity of PLD for increased production of PA (24–26). Model simulations show that the MARCKS feedback mechanism synergizes with these new feedback loops to polarize PLC/PKC signaling in response to shallow gradients of receptor occupancy and over an appreciable range of midpoint occupancy. Subtle asymmetry of the cell geometry can also polarize signaling. Focusing on the molecular details, simulations suggest that DAG kinases, the enzymes responsible for turnover of DAG, exert a critical and surprisingly

positive influence on the responsiveness of the circuit. Finally, we applied the predicted receptor occupancy conditions for polarization to a two-state model of cell movement in a hybrid (stochastic/continuum) model of wound invasion. This model predicts a hierarchy of chemotactic waves that drive more efficient collective invasion than a single chemotactic front. With this framework, we can proceed to link signal transduction mechanisms at the molecular level to individual and collective cell movements directed by chemoattractant gradients in tissues.

3.2 Results

3.2.1 *New models of the PLC/PKC pathway based on putative feedback mechanisms indicated in the literature*

We formulated a biochemically realistic description of the chemotactic sensing circuit in fibroblasts, retaining the differential PIP₂ buffering by MARCKS from the Mohan model (16) and considering two additional PFLs based on published evidence (Fig. 3.1A; see also *Materials and Methods* and *Appendix B*). The first, PFL 1, considers the modulation of PLC recruitment by phosphatidic acid (PA), the lipid produced by phosphorylation of DAG by DAG kinases. Using a detergent-phospholipid mixed micelle assay system, it was shown that inclusion of PA enhanced PIP₂ hydrolysis catalyzed by either unphosphorylated or tyrosine-phosphorylated PLC γ 1, by reducing the apparent K_m for the reaction (23). The details of how PA affects PLC activity are not completely understood, but the reduction of the apparent K_m is consistent with PA-mediated stabilization of PLC γ 1 association with the membrane, akin to the effect of the non-catalytic interaction of PLC δ with PIP₂ (27). Therefore, we modeled the effect of PA as an increased lifetime of the receptor-PLC γ 1 complex at the membrane (Fig. 3.1A).

To simplify and generalize the handling of receptor dynamics in this model, and considering that receptor activation is patterned by an external ligand, we assume a steady gradient of occupied/active receptors, r , that is linear in the direction of the cell's long axis (on both the top and bottom of the cell) rather than along the cell's contour (Fig. 3.1B & 3.1C). In the expression for r , $rfrac$ is the average receptor occupancy, expressed as a fraction of a characteristic receptor density of $130 \mu\text{m}^{-2}$, or $10^5/\text{cell}$. The parameter $rsteep$ is the relative steepness of the receptor occupancy gradient across the cell; for example, a value of $rsteep = 0.1$ corresponds to a 10% difference between the front and back of the cell.

3.2.2 Stabilization of PLC recruitment by phosphatidic acid (PFL 1), combined with neutralization of MARCKS by PKC, promotes sensitive and robust gradient sensing

Considering the network depicted in Fig. 3.1A, with PFL 1 but not PFL 2, we evaluated the ability of receptor occupancy gradients (characterized by midpoint occupancy and % steepness) to polarize DAG and active PKC. For each of five gradient steepness values, ranging from 0% (uniform stimulation) up to 67% (2-fold) difference across the cell, simulations were run varying the value of the midpoint receptor occupancy, $rfrac$. All simulations were run sufficiently long to allow a steady state to be achieved, followed by an equally long period with the gradient reversed to check the stability of the spatial pattern. The steady-state concentrations of active PKC at the front and back of the cell are plotted versus $rfrac$ (Fig. 3.2A). In some simulations, the spatial pattern oscillated, in which case the maximum and minimum values of the oscillation at each end of the cell are plotted. For examples of the simulated time courses, showing the transient behavior with sustained oscillations where applicable, see Fig. 3.3 and Fig. 3.4. The PKC activity pattern was reversible for all but one of these simulated conditions. The

exception is marked with an asterisk in Fig. 3.2A, signifying lack of reversibility here and in subsequent figures of this paper.

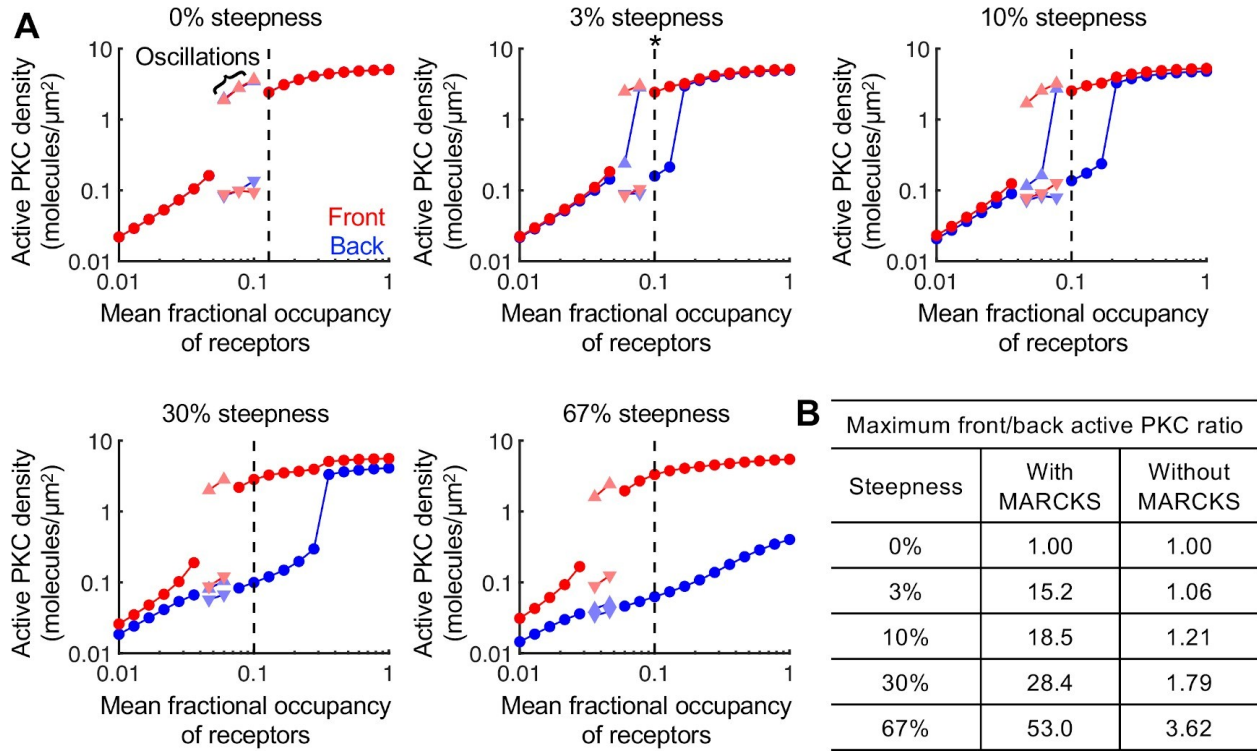


Figure 3.2 Gradient amplification by PFL 1 combined with regulation of MARCKS. (A) The concentration of active PKC molecules at the front (red circle) and back (blue circle) of the cell are plotted as a function of the mean fractional occupancy of receptors, r_{frac} , for varying values of gradient steepness. When the simulations produced oscillations, the maxima (upward-pointing triangles) and minima (downward-pointing triangles) of the oscillations are plotted; the front and back are still denoted by shades of red and blue, respectively. The simulation achieving steady state with the maximum front/back ratio is denoted by the dashed vertical line. For these simulations, the direction of the gradient was reversed after 20,000 s. If the active PKC pattern failed to reverse in response, the simulation is marked with an asterisk. (B) Table showing the maximum front/back ratio for each gradient steepness in simulations run with PFL1 and either with or without MARCKS protein.

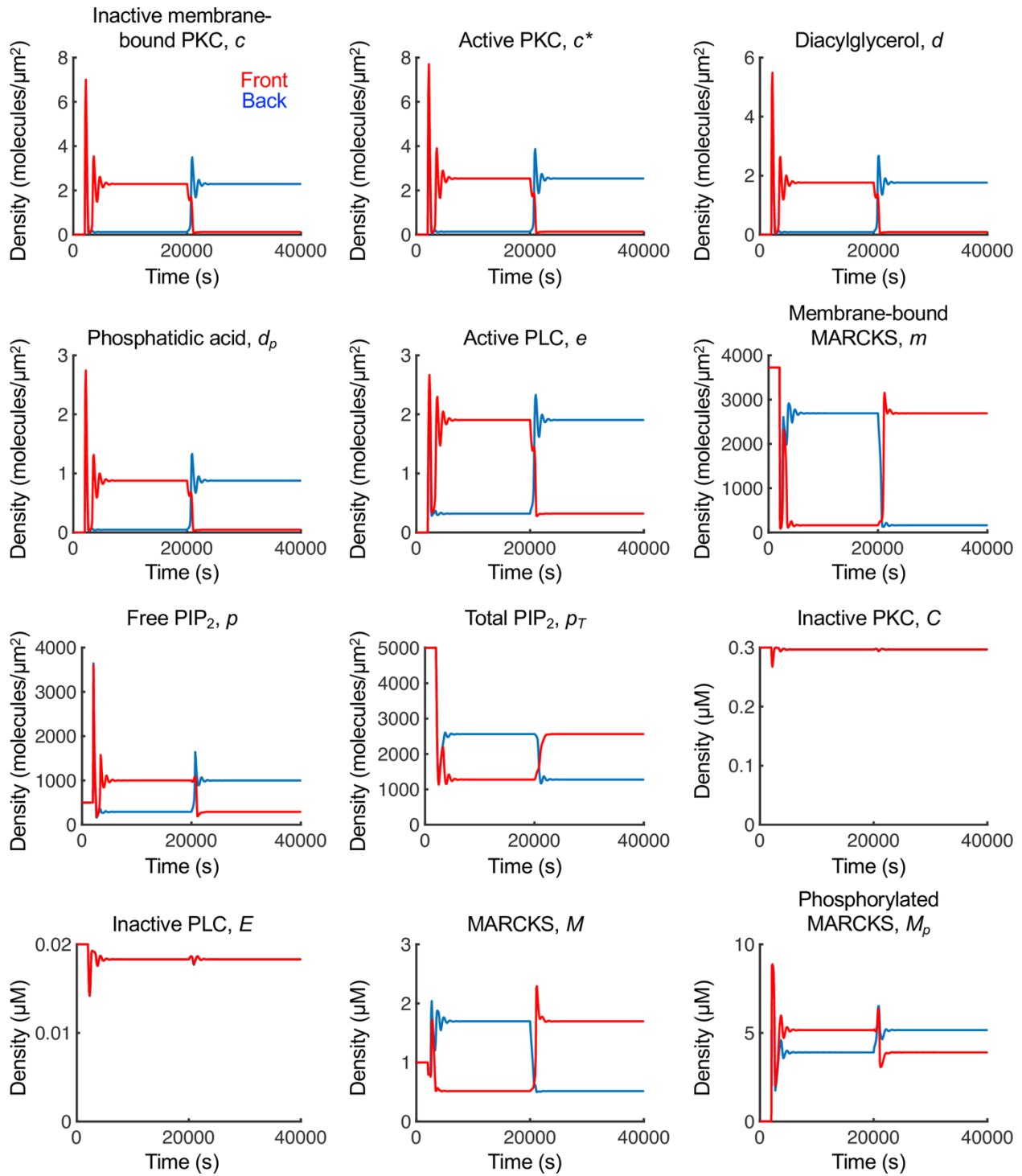


Figure 3.3 Time courses of all model species for Fig. 3.2A, 10% steepness and $rfrac = 0.1$.

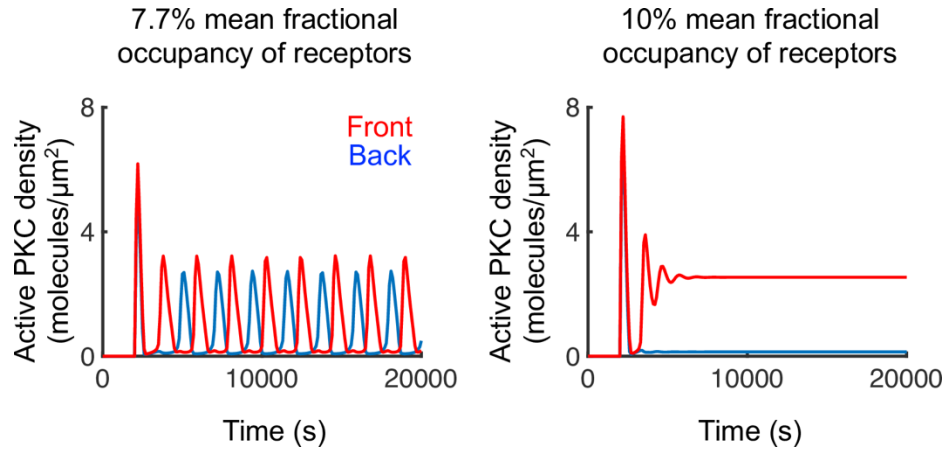


Figure 3.4 Transition from oscillations to stable pattern as $rfrac$ is increased (10% steepness).

For simulations that achieved steady state, the degree of polarization is quantified as the ratio of active PKC at the front of the cell over that of the back of the cell, and the value of $rfrac$ where this ratio is maximum is marked on each of the plots in Fig. 3.2A. For receptor occupancy gradients as shallow as 3%, we found maximum front/back ratios exceeding 10, indicating strong and sensitive polarization of the PLC/PKC pathway. Another quality of the gradient sensing response is its robustness, of which several features might be considered. For example, across the range of % steepness values, the greatest degree of polarization is consistently achieved at approximately the same value of $rfrac$ (≈ 0.1), and polarized patterns exhibit a consistent density of active PKC at the front of the cell. The aspect of greatest interest to us, however, is the range of $rfrac$ values that elicit polarization for a given % steepness, which we refer to as dose-response robustness. As might be expected, dose-response robustness is enhanced as gradient steepness is increased (Fig. 3.2A); at a modest steepness of 10% (typical in magnitude of chemotaxis experiments), the range of $rfrac$ values for which steady polarization would be evident spans a factor of 2. The range doubles if oscillatory simulations with consistently high front/back ratio are included.

It should be noted that the general inability to polarize the gradient sensing circuit at high *rfrac* is not caused by saturation of receptor occupancy, as would be expected at high concentrations of chemoattractant; in this model, the relative steepness of receptor activation is fixed. Rather, high receptor activation promotes ignition of the positive feedback at the back of the cell as well as at the front.

In previous work (16), it was shown that a single positive feedback was not sufficient for a demonstratively amplified response, i.e., without differential buffering of PIP₂ by MARCKS. Accordingly, simulations with PFL 1 but no MARCKS show similar dose responsiveness with respect to *rfrac* but inconsequential polarization (Fig. 3.2B). These results identify a promising gradient sensing circuit that combines differential buffering of PIP₂ by MARCKS, and the amplification of PLC recruitment by PA, regulation mechanisms supported by evidence in the literature.

3.2.3 Analysis of the mechanisms driving PLC/PKC polarization

The differential buffering of PIP₂ by MARCKS was described in detail previously (16), and it is important to understand this concept in the context of the present model as well. Phosphorylation of MARCKS by active, DAG-bound PKC liberates PIP₂ locally, further enhancing DAG production by positive feedback. A key aspect of differential buffering is the maintenance of certain intracellular gradients. In the cytosol, PLC and PKC are close to uniform, whereas there is a gradient of phosphorylated versus unphosphorylated MARCKS in the cytosol. Accordingly, a substantial increase in the diffusivities of cytosolic MARCKS species breaks the polarization of the present model (Fig 3.5A). A large decrease in the diffusivities also decreases polarization, but modestly so. The optimum with respect to diffusivity has been attributed to the

ability of dephosphorylated MARCKS to diffuse to the rear of the cell before re-binding PIP₂ (16). The other important gradients are of total and free PIP₂ in the plasma membrane. MARCKS-bound PIP₂ is protected from hydrolysis, and therefore its spatial range by diffusion is substantial. Thus, net diffusion of MARCKS-bound PIP₂ from back to front supplies the front of the cell with substrate, allowing the free PIP₂ density to be much higher at the front despite the much higher PLC activity there. Accordingly, reducing the diffusivities of total PIP₂ and membrane-associated MARCKS prevents polarization, whereas increasing those diffusivities enhances the extent of polarization (Fig. 3.5B).

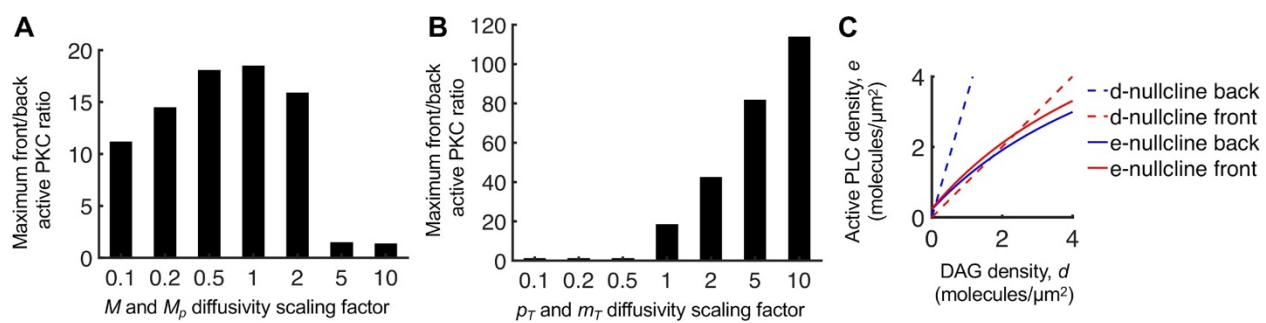


Figure 3.5 Analysis of the mechanisms driving PLC/PKC polarization. (A) Sensitivity of the results in Fig. 3.2A, 10% gradient steepness, to the indicated fold-changes in MARCKS (M and M_p) cytosolic diffusivities (1 = base case). (B) Sensitivity of the results in Fig. 3.2A, 10% gradient steepness, to the indicated fold-changes in total PIP₂ and membrane-associated MARCKS (p_T and m_T) membrane diffusivities (1 = base case). (C) Plot of the d - and e -nullclines (Appendix B) evaluated at the front and back of the cell for the base-case parameters as in Fig. 3.2A, with 10% gradient steepness and $rfrac = 0.1$.

To further explain the polarization of the present gradient sensing circuit, we developed a steady-state analysis (Appendix B), with the simplifying assumption that diffusion of active PLC and DAG-containing species are negligible relative to associated reaction terms. We derived nullcline expressions for the membrane-recruited PLC and for the sum of free and PKC-bound DAG, which we refer to as the e - and d -nullclines. The intersections of these two curves are

fixed points. To construct these curves on a (d, e) phase plane, certain other variables must be specified. The e -nullcline includes the local activated receptor density, r , and the cytosolic PLC concentration, E . The former is the input to the simulation, with different values at the front and back of the cell, whereas the latter is close to spatially uniform and determined from the simulation. The d -nullcline is a straight line with a slope that is inversely proportional to the free PIP_2 concentration, with different values at the front and back of the cell determined from the simulation. The phase-plane plot for the case of 10% gradient, $rfrac = 0.1$ from Fig.

3.2A illustrates how PFL 1 synergizes with the regulation of MARCKS (Fig 3.5C). PFL 1 is directly responsible for the positive slope of the e -nullcline; without PFL 1, the e -nullcline has zero slope. In conjunction, regulation of MARCKS is directly responsible for the PIP_2 density being higher (lower slope of the d -nullcline) at the front versus the back of the cell; without MARCKS, free PIP_2 can only be lower, not higher, at the front (16). This analysis also shows how the situation changes for lower or higher $rfrac$, lending insight into dose-response robustness (Fig. 3.6).

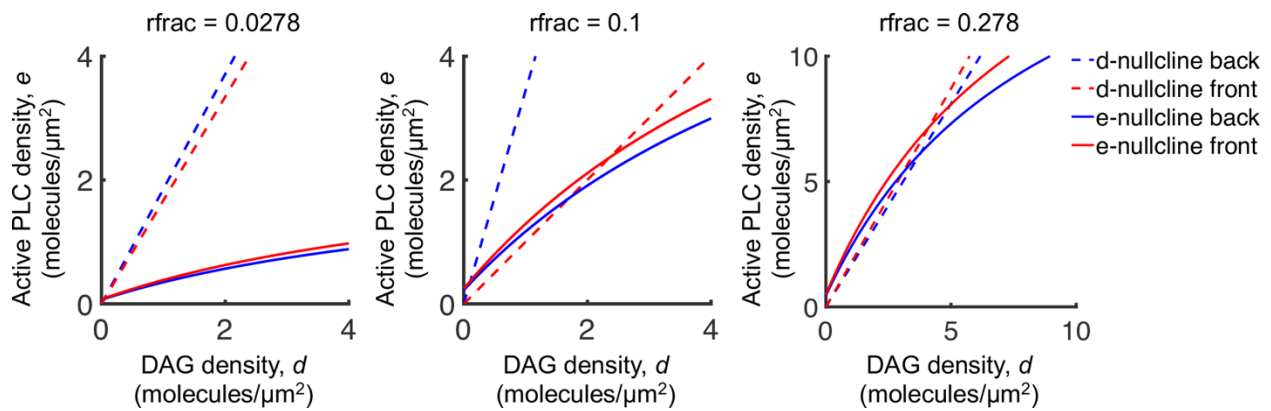


Figure 3.6 Phase plots for different $rfrac$ values. These correspond to the simulations analyzed in Fig. 3.2A with 10% gradient steepness. The plot with $rfrac = 0.1$ is the same as in Fig. 3.5A. When $rfrac = 0.0278$, DAG is low at both the front and back of the cell; with $rfrac = 0.278$, DAG is high at both the front and back of the cell.

3.2.4 Subtle asymmetry in cell morphology polarizes the PLC/PKC network with PFL 1 and influences external gradient sensing

Given the demonstrated sensitivity of the present gradient sensing circuit and its dependence on diffusion of MARCKS in the cytosol, we reasoned that a slight asymmetry in cell morphology might be a sufficiently strong spatial cue to polarize signaling in response to uniform receptor occupancy. To test this, the cell geometry was altered such that the back end of the cell was blunted compared to the front end (Fig. 3.7A). With uniform stimulation and the same parameter set used in Fig. 3.2A, the shape asymmetry polarized the signaling network, disfavoring the blunted end, for a range of $rfrac$ values (Fig. 3.7B). As expected, this polarization requires a gradient of phosphorylated MARCKS, with a dependence on cytosolic MARCKS diffusivities similar to polarization induced by an external gradient (Fig. 3.7C, compare to Fig. 3.5A).

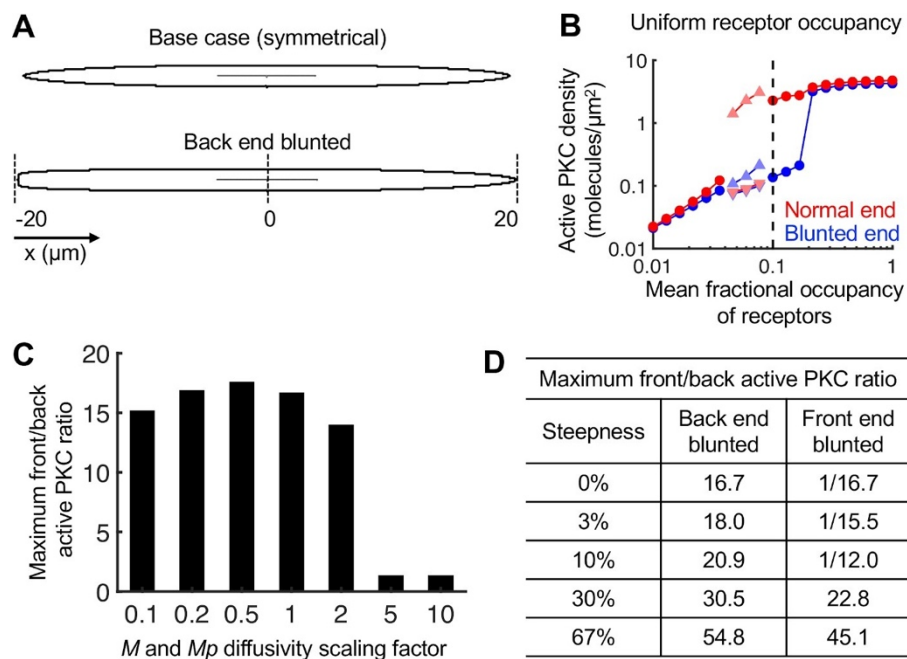


Figure 3.7 Subtle asymmetry in cell morphology causes spontaneous polarization of the proposed PLC/PKC network and influences external gradient sensing. (A) Comparison of the symmetric cell geometry versus the asymmetric cell geometry. (B) Results for the asymmetric geometry with uniform receptor occupancy (0% gradient steepness) show spontaneous polarization of the system for a particular range of receptor occupancy values. Symbols have the same meanings as in Fig. 3.2A. (C) Sensitivity of the results in B to the indicated fold-changes in MARCKS (M and M_p) cytosolic diffusivities (1 = base case). (D) Table showing the maximum front/back active PKC ratio for each gradient steepness indicated using the asymmetric geometry. Consistent with the rest of the paper, the front and back of the cell refer to the ends with the highest and lowest receptor activation, respectively. For the front-end blunted simulations where the ratio is less than 1 (internal gradient opposite the external gradient), the inverse of the ratio is indicated.

The tendency of the asymmetric cell geometry to polarize was also tested with receptor occupancy gradients in either direction (Fig. 3.7D). Consistent with the rest of the paper, the front of the cell refers here to the right end, with the highest receptor occupancy, and the back of the cell is at the left end, with the lowest receptor occupancy. With the blunt end of the cell at the back, the maximum degree of active PKC polarization is only modestly affected by receptor occupancy gradients of 3% and 10%, relative to uniform stimulation, whereas 30% and 67% gradients elicit substantially greater polarization similar to the symmetric geometry

(compare Fig. 3.7D and Fig. 3.2B). Consistent with that trend, when the blunt end of the cell was at the front (right-to-left gradient), the shape effect opposes the influence of the receptor occupancy gradient and dominates for 3% and 10% gradients, whereas the steeper gradients were sufficient to overcome the geometry effect. These results indicate that the cell's local morphology can readily alter or play a dominant role in the polarization of PLC/PKC signaling.

3.2.5 The model predicts a critical role of DAG kinases affecting the responsiveness of the gradient sensing network through PFL 1

Having characterized and explained how PFL 1 influences polarization of the signaling network, we considered the robustness of this system to substantial changes in rate parameters. Each of the rate constants and affinity parameters was increased by 3X and reduced to 0.3X to yield a full order-of-magnitude range, and the analysis shown in Fig. 3.2A was repeated for each. A plot of the maximum front/back ratios of activated PKC shows that polarization is fairly robust to a 3-fold change of each parameter in at least one direction (Fig. 3.8). The changes that break the polarization are those that weaken PLC recruitment, alter MARCKS phosphorylation by PKC (as explored in (16)), or alter lipid metabolism. The three parameters associated with the latter (k_{DAGK} , k_{PAP} , and $k_{basal,dp}$) are pseudo-first-order rate constants that reflect enzymatic metabolism of DAG and PA. Reasoning that the interconversion of DAG and PA is a pivotal aspect that needs to be understood, we devised a simple steady-state analysis assuming negligible diffusion of DAG and PA (*Appendix B*). This analysis predicts a consistent proportional relationship between the concentrations of DAG and PA. To verify this conclusion, the steady-state concentration of PA at the front of the cell was plotted versus that of DAG for all of the

simulations analyzed in Fig. 3.2A; each of these points lies approximately on the line predicted by the analytical expression (Fig. 3.9A).

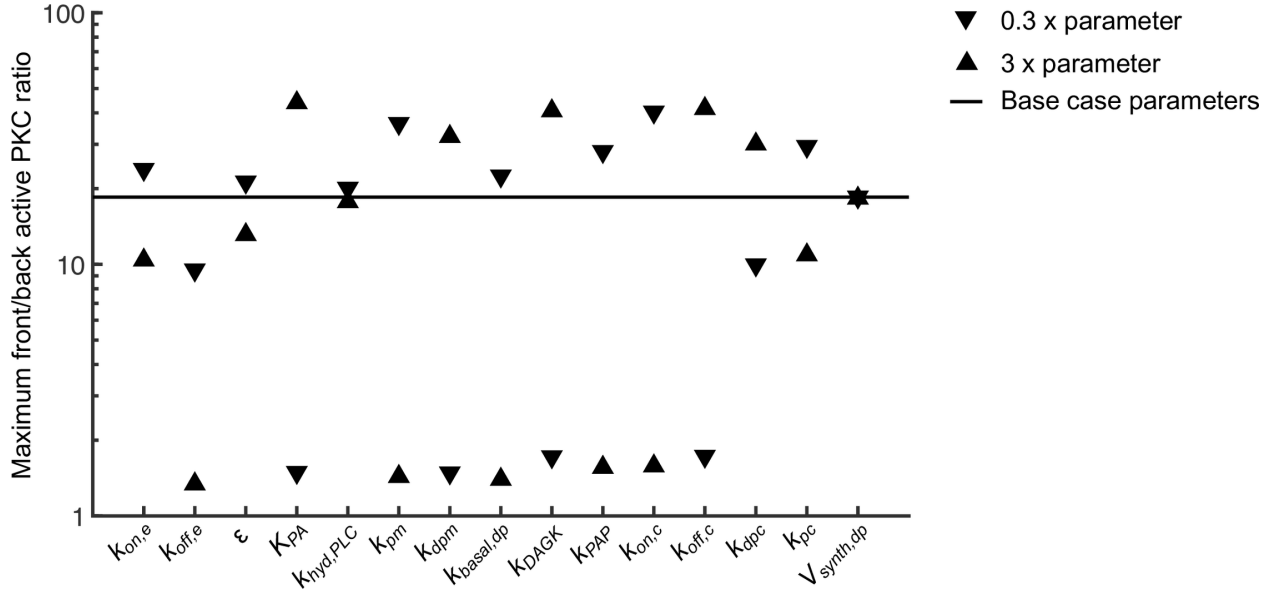


Figure 3.8 Systematic variation of kinetic parameters (no PFL 2).

The analysis shows that the activity of DAG kinases, reflected in the value of the rate constant, k_{DAGK} , directly alters the PA/DAG ratio. Intuitively, diminishing DAG kinase activity is expected to result in higher DAG and active PKC levels; however, in the model with PFL 1 and a nominal 10% gradient of receptor occupancy, a reduction of k_{DAGK} to 0.3 times its base value ablates polarization, whereas an increase of k_{DAGK} to 3 times its base value substantially enhances the degree of polarization and dose-response robustness (Fig. 3.9B). Analysis of DAG and PA levels for 1x and 3x k_{DAGK} (Fig. 3.9C) shows that as the parameter is increased, the density of DAG at the cell front is decreased as expected, but only modestly so (~30% reduction) because of the substantially increased abundance of PA; at the rear of the cell, the impact on DAG is

relatively far greater (~70% reduction). These effects of increased k_{DAGK} extend to receptor-activation gradients with 3% steepness (Fig. 3.9D).

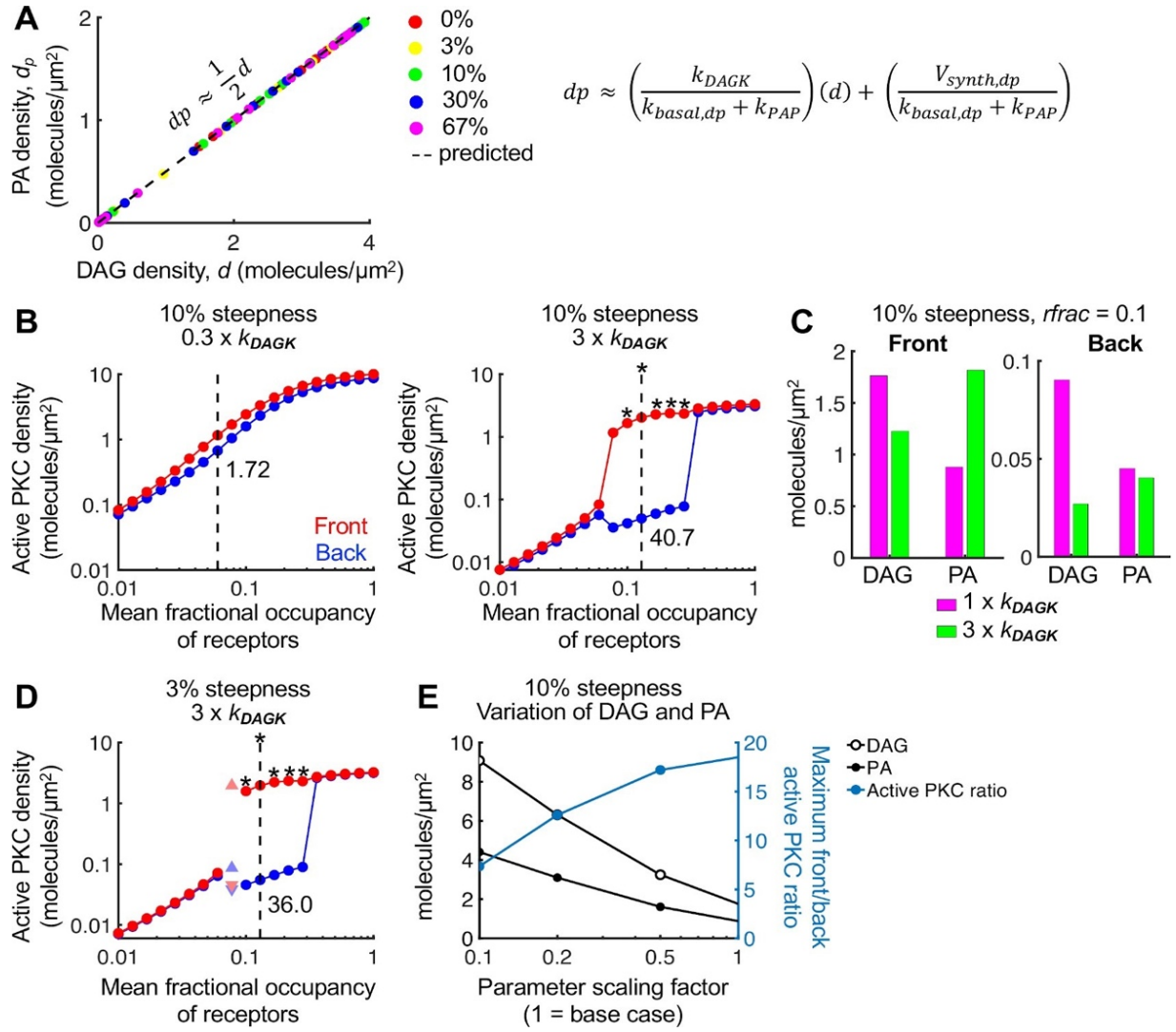


Figure 3.9 Variation of PA/DAG ratio modulates the sensitivity and dose response of the pathway. (A) The final steady-state concentration of PA (d_p) is plotted versus the concentration of DAG (d) at the front of the cell for each simulation presented in Fig. 3.2. These points fall along the line predicted by the equation shown, for which net diffusion of lipids is assumed to be slow. (B) Relative to the parameter set associated with Fig. 3.2, the parameter k_{DAGK} was taken at 0.3 or 3 times its base value, at 10% gradient steepness. Colors and symbols have the same meanings as in Fig. 3.2A. The maximum front/back ratio is shown underneath the symbols. (C) Bar plots comparing the DAG and PA steady-state concentrations at the front and back of the cell for 1x and 3x k_{DAGK} simulations, with 10% steepness and $rfrac = 0.1$. (D) Same as B, but with 3% gradient steepness. For B-D, the direction of the gradient was reversed after 20,000 s. If the active PKC pattern failed to reverse in response, the simulation is marked with an asterisk. (E) The parameter scaling factor refers to the fold-change by which the parameters k_{DAGK} , k_{PAP} , $k_{basal,dp}$, and K_{PA} were decreased, while the parameter $k_{off,c}$ was divided by the scaling factor to increase its value. These parameter changes increase DAG and PA levels at the front of the cell systematically, while maintaining approximately the same PA/DAG ratio and comparable effects of PA and DAG on PFL 1 and PKC recruitment, respectively.

To further test this analysis, we predicted that we could increase the steady-state levels of both DAG and PA, while maintaining the same PA/DAG ratio, by proportional reduction of all three of k_{DAGK} , k_{PAP} , and $k_{basal,dp}$. To normalize for these changes at the level of PFL 1 and PKC activity, we applied the same reduction factor to the PA-PLC affinity parameter, K_{PA} , and to the DAG-PKC affinity (by increasing $k_{off,c}$). With these changes, we were able to maintain polarization while increasing DAG and PA levels by almost an order of magnitude (Fig. 3.9E).

3.2.6 PKC-mediated activation of PLD (PFL 2) confers less responsiveness than PFL 1, but the two feedbacks can synergize in the polarization of PLC/PKC signaling

The other putative source of feedback we consider is the ability of active PKC to amplify the hydrolysis of phosphatidylcholine by PLD, producing PA and additional DAG upon dephosphorylation of PA (PFL 2). Parameters characterizing PFL 2 are a saturation constant, K_{PLD} , gain parameter, γ , and Hill coefficient, n . Extensive parameter sweeps of K_{PLD} and γ were performed with n fixed at either 1 (Michaelian sensitivity) or 2 (modestly ultrasensitive). At a 10% gradient in receptor activation, PFL 2 along with the regulation of MARCKS was unable to polarize DAG and active PKC with $n = 1$, whereas with $n = 2$, a particular combination of K_{PLD} and γ values yielded strong polarization; however, the degree of polarization and dose-response robustness are less than those with PFL 1 instead (Fig. 3.10A). That said, ultrasensitive PFL 2 shows synergy when combined with PFL 1. Firstly, the inclusion of both PFLs (with re-optimization of K_{PLD} and γ for PFL 2) allowed for polarization without MARCKS (Fig. 3.10B). When all three feedbacks (PFLs 1 and 2 and regulation of MARCKS) were present, both the degree of polarization and the dose-response robustness were dramatically enhanced, at the expense of reversibility (Fig. 3.10C). Consistent with these conclusions,

polarization of the system with PFL 2 is broken by 3-fold changes in parameters that influence PA levels (k_{DAGK} or K_{PLD}) except when all three feedbacks are included (Fig. 3.11).

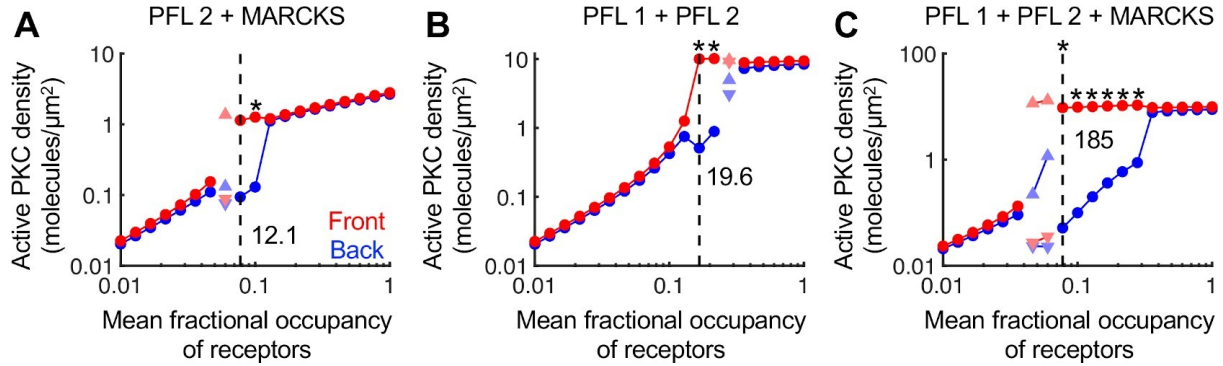


Figure 3.10 PFL 2 confers less responsiveness than PFL 1, but the two can synergize in the polarization of PLC/PKC signaling. The simulations shown are all at a 10% gradient of receptor occupancy. All colors, symbols, and values have the same meanings as in previous figures. (A) PFL 2 and MARCKS regulation but no PFL 1. For PFL 2, the parameters K_{PLD} and $\gamma V_{synth,dp}$ are set at 1 and 1, respectively. (B) PFL 1 and PFL 2 but no MARCKS. The parameters K_{PLD} and $\gamma V_{synth,dp}$ are set at 0.1 and 10, respectively. (C) All three feedbacks are included, and K_{PLD} and $\gamma V_{synth,dp}$ are set as in B. For all of these simulations, the direction of the gradient was reversed after 20,000 s. If the active PKC pattern failed to reverse in response, the simulation is marked with an asterisk.

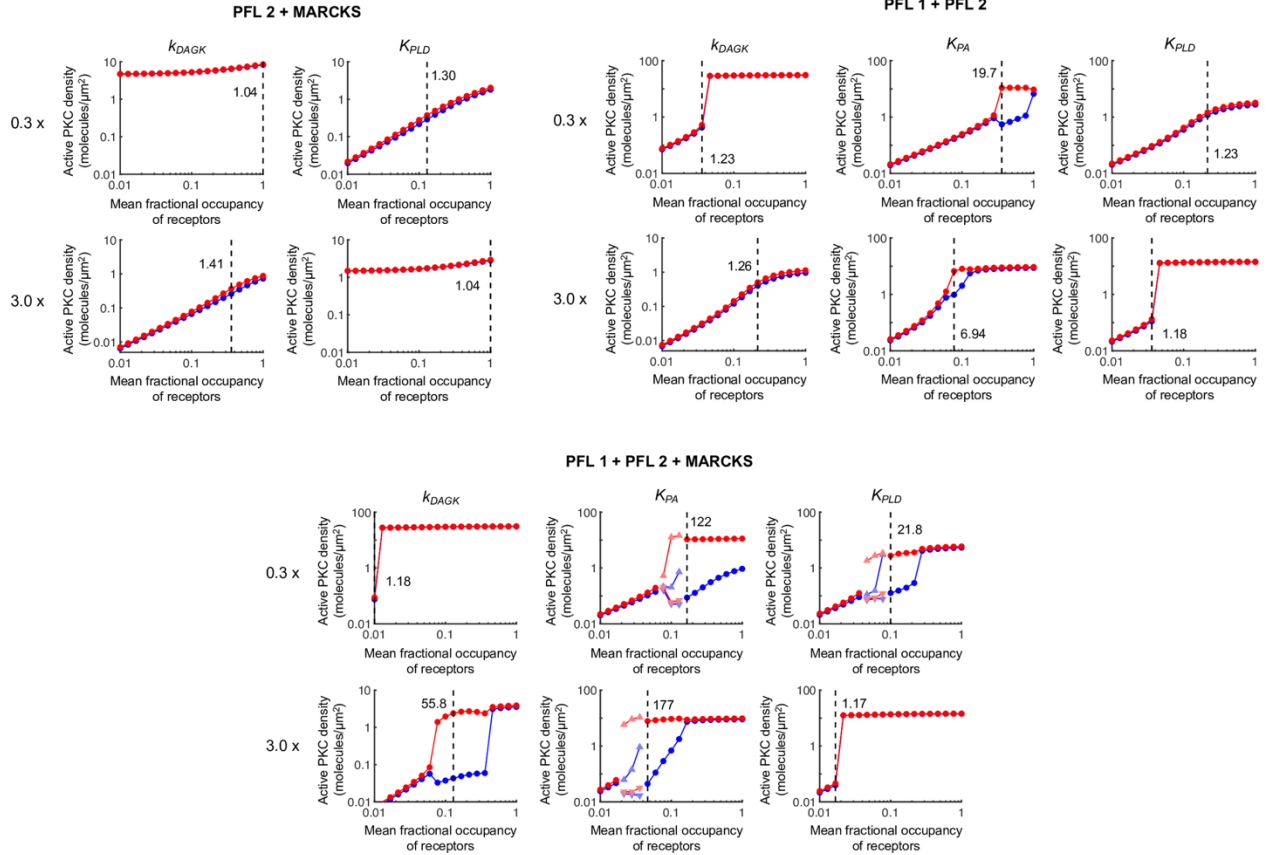


Figure 3.11 Variation of key parameters with PFL 2 included in the system. The parameters targeted were k_{DAGK} , which affects the conversion of DAG to PA; K_{PA} , which affects the PA-PLC affinity in PFL 1; and K_{PLD} , which affects the sensitivity of PFL 2 to active PKC. Each parameter was decreased to 0.3X and increased to 3X. Each plot shows active PKC density vs. $rfrac$ for 10% gradient steepness, as in Fig. 3.10.

The following section including the text, model development and analysis, and figure 3.12 were created or performed by Dr. Anisur Rahman.

3.2.7 Thresholds for chemotactic migration matching those of DAG/PKC polarization yield efficient collective invasion and chemotactic wavelets in simulations of wound invasion

Having characterized the polarization of the proposed PLC/PKC network, we asked how it might influence directed cell migration in a physiological context. To address this, we adapted a hybrid simulation of wound invasion, in which the concentration of PDGF evolves as a

continuum in one dimension, and fibroblasts are treated as motile line segments (28). A key prediction of the previous wound invasion model, which did not consider a polarizable gradient sensing mechanism, is that the cells can collectively generate a PDGF gradient through receptor-mediated endocytosis and lysosomal degradation (29), a concept that has since been verified in experimental systems (30–33). Thus, fibroblast invasion of the simulated wound is guided by a chemotactic wave. This model was modified such that chemotaxis is switched on or off according to the receptor activation conditions that yield polarization of PKC activity for the modestly robust model and base-case parameters used to generate the results shown in Fig. 3.2. When chemotaxis is switched off, the cell moves in a random direction (left or right). The cell migration parameters were chosen to be consistent with experimentally measured migration speed and chemotactic (forward migration) index values (10,11).

The movements of the cells in the simulation may be animated to visualize the collective behavior (Fig. 3.12A), and the progress of the cell population shows substantially faster invasion relative to simulations in which chemotaxis was not allowed (random migration only) (Fig. 3.12B). This was anticipated because of the chemotactic behavior, but inspection of the simulations revealed an emergent property of the system. While the major chemotactic wave at the leading front of the cell population, located within the steepest gradient in PDGF concentration, remains a primary feature (Fig. 3.12C), the present model predicts the existence of chemotactic wavelets that arise and propagate within the plateau region of the PDGF concentration profile (Fig. 3.12D). Thus, in the present model, significant chemotaxis occurs throughout the wound (Fig. 3.12C & 3.12D), as cells that enter the simulated wound at later times are able to create and follow the mesoscopic waves to explore more of the space. These results show that even modest dose-response robustness of the circuit is sufficient to affect

chemotaxis in tissues, where chemoattractant gradients are dynamic. Indeed, it is the dynamic nature of the gradients that makes this possible.

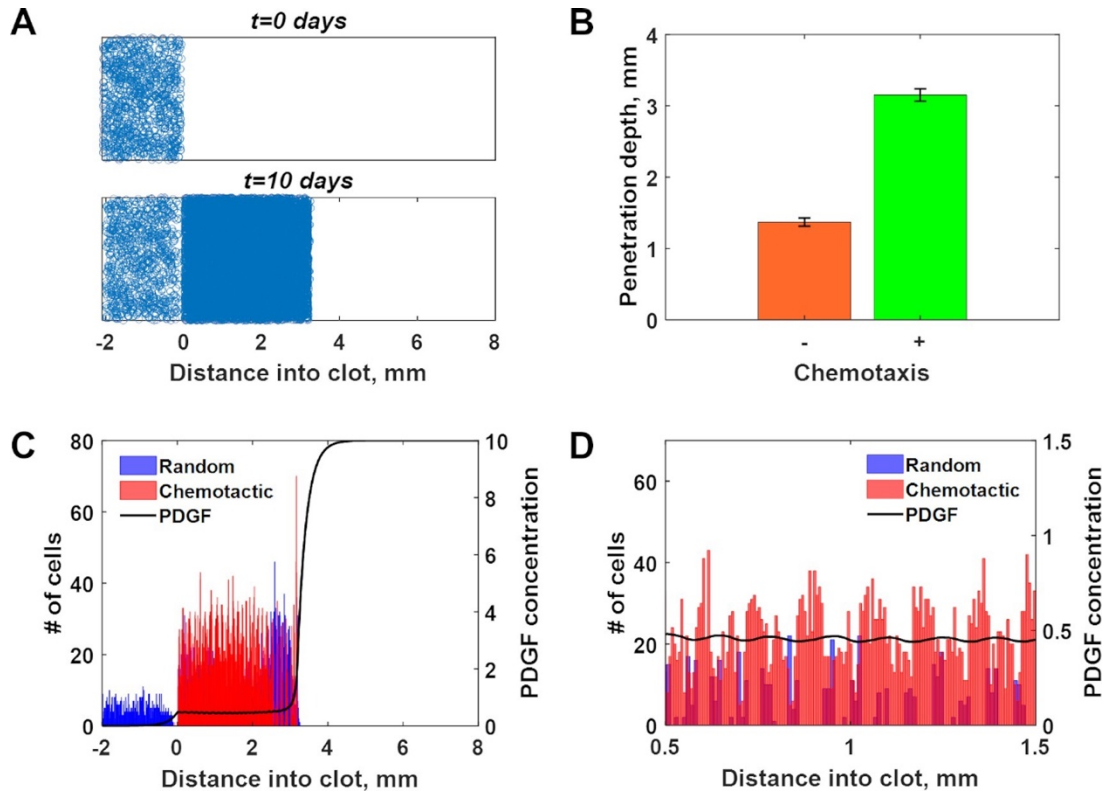


Figure 3.12 Simulation of wound invasion with chemotactic switching based on DAG/PKC polarization. (A) Depiction of individual cells in the hybrid simulation, in which the concentration of PDGF is modeled as a continuum. The cells are initially seeded in the adjacent dermis; position along the vertical dimension is for visualization only. As time elapses, the cells invade and populate the clot region through a combination of directed migration and proliferation. (B) Depth of penetration into the wound at $t = 10$ days for random migration only or with chemotaxis allowed (mean \pm s.d., $n = 10$ simulations each). (C) Spatial profiles of cell densities (randomly or chemotactically migrating) and dimensionless PDGF concentration. (D) Zoomed-in view of the cell density and PDGF concentration profiles for 1 mm length of the clot region, showing chemotactic wavelets.

3.3 Discussion

3.3.1 Novel ways that lipid signaling might enhance chemotactic gradient sensing, corroborated by modeling

While the bulk of the signal transduction literature focuses on proteins and their regulation by phosphorylation, it is easy to forget the significance of lipid second messengers. In the context of spatial sensing and directed cell migration, phosphoinositides and other plasma membrane lipids are uniquely positioned, owing to their peripheral location, slow diffusion, relative abundance, and diversity of lipid-protein interactions (14,34). For more than two decades, research on lipid-mediated mechanisms of chemotactic gradient sensing has emphasized signaling through class I phosphoinositide 3-kinases (PI3Ks), which phosphorylate PIP₂ to produce phosphatidylinositol (3,4,5)-trisphosphate (35,36). That lipid and its breakdown product, phosphatidylinositol (3,4)-bisphosphate, interact with a host of signaling proteins that locally enhance F-actin polymerization by affecting activation of the Arp2/3 complex (37). However, in most cell types tested, PI3K signaling is not absolutely required for chemotaxis, and, in fibroblasts and macrophages, even the Arp2/3 complex is dispensable for chemotaxis (10,11). For chemotaxis of fibroblasts and other mesenchymal cells, PLC/PKC signaling is required, and so increased focus on this pathway and on DAG as a lipid second messenger is warranted.

The present models consider the dynamics of lipid signaling beyond DAG. Plasma-membrane DAG is phosphorylated by DAG kinases to produce PA, a lipid second messenger in its own right (17,18). With PFL 1, we considered the ability of PA to enhance the observed affinity of PLC γ for PIP₂ (23), presumably by increasing the lifetime of enzyme binding to membranes. We note that PLC β 1 activity, which is fostered by G protein-coupled receptor

signaling, is also promoted by PA (38). In the model, this putative feedback locally enhances PLC recruitment by activated receptors and the hydrolysis of PIP₂. This effect of PA at the cell's leading edge offsets the action of DAG kinases in metabolizing DAG. As a single feedback, PFL 1 was not sufficient to polarize signaling in the model, requiring also the recruitment and activation of PKC by DAG. The necessary action of PKC could involve either or both of two mechanisms. The more potent of the two is the neutralizing phosphorylation of MARCKS by PKC, which directly synergizes with the enhancement of PLC recruitment by enhancing the supply of PIP₂ substrate. The less direct route is PFL 2, by which PKC enhances the activity of PLD; PLD hydrolyzes phosphatidylcholine to produce PA and thus presents a parallel pathway for DAG generation. Highlighting the weaker influence of PFL 2 on polarization in the model, it was necessary to add positive cooperativity with respect to active PKC and to fine-tune the values of the PFL 2-associated parameters. As one might expect, including all three feedback mechanisms in the model, with the provisions for PFL 2, yielded the most sensitive and robust gradient sensing circuit.

3.3.2 Robustness and reversibility of polarization

The key challenges met to varying degrees by our models is to achieve polarization in shallow gradients and for an appreciable range of chemoattractant concentration (dose-response robustness). These two aspects go hand in hand for our models: greater sensitivity and degree of polarization were generally accompanied by greater dose-response robustness. These positive aspects could be enhanced, through changes to the parameter values or addition of a feedback, but with loss of reversibility; the system is polarized and tends to remain locked in place even when the gradient is reversed. This observation is consistent with analyses of other gradient

sensing models that show a tradeoff between amplification and self-locking behavior (39–42). Self-locking is generally considered undesirable, because it precludes a prompt response to dynamic changes in the chemoattractant gradient. To adjust the directionality of movement, a cell with its chemotactic signaling polarity locked would have to execute a turn. For a gradual response such as wound invasion, such a system might be adequate or even advantageous. Obviously, with a 1D wound geometry, persistent chemotaxis would yield the maximum rate of invasion. But even with instantaneous switching between polarization states, our hybrid invasion model showed efficient invasion, with chemotactic waves arising throughout the volume of the wound occupied by cells.

As suggested previously, a gradient sensing circuit capable of polarizing in response to shallow gradients can also polarize in response to an asymmetric cell geometry (16). This is not a generality, however. In the context of this model, it is particular to the proposed regulation of MARCKS, where the local ratio of plasma membrane area to cytosolic volume affects the dynamics. This follows basic ideas discussed in detail elsewhere (43–47). If sensitivity to morphology were significant, it could act as an additional feedback mechanism. On the other hand, from the perspective of sensing external gradients, any such intrinsic cue might be considered a detriment.

3.3.3 Testable hypotheses guided by the models

Analysis of the present models offers a guide for experiments designed to test certain predictions, with polarization of DAG in chemotaxing cells as the essential readout. At a phenomenological level, a basic prediction of the models is that there is a minimum threshold of receptor activation, determined by the chemoattractant concentration, below which the pathway

cannot polarize. Considering the heterogeneity in a cell population, for a suitable gradient one should expect to find subpopulations that do or do not show DAG polarization. For the shallow gradients typically achieved in chemotaxis chambers, an upper bound on receptor activation is also predicted. Whether or not either the minimum threshold or upper bound can be exceeded would depend on a cell's expression level of the cognate receptor.

Regarding molecular mechanisms, the most basic prediction is the requirement for PKC activity, which may be readily tested using isoform-selective inhibitors. The regulation of MARCKS requires PKC activity, whereas modulation of PLD requires interaction with membrane-associated PKC but not PKC kinase activity (48,49). From there, perturbations affecting MARCKS and PLD may be pursued. The line of experimentation outlined above does not address PFL1, which does not rely on PKC. The prediction most directly related to PFL 1 concerns the role of DAG kinases, which consume DAG but produce PA in the process. It is predicted that even a partial inhibition of DAG kinase activity (achieved either pharmacologically (50,51) or by depleting DAG kinase isoforms), while increasing DAG on a whole-cell level, would abrogate polarization for all doses of chemoattractant. Conversely, enhancement of DAG kinase activity, which might be achieved by overexpressing one or more of the isoforms, is predicted to enhance the dose-response robustness of polarization by increasing the upper bound of receptor activation. If true, more cells would be able to polarize at higher concentrations of chemoattractant.

Finally, the effect of cell geometry could be tested by co-expression of or labeling with a fluorescent, cytosolic volume marker. Imaged by epifluorescence, the marker would quantify the local height of the cytoplasm; the lower this quantity in a lamellipod, the higher the membrane

area/volume, and the more likely the DAG is to be enriched there if the predicted geometry effect is significant.

3.3.4 Limitations of the models

The purpose of these models is to provisionally test the plausibility of the proposed feedback mechanisms. Modeling of stochastic effects and three-dimensional cell geometries with moving boundaries would make the simulations more realistic, with far greater computational expense. The topology of the signaling network is also by no means complete. As already noted, certain details of the mechanisms considered are incompletely understood, and other mechanisms not considered here might also contribute. Regarding the latter, one might consider other possible roles of the lipids involved. Whereas we focused on the putative influence of PA on PLC, PA has also been reported to enhance phosphatidylinositol 4-phosphate 5- kinase activity (52), which could boost the rate of PIP₂ generation. In principle, we would expect this effect to amplify PFL 1. PIP₂ also functions in other capacities that could impact PLC/PKC signaling and chemotaxis. For one, PIP₂ is the preferred substrate of class I PI3Ks. Although PI3K signaling is not absolutely required for mesenchymal chemotaxis, PI3K competes with PLC for the common substrate and could be influenced by MARCKS (53). PIP₂ is also bound by the actin-modifying proteins cofilin and profilin at the plasma membrane (54). Local modulation of free PIP₂ and its hydrolysis by active PLC is expected to impact cofilin and profilin functions in chemotaxis (55,56). Finally, we note that PIP₂ is a cofactor for PLD, influencing the enzyme's membrane localization and activity (57).

One of the key experimental observations that we have yet to adequately explain is the ability of phorbol ester (a DAG mimic) to elicit fibroblast chemotaxis when presented as a

shallow gradient, even in PLC γ 1-null cells (11). This scenario is akin to the model with PFL 2 only and no MARCKS, for which we could not find any set of parameter values that yielded polarization of PKC activity in response to a shallow ($\leq 10\%$) gradient. Whether or not a phorbol ester gradient polarizes DAG/PKC is presently unknown; it is possible that chemotaxis occurs regardless. If polarization does occur in PLC-null cells executing phorbol ester chemotaxis, the nature of the underlying mechanisms will need to be clarified.

3.4 Materials and Methods

3.4.1 Models of PLC/PKC signaling

The reaction-diffusion models are composed of partial differential equations and associated boundary and initial conditions. The species in the models and their interactions are described here; mathematical details and justifications for chosen parameter values are given in *Appendix B*. Within that document, model species, their diffusivity values, and initial conditions are listed in Table B.1, and rate equations and base-case values of rate constants are listed in Table B.2. Cytosolic species, signified by capital letters, have local concentrations in μM , whereas membrane species, signified by lowercase letters, have local densities in $\#/\mu\text{m}^2$. Rather than explicitly model the ligand-receptor dynamics, in this work we assume a linear profile of active receptors (r) as the model input, calculated from Eq. 3.1.

$$r = 130 \, rfrac \left[1 + rsteep \left(\frac{x}{40} \right) \right] \quad (3.1)$$

As explained under Results, the prefactor determines the midpoint value of r ; when the dimensionless $rfrac = 1$, the midpoint value of $r = 130/\mu\text{m}^2$, corresponding to approximately $1 \times 10^5/\text{cell}$. The distance from the midpoint, x , is in μm , and it is scaled by the cell length of $40 \mu\text{m}$.

Therefore, r_{steep} is the fractional gradient steepness; a value of $r_{steep} = 0.1$, for example, corresponds to a 10% difference between the values of r at the extreme front and back of the cell.

Referring to the diagram shown in Fig 3.1A, activated receptors recruit inactive PLC enzyme (E) from the cytosol to form active PLC at the membrane (e). Active PLC hydrolyzes PIP_2 (free-density p). In the absence of stimulation, the density of PIP_2 is maintained through basal synthesis and turnover. PIP_2 hydrolysis by PLC generates the lipid second messenger, DAG (d). DAG is phosphorylated by DAG kinases to produce PA (d_p), which can be dephosphorylated by phosphatidic acid phosphatases to recover DAG (22,58); these are modeled as pseudo-first-order reactions. Like PIP_2 , PA is also subject to basal generation and consumption; however, basal generation of PA is intentionally very low. DAG recruits catalytically competent but inactive PKC (C) from the cytosol by reversible binding of the tandem C1 domain of PKCs, forming active PKC (c^*) at the membrane (59). Membrane-bound PKC is sensitive to dephosphorylation, and so the active PKC is converted to an inactive, membrane-bound form (c); this species is either autophosphorylated to regenerate active PKC or it dissociates to join the cytosolic pool. MARCKS is an abundant substrate of PKC that is present in both cytosolic and membrane-bound forms (14). The unphosphorylated, cytosolic form (M) inserts into the plasma membrane via its myristoyl group and interacts with PIP_2 via its effector domain; the latter is a high-avidity, electrostatic interaction, and thus, MARCKS sequesters a substantial fraction of the intracellular PIP_2 (13,60). The membrane-bound forms of MARCKS (m) are phosphorylated by active PKC, causing loss of affinity for the plasma membrane and liberation of PIP_2 ; the phosphorylated form of MARCKS (M_p) is cytosolic (12). MARCKS is dephosphorylated in the cytosol by a pseudo-first-order reaction to complete the cycle.

Imposed on this basic network structure are two additional PFLs. As described under Results, PFL 1 considers that the PA engages PLC in complex with activated receptors and thus extends the enzyme's mean lifetime (or, reduces its effective off-rate) at the plasma membrane. The net rate of PLC recruitment, V_{PLC} , is given by Eq. 3.2.

$$V_{PLC} = k_{on,e}(r - e)E|_S - k_{off,e} \left(\frac{1 + \varepsilon K_{PA} d_p}{1 + K_{PA} d_p} \right) e \quad (3.2)$$

In this equation, the parameters characterizing PFL 1 are K_{PA} , the equilibrium constant of PA-PLC interaction, and ε , a dimensionless escape probability (see *Appendix B*). With either K_{PA} set to zero or ε set to 1, PFL 1 is turned off. PFL 2 considers that active PKC engages and enhances the activity of PLD. This influence on the rate of PA synthesis, V_{PLD} , is modeled as a Hill function in Eq. 3.3.

$$V_{PLD} = V_{synth,dp} \left(\frac{1 + \gamma (K_{PLD} c^*)^n}{1 + (K_{PLD} c^*)^n} \right) \quad (3.3)$$

In this equation, the parameters characterizing PFL 2 are K_{PLD} , a saturation constant, γ , a dimensionless gain parameter, and n , the Hill coefficient. With either K_{PLD} set to zero or γ set to 1, PFL 2 is turned off.

3.4.2 Implementation of PLC/PKC models

The partial differential equation models are implemented in Virtual Cell (<http://www.vcell.org>), a computational environment for modeling and simulation in cell biology (61). The Biomodel and primary simulations are publicly available in Virtual Cell under user name jnosbis, Biomodel name 'Nosbisch chemotaxis 2020'. As in Mohan et al. (16), the base two-dimensional geometry is an ellipse with a major axis length of 40 μm and minor axis length of 1.8 μm (Fig 3.1B); these dimensions were selected according to the important dimensions of a migrating fibroblast. For the asymmetric geometry considered in Fig. 3.7, the left end of the

ellipse was blunted by changing the y -component of the ellipse equation to have an exponent of 6, rather than 2, for negative values of x .

Virtual Cell uses a finite-volume method to numerically solve the reaction-diffusion equations, and the Fully-Implicit Finite Volume (variable time step) solver was used, with voxel dimensions of $\Delta x = \Delta y = 0.1 \mu\text{m}$ and a maximum time step of 0.1 s. We confirmed that the computational results were not significantly affected by modest changes to those values. The initial conditions are such that the system is stationary in the absence of stimulation. Simulations were run for 20,000 s to ensure either a steady state or sustained oscillations. For all simulations, the reversibility of the spatial pattern was assessed by reversing the gradient of PDGF receptor activation across the cell after a steady state was reached and extending the simulation for another 20,000 s. If the spatial pattern achieved a steady state but failed to reverse, then we considered that simulation to display locking behavior, and the simulation is marked with an asterisk.

The following section including the text, model development and analysis, and figure 3.13 were created or performed by Dr. Anisur Rahman.

3.4.3 Wound healing model

The model of collective cell migration is adapted from the hybrid simulation strategy of Monine and Haugh, described in detail previously (28). Briefly, the dimensionless PDGF concentration, u , is treated as a continuum, subject to synthesis (only in the clot), interstitial diffusion, intrinsic degradation, and degradation by cells (receptor-mediated endocytosis). Local receptor activation, r , is given by the algebraic function, $r = u^2/(1 + u + u^2)$, based on a quasi-steady-state approximation (29); therefore, $u = 1$ corresponds to $r = 1/3$. The local value of r ,

along with the calculated cell density, determines the cell-mediated degradation of PDGF and the net rate of cell proliferation or death. The original code was adapted from C to MATLAB; the version that was implemented to generate the results shown in Fig. 3.12 is provided in the Supporting Information (S2 Text) of this published paper (see citation on pg. 55). The difference in the new model is that the migration behavior, rather than depending on intracellular signaling in an analog fashion, switches between random and chemotactically biased states. In the random state, the cells move with a diffusivity $D_{v1} = 3 \times 10^{-4} \text{ mm}^2/\text{h}$. Considering a persistence time of $\sim 0.5\text{--}1 \text{ h}$ for fibroblasts, this corresponds to a cell speed of $\sim 0.03 \text{ mm/h}$ ($\sim 0.5 \text{ }\mu\text{m/min}$) (62). In the chemotactic state, the cell movement is governed by diffusion and convection. For the base case, the chemotactic (convective) velocity in the direction of the PDGF gradient, S_{tax} , was chosen as 0.03 mm/h to match the cell speed estimate given above. The random component of the chemotactic cells' movements was set to a lower value of $D_{v2} = 1 \times 10^{-4} \text{ mm}^2/\text{h}$ to represent noise in the cell's movement up-gradient. It is envisioned that the cells' movements in the other two orthogonal dimensions of the tissue would be comparable regardless of migration state, and therefore a rough estimate of the associated chemotactic (forward migration) index is $\sim 1/3$, a modest value considering that measured population estimates of this forward migration index are ≈ 0.2 and include tracks of chemotaxing and non-chemotaxing cells (11).

The switching between random and chemotactic migration were taken from the approximate cut-offs between non-polarizing and polarizing conditions indicated in Fig 3.2, supplemented with additional data for $r_{steep} = 0.2, 0.4, \text{ and } 0.5$. For each value of r_{steep} , the lower and upper bounds of r_{frac} were approximated (at $r_{steep} = 0.67$, it was found that the upper bound, if it exists, is $\gg 1$), with oscillations considered non-polarizing. These data were used to construct a relationship between the value of r_{frac} (the variable r calculated in the wound

healing model) and the corresponding minimum value of r_{steep} required for polarization; in the wound healing model, r_{steep} was equated to $\Delta r/r$, where Δr is the difference in r values evaluated $\pm 20 \mu\text{m}$ from the midpoint (matching the cell length in the PLC/PKC models). The relationship was fit to Eq. 3.4, reminiscent of an inter-molecular potential.

$$\left(\frac{\Delta r}{r}\right)_{min} = 0.01 + a \left[\left(\frac{r_{opt}}{r}\right)^n - \frac{n}{m} \left(\frac{r_{opt}}{r}\right)^m + \frac{n}{m} - 1 \right] \quad (3.4)$$

The first term, 0.01, is an homage to the notion that the limit of spatial gradient sensing is a $\sim 1\%$ difference across a cell's length (63). The other constant parameter values are $a = 1.7$, $r_{opt} = 0.12$, $n = 2$, and $m = 1.5$. A plot of Eq. 3.4 with these parameter values is shown in Fig. 3.13.

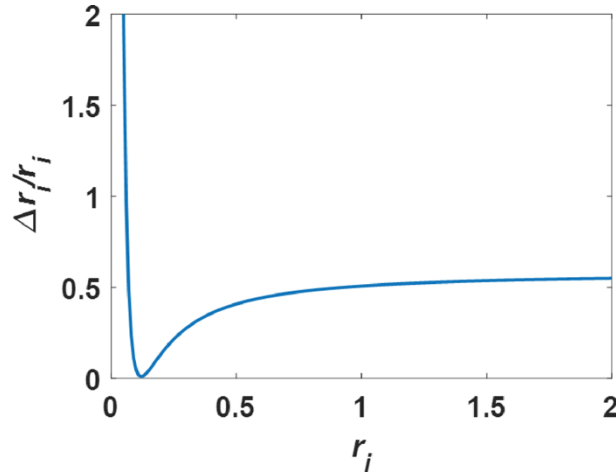


Figure 3.13 Plot of Eq. 3.4. For each cell i in the simulation, its mean receptor activation r_i and the difference in receptor activation across its length Δr_i were calculated. Cells with receptor activation states above the curve engaged in chemotaxis, whereas those with states below the curve engaged in random migration only.

3.5 Acknowledgments

We acknowledge use of the freely available Virtual Cell software (supported by NIH Grant Number R24 GM134211 from the National Institute for General Medical Sciences).

3.6 References

1. Swaney KF, Huang C, Devreotes PN. Eukaryotic chemotaxis: a network of signaling pathways controls motility, directional sensing, and polarity. *Annual Review of Biophysics*. 2010. June 9;;39(1):265–89.
2. Deuel TF, Kawahara RS, Mustoe TA, Pierce GF. Growth factors and wound healing: platelet-derived growth factor as a model cytokine. *Annual Review of Medicine*. 1991. February;42(1):567–84.
3. Singer AJ, Clark RAF. Cutaneous wound healing. *New England Journal of Medicine*. 1999. September 2;;341(10):738–46. 10.1056/NEJM199909023411006.
4. Werner S, Grose R. Regulation of wound healing by growth factors and cytokines. *Physiological Reviews*. 2003. July 1;;83(3):835–70. 10.1152/physrev.2003.83.3.835.
5. Eming SA, Martin P, Tomic-Canic M. Wound repair and regeneration: Mechanisms, signaling, and translation. *Science Translational Medicine*. 2014. December 3;;6(265):265sr6 10.1126/scitranslmed.3009337.
6. Artemenko Y, Lampert T, Devreotes P. Moving towards a paradigm: common mechanisms of chemotactic signaling in *Dictyostelium* and mammalian leukocytes. *Cell Mol Life Sci*. 2014. October;71(19):3711–47. 10.1007/s00018-014-1638-8.
7. Bear JE, Haugh JM. Directed migration of mesenchymal cells: where signaling and the cytoskeleton meet. *Current Opinion in Cell Biology*. 2014;30:74–82. 10.1016/j.ceb.2014.06.005.
8. Monypenny James, Zicha Daniel, Higashida Chiharu, Ocegüera-Yanez Fabian, Narumiya Shuh, Watanabe Naoki. Cdc42 and Rac Family GTPases regulate mode and speed but not direction of primary fibroblast migration during platelet-derived growth factor-dependent chemotaxis. *Molecular and Cellular Biology*. 2009. May 15;;29(10):2730–47. 10.1128/MCB.01285-08.
9. Melvin A, Welf E, Wang Y, Irvine D, Haugh J. In Chemotaxing fibroblasts, both high-fidelity and weakly biased cell movements track the localization of PI3K signaling. *Biophysical Journal*. 2011;100(8):1893–901. 10.1016/j.bpj.2011.02.047.
10. Wu C, Asokan S, Berginski M, Haynes E, Sharpless N, Griffith J, et al. Arp2/3 Is critical for lamellipodia and response to extracellular matrix cues but is dispensable for chemotaxis. *Cell*. 2012. March 2;;148(5):973–87. 10.1016/j.cell.2011.12.034.
11. Asokan S, Johnson H, Rahman A, King S, Rotty J, Lebedeva I, et al. Mesenchymal chemotaxis requires selective inactivation of Myosin II at the leading edge via a noncanonical PLC γ /PKC α pathway. *Developmental Cell*. 2014. December 22;;31(6):747–60. 10.1016/j.devcel.2014.10.024.

12. Seykora John T., Monn Myat Monn, Allen Lee-Ann H., Ravetch Jeffrey V., Aderem Alan. Molecular determinants of the myristoyl-electrostatic switch of MARCKS. *Journal of Biological Chemistry*. 1996. August 2,;271(31):18797–802. 10.1074/jbc.271.31.18797.
13. Glaser Michael, Wanaski Stephen, Buser Carolyn A., Boguslavsky Valentina, Rashidzada Wahid, Morris Andrew, et al. Myristoylated alanine-rich C kinase substrate (MARCKS) produces reversible inhibition of phospholipase C by sequestering phosphatidylinositol 4,5-bisphosphate in lateral domains. *Journal of Biological Chemistry*. 1996. October 18,;271(42):26187–93. 10.1074/jbc.271.42.26187.
14. McLaughlin S, Wang J, Gambhir A, Murray D. PIP₂ and proteins: Interactions, organization, and information flow. *Annual Review of Biophysics and Biomolecular Structure*. 2002. June;31(1):151–75.
15. Wang Jiyao, Gambhir Alok, Hangyas-Mihalyne Gyongyi, Murray Diana, Golebiewska Urszula, McLaughlin Stuart. Lateral sequestration of phosphatidylinositol 4,5-bisphosphate by the basic effector domain of myristoylated alanine-rich C kinase substrate is due to nonspecific electrostatic interactions. *Journal of Biological Chemistry*. 2002. September 13,;277(37):34401–12. 10.1074/jbc.M203954200.
16. Mohan K, Nosbisch JL, Elston TC, Bear JE, Haugh JM. A reaction-diffusion model explains amplification of the PLC/PKC pathway in fibroblast chemotaxis. *Biophysical Journal*. 2017. July 11,;113(1):185–94. 10.1016/j.bpj.2017.05.035.
17. Wang X, Devaiah SP, Zhang W, Welti R. Signaling functions of phosphatidic acid. *Progress in Lipid Research*. 2006;45(3):250–78. 10.1016/j.plipres.2006.01.005.
18. Jang J, Lee CS, Hwang D, Ryu SH. Understanding of the roles of phospholipase D and phosphatidic acid through their binding partners. *Progress in Lipid Research*. 2012. April;51(2):71–81. 10.1016/j.plipres.2011.12.003.
19. Liscovitch M, Czarny M, Fiucci G, Tang X. Phospholipase D: molecular and cell biology of a novel gene family. *The Biochemical Journal*. 2000. February 1,;345 Pt 3(3):401–15.
20. van Blitterswijk WJ, Houssa B. Properties and functions of diacylglycerol kinases. *Cellular Signalling*. 2000;12(9):595–605.
21. Jenkins G, Frohman M. Phospholipase D: a lipid centric review. *Cell Mol Life Sci*. 2005. October;62(19):2305–16.
22. Mérida I, Avila-Flores A, Merino E. Diacylglycerol kinases: at the hub of cell signalling. *The Biochemical Journal*. 2008. January 1,;409(1):1–18. 10.1042/BJ20071040.
23. Jones GA, Carpenter G. The regulation of phospholipase C-γ1 by phosphatidic acid. *J Biol Chem*. 1993. October/05,;268(28):20845–50.

24. Eldar H, Ben-Av P, Schmidt U S, Livneh E, Liscovitch M. Up-regulation of phospholipase D activity induced by overexpression of protein kinase C- α . Studies in intact Swiss/3T3 cells and in detergent-solubilized membranes in vitro. *Journal of Biological Chemistry*. 1993. June 15,;268(17):12560–4.
25. Lee Y H, Kim H S, Pai J K, Ryu S H, Suh P G. Activation of phospholipase D induced by platelet-derived growth factor is dependent upon the level of phospholipase C- γ 1. *Journal of Biological Chemistry*. 1994. October 28,;269(43):26842–7.
26. Henage LG, Exton JH, Brown HA. Kinetic analysis of a mammalian phospholipase D: allosteric modulation by monomeric GTPases, protein kinase C, and polyphosphoinositides. *The Journal of Biological Chemistry*. 2006. February 10,;281(6):3408–17. 10.1074/jbc.M508800200.
27. Rebecchi M, Peterson A, McLaughlin S. Phosphoinositide-specific phospholipase C- δ 1 binds with high affinity to phospholipid vesicles containing phosphatidylinositol 4,5-bisphosphate. *Biochemistry*. 1992. December 29,;31(51):12742 10.1021/bi00166a005.
28. Monine MI, Haugh JM. Cell population-based model of dermal wound invasion with heterogeneous intracellular signaling properties. *Cell Adhesion & Migration*. 2008. April 1,;2(2):137–45.
29. Haugh JM. Deterministic model of dermal wound invasion incorporating receptor-mediated signal transduction and spatial gradient sensing. *Biophysical Journal*. 2006;90(7):2297–308. 10.1529/biophysj.105.077610.
30. Venkiteswaran G, Lewellis S, Wang J, Reynolds E, Nicholson C, Knaut H. Generation and dynamics of an endogenous, self-generated signaling gradient across a migrating tissue. *Cell*. 2013. October 24,;155(3):674–87. 10.1016/j.cell.2013.09.046.
31. Donà Erika, Barry Joseph D, Valentin Guillaume, Quirin Charlotte, Khmelinskii Anton, Kunze Andreas, et al. Directional tissue migration through a self-generated chemokine gradient. *Nature*. 2013. November 14,;503(7475):285–9. 10.1038/nature12635.
32. Muinonen-Martin AJ, Susanto O, Zhang Q, Smethurst E, Faller WJ, Veltman DM, et al. Melanoma cells break down LPA to establish local gradients that drive chemotactic dispersal. *PLoS Biology*. 2014. October;12(10):e1001966 10.1371/journal.pbio.1001966.
33. Tweedy Luke, Knecht David A, Mackay Gillian M, Insall Robert H. Self-generated chemoattractant gradients: attractant depletion extends the range and robustness of chemotaxis. *PLoS Biology*. 2016. March 1,;14(3):e1002404 10.1371/journal.pbio.1002404.
34. Insall RH, Weiner OD. PIP3, PIP2, and Cell Movement—Similar messages, different meanings? *Developmental Cell*. 2001;1(6):743–7. 10.1016/s1534-5807(01)00086-7.

35. Devreotes Peter, Janetopoulos Chris. Eukaryotic chemotaxis: Distinctions between directional sensing and polarization. *Journal of Biological Chemistry*. 2003. June 6;;278(23):20445–8. 10.1074/jbc.R300010200.
36. Ridley AJ, Schwartz MA, Burridge K, Firtel RA, Ginsberg MH, Borisy G, et al. Cell migration: Integrating signals from front to back. *Science*. 2003. December 5;;302(5651):1704–9. 10.1126/science.1092053.
37. Rotty Jeremy D, Wu Congying, Bear James E. New insights into the regulation and cellular functions of the ARP2/3 complex. *Nature Reviews. Molecular Cell Biology*. 2013. January 1;;14(1):7–12. 10.1038/nrm3492.
38. Litosch I, Pujari R, Lee SJ. Phosphatidic acid regulates signal output by G protein coupled receptors through direct interaction with phospholipase C- β 1. *Cellular Signalling*. 2009. September;21(9):1379–84. 10.1016/j.cellsig.2009.04.005.
39. Meinhardt H. Orientation of chemotactic cells and growth cones: models and mechanisms. *Journal of Cell Science*. 1999. September 1;;112(17):2867–74.
40. Iglesias PA, Levchenko A. Modeling the cell's guidance system. *Sci Signal*. 2002. - September-03 00:00:00;2002(148).
41. Subramanian KK, Narang A. A mechanistic model for eukaryotic gradient sensing: spontaneous and induced phosphoinositide polarization. *J Theor Biol*. 2004. November;231(1):49–67. 10.1016/j.jtbi.2004.05.024.
42. Jilkin A, Edelstein-Keshet L. A comparison of mathematical models for polarization of single eukaryotic cells in response to guided cues. *PLoS Computational Biology*. 2011. April 1;;7(4):e1001121 10.1371/journal.pcbi.1001121.
43. Haugh JM. Membrane-binding/modification model of signaling protein activation and analysis of its control by cell morphology. *Biophysical Journal*. 2007;92(11):L9–L95.
44. Meyers J, Craig J, Odde D. Potential for control of signaling pathways via cell size and shape. *Current Biology*. 2006. September 5;;16(17):1685–93. 10.1016/j.cub.2006.07.056.
45. Neves SR, Tsokas P, Sarkar A, Grace EA, Rangamani P, Taubenfeld SM, et al. Cell shape and negative links in regulatory motifs together control spatial information flow in signaling networks. *Cell*. 2008. May 16;;133(4):666–80. 10.1016/j.cell.2008.04.025.
46. Rangamani P, Lipshtat A, Azeloglu E, Calizo R, Hu M, Ghassemi S, et al. Decoding information in cell shape. *Cell*. 2013. September 12;;154(6):1356–69. 10.1016/j.cell.2013.08.026.
47. Schmick M, Bastiaens PH. The interdependence of membrane shape and cellular signal processing. *Cell*. 2014. March 13;;156(6):1132–8. 10.1016/j.cell.2014.02.007.

48. Singer William D., Brown H. Alex, Jiang Xuejun, Sternweis Paul C. Regulation of phospholipase D by protein kinase C is synergistic with ADP-ribosylation factor and independent of protein kinase activity. *Journal of Biological Chemistry*. 1996. February 23,;271(8):4504–10. 10.1074/jbc.271.8.4504.
49. Hu T, Exton JH. Mechanisms of regulation of phospholipase D1 by protein kinase C α . *Journal of Biological Chemistry*. 2003. January 24,;278(4):2348–55. 10.1074/jbc.M210093200.
50. Jiang Y, Sakane F, Kanoh H, Walsh JP. Selectivity of the diacylglycerol kinase inhibitor 3-{2-(4-(bis-(4-fluorophenyl)methylene)-1-piperidinyl)ethyl}-2,3-dihydro-2-thioxo-4(1H)quinazolinone (R59949) among diacylglycerol kinase subtypes. *Biochemical Pharmacology*. 2000. April 1,;59(7):763–72. 10.1016/s0006-2952(99)00395-0.
51. Liu K, Kunii N, Sakuma M, Yamaki A, Mizuno S, Sato M, et al. A novel diacylglycerol kinase α -selective inhibitor, CU-3, induces cancer cell apoptosis and enhances immune response. *J Lipid Res*. 2016. -March-01;57(3):368–79. 10.1194/jlr.M062794.
52. Jarquin-Pardo M, Fitzpatrick A, Galiano FJ, First EA, Davis JN. Phosphatidic acid regulates the affinity of the murine phosphatidylinositol 4-phosphate 5-kinase-I β for phosphatidylinositol-4-phosphate. *Journal of Cellular Biochemistry*. 2007;100(1):112–28. 10.1002/jcb.21027.
53. Ziemba BP, Falke JJ. A PKC-MARCKS-PI3K regulatory module links Ca²⁺ and PIP3 signals at the leading edge of polarized macrophages. *PLoS ONE*. 2018. May 1,;13(5):e0196678 10.1371/journal.pone.0196678.
54. Janmey PA, Bucki R, Radhakrishnan R. Regulation of actin assembly by PIP₂ and other inositol phospholipids: An update on possible mechanisms. *Biochemical and Biophysical Research Communications*. 2018. November 25,;506(2):307 10.1016/j.bbrc.2018.07.155.
55. Le Clainche Christophe, Carlier Marie-France. Regulation of actin assembly associated with protrusion and adhesion in cell migration. *Physiological Reviews*. 2008. April 1,;88(2):489–513. 10.1152/physrev.00021.2007.
56. Bravo-Cordero JJ, Hodgson L, Condeelis J. Directed cell invasion and migration during metastasis. *Current Opinion in Cell Biology*. 2011;24(2):277–83. 10.1016/j.ceb.2011.12.004.
57. Weernink PAO, de Jesus ML, Schmidt M. Phospholipase D signaling: Orchestration by PIP2 and small GTPases. *Naunyn-Schmied Arch Pharmacol*. 2007. February;374(5–6):399–411.
58. Brindley DN, Waggoner DW. Phosphatidate phosphohydrolase and signal transduction. *Chemistry and Physics of Lipids*. 1996;80(1):45–57.

59. Newton AC. Regulation of the ABC kinases by phosphorylation: Protein kinase C as a paradigm. *The Biochemical Journal*. 2003. March 1,;370(Pt 2):361–71. 10.1042/BJ20021626.
60. Gambhir A, Hangyás-Mihályné G, Zaitseva I, Cafiso DS, Wang J, Murray D, et al. Electrostatic sequestration of PIP₂ on phospholipid membranes by basic/aromatic regions of proteins. *Biophysical Journal*. 2004. April;86(4):2188–207. 10.1016/S0006-3495(04)74278-2.
61. Cowan AE, Moraru II, Schaff JC, Slepchenko BM, Loew LM. Spatial modeling of cell signaling networks. *Methods in Cell Biology*. 2012;100:195–221.
62. Lauffenberger DA, Linderman J. *Receptors*. US: Oxford University Press; 1993.
63. Zigmond Sally H. Ability of polymorphonuclear leukocytes to orient in gradients of chemotactic factors. *The Journal of Cell Biology*. 1977. November 1,;75(2):606–16.

CHAPTER 4

A Structure-Based Model of PLC γ 1 Activation

4.1 Introduction

Chemotaxis, the process by which cells direct their migration based on a soluble chemical cue, is a critical process for a number of biological phenomena including embryonic development, the immune response, and wound healing (1). Fibroblasts, a type of mesenchymal cell, respond chemotactically to gradients of platelet-derived growth factor (PDGF) through a phospholipase C (PLC)/ protein kinase C (PKC) signaling pathway (2). Aberrant activation of PLC γ 1, the specific isozyme of PLC involved in this pathway, has been implicated in a number of disease states, including immune disorders and cancer metastasis (3, 4). Recent experimental work revealing the structure of PLC γ 1 has provided more detail into the multi-step mechanism of PLC γ 1 activation from its basally autoinhibited state (5, 6). Based on these findings, we developed a rule-based model to study the kinetics of PLC γ 1 activation and investigate how known mutations of this enzyme may be functioning in cancer and other diseases.

To date, 13 mammalian isozymes of PLC, classified in 6 different families based on their structures, have been identified. Common to all PLC isozymes is their enzymatic function: calcium-dependent hydrolysis of phosphatidylinositol-4,5-bisphosphate (PIP₂) to form diacylglycerol (DAG) and inositol-1,4,5-triphosphate (IP₃) (7). This activity is basally autoinhibited by an X-Y linker that separates the X- and Y-boxes of the catalytic core. For the PLC γ 1 isozyme, this X-Y linker region contains a split PH domain, two SH2 domains, and an SH3 domain. In the absence of stimulation, these X-Y linker domains sit atop the catalytic core and prevent the core from interacting with lipids at the plasma membrane (8). PLC γ 1 activation can be mediated by receptor tyrosine kinases (RTKs), G-protein coupled receptors, cytokine receptors, and T cell receptors (9). When activating signals are present, PLC γ 1 is

phosphorylated, leading to a structural rearrangement that shifts the X-Y linker off the catalytic core, allowing the enzyme to bind to the membrane and hydrolyze PIP₂ (6, 8).

In this work, we developed a rule-based model to study the kinetics of PLC γ 1 activation. In rule-based modeling, molecular interactions are specified by reaction rules that, when applied to molecules and their constituent domains/motifs, generate a reaction network. One advantage of rule-based modeling is that anything that is not explicitly constrained by a rule is allowed (10). Thus, rules formulated to characterize the canonical path of PLC γ 1 activation automatically generated all possible molecular states and interactions. Using this model, we investigated the effects of particular steps in the mechanism on the kinetics and steady-state level of PLC γ 1 activation. This approach also allowed us to postulate how known PLC γ 1 mutations, which have been implicated in disease states and cancer and exhibit increased phospholipase activity of PLC γ 1 *in vitro* (5), disrupt autoregulation. Two mechanisms that have been proposed to explain this behavior include mutations that disrupt the autoinhibition of the catalytic core provided by the cSH2 domain or mutations that increase the affinity of the uninhibited form of PLC γ 1 for the membrane (5, 6). Our simulations varying the appropriate reaction rates for each mechanism were able to reproduce the increased levels of activity, while also predicting faster activation kinetics for mutations affecting the autoinhibition and slower kinetics for changes affecting the rate of membrane binding.

Having characterized the mechanism of PLC γ 1 activation, we sought to test the role of the activation dynamics on the polarization of PLC/PKC signaling during chemotactic gradient sensing. To do this, we substituted the full PLC γ 1 activation network into the model of PLC/PKC polarization described in Chapter 3. Using a modified version of Positive Feedback Loop (PFL) 1, in which the rate of uninhibited PLC γ 1 binding to the membrane is increased in

proportion to the concentration of phosphatidic acid (PA), we found that this extended model was able to replicate previous model predictions regarding the synergistic effects of PFL 1, PFL 2, and the regulation of MARCKS on the ability of the system to polarize as well as the critical role of DAG kinases regulating the lipid metabolism of the system. In varying the reaction rates associated with mechanisms of aberrant PLC γ 1 activation, we predict that the increased levels of activity are accompanied by a diminished ability to polarize the signaling pathway.

4.2 Materials and Methods

4.2.1 Rule-based model of PLC γ 1 activation

Our model specifies two molecules, the receptor tyrosine kinase (RTK), which is assumed to be in its active and phosphorylated state, with a phosphotyrosine site for enzyme recruitment, and the enzyme PLC γ 1. The PLC γ 1 molecule includes the nSH2 and cSH2 domains, the Tyr783 phosphorylation site, and the catalytic core. The Tyr783 site has two states, phosphorylated or unphosphorylated, and the core has two states, active or inactive. The cell volume is set at 5000 μm^3 , typical of a large fibroblast cell (11), with the concentration of PLC γ 1 equal to 0.02 μM to remain consistent with the PLC/PKC polarization model from Chapter 3. The concentration of the RTK (on a whole-cell basis) was set equal to 0.05 μM , or it was varied from 0.005 – 0.05 μM to assess the dose response. The full reaction network showing all 17 species and 53 reactions is illustrated in Figure 4.1, and the values for the base-case rate constants are provided in Table 4.1.

Table 4.1 Brief reaction rule description with base case values for the associated rate constants

#	Reaction Rule	Rate constant	Base value
1	nSH2 binding to RTK when core is inactive	k_{on_nSH2}	$1 \mu\text{M}^{-1}\text{s}^{-1}$
2	nSH2 binding to RTK when core is active	$k_{on_nSH2_2}$	$\chi k_{on_nSH2} \mu\text{M}^{-1}\text{s}^{-1}$ $\chi = 1000$
3	nSH2 unbinding RTK	k_{off_nSH2}	1s^{-1}
4	Tyr783 phosphorylation	k_{phos}	1s^{-1}
5	Tyr783 dephosphorylation	k_{dephos}	1s^{-1}
6	cSH2 unbinding core	$k_{unbind,c}$	1s^{-1}
7	cSH2 binding core	$k_{bind,c}$	100s^{-1}
8	cSH2 binding Tyr783	$k_{bind,p}$	100s^{-1}
9	cSH2 unbinding Tyr783	$k_{unbind,p}$	1s^{-1}
10	core activation with nSH2 bound	k_{act_2}	$\chi k_{act} \text{s}^{-1}$
11	core activation with nSH2 unbound	k_{act}	0.01s^{-1}
12	core inactivation	k_{inact}	0.1s^{-1}

The values for k_{on_nSH2} and k_{off_nSH2} are set at $1 \mu\text{M}^{-1}\text{s}^{-1}$ and 1s^{-1} , respectively, yielding a dissociation constant of $1 \mu\text{M}$ consistent with the reported ranges for SH2 domain interactions with phosphotyrosines (12, 13). The rate $k_{on_nSH2_2}$ is related to k_{on_nSH2} by a factor χ set equal to 1000 to account for the faster rate of binding expected when PLC γ 1 is already bound to the membrane (14). This value takes into account both the closer proximity of the nSH2 domain to the receptor as well as the likelihood of a more favorable orientation for binding. The rates k_{act} and k_{act_2} are also linked by the factor χ and are set at 0.01s^{-1} and 10s^{-1} while k_{inact} is set at 0.1s^{-1} . These rates yield fast membrane binding when the enzyme is bound to the RTK, and much slower binding when the enzyme is being activated directly from the cytosol which we expect to be highly disfavored. The rates for the cSH2 domain binding and unbinding the core

and Tyr783 are set at 100 s^{-1} and 1 s^{-1} for both interactions, representing rapid interactions that favor the bound state. The phosphorylation and dephosphorylation rate constants were both set at 1 s^{-1} and were systematically varied in this work. A summary of the binding rates and modifications specified by the reaction rules follows and a molecular depiction of these rules is shown in Figure 4.2.

PLC γ 1 is basally autoinhibited through the reversible binding of the cSH2 domain to the core, provided that the cSH2 is unbound and the core is inactive. PLC γ 1 can be recruited from the cytosol to the membrane via the nSH2 binding to the phosphotyrosine site on the RTK. The nSH2 domain can dissociate from the RTK at any point. While PLC γ 1 is bound to the RTK, Tyr783 can be phosphorylated by the RTK. When the cSH2 domain is not bound to the core, it can reversibly bind to phosphorylated Tyr783 instead. The cSH2 domain protects phosphorylated Tyr783 from dephosphorylation; only when phosphorylated Tyr783 is unbound can it be dephosphorylated. When the core is not bound by cSH2, it can bind to the membrane and thus become active, regardless of the phosphorylation state of Tyr783. This can happen by direct recruitment from the cytosol or, with a frequency enhanced by the aforementioned factor χ when the nSH2 is bound to the RTK. The use of the same enhancement factor satisfies detailed balance for the assembly of the canonically active state, in which both the nSH2 is bound to RTK and the core is bound to membrane.

Rule

Molecular Depiction

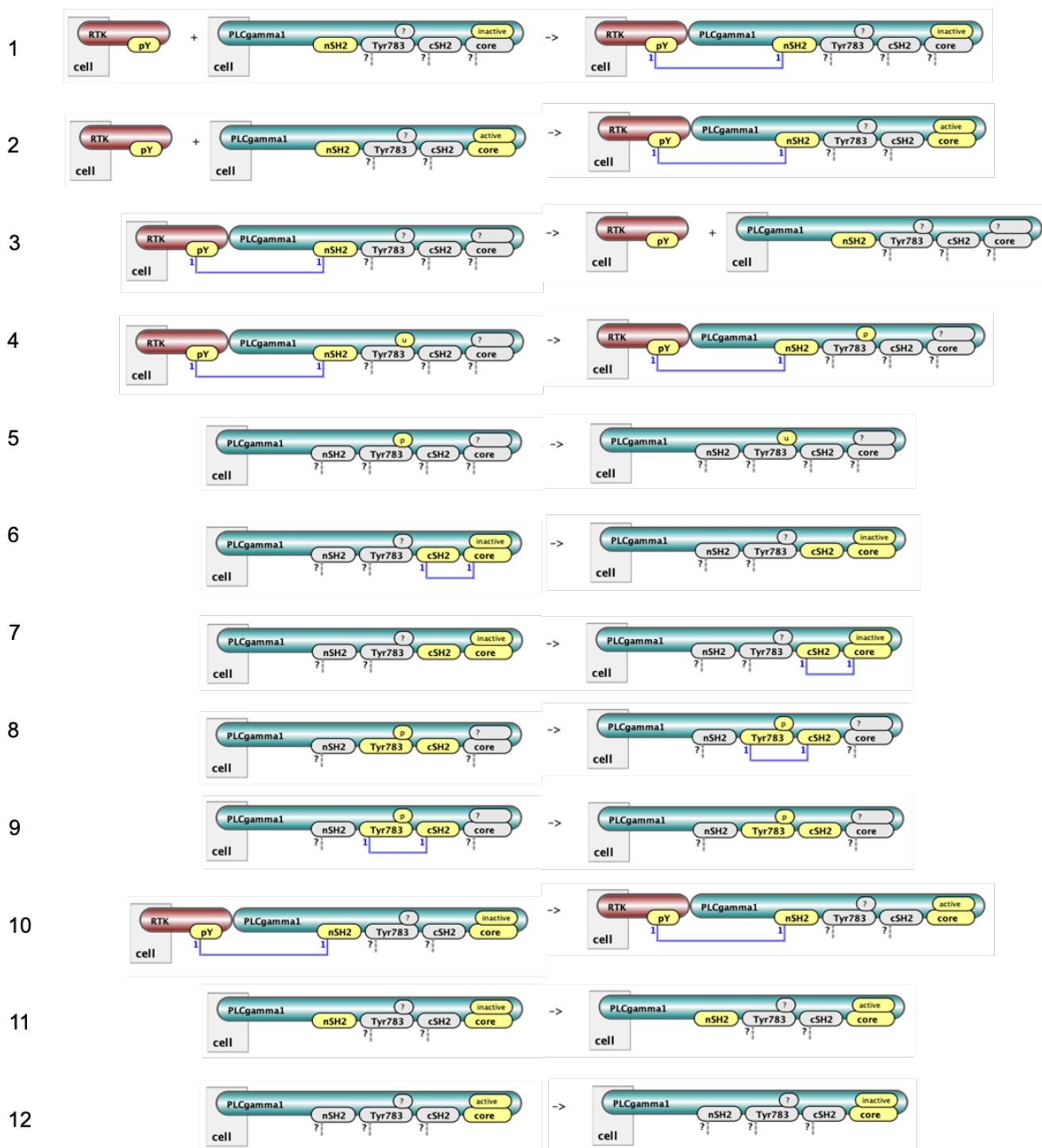


Figure 4.2 A molecular depiction of the reaction rules described in Table 4.1. All domains and states shown in yellow represent features of the reaction rule that were purposely specified. The sites in grey mean that domain can be in any state and bound or unbound when the rule is applied.

4.2.2 Implementation of the rule-based model

Using the Virtual Cell (VCell) software environment, twelve reaction rules were specified to describe the types of modifications and interactions allowed in the activation of PLC γ 1 as well as the values of those associated rate constants (Fig. 4.2, Table 4.1). From those rules, the BioNetGen modeling engine generated a network of 17 species and 53 reactions to describe all possible molecular states (Fig. 4.1). This reaction network was solved using VCell's Combined Stiff Solver (IDA/CVODE) with a maximum time step of 1 s. The solver was run for 5×10^3 s to ensure the system reached a steady state.

4.2.3 Combining the PLC γ 1 activation model with the PLC/PKC polarization model

The PLC γ 1 activation model was combined with the PLC/PKC polarization described in Chapter 3. To do this, the reaction V_{PLC} was replaced with the network of species and reactions generated for the PLC γ 1 activation model. This required the addition of 16 new species (the RTK species was omitted) to the polarization model with 5 in the cytosol and 11 at the membrane. As the receptor is not explicitly modeled in the polarization model, reactions involving binding to the RTK in the activation model were replaced with the expression $(r - e)$. This expression is analytically calculated in the polarization model to describe the number of active receptors (r) that are not bound by active PLC (e). In this combined model, e is equal to the sum of the RTK-bound species when it is used in the expression $(r - e)$, and is equal to the sum of the active species when it is used in the PIP₂ hydrolysis reaction, $V_{hyd,PLC}$.

In Chapter 3, PFL 1 is described, considering the hypothetical effect of PA on extending the lifetime of PLC in complex with the receptor at the membrane. This feedback was modeled by reducing the off-rate of PLC at the membrane in proportion to the concentration of

phosphatidic acid (PA), defined as d_p in the model. In the present, combined model, a modification of PFL 1 was considered instead, with the rate of activation of PLC γ 1 binding to the membrane (k_{act}) increasing in proportion to d_p as given by the following expression; the constant K_{PA} is defined in a manner consistent with the corresponding parameter in the original PFL 1 and with the same value of $10 \mu\text{m}^2$.

$$k_{act} (1 + K_{PA}d_p) \text{ and } k_{act_2} (1 + K_{PA}d_p)$$

The initial concentration of PLC γ 1 was set at $0.02 \mu\text{M}$ to match both models. Consistent with the polarization model, the diffusivities of all cytosolic PLC γ 1 species were set at $19 \mu\text{m}^2/\text{s}$, and the diffusivities for all receptor and/or membrane-bound species were set at $0.01 \mu\text{m}^2/\text{s}$. All other initial concentrations, diffusion constants, and rate constants remained the same as the base case values in the polarization model described in Chapter 3 and Appendix B. This includes the on- and off-rates for PLC binding to the receptor, which are set at $0.1 \mu\text{M}^{-1}\text{s}^{-1}$ and 0.1s^{-1} , respectively. Aside from this change to the on- and off-rates of PLC binding the receptor to match the polarization model, all rate constants remained the same as the base case values for the reactions from the PLC γ 1 activation model.

4.3 Results

4.3.1 A structure-based model of PLC γ 1 activation

We developed a model of PLC γ 1 to study its activation kinetics in light of recent structural data elucidating a multi-step activation process involving multiple domains and phosphorylation. The PLC γ 1 enzyme is basally autoinhibited by an X-Y linker region containing

a number of regulatory domains (e.g. PH, SH2, and SH3 domains) that sit on top of the enzyme's catalytic core and prevent it from interacting with lipids at the plasma membrane. The full network of reactions is depicted in Figure 4.1, while a cartoon depiction (Fig. 4.3A) and the associated reaction terms (Fig. 4.3B) in Figure 4.3 describe the canonical path for PLC γ 1 activation. This series of steps starts with an active RTK, such as PDGF receptors, which has a phosphotyrosine residue on the C-terminal tail. The N-terminal SH2 (nSH2) domain of the autoinhibited PLC γ 1 enzyme binds to the phosphotyrosine residue of the receptor, thus recruiting the inactive enzyme from the cytosol. Once bound, the receptor phosphorylates the Tyr783 residue of PLC γ 1, which is located between the C-terminal SH2 (cSH2) domain and the SH3 domain. The cSH2 domain is usually bound to a C2 domain next to the Y-box of the catalytic core, an interaction that prevents the cSH2 domain from readily binding phosphotyrosine while also effectively covering the surface of the core providing autoinhibition. When Tyr783 is phosphorylated, it serves as an intramolecular ligand that competes with the C2 domain for binding the cSH2 domain. Upon the cSH2 domain binding Tyr783, a substantial rearrangement occurs that shifts the X-Y linker region off of the catalytic core. This exposes a hydrophobic ridge on the catalytic core allowing the enzyme to insert itself into the membrane and start hydrolyzing PIP₂ into DAG and IP₃ (6).

This description of PLC γ 1 activation permits a two-step inactivation process for the enzyme to completely dissociate from the membrane (Fig. 4.3C). When the core is bound to the membrane and actively hydrolyzing PIP₂, it is possible for the nSH2 domain to dissociate from the RTK. While the core is independently bound to the membrane, it remains active. Given the close proximity of the enzyme to the receptor, the nSH2 domain has a chance to rebind the receptor. By the same token, while the nSH2 domain is bound to the receptor, the core may

dissociate from the membrane and become inactive; however, it remains in close proximity to the membrane and has a chance to rebind. Only when the nSH2 domain unbinds the receptor and the core dislodges from the membrane will PLC γ 1 return to the cytosol. We predicted that this two-step inactivation process controls the lifetime of the enzyme at the membrane.

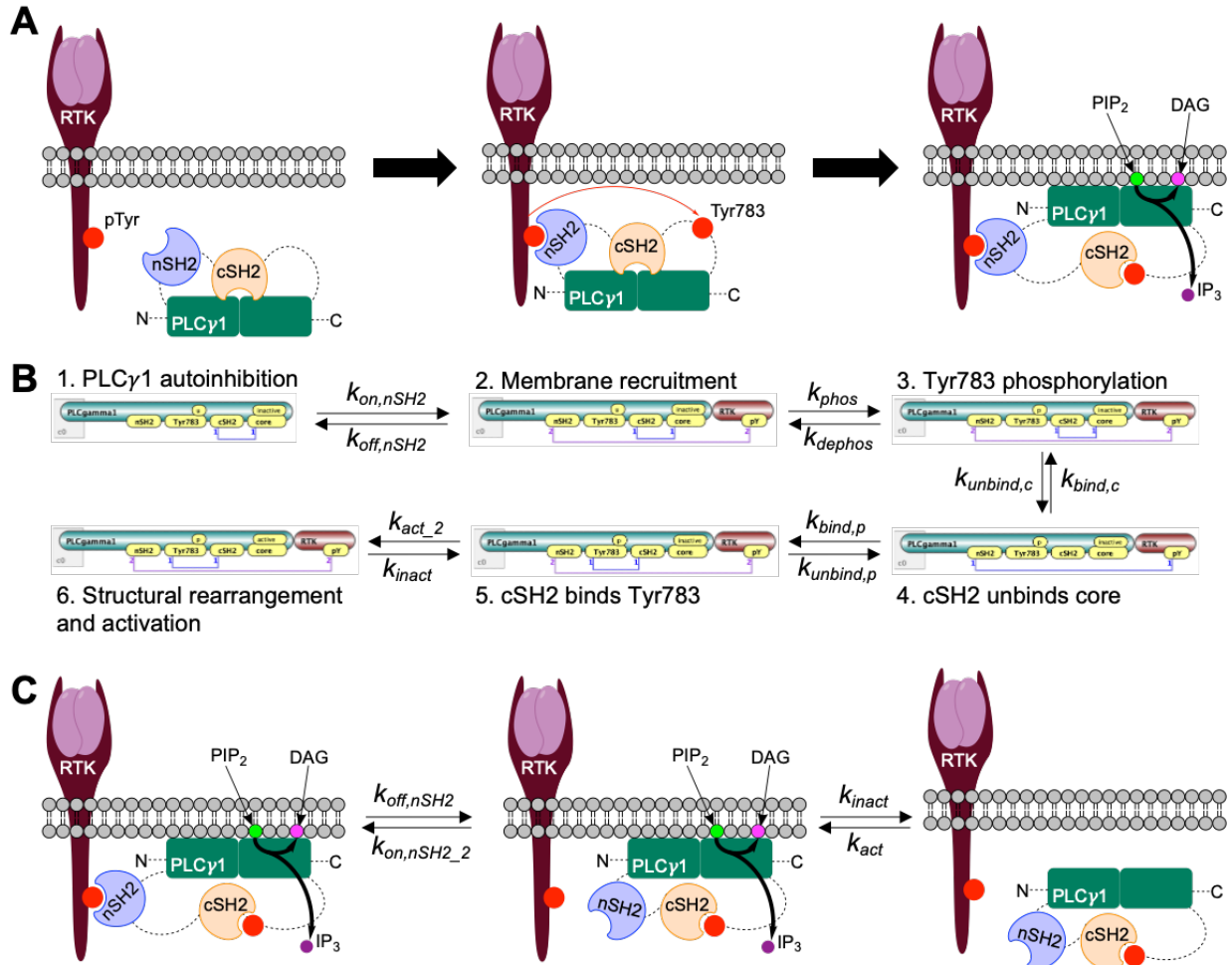


Figure 4.3 Illustration of PLC γ 1 activation. (A) Cartoon depicting the steps of PLC γ 1 activation. Shown is the regulatory and catalytic regions of the PLC γ 1 enzyme oriented in the N-terminal to C-terminal direction. The catalytic core separated into an X and Y box are shown in green with the regulatory X-Y linker region containing the nSH2 and cSH2 domains on top. The dimerized and activated RTK is shown in the membrane with a phosphotyrosine site shown. (B) Molecular depiction of the canonical pathway for PLC γ 1 activation in the model with reaction rates shown for each step. (C) Cartoon showing the two-step inactivation process for PLC γ 1.

4.3.2 Tyr783 phosphorylation helps relieve autoinhibition leading to PLC γ 1 activation

Considering the proposed role of Tyr 783 phosphorylation in occupying cSH2 and thus relieving the autoinhibition of PLC γ 1, we explored the effects of the Tyr783 phosphorylation and dephosphorylation rates and the affinity of the cSH2 domain binding to phospho-Tyr783 ($K_p = k_{bind,p}/k_{unbind,p}$) on the level of PLC γ 1 activation. Tyr783 can only be phosphorylated when the nSH2 domain is bound to the receptor, and it cannot be dephosphorylated when the cSH2 domain is bound.

We first considered two extreme cases in which the PLC γ 1 enzyme was “mutated” such that it could not be phosphorylated (nonphosphorylatable) or it was constitutively phosphorylated (phosphomimetic). These mutants served as limiting cases for PLC γ 1 activity, while variations were made to the phosphorylation and dephosphorylation rates to explore intermediate behavior. Our model description permits PLC γ 1 activation without phosphorylation of Tyr783, in the infrequent event that the cSH2 domain spontaneously unbinds the core, and the core binds to the membrane and becomes active before the autoinhibitory influence of cSH2 is reestablished. This results in the low level of activation seen for the nonphosphorylatable mutant (Fig. 4.4A). For the phosphomimetic case, increasing the value of $k_{bind,p}$ (and thus K_p) resulted in progressively higher levels of PLC γ 1 activity for a given receptor input with a key prediction being that $K_p \gg 1$ is required, but the value K_p need not be greater than or even comparable to K_c , the affinity constant of the autoinhibition; with $K_p = 10$ and $K_c = 100$, the phosphomimetic “mutant” is substantially activated relative to the nonphosphorylatable one (Fig. 4.4A). Even modest relief of a strong autoinhibition is effective relative to no relief.

Considering then the “wild-type” PLC γ 1, with varying rates of Tyr783 phosphorylation (Fig. 4.4B) or dephosphorylation (Fig. 4.4C), it is increasingly more or less likely for the cSH2

domain to be occupied by the Tyr783 site and not the core, leading to higher levels of activation. Interestingly, the effect of increasing the phosphorylation rate apparently saturates (Fig. 4.4B; compare k_{phos} values of 10 and 100 s⁻¹) well below the level of the phosphomimetic case, suggesting that the full model is parameterized in such a way that a substantial portion of the PLC γ 1 in the cytosol is dephosphorylated between encounters with the RTK.

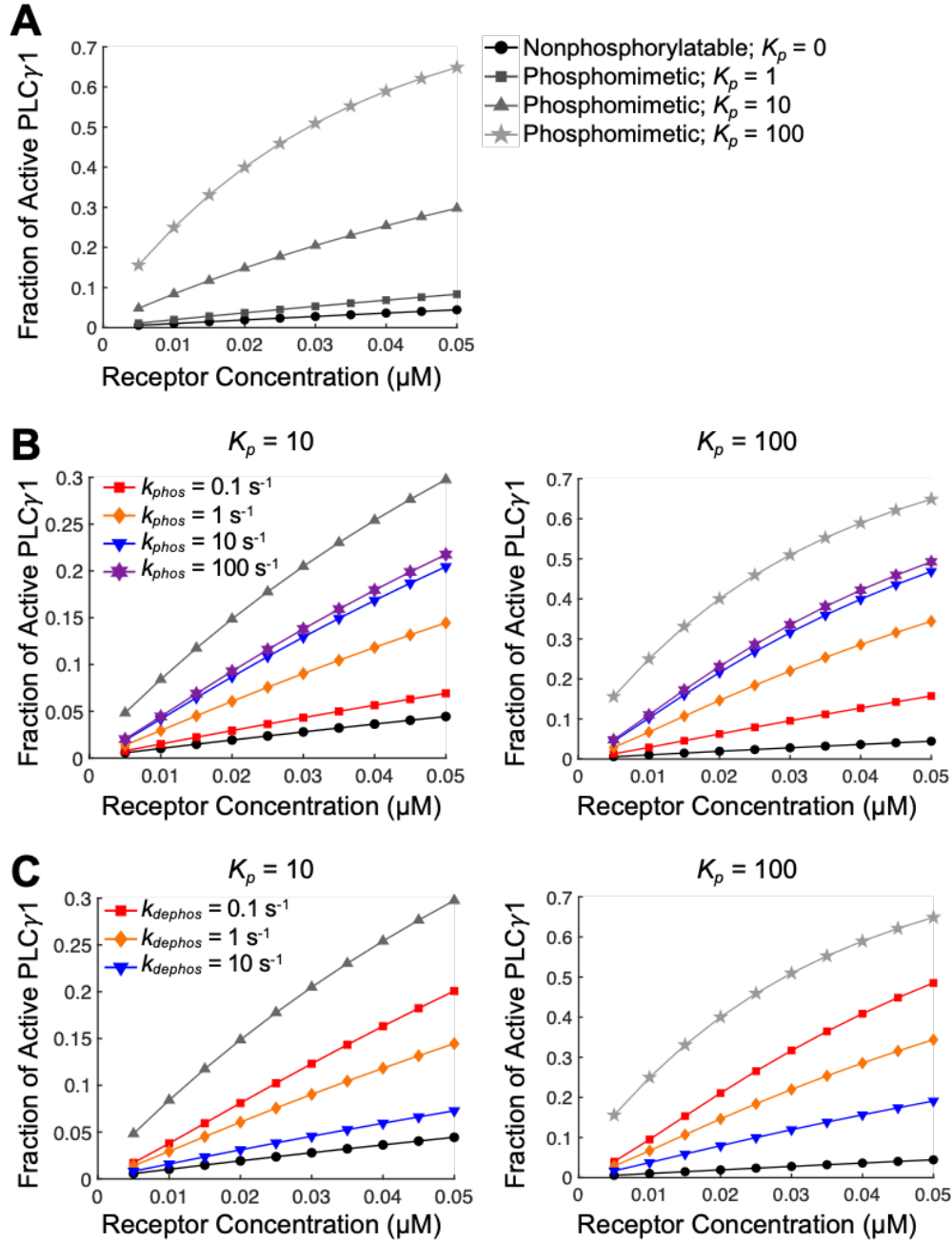


Figure 4.4 Dose-response dynamics for Tyr783 phosphorylation. (A) The fraction of active PLC γ 1 is plotted as a function of the initial receptor concentration while the parameter K_p was varied. The legend for this plot corresponds to the same line color and symbols used in plots for B and C. Plots where the Tyr783 phosphorylation rate (B) and dephosphorylation rate (C) were varied for $K_p = 10$ and $K_p = 100$.

4.3.3 The parameter k_{act} increases the lifetime of active PLC γ 1 at the membrane

Given the ability of PLC γ 1 phosphorylation to increase enzyme activation, we asked whether this effect is accompanied by an increased lifetime of the enzyme at the membrane. To test this, we ran the simulation for 5000 s to achieve steady-state and then switched off the reactions that allow PLC γ 1 to be recruited from the cytosol. Running the simulation for 5000 s more, we were able to monitor the decay of the active species in time. The half-life for decay, calculated as the time it takes for the fraction of active PLC γ 1 to reach half its steady-state concentration, remained relatively insensitive to k_{phos} despite ten-fold changes in the rate in either direction (Fig. 4.5A).

The reaction rate, k_{act} , was analyzed in a similar manner such that k_{act} and k_{act_2} were both varied ten-fold in either direction relative to the base case value. After 5000 s, the rates k_{on_nSH2} and k_{act} but not k_{act_2} were set equal to zero. The time courses for the decay of active PLC γ 1 clearly show slower rates of decay with increasing rates of k_{act} corresponding with higher values for the half-life of decay (Fig 4.5B). This slower decay, or increased lifetime at the membrane, with increasing values of k_{act} suggests that the ability of the enzyme to quickly rebind the membrane when it is still anchored to the receptor by the nSH2 domain is playing an important role in maintaining the activity of PLC γ 1. Changing certain other parameters, including the phosphorylation rate, does not have this effect.

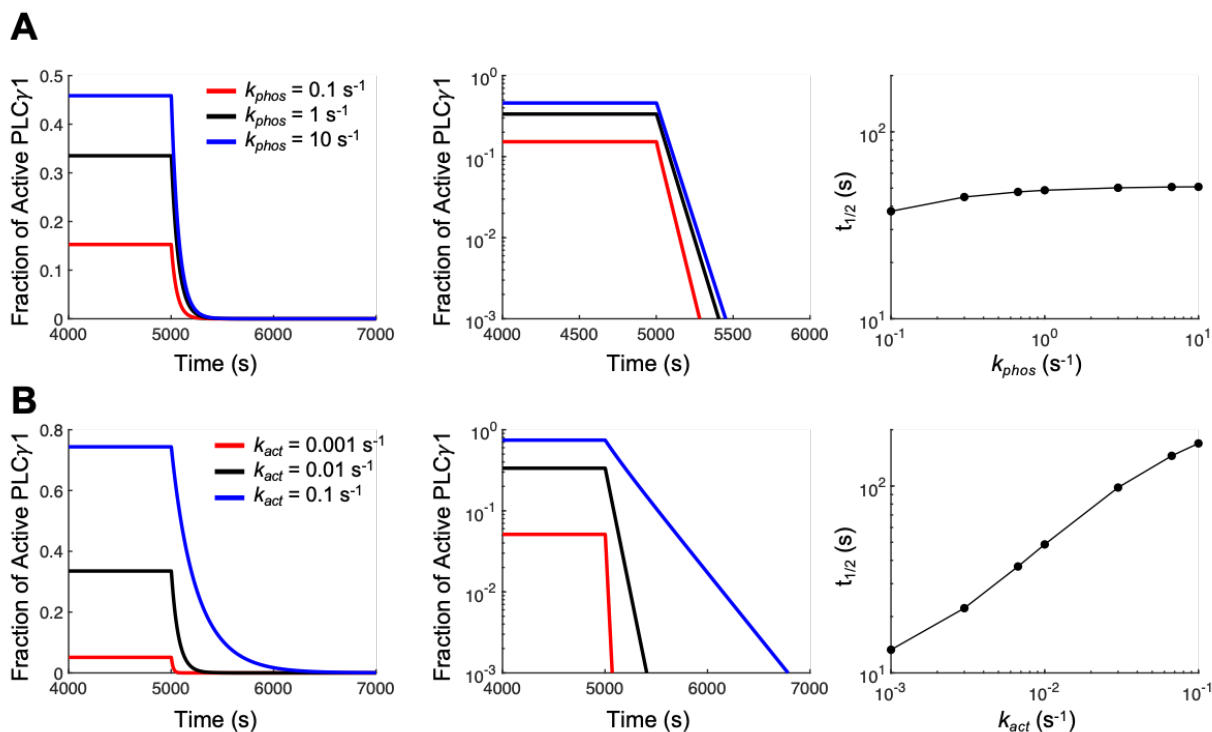


Figure 4.5 Decay of active species once PLC γ 1 can no longer leave the cytosol. Time courses for (A) k_{phos} and (B) k_{act} showing the decay of active PLC γ 1 species once the rates k_{on_nSH2} and k_{act} were set to zero at 5000 s preventing any PLC γ 1 from leaving the cytosol. The second plot shows the same time course on a log scale for the fraction of active PLC γ 1. The third plot shows the half-life for decay, calculated as the time it takes for the fraction of active PLC γ 1 to reach half its steady-state concentration.

4.3.4 Activating mutations and their effect on the kinetics of PLC γ 1 activation

A number of mutations in the PLC γ 1 enzyme have been implicated in various disease states and cancers, and *in vitro* activity assays have been used to confirm that such disease-linked substitutions or deletions possess higher phospholipase activity. Now that the full structure of the PLC γ 1 enzyme has been reported, the mutations can be mapped to the structure of the protein. Although these mutations were distributed in a few different regions, they all appear to overlap with the surfaces associated with autoinhibition of PLC γ 1 (5). Two possible mechanisms

describing how these mutations are functioning include disruption of the cSH2 interaction with the core and enhancement of the affinity of the core for the membrane (6).

Using our model, we mimicked the mechanisms attributed to these mutations by varying parameters associated with the cSH2 domain binding the core ($K_c = k_{bind,c}/k_{unbind,c}$) (Fig. 4.6A) and the uninhibited enzyme binding the membrane ($K_a = k_{act}/k_{inact}$) (Fig. 4.6B). We found that varying the K_c parameters, such that the cSH2 domain interaction with the core is hampered, resulted in increased levels of PLC γ 1 activity consistent with the *in vitro* experimental results. Moreover, we observed that the time to reach half of the steady-state was shorter (faster kinetics) for all of the mutated K_c parameter sets (Fig. 4.6C). Varying the K_a parameters, such that the uninhibited enzyme has higher affinity for the membrane, also resulted in higher PLC γ 1 activity; however, in contrast to decreasing K_c , increasing K_a yields slower activation kinetics (Fig. 4.6D). Considering all of the hypothetical mutants, there is greater than five-fold difference in the $t_{1/2}$ values when $K_p = 100$, and that increases to seven-fold when $K_p = 10$ (Fig. 4.7). This stark difference in activation kinetics could be used to help distinguish and characterize the actual PLC γ 1 mutants.

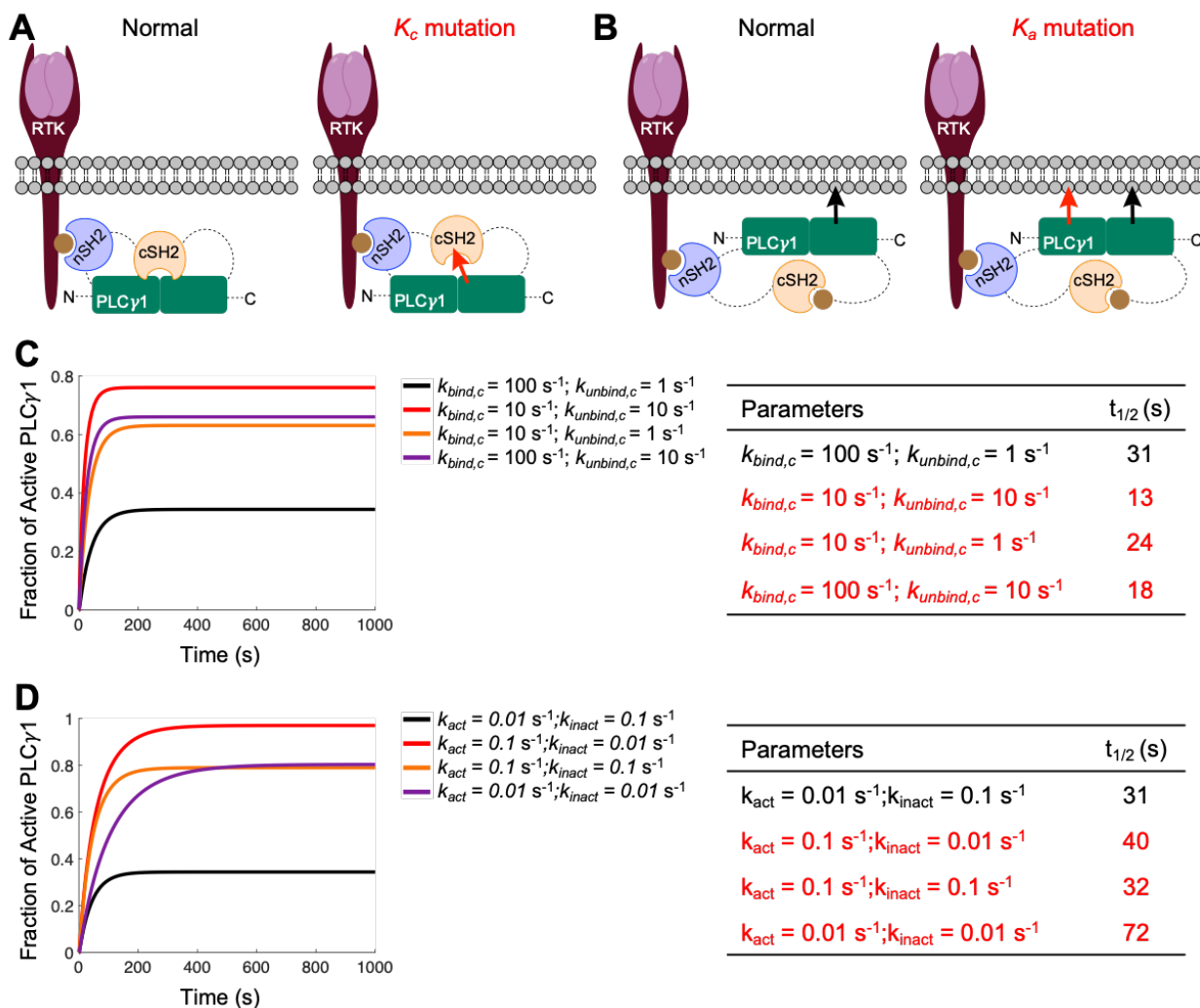


Figure 4.6 The effects of activation mutations on the kinetics of PLC γ 1 activation. (A) Cartoon depicting the effects of K_c mutations on the location of the cSH2 relative to the core. (B) Cartoon depicting the effects of K_a mutations on the ability of the uninhibited enzyme to bind the membrane. Time course plotting the saturation of the fraction of active PLC γ 1 when the (C) K_c parameters and (D) K_a parameters were varied with the wild-type case shown in black. The table shows the half-life for saturation, calculated as the time it takes for the fraction of active PLC γ 1 to reach half its steady-state concentration.

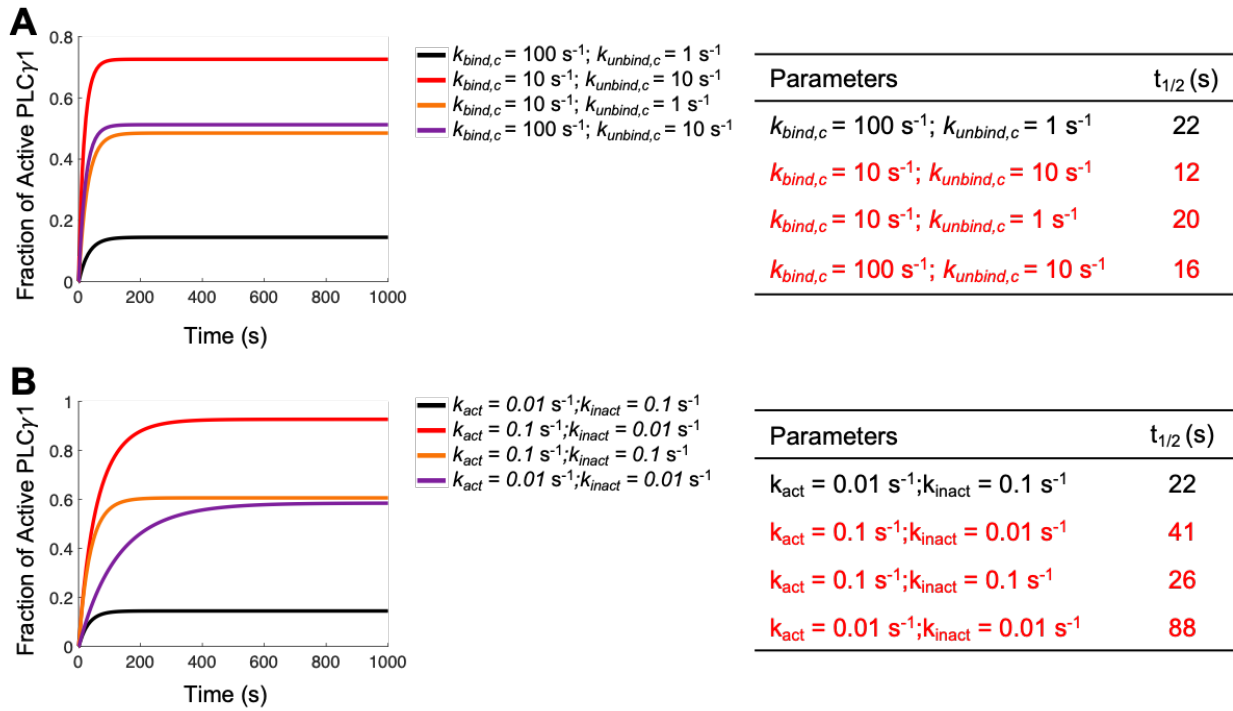


Figure 4.7 The effects of activation mutations on the kinetics of PLC γ 1 activation ($K_p = 10$). Time course plotting the saturation of the fraction of active PLC γ 1 when the (A) K_c parameters and (B) K_a parameters were varied with the wild-type case shown in black. The table shows the half-life for saturation, calculated as the time it takes for the fraction of active PLC γ 1 to reach half its steady-state concentration.

4.3.5 A modified version of PFL 1 can amplify the signaling pathway in a combined model of PLC γ 1 activation and PLC/PKC polarization

In the PLC/PKC polarization model presented in Chapter 3, a feedback loop, PFL 1, was proposed to consider the modulation of PLC recruitment to the membrane by phosphatidic acid (PA). We found that the proposed ability of PA to increase the lifetime of PLC in complex with the receptor at the membrane synergized with the regulation of MARCKS by PKC to promote sensitive and robust polarization. Our earlier analysis of the reaction rate k_{act} in the PLC γ 1 activation model showed that the lifetime of active PLC γ 1 is sensitive to this rate. Hence, we decided to merge the PLC/PKC polarization model with the PLC γ 1 activation model and see if

we could reproduce the effects of PFL 1 but with a more detailed hypothesis of how PA influences PLC γ 1 activation.

A description of how the two models were combined is explained in the Materials and Methods Section 4.2.3. Of note is that all the base-case values for the reaction rates in the polarization model and the activation model remained the same in the combined model, and the rates for k_{on_nSH2} and k_{off_nSH2} were chosen to remain consistent with the $k_{on,e}$ and $k_{off,e}$ rates from the polarization model. Modified PFL 1, PFL 1*, was implemented to replace PFL 1 from the polarization model which increased the rate k_{act} in proportion to the PA concentration. Results from the combined model with PFL 1* and MARCKS at a gradient steepness of 10% show that PFL 1* is able to synergize with MARCKS to amplify the signaling pathway and even to a slightly higher value than what was observed with PFL 1 in the polarization model. The combined model did not produce the oscillatory dynamics observed in the polarization model for this set of parameters (Fig. 4.8A). The time courses for the simulations showing the highest amplification also displayed slightly different kinetics (Fig. 4.8B). The initial spike of PKC activity when the gradient is applied at 2000 s has been attributed to the rapid release of PIP₂ by MARCKS when PKC is activated. This feature is less prominent in the combined model, suggesting that the kinetics of PLC γ 1 activation are somewhat slower.

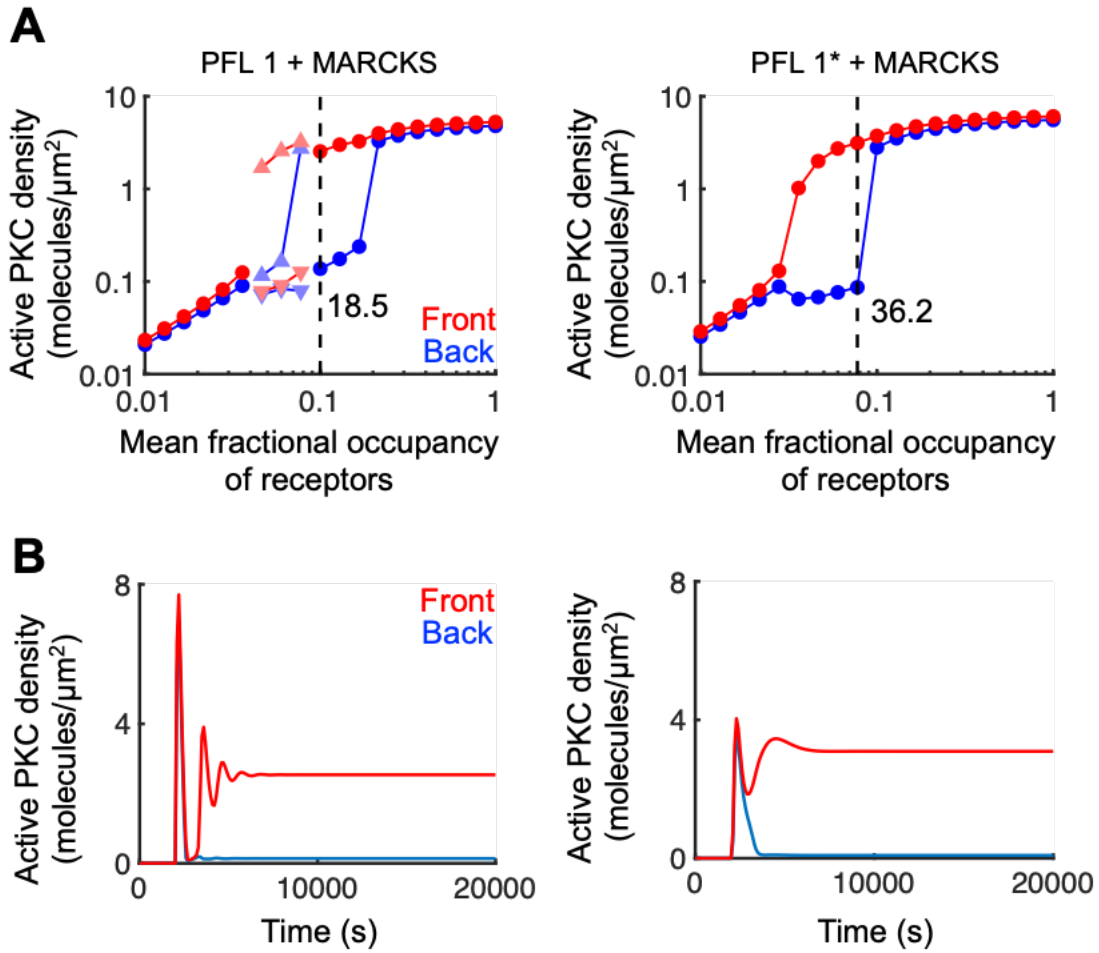


Figure 4.8 Gradient amplification by PFL 1* combined with the regulation of MARCKS in a combined model of PLC γ 1 activation and PLC/PKC polarization. (A) The concentration of active PKC molecules at the front (red circle) and back (blue circle) of the cell are plotted as a function of the mean fractional occupancy of receptors, r_{frac} , for varying values of gradient steepness. When the simulations produced oscillations, the maxima (upward-pointing triangles) and minima (downward-pointing triangles) of the oscillations are plotted; the front and back are still denoted by shades of red and blue, respectively. The simulation achieving steady state with the maximum front/back ratio is denoted by the dashed vertical line and its time course is plotted in (B).

The combined model with PFL 1* was able to recapitulate key findings from the polarization model, including the critical role of DAG kinases in the responsiveness of the system. The combined model showed that reducing the rate k_{DAGK} by 0.3 times its base value

greatly diminished the polarization of the pathway, whereas increasing the rate to 3 times its base value enhanced the amplification (Fig. 4.9A). Performing an analysis of the DAG and PA concentrations at the front and back of the cell as k_{DAGK} was increased demonstrates a similar explanation for this observation: the concentration of DAG at the back of the cell is reduced to a much greater extent than it is at the front when the rate of k_{DAGK} was increased (Fig. 4.9B). When PFL 2 from the polarization model was added to the combined model with PFL 1* and MARCKS, the level of amplification was substantially increased in line with the observed synergistic effect of all three feedback mechanisms in the polarization model (Fig. 4.9C).

Using the combined model with PFL 1* and MARCKS, we wanted to test what effects the activating mutations would have on the polarization of the pathway. To this end, we tested the K_c and K_a mutation mechanisms by increasing $k_{unbind,c}$ by 10 times its base case value and decreasing k_{inact} by 10 times its base case value. Noting that these parameter variations shifted the dose response to lower levels of mean fractional occupancy, we observed that both of these mutations diminished the polarization of the pathway (Fig. 4.9D).

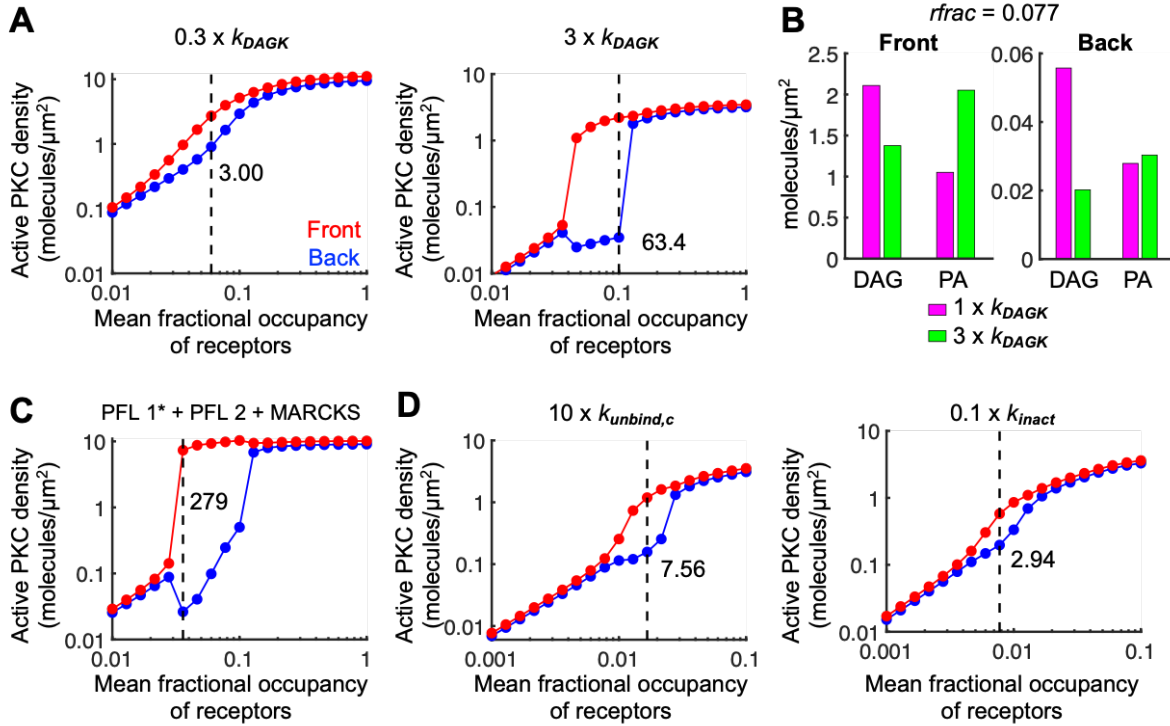


Figure 4.9 The effect of parameter variations on the sensitivity of the pathway. (A) Relative to the base case parameter set associated with the PLC/PKC polarization model, the parameter k_{DAGK} was taken at 0.3 or 3 times its base value. Colors and symbols have the same meanings as in Figure 4.8. The maximum front/back ratio is shown underneath the symbols. (B) Bar plots comparing the DAG and PA steady-state concentrations at the front and back of the cell for $1 \times$ and $3 \times k_{DAGK}$ simulations, with $r_{frac} = 0.077$. (C) PFL 2 is added to PFL 1* and MARCKS and the parameters K_{PLD} and $\gamma V_{synth,dp}$ are set at 0.1 and 10, respectively. (D) The parameters $k_{unbind,c}$ and k_{inact} are taken at $10 \times$ and $0.1 \times$ their base case values listed in Table 4.1.

4.4 Discussion

Recent work detailing the structure of the full-length PLC γ 1 enzyme elucidated a more detailed mechanism for its activation (5, 6). This multi-step process relies on the coordination and interaction of a number of different domains along with the phosphorylation of Tyr783 in order to relieve the basal autoinhibition of the enzyme when an activating signal is present. While the activation of PLC γ 1 is important for chemotaxis, platelet aggregation, and T cell activation in the immune response (2, 15, 16), failure to regulate the activation of PLC γ 1

enzymes has been implicated in the emergence of immune disorders and some cancers (3). To better understand the kinetics of PLC γ 1 activation, we developed a rule-based model using the BioNetGen modeling engine in VCell to investigate how the domain interactions, binding rates, and the phosphorylation of Tyr783 impact the activation of the enzyme.

We first investigated the phosphorylation of Tyr783 and its role in releasing the autoinhibition of the enzyme. The phosphorylation itself is not expected to affect the autoinhibition; however, it serves as a binding site for the cSH2 domain which is normally bound to a C2 domain blocking the catalytic core. When the cSH2 domain binds Tyr783, a structural rearrangement occurs that uncovers the core enabling it to bind the membrane. Our simulations indicated faster rates of phosphorylation and cSH2 binding Tyr783 could increase the magnitude of PLC γ 1 activation. Most evidence indicates that Tyr783 is necessary for releasing the autoinhibition of the PLC γ 1 enzyme; however, a number of other experiments have identified additional sites of phosphorylation that play a role in activation. Depending on the cell type, the receptor, and whether experiments were carried out *in vitro* or in whole cells, different phosphorylation sites have been shown to either increase the level of activity or can even serve as a replacement for Tyr783 (17-19). In future work, this model can be used to try to distinguish between these different phosphorylation sites and predict how they function in the activation of PLC γ 1.

This model predicted that certain reaction rates affected the lifetime of active PLC γ 1 species. We found that the fast dynamics of Tyr783 phosphorylation made the lifetime relatively insensitive to changes in the parameter k_{phos} but increasing k_{act} led to a much longer lifetime of the active species. We attributed this response to the two-step inactivation process that requires the enzyme to dissociate from the membrane and the receptor before it reenters the cytosol.

Increasing the rate of k_{act} allowed for the enzyme to quickly rebind the membrane if it was still bound to the receptor when it dissociated. We can see how this two-step method of inactivation can lead to a number of futile cycles of the enzyme unbinding then rebinding the receptor or the membrane to prolong activation. This method of increasing enzyme activation by increasing the lifetime of the enzyme at the membrane was explored in Chapter 3 with PFL 1. We proposed PA was able to increase the rate of PIP₂ hydrolysis by increasing the time the PLC enzyme was at the membrane. We modeled this as a decrease in the effective off-rate of the PLC enzyme in proportion to the concentration of the enzyme present. In our combined model with a more comprehensive look at PLC γ 1 activation, we modified PFL 1 from the polarization model and made the rate k_{act} increase in proportion to the concentration of PA. The results from the combined model indicated the modified feedback loop in conjunction with the regulation of MARCKS could polarize the pathway providing additional support for the role of PA in increasing PLC γ 1 activity by increasing the lifetime of the active species at the membrane.

This model was also able to reproduce reported results from mutant PLC γ 1 experiments that showed a number of disease- and cancer-associated mutations caused increased enzyme activity (5). Two mechanisms that have been postulated to explain the function of these activation mutations include disruptions to the cSH2 domain and its ability to maintain autoinhibition (K_c mutations) and mutations to the enzyme that allow the uninhibited form to more readily bind the membrane (K_a mutations). While both mutations led to increased activity, the K_c mutations sped up the kinetics suggesting the K_c mutations shifted the equilibrium of the system while the K_a mutations drastically slowed down the kinetics. Another mechanism that has been speculated for the function of the activation mutations include mutations in nSH2 domain that increase its affinity for phosphorylated kinases. In our model, this would involve mutations

affecting $K_n = k_{on_nSH2} / k_{off_nSH2}$ which would most certainly increase the concentration of the active species.

Despite the prevalence of PLC γ 1 mutants in cancer and disease, there are currently no drug compounds or pharmacological inhibitors available for the study and treatment of PLC-related diseases (3). With the new PLC γ 1 structural data, it's possible that drugs could be developed to selectively target the activation process of the enzyme e.g. compounds that help stabilize the cSH2 domain providing autoinhibition. This model is limited by only including a few of the domains that are pertinent to its regulation. In the future, we could expand this model to include additional domains such as the PH and SH3 domains. While this contributes to an increase in the combinatorial complexity of the system, it would allow us to investigate other mechanisms of disease. For example, the split PH domain in the X-Y linker is also associated with maintaining the autoinhibition of the core. It binds to the hydrophobic ridge of the core while also interacting with the cSH2 domain (6). As a result, mutations in the split PH domain could also contribute to the unregulated release of autoinhibition. The SH3 domain, also found in the X-Y linker, interacts with a number of signaling and adaptor proteins, which has made it a potential drug target for PLC γ 1 (20). When proteins bind the SH3 domain, they could help stabilize the autoinhibited form. On the other hand, the SH3 domain binds to the cSH2 to help maintain autoinhibition and mutations in the SH3 domain could lead to disruptions in autoinhibition similar to the PH domain. By using an expanded version of this model, we can try to address some of these questions and gain a better understanding of how PLC γ 1 functions in cancer and disease.

4.5 Acknowledgments

We acknowledge use of the freely available Virtual Cell software (supported by NIH Grant Number R24 GM134211 from the National Institute for General Medical Sciences).

4.6 References

1. Swaney KF, Huang C, Devreotes PN. Eukaryotic chemotaxis: a network of signaling pathways controls motility, directional sensing, and polarity. *Annual Review of Biophysics*. 2010 Jun 9;;39(1):265-89.
2. Asokan S, Johnson H, Rahman A, King S, Rotty J, Lebedeva I, et al. Mesenchymal chemotaxis requires selective inactivation of Myosin II at the leading edge via a noncanonical PLC γ /PKC α pathway. *Developmental Cell*. 2014 Dec 22;;31(6):747-60.
3. Koss H, Bunney TD, Behjati S, Katan M. Dysfunction of phospholipase C γ in immune disorders and cancer. *Trends in Biochemical Sciences*. 2014;39(12):603-11.
4. Sala G, Dituri F, Raimondi C, Previdi S, Maffucci T, Mazzeletti M, et al. Phospholipase C γ 1 is required for metastasis development and progression. *Cancer Research*. 2008 Dec 15;;68(24):10187.
5. Liu Y, Bunney TD, Khosla S, Macé K, Beckenbauer K, Askwith T, et al. Structural insights and activating mutations in diverse pathologies define mechanisms of deregulation for phospholipase C γ enzymes. *EBioMedicine*. 2020;51:102607.
6. Hajicek N, Keith NC, Siraliev-Perez E, Temple BR, Huang W, Zhang Q, et al. Structural basis for the activation of PLC- γ isoforms by phosphorylation and cancer-associated mutations. *eLife*. 2019;8(2019).
7. Gresset A, Sondek J, Harden TK. The phospholipase C isoforms and their regulation. 2012th ed. Dordrecht: Springer Netherlands; 2012.
8. Hajicek N, Charpentier TH, Rush JR, Harden TK, Sondek J. Auto-inhibition and phosphorylation-induced activation of PLC- γ isoforms. *Biochemistry*. 2013 Jul 9;;52(28).
9. Yang YR, Choi JH, Chang J, Kwon HM, Jang H, Ryu SH, et al. Diverse cellular and physiological roles of phospholipase C- γ 1. *Advances in Enzyme Regulation*. 2012 Jan;52(1):138-51.
10. Blinov ML, Schaff JC, Vasilescu D, Moraru II, Bloom JE, Loew LM. Compartmental and spatial rule-based modeling with Virtual Cell. *Biophysical Journal*. 2017;113(7):1365-72.
11. Mitsui Y, Schneider EL. Relationship between cell replication and volume in senescent human diploid fibroblasts. *Mechanisms of Ageing and Development*. 1976;5(1):45-56.
12. Ladbury JE, Lemmon MA, Zhou M, Green J, Botfield MC, Schlessinger J. Measurement of the binding of tyrosyl phosphopeptides to SH2 domains: a reappraisal. *Proceedings of the National Academy of Sciences - PNAS*. 1995;92(8):3199-203.

13. Ottinger EA, Botfield MC, Shoelson SE. Tandem SH2 domains confer high specificity in tyrosine kinase signaling. *The Journal of Biological Chemistry*. 1998;273(2):729-35.
14. Oh D, Ogiue-Ikeda M, Jadwin JA, Machida K, Mayer BJ, Yu J. Fast rebinding increases dwell time of Src homology 2 (SH2)-containing proteins near the plasma membrane. *Proceedings of the National Academy of Sciences - PNAS*. 2012;109(35):14024-9.
15. Zheng Y, Adams T, Zhi H, Yu M, Wen R, Newman PJ, et al. Restoration of responsiveness of phospholipase C γ 2-deficient platelets by enforced expression of phospholipase C γ 1. *PloS One*. 2015;10(3):e0119739.
16. Smith-Garvin JE, Koretzky GA, Jordan MS. T Cell Activation. *Annual Review of Immunology*. 2009 Apr 23;27(1):591-619.
17. Serrano CJ, Graham L, DeBell K, Rawat R, Veri MC, Bonvini E, et al. A new tyrosine phosphorylation site in PLC $\{\gamma\}$ 1: The role of tyrosine 775 in immune receptor signaling. *The Journal of Immunology*. 2005 May 15;174(10):6233.
18. Gresset A, Hicks SN, Harden TK, Sondek J. Mechanism of phosphorylation-induced activation of phospholipase C- γ isozymes. *The Journal of Biological Chemistry*. 2010 Nov 12;285(46):35836-47.
19. Poulin B, Sekiya F, Rhee SG. Intramolecular interaction between phosphorylated tyrosine-783 and the C-terminal Src homology 2 domain activates phospholipase C- 1. *Proceedings of the National Academy of Sciences - PNAS*. 2005 Mar 22;102(12):4276-81.
20. Tripathi N, Vetrivel I, Téletchéa S, Jean M, Legembre P, Laurent AD. Investigation of phospholipase C γ 1 interaction with SLP76 using molecular modeling methods for identifying novel inhibitors. *International Journal of Molecular Sciences*. 2019 Sep 23;20(19):4721.

CHAPTER 5

Summary and Future Directions

5.1 Summary of Work and Important Insights

This work was motivated by recent insights into fibroblast chemotaxis, indicating the necessity of PLC γ 1 and PKC α in PDGF gradient sensing, the strongly polarized intracellular gradient of DAG, and the requirement for inactivation of Myosin IIA at the leading edge to create the asymmetric force needed for directed cell migration (1). Although these experiments were able to elucidate the pathway responsible for gradient sensing in mesenchymal cells, it was not clear how the cells interpret a shallow external gradient of chemoattractant to execute a robust chemotactic response. To answer this question, we developed a mechanistic model of the PLC/PKC signaling pathway to analyze proposed feedback mechanisms and assess their role in polarizing the intracellular signaling pathway in response to gradients of PDGF. We also developed a rule-based model of PLC γ 1 activation to study the kinetics of enzyme activation. This activation model was combined with the polarization model to investigate how changes in PLC γ 1 activation affect the polarization of PLC/PKC pathway.

We start by describing the formulation and analysis of our mechanistic, reaction-diffusion model, which to our knowledge, is the first mathematical model to describe gradient sensing through the PLC/PKC signaling pathway. In particular, we investigated the role of MARCKS as a feedback mechanism and found that the regulation of MARCKS by active PKC is capable of amplifying the pathway. The bias in PKC activation and thus MARCKS phosphorylation at the front of the cell leads to an increase in the availability of the PLC substrate, PIP₂, as MARCKS dissociates from the membrane and enters the cytosol. The faster diffusion of cytosolic MARCKS allows the unphosphorylated form to accumulate and rebind PIP₂ at the rear of the cell to suppress signaling. This buffering-ability of MARCKS to differentially control the rear versus front densities of free PIP₂ is a new concept in the study of gradient sensing; however, by

itself this mechanism is incapable of polarizing PLC/PKC signaling in response to shallow gradients ($\leq 10\%$), and this system lacks robustness to modest changes in the midpoint concentration of PDGF.

To address these issues, we considered two new feedback loops supported by experimental evidence in the literature, introducing an additional lipid species, PA, an intermediate in the metabolism of DAG. For PFL 1, the effective off-rate for PLC dissociating from the membrane decreases in proportion to the concentration of PA. This results in an increased lifetime of the PLC active state, based on experiments showing that PA binds to PLC γ 1 and increases the rate of PIP₂ hydrolysis (through reduction of the apparent Michaelis constant, K_m) in a detergent-phospholipid mixed micelle assay system (2). For PFL 2, the production of PA is enhanced by the concentration of active PKC which is based on experiments showing PKC can interact with and promote activity of the PA-producing enzyme, PLD (3-5). We found that the MARCKS feedback mechanism synergizes with PFLs 1 and 2 to polarize PLC/PKC signaling in response to shallow gradients of receptor occupancy and over an appreciable range of midpoint occupancy. Our simulations also implicated DAG kinases, enzymes responsible for converting DAG to PA, as critical players in the responsiveness of this pathway. Lipid metabolism may be a heretofore unappreciated yet crucial feature of gradient sensing via the PLC/PKC pathway.

PLC γ 1, the specific isozyme of PLC involved in fibroblast chemotaxis, is basally autoinhibited and has a much more complex path to activation than simply binding the receptor at the membrane. Recent work detailing the structure of the full-length PLC γ 1 enzyme elucidated a more detailed mechanism for its activation (6). To better understand the kinetics of PLC γ 1 activation, we developed a rule-based model to investigate how the domain interactions, binding

rates, and the phosphorylation of Tyr783 impact the activation of the enzyme. Results from the PLC γ 1 activation model suggest that the rate of uninhibited PLC γ 1 binding to the membrane sensitively affects the lifetime of the active enzyme. Given the similarity of this mechanism to the action of PFL 1 in the PLC/PKC polarization model, we created a modified version of PFL 1, in which the activation rate was increased in proportion to the concentration of PA. Like the original PFL 1, this modified version synergizes with the MARCKS feedback to polarize the PLC/PKC signaling pathway. We found our model was also able to reproduce the increased levels of activity associated with known mutations of PLC γ 1 while also predicting faster activation kinetics for mutations affecting the autoinhibition and slower kinetics for mutations affecting the rate of membrane binding. The combined model of PLC γ 1 activation and PLC/PKC polarization predicted that these activating mutations impair the polarization of the pathway in response to shallow gradients of chemoattractants.

5.2 Future Modeling and Experimental Work

Our mechanistic models of PLC/PKC signaling with newly considered positive feedback loops characterize polarization of the pathway in shallow gradients of PDGF or other chemoattractants, offering explanations of how this pathway is used by chemotaxing fibroblasts. This model preserves a certain economy of parameters, and thus is not comprehensive. With further experimental study, we may find that the proposed feedbacks are not contributing to the signaling amplification, while other mechanisms not explored here are important. For example, we investigated the role of PA on PLC, but PA has also been shown to enhance phosphatidylinositol 4-phosphate 5-kinase activity, which increases the production of PIP₂ (7). We would expect this feedback to synergize with PFL 1, leading to greater amplification of the

pathway. Our PLC γ 1 activation model is also limited in that it only accounts for a subset of the domains and phosphorylation sites associated with regulation of the enzyme. Both the split PH and SH3 domains in the regulatory X-Y linker region of the enzyme interact with the core and may play important roles in controlling the stabilization of the autoinhibited state (6). In the present model, such effects are included only implicitly, in describing the interaction of the cSH2 domain with the core. Multiple mutations affecting the activity of PLC γ 1 have also been reported in these domains, warranting further study (Fig. 5.1). A handful of studies have also reported conflicting results on the ability of PLC γ 1 phosphorylation sites besides Tyr783 to enhance activation of the enzyme, and further experimental and modeling efforts could be directed toward deciphering these results and interpreting how the sites contribute to the activation process (8-10).

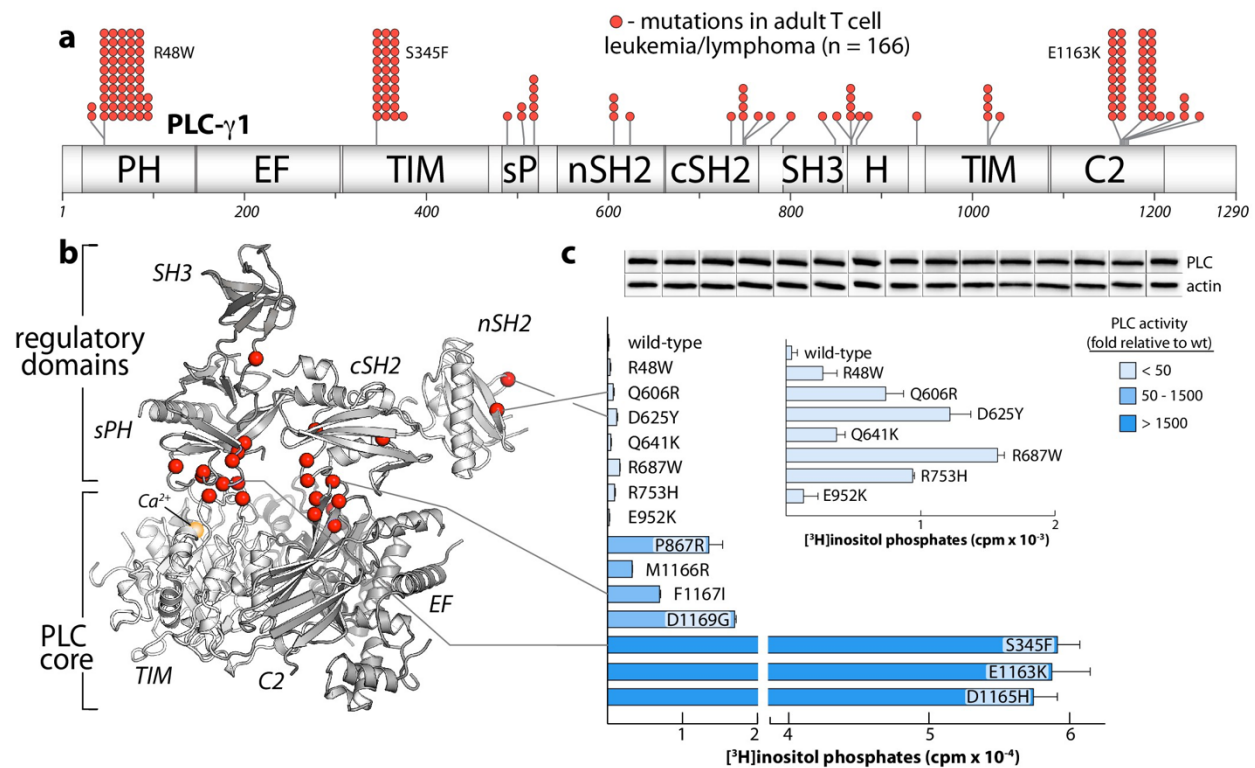


Figure 5.1 Substitutions of PLC- γ 1 found in cancers activate the enzyme. (a) Position (n = 26) and frequency of substitutions (red spheres) in PLC- γ 1 for a cohort of 370 patients with adult T cell leukemia/lymphoma. (b) Mutations from (a) mapped onto the structure of PLC- γ 1. (c) Basal phospholipase activity of mutant forms of PLC- γ 1 in cells. Data represent the mean \pm SEM of triplicate samples from a single experiment representative of three independent experiments. *Inset* shows mutant forms of PLC- γ 1 with the lowest relative basal activity. Immunoblots of cell lysates are presented in the same order as the bar graph. Reprinted from eLife 2019;8:e51700 DOI: [10.7554/eLife.51700](https://doi.org/10.7554/eLife.51700), Hajicek et al. Structural basis for the activation of PLC- γ isoforms by phosphorylation and cancer-associated mutations, Copyright (2019) Hajicek et al. This article is distributed under the terms of the Creative Commons Attribution 4.0 International License (creativecommons.org/licenses/by/4.0/), which permits unrestricted use and redistribution.

Our differential equation models are deterministic, but adding stochasticity to the model would enable a more realistic view of the dynamics of the pathway and enable us to investigate phenomena such as spontaneous polarization and breakdown of polarity. To simulate all species in our model stochastically would be exceedingly computationally expensive; however, a hybrid strategy, where highly abundant cytosolic species are still treated deterministically while the

membrane-bound species are treated stochastically, might address this problem (11). Both Chapter 2 and Chapter 3 explored the effects of asymmetric cell geometry and found them to be important, on par with asymmetric receptor occupancy. In future modeling work, a three-dimensional and deformable geometry, more representative of the shape of a fibroblast and how it changes over time could provide valuable insights (12).

Another layer of complexity is linking polarization of the pathway at the level of a single cell to multi-cell dynamics in tissues, as envisioned in cutaneous wound healing. We were able to link the thresholds of polarization based on PDGF gradient conditions from our PLC/PKC polarization model to a one-dimensional wound invasion model, in which only the cells that are experiencing the PDGF gradient conditions necessary for polarization exhibit chemotactic motility. As a bridge between these two scales of complexity, it would also be interesting to link our polarization model to the mechanics of cell migration such as how the inactivation of Myosin IIA by active PKC affects adhesion formation and actin polymerization (13).

An analysis of our mechanistic models has also provided a number of experimentally testable predictions. One of the most basic predictions is the requirement for PKC activity for both the regulation of MARCKS and feedback on PLD through PFL 2. The necessity of PKC α in polarizing the pathway can be tested using isoform-selective inhibitors such as Gö6976 (14). If PKC α is required for signal amplification then perturbations affecting MARCKS and PLD individually could be pursued. A testable prediction of PFL 1 concerns the role of DAG kinases. Based on our results, a partial inhibition of DAG kinase activity using inhibitors (15, 16) or by depleting DAG kinase isoforms would prevent polarization of the pathway while overexpressing one or more of the DAG kinase isoforms should enhance polarization with more cells polarizing at higher concentrations of chemoattractant.

5.3 Outlook

In this work, we have developed models for PLC/PKC signaling polarization in fibroblast cells exposed to a gradient of chemoattractant and PLC γ 1 activation kinetics. While these models have direct implications for the study of fibroblast dysfunction in chronic wounds (17), aberrant activation of the PLC γ 1 and PKC α enzymes is also associated with numerous other pathological conditions. Both enzymes have been implicated in tumor development and metastasis of multiple cancers (18-21) while PLC γ 1 is associated with inflammatory and autoimmune diseases related to T cell receptor signaling (18, 22) and PKC α is associated with cardiovascular diseases like heart failure and atherosclerosis (23, 24). To gain a better understanding of the mechanisms driving these diseases and cancers, the study of PLC/PKC signaling will continue to be of vital importance.

5.4 References

1. Asokan S, Johnson H, Rahman A, King S, Rotty J, Lebedeva I, et al. Mesenchymal chemotaxis requires selective inactivation of Myosin II at the leading edge via a noncanonical PLC γ /PKC α pathway. *Developmental Cell*. 2014 Dec 22;;31(6):747-60.
2. Jones GA, Carpenter G. The regulation of phospholipase C- γ 1 by phosphatidic acid. *J Biol Chem*. 1993 10/05;;268(28):20845-50.
3. H Eldar, P Ben-Av, U S Schmidt, E Livneh, M Liscovitch. Up-regulation of phospholipase D activity induced by overexpression of protein kinase C- α . Studies in intact Swiss/3T3 cells and in detergent-solubilized membranes in vitro. *Journal of Biological Chemistry*. 1993 Jun 15;;268(17):12560-4.
4. Y H Lee, H S Kim, J K Pai, S H Ryu, P G Suh. Activation of phospholipase D induced by platelet-derived growth factor is dependent upon the level of phospholipase C- γ 1. *Journal of Biological Chemistry*. 1994 Oct 28;;269(43):26842-7.
5. Henage LG, Exton JH, Brown HA. Kinetic analysis of a mammalian phospholipase D: allosteric modulation by monomeric GTPases, protein kinase C, and polyphosphoinositides. *The Journal of biological chemistry*. 2006 Feb 10;;281(6):3408-17.
6. Hajicek N, Keith NC, Siraliev-Perez E, Temple BR, Huang W, Zhang Q, et al. Structural basis for the activation of PLC- γ isozymes by phosphorylation and cancer-associated mutations. *eLife*. 2019;8(2019).
7. Jarquin-Pardo M, Fitzpatrick A, Galiano FJ, First EA, Davis JN. Phosphatidic acid regulates the affinity of the murine phosphatidylinositol 4-phosphate 5-kinase-I β for phosphatidylinositol-4-phosphate. *Journal of Cellular Biochemistry*. 2007;100(1):112-28.
8. Serrano CJ, Graham L, DeBell K, Rawat R, Veri MC, Bonvini E, et al. A new tyrosine phosphorylation site in PLC γ 1: The role of tyrosine 775 in immune receptor signaling. *The Journal of Immunology*. 2005 May 15;;174(10):6233.
9. Gresset A, Hicks SN, Harden TK, Sondek J. Mechanism of phosphorylation-induced activation of phospholipase C- γ isozymes. *The Journal of Biological Chemistry*. 2010 Nov 12;;285(46):35836-47.
10. Poulin B, Sekiya F, Rhee SG. Intramolecular interaction between phosphorylated tyrosine-783 and the C-terminal Src homology 2 domain activates phospholipase C-1. *Proceedings of the National Academy of Sciences - PNAS*. 2005 Mar 22;;102(12):4276-81.
11. Schaff JC, Gao F, Li Y, Novak IL, Slepchenko BM. Numerical Approach to Spatial Deterministic-Stochastic Models Arising in Cell Biology. *PLoS Computational Biology*. 2016 Dec 13;;12(12):e1005236.

12. Nickaen M, Novak IL, Pulford S, Rumack A, Brandon J, Slepchenko BM, et al. A free-boundary model of a motile cell explains turning behavior. *PLoS computational biology*. 2017 Nov;13(11):e1005862.
13. Vicente-Manzanares M, Choi CK, Horwitz AR. Integrins in cell migration - the actin connection. *Journal of Cell Science*. 2009 Jan 15;122(2):199-206.
14. Martiny-Baron G, Kazanietz MG, Mischak H, Blumberg PM, Kochs G, Hug H, et al. Selective inhibition of protein kinase C isozymes by the indolocarbazole Gö 6976. *The Journal of Biological Chemistry*. 1993 May 5;268(13):9194.
15. Jiang Y, Sakane F, Kanoh H, Walsh JP. Selectivity of the diacylglycerol kinase inhibitor 3-{2-(4-[bis-(4-fluorophenyl)methylene]-1-piperidiny)ethyl}-2,3-dihydro-2-thioxo-4(1H)quinazolinone (R59949) among diacylglycerol kinase subtypes. *Biochemical Pharmacology*. 2000 April 1;59(7):763-72.
16. Liu K, Kunii N, Sakuma M, Yamaki A, Mizuno S, Sato M, et al. A novel diacylglycerol kinase α -selective inhibitor, CU-3, induces cancer cell apoptosis and enhances immune response. *J Lipid Res*. 2016 -03-01;57(3):368-79.
17. Wall IB, Moseley R, Baird DM, Kipling D, Giles P, Laffafian I, et al. Fibroblast dysfunction is a key factor in the non-healing of chronic venous leg ulcers. *Journal of Investigative Dermatology*. 2008;128(10):2526-40.
18. Koss H, Bunney TD, Behjati S, Katan M. Dysfunction of phospholipase C γ in immune disorders and cancer. *Trends in Biochemical Sciences*. 2014;39(12):603-11.
19. Sala G, Dituri F, Raimondi C, Previdi S, Maffucci T, Mazzeo M, et al. Phospholipase C γ 1 is required for metastasis development and progression. *Cancer Research*. 2008 Dec 15;68(24):10187.
20. Kang J. Protein kinase C (PKC) isozymes and cancer. *New Journal of Science*. 2014 May 4;2014:1-36.
21. Garg R, Benedetti LG, Abera MB, Wang H, Abba M, Kazanietz MG. Protein kinase C and cancer: what we know and what we do not. *Oncogene*. 2013;33(45):5225-37.
22. Fu G, Chen Y, Yu M, Podd A, Schuman J, He Y, et al. Phospholipase C γ 1 is essential for T cell development, activation, and tolerance. *The Journal of Experimental Medicine*. 2010;207(2):309-18.
23. Konopatskaya O, Poole AW. Protein kinase C α : disease regulator and therapeutic target. *Trends in Pharmacological Sciences*. 2009;31(1):8-14.

24. Weeks KL, McMullen JR. Divergent effects of PKC (protein kinase C) α in the human and animal heart? Therapeutic implications for PKC inhibitors in cardiac patients. *Circulation. Genomic and Precision Medicine*. 2018 Mar;11(3):e002104.

APPENDICES

Appendix A

A.1 Modeling Details for Chapter 2

A.1.1 Reaction-diffusion model: general considerations

Molecular species (Table A.1) reside in either the cytosol or the plasma membrane. In general terms, taking C_i as the concentration of cytosolic species i (μM), the reaction diffusion (conservation) equations are posed as follows.

$$\frac{\partial C_i}{\partial t} = D_i \nabla^2 C_i + R_{V,i}$$

Here, t is time (s), D_i is the molecular diffusivity of species i ($\mu\text{m}^2/\text{s}$), and $R_{V,i}$ is the volumetric production rate of species i ($\mu\text{M}/\text{s}$). The boundary condition for each species at the membrane surface, S , equates the diffusive flux due to Fick's first law to the net rate of production at the membrane, $R_{S,i}$ ($\mu\text{m}^{-2} \text{s}^{-1}$)

$$D_i(\mathbf{n} \cdot \nabla C_i)|_S = (0.00166 \mu\text{M} \mu\text{m}^3) R_{S,i}$$

The constant on the right-hand side incorporates Avogadro's number and the conversion of volume units from L to μm^3 . This is done automatically in the Virtual Cell software.

For the membrane species, taking c_i as the area density of membrane species i ($\#/\mu\text{m}^2$), the reaction-diffusion (conservation) equations are generally of the following form:

$$\frac{\partial c_i}{\partial t} = D_i \nabla^2 c_i + r_i$$

Here, r_i is the production rate of membrane species i .

A.1.2 Molecular diffusivities

Diffusivities of receptor species and membrane-bound PLC are each assigned $D = 0.01 \mu\text{m}^2/\text{s}$, which is typical of transmembrane receptors and effectively immobile. We assume approximate equivalence of the diffusivities for PIP_2 , DAG, DAG-PKC, and DAG-PKC*, with a nominal lipid diffusion value of $D = 0.5 \mu\text{m}^2/\text{s}$. Diffusivities of cytosolic species vary modestly according to hydrodynamic radius, scaling approximately with molecular weight (MW) as $D \propto MW^{-1/3}$ and are of the order of magnitude estimated from photobleaching measurements in cytoplasm (1). Of these, only the diffusivities of MARCKS/phospho-MARCKS affect the results, and these were systematically varied as described in *Chapter 2*.

Table A.1 List of model species, their diffusivities, and their initial concentrations/densities.

Variable	Description	Localization	Diffusivity ($\mu\text{m}^2/\text{s}$)	Initial condition
E	Inactive PLC enzyme	cytosol	19	$0.03 \mu\text{M}$
M	Unphosphorylated MARCKS	cytosol	32	$1 \mu\text{M}$
M_p	Phosphorylated MARCKS	cytosol	32	0
C	Inactive PKC	cytosol	24	$0.3 \mu\text{M}$
r_0	Free receptor	membrane	0.01	$130 \mu\text{m}^{-2}$
r_1	Receptor-ligand complex	membrane	0.01	0
r_2	Receptor dimer (active)	membrane	0.01	0
e	Active PLC enzyme	membrane	0.01	0
p_T	Total PIP_2	membrane	0.5	$5000 \mu\text{m}^{-2}$
m_T	Total membrane MARCKS	membrane	0.5	$3727 \mu\text{m}^{-2}$
d	Free DAG	membrane	0.5	0
c^*	Active DAG-PKC	membrane	0.5	0
c	Inactive DAG-PKC	membrane	0.5	0

A.1.3 Receptor dynamics

We adopt our previously published model, which was trained on kinetic measurements of PDGF receptor phosphorylation (2, 3), with the local concentration of PDGF ligand, $[L]$, as the input. The production rates, in units of $\# \mu m^{-2} s^{-1}$, and their associated fit or estimated parameters are as follows.

$$\begin{aligned} r_{r_0} &= k_t(130 \mu m^{-2} - r_0) - k_{off,L} \left(\frac{[L]}{K_{D,L}} r_0 - r_1 \right) \\ r_{r_1} &= k_{off,L} \left(\frac{[L]}{K_{D,L}} r_0 - r_1 \right) - k_t r_1 - 2(k_x r_1^2 - k_{-x} r_2) \\ r_{r_2} &= k_x r_1^2 - k_{-x} r_2 - k_e r_2 \end{aligned}$$

The rate constants are $k_t = 0.02/60 \text{ s}^{-1}$, $k_{off,L} = 0.1 \text{ s}^{-1}$ (arbitrarily fast), $K_{D,L} = 1.5 \text{ nM}$, $k_x = 0.3/60/130 \mu m^2 s^{-1}$, $k_{-x} = 0.07/60 \text{ s}^{-1}$, $k_e = 0.15/60 \text{ s}^{-1}$. The initial surface receptor density of $130 \mu m^{-2}$ corresponds to approximately 10^5 per cell.

A.1.4 Production rates for the PLC/PKC pathway

For the variables downstream of the receptor species, we define here the production rates for the cytosolic species, $R_{V,i}$ and $R_{S,i}$, and for the membrane species, r_i , in terms of the rates of particular transformations, V_j .

Inactive PLC enzyme (E): Diffusion only in the cytoplasm; recruited to the membrane with net flux V_{PLC} .

$$R_{V,E} = 0; \quad R_{S,E} = -V_{PLC}$$

Unphosphorylated MARCKS (M): Generated by dephosphorylation of MARCKS at rate V_{dpM} ; recruited to the membrane with net flux V_{MARCKS} .

$$R_{V,M} = V_{dpM}; \quad R_{S,M} = -V_{MARCKS}$$

Phosphorylated MARCKS (M_p): Consumed by dephosphorylation of MARCKS; generated at the membrane, coincident with phosphorylation of membrane-associated MARCKS, with flux V_{pm} .

$$R_{V,M_p} = -V_{dpM}; \quad R_{S,M_p} = V_{pm}$$

Inactive PKC (C): Diffusion only in the cytoplasm; binds DAG in an active form with net flux V_{PKC} , and is released from DAG as the inactive form with flux $V_{off,c}$.

$$R_{V,C} = 0; \quad R_{S,C} = -V_{PKC} + V_{off,c}$$

We turn now to the production rates of the remaining membrane species.

Active PLC enzyme (e): Recruited with the aforementioned net flux V_{PLC} .

$$r_e = V_{PLC}$$

Total PIP₂ (p_T): Synthesized with rate $V_{synth,p}$; consumed with basal and active PLC-mediated rates $V_{hyd,basal}$ and $V_{hyd,PLC}$, respectively.

$$r_{p_T} = V_{synth} - V_{hyd,basal} - V_{hyd,PLC}$$

Total membrane MARCKS (m_T): Recruited to the membrane with the aforementioned net flux V_{MARCKS} ; released from the membrane, coincident with phosphorylation of membrane-associated MARCKS, with the aforementioned flux V_{pm} .

$$r_{m_T} = V_{MARCKS} - V_{pm}$$

Free DAG (d): Produced from active PLC-mediated hydrolysis of PIP_2 with the aforementioned rate $V_{hyd,PLC}$; consumed via DAGK-mediated phosphorylation with net rate V_{DAGK} . Also, free DAG is reduced/recovered by binding/dissociation of PKC species, with the aforementioned fluxes V_{PKC} and $V_{off,c}$.

$$r_d = V_{hyd,PLC} - V_{DAGK} - V_{PKC} + V_{off,c}$$

Active DAG-PKC (c^*): Recruited from the cytosol with the aforementioned flux, V_{PKC} .

Deactivated via dephosphorylation with rate V_{dpc} . Recovered via intra- and inter-molecular phosphorylation of the inactive form with rates V_{pc1} and V_{pc2} , respectively.

$$r_{c^*} = V_{PKC} - V_{dpc} + V_{pc1} + V_{pc2}$$

Inactive DAG-PKC (c): Generated via dephosphorylation of the active form with the aforementioned rate V_{dpc} . Lost via intra and inter-molecular phosphorylation of the inactive form, with the aforementioned rate V_{pc1} and V_{pc2} , respectively, and via dissociation from DAG with the aforementioned flux $V_{off,c}$.

$$r_c = V_{dpc} - V_{pc1} - V_{pc2} - V_{off,c}$$

A.1.5 Rate laws for the PLC/PKC pathway

All rate laws describing the transformations downstream of receptor activation are listed in Table A.2. Like the receptor dynamics, most of the rate laws are based on simplified, mass-action principles. In the category of heterogeneous binding (recruitment from the cytosol to the membrane), we assume a net rate with the form

$$V = k_{on}c_jC_i|_S - k_{off}c_i,$$

where c_i is the density of the membrane species to which species i binds. This is assumed to apply to V_{PLC} (PLC binding to receptor, ignoring PFL1) and V_{PKC} (PKC binding to DAG).

Another category of simple reactions is that of the pseudo-first-order reactions, where the corresponding enzymatic activity catalyzing the reaction is implied to be constant. Such rate laws take the form

$$V = k_{rxn}C_i \text{ or } V = k_{rxn}c_i$$

for a cytosolic or membrane species, respectively. This form is assumed to apply to V_{dpM} (dephosphorylation of MARCKS), $V_{hyd,basal}$ (basal rate of PIP₂ consumption, which could be by hydrolysis or dephosphorylation), $V_{off,c}$ [dissociation of inactive PKC from DAG (followed by rapid re-phosphorylation in the cytosol)], V_{DAGK} (consumption of DAG, e.g. by the action of DAG kinase), V_{pci} (intramolecular autophosphorylation of PKC while bound to DAG), and V_{dpc} (dephosphorylation of PKC while bound to DAG).

Finally, a third category of simple reactions is the pseudo-second-order (enzymatic) reaction in the membrane, of the form

$$V = k_{rxn}c_jc_i.$$

This is assumed to apply to $V_{hyd,PLC}$ [PLC-catalyzed PIP₂ hydrolysis; species e, p (free PIP₂)], and V_{pm} [MARCKS phosphorylation; species c^*, m], and V_{pc2} (intermolecular autophosphorylation of PKC while bound to DAG; species c^*, c).

This leaves only two unique rate laws: V_{synth} and V_{MARCKS} . For the former, we assume by default that the PIP₂ synthesis rate is constant. For V_{MARCKS} (binding of unphosphorylated MARCKS to the membrane), we assume that MARCKS initially associates with the membrane via reversible insertion of its myristoyl lipid and is stabilized by quasi-equilibrium binding to PIP₂. For the sake of simplicity, we model the polybasic motif of MARCKS as three equivalent binding sites for PIP₂. Defining m_i as the density of membrane-bound MARCKS with i molecules of PIP₂ bound, p as the density of free (unbound) PIP₂, and K_{PIP2} as the (single-site) equilibrium constant of MARCKS-PIP₂ binding,

$$m_i = \left(\frac{4-i}{i}\right) K_{PIP2} p m_{i-1}$$

$$m_1 = 3K_{PIP2} p m_0; \quad m_2 = K_{PIP2} p m_1; \quad m_3 = \frac{K_{PIP2} p m_2}{3}$$

If we take m_T as the sum of m_i , and assume that only m_0 can dissociate from the membrane, we obtain the rate law as follows.

$$m_T = m_0 \{1 + 3K_{PIP2} p [1 + K_{PIP2} p (1 + K_{PIP2} p / 3)]\} = m_0 (1 + K_{PIP2} p)^3$$

$$V_{MARCKS} = k_{on,m} M|_S - \frac{k_{off,m} m_T}{(1 + K_{PIP2} p)^3}$$

This makes sense if one considers the probability that any of the 3 equivalent PIP₂-binding sites on MARCKS is unoccupied; that probability is equal to $1/(1 + K_{PIP_2}p)$.

In this formulation, we must distinguish the density of free PIP₂, p , from the density of total PIP₂, p_T . We define the function $g(K_{PIP_2}p)$ as the average number of PIP₂ molecules bound per molecule of MARCKS:

$$g(K_{PIP_2}p) = \frac{1}{m_T} \sum_{i=1}^3 im_i = \frac{3K_{PIP_2}p[1 + K_{PIP_2}p(2 + K_{PIP_2}p)]}{(1 + K_{PIP_2}p)^3} = \frac{3K_{PIP_2}p}{1 + K_{PIP_2}p}$$

This result makes sense if one considers that each molecule of MARCKS at the membrane offers 3 PIP₂ binding sites, each with fractional occupancy $K_{PIP_2}p/(1 + K_{PIP_2}p)$. From the definition of p ,

$$p = p_T - g(K_{PIP_2}p)m_T$$

Solving the resulting quadratic equation for p ,

$$p = \frac{K_{PIP_2}p_T - 3K_{PIP_2}m_T - 1 + [(K_{PIP_2}p_T - 3K_{PIP_2}m_T - 1)^2 + 4K_{PIP_2}p_T]^{1/2}}{2K_{PIP_2}}$$

Table A.2 Reaction rate expressions describing the PLC/PKC pathway. Note that the free PIP₂ concentration, p , is calculated based on the variables p_T and m_T , assuming pseudo-equilibrium of PIP₂-MARCKS interactions.

Rate	Description	Expression	Base parameters
V_{PLC}	Net PLC binding	$k_{on,e}r_2E _S - k_{off,e}e$	$k_{on,e}$: 10 $\mu\text{M}^{-1}\text{s}^{-1}$ $k_{off,e}$: 0.1 s^{-1}
V_{synth}	Production of free PIP ₂	$V_{synth}(\text{constant})$	2.5 $\mu\text{m}^{-2}\text{s}^{-1}$
$V_{hyd,basal}$	Basal PIP ₂ consumption	$k_{hyd,basal}p$	$k_{hyd,basal}$: 0.005 s^{-1}
$V_{hyd,PLC}$	PIP ₂ hydrolysis by PLC	$k_{hyd,PLC}ep$	$k_{hyd,PLC}$: 0.005 $\mu\text{m}^{-2}\text{s}^{-1}$ $k_{on,m}$: 792 $\mu\text{M}^{-1}\mu\text{m}^{-2}\text{s}^{-1}$
V_{MARCKS}	Net MARCKS binding to PIP ₂	$k_{on,m}M _S - \frac{k_{off,m}m_T}{(1 + K_{PIP_2}p)^3}$	$k_{off,m}$: 1 s^{-1} K_{PIP_2} : 0.00135 μm^2
V_{pm}	MARCKS phosphorylation	$k_{pm}c^*m_T$	k_{pm} : 1 $\mu\text{m}^2\text{s}^{-1}$
V_{dpm}	MARCKS dephosphorylation	$k_{dpm}M_p$	k_{dpm} : 1 s^{-1}
$V_{basal,dp}$	Basal PA consumption	$k_{basal,dp}d_p$	$k_{basal,dp}$: 1 s^{-1}
V_{DAGK}	DAG consumption	$k_{DAGK}d$	k_{DAGK} : 1 s^{-1}
V_{PKC}	Net PKC binding to DAG	$k_{on,c}dC _S - k_{*off,c}c^*$	$k_{on,c}$: 1 $\mu\text{M}^{-1}\text{s}^{-1}$ $k_{*off,c}$: 0.1 s^{-1}
V_{dpc}	Dephosphorylation of PKC	$k_{dpc}c^*$	k_{dpc} : 1 s^{-1}
V_{pc1}	PKC phosphorylation (intra)	$k_{pc1}c$	k_{pc1} : 1 s^{-1}
V_{pc2}	PKC phosphorylation (inter)	$k_{pc2}c$	k_{pc2} : 0 $\mu\text{m}^2\text{s}^{-1}$
$V_{off,c}$	Dissociation of inactive PKC	$k_{off,c}c$	$k_{off,c}$: 0.1 s^{-1}

A.1.6 Specification of adjustable parameters

PLC activity: The parameters $k_{on,e}$ and $k_{off,e}$ were chosen to yield fast kinetics and an effective dissociation constant of 10 nM, reflecting the binding of the PLC SH2 domains (4). The initial PLC concentration of 0.03 μM (30 nM) is a nominal value corresponding to $\sim 4 \times 10^4$ copies per cell. With these parameters assumed, the value of $k_{hyd,PLC}$ was adjusted so that the PDGF gradient stimulation would elicit substantial hydrolysis of PIP₂.

PIP₂ dynamics: We assume an initial total PIP₂ density (p_T) of 5000 μm^{-2} , which corresponds to a concentration ~ 10 μM on a whole-cell volume basis. Given the proposed role of MARCKS as a PIP₂ buffer, we assume that 90% of the PIP₂ is sequestered by MARCKS in resting cells; i.e., the initial free PIP₂ density p was 500 μm^{-2} , as determined by the ratio of $V_{\text{synth}}/k_{\text{hyd,basal}}$. The value of $k_{\text{hyd,basal}} = 0.005 \text{ s}^{-1}$ corresponds to a lifetime of 3 minutes, consistent with turnover measurements (6).

MARCKS dynamics: As stated in *Chapter 2*, we assume a total cellular concentration of MARCKS of 10 μM , similar to the abundance of PIP₂ (5). MARCKS is predominantly membrane-localized in resting cells, and so we assume that 90% is membrane-associated. This set the initial value of M at 1 μM , and, considering the assumed geometry of the cell, the initial value of m_T was set at 3727 μm^{-2} . The latter value, together with the assumed initial values of $p_T = 5000 \mu\text{m}^{-2}$ and $p = 500 \mu\text{m}^{-2}$, constrained the value of K_{PIP_2} at 0.00135 μm^2 and thus the value of m_0 . The initial ratio of m_0/M constrains the ratio of $k_{\text{on},m}/k_{\text{off},m}$, and we set a nominal value of $k_{\text{off},m} = 1 \text{ s}^{-1}$. The resulting on-rate of $k_{\text{on},m} = 792 \mu\text{M}^{-1} \mu\text{m}^{-2} \text{ s}^{-1}$ corresponds to a value of $\approx 1 \mu\text{m} \text{ s}^{-1}$ (with unit conversions and Avogadro's number), which is the same magnitude as D_M/L ; i.e., MARCKS insertion is close to diffusion-limited. As discussed in *Chapter 2*, the MARCKS phosphorylation and dephosphorylation rate constants, k_{pm} and k_{dpM} , were systematically varied, and the values listed in Table A.2 were selected for further analysis.

DAG and PKC dynamics: The rate constant k_{DAGK} was assigned a nominal value of 1 s^{-1} which determines the magnitude of d . Together with the initial concentration of PKC (nominally, 0.3 μM), the kinetics of DAG binding ($k_{\text{on},c} = 1 \mu\text{M}^{-1} \text{ s}^{-1}$ and $k_{\text{off},c} = 0.1 \text{ s}^{-1}$, for a dissociation

constant of 0.1 μM , which is lower for the full-length PKC than the individual C1 domains (7,8)), and the kinetics of PKC dephosphorylation and rephosphorylation (both nominally 1 s^{-1}), the magnitude of active PKC, c^* , is determined. This can be adjusted along with k_{pc} to affect the rate of MARCKS phosphorylation.

A.1.7 Scaling analysis of MARCKS phosphorylation, diffusion, and dephosphorylation

The conservation equation and membrane boundary condition for phosphorylated MARCKS are reprised as follows.

$$\frac{\partial M_p}{\partial t} = D_{Mp} \nabla^2 M_p - k_{dpm} M_p$$

$$D_{Mp} (\mathbf{n} \cdot \nabla M_p)|_S = (0.00166 \mu\text{M} \mu\text{m}^3) k_{pm} c^* m_T$$

The partial differential equation implies a dynamic length scale, δ , over which the gradient in M_p significantly varies:

$$\delta = \left(\frac{D_{Mp}}{k_{dpm}} \right)^{1/2}$$

The boundary condition implies that

$$D_{Mp} \frac{\Delta M_p}{\delta} \sim (0.00166 \mu\text{M} \mu\text{m}^3) k_{pm} c^* m_T$$

$$\Delta M_p \sim (0.00166 \mu\text{M} \mu\text{m}^3) \frac{k_{pm}}{(D_{Mp} k_{dpm})^{1/2}} c^* m_T$$

where ΔM_p is the magnitude of the variation in M_p . The above indicates that $k_{pm}/k_{dpm}^{1/2}$ is a key parameter grouping that determines the optimal gradient in phospho-MARCKS.

The output of the model indicates that the sum of M_p and M is approximately uniform at steady state (Fig. 2.5D), and so $\Delta M \approx -\Delta M_p$. This is expected when $D_{M_p} = D_M$ (as assumed in most of the simulations) and the diffusion of membrane-bound MARCKS is relatively slow. To show this,

$$\begin{aligned}\frac{\partial(M_p + M)}{\partial t} &= D_M \nabla^2(M_p + M) = 0 \\ D_M(\mathbf{n} \cdot \nabla(M_p + M))|_S &= (0.00166 \mu\text{M} \mu\text{m}^3)(V_{pm} - V_{MARCKS}) \\ \frac{\partial m}{\partial t} &= D_M \nabla^2 m + V_{MARCKS} - V_{pm} = 0 \\ D_M(\mathbf{n} \cdot \nabla(M_p + M))|_S &= (0.00166 \mu\text{M} \mu\text{m}^3) D_M \nabla^2 m \approx 0\end{aligned}$$

We conclude that the variation in M , ΔM , which determines the differential binding of MARCKS to PIP₂, is equal to and opposite ΔM_p .

A.2 References

1. Seksek, O., J. Biwersi, and A. S. Verkman. 1997. Translational diffusion of macromolecule-sized solutes in cytoplasm and nucleus. *J. Cell Biol.* 138:131-142.
2. Park, C. S., I. C. Schneider, and J. M. Haugh. 2003. Kinetic analysis of platelet-derived growth factor receptor/phosphoinositide 3-kinase/Akt signaling in fibroblasts. *J. Biol. Chem.* 278:37064-37072.
3. Schneider, I. C., and J. M. Haugh. 2005. Quantitative elucidation of a distinct spatial gradient-sensing mechanism in fibroblasts. *J. Cell Biol.* 171:883-892.
4. Ladbury, J. E., M. A. Lemmon, M. Zhou, J. Green, M. C. Botfield, and J. Schlessinger. 1995. Measurement of the binding of tyrosyl phosphopeptides to SH2 domains: a reappraisal. *Proc. Natl. Acad. Sci. U.S.A.* 92:3199-3203.
5. McLaughlin, S., J. Y. Wang, A. Gambhir, and D. Murray. 2002. PIP2 and proteins: interactions, organization, and information flow. *Annu. Rev. Biophys. Biomol. Struct.* 31:151-175.
6. Batty, I. H., R. A. Currie, and C. P. Downes. 1998. Evidence for a model of integrated inositol phospholipid pools implies an essential role for lipid transport in the maintenance of receptor-mediated phospholipase C activity in 1321N1 cells. *Biochem. J.* 330:1069-1077.
7. Oancea, E., and T. Meyer. 1998. Protein kinase C as a molecular machine for decoding calcium and diacylglycerol signals. *Cell* 95:307-318.
8. Ananthanarayanan, B., R. V. Stahelin, M. A. Digman, and W. Cho. 2003. Activation mechanisms of conventional protein kinase C isoforms are determined by the ligand affinity and conformational flexibility of their C1 domains. *J. Biol. Chem.* 278:46886-46894.

Appendix B

B.1 Modeling Details for Chapter 3

B.1.1 General forms of the differential equations and boundary conditions

Species (Table B.1) reside in either the cytosol or the plasma membrane. For each cytosolic species i , we can write a general conservation equation as follows.

$$\frac{\partial C_i}{\partial t} = D_i \nabla^2 C_i + R_{V,i}$$

Here, C_i is the local concentration of species i (μM), t is time (s), D_i is the molecular diffusivity of species i ($\mu\text{m}^2/\text{s}$), and $R_{V,i}$ is the volumetric production rate of species i ($\mu\text{M}/\text{s}$). The associated boundary condition at the plasma membrane surface, S , equates the diffusive flux to the net rate of production at the membrane, $R_{S,i}$ ($\mu\text{m}^{-2}\text{s}^{-1}$).

$$D_i(\mathbf{n} \cdot \nabla C_i)|_S = (0.00166 \mu\text{M} \mu\text{m}^3) R_{S,i}$$

The constant on the right-hand side incorporates Avogadro's number and the conversion of volume units from L to μm^3 , which is done automatically in Virtual Cell. For each membrane species i , conservation equations have the following form:

$$\frac{\partial c_i}{\partial t} = D_i \nabla^2 c_i + r_i$$

Here, c_i is the local area density of membrane species i ($\#/\mu\text{m}^2$), D_i is the molecular diffusivity of membrane species i ($\mu\text{m}^2/\text{s}$), and r_i is the production rate of membrane species i .

B.1.2 Molecular diffusivities and initial concentrations

The assigned diffusivity of receptor-bound PLC is $0.01 \mu\text{m}^2/\text{s}$, which is typical of transmembrane receptors and effectively immobile. We assigned diffusivities for PIP_2 , DAG, PA, DAG-PKC, and DAG-PKC* equal to $0.5 \mu\text{m}^2/\text{s}$, a value typical for plasma membrane lipids. Diffusivities of cytosolic species vary modestly according to hydrodynamic radius, scaling approximately with molecular weight (MW) as $D \propto \text{MW}^{-1/3}$ and are of the order of magnitude estimated from photobleaching measurements in cytoplasm. These diffusivity values are the same as those assumed in Mohan et al. (1). Initial conditions are also the same as in Mohan et al., except for the initial concentration of inactive PLC enzyme, which was modestly reduced from 0.03 to $0.02 \mu\text{M}$. As explained previously (1), the initial abundance of membrane-bound MARCKS, together with its affinity for PIP_2 , was chosen such that 90% of the PIP_2 molecules and 90% of the MARCKS molecules in the cell are initially in complex.

Table B.1 List of model species, their diffusivities, and their initial concentrations/ densities

Variable	Description	Compartment	Diffusivity ($\mu\text{m}^2/\text{s}$)	Initial Condition
E	Inactive PLC enzyme	Cytosol	19	$0.02 \mu\text{M}$
M	Unphosphorylated MARCKS	Cytosol	32	$1 \mu\text{M}$
M_p	Phosphorylated MARCKS	Cytosol	32	0
C	Inactive PKC	Cytosol	24	$0.3 \mu\text{M}$
e	Active PLC enzyme	Membrane	0.01	0
p_T	Total PIP_2	Membrane	0.5	$5000 \mu\text{m}^{-2}$
m_T	Total membrane MARCKS	Membrane	0.5	$3727 \mu\text{m}^{-2}$
d	Free DAG	Membrane	0.5	0
d_p	PA	Membrane	0.5	0
c^*	Active DAG-PKC	Membrane	0.5	0
c	Inactive DAG-PKC	Membrane	0.5	0

B.1.3 Production rates

Here, we define the aforementioned production rates for the cytosolic species ($R_{V,i}$ and $R_{S,i}$) and membrane species (r_i) in terms of the net rates of reactions, V_j . Rate law expressions for the V_j 's are covered in the next section.

Inactive PLC enzyme (E): Recruited to the membrane with net flux V_{PLC} .

$$R_{V,E} = 0; \quad R_{S,E} = -V_{PLC}$$

Unphosphorylated MARCKS (M): Generated by dephosphorylation at rate V_{dpM} ; recruited to the membrane with net flux V_{MARCKS} .

$$R_{V,M} = V_{dpM}; \quad R_{S,M} = -V_{MARCKS}$$

Phosphorylated MARCKS (M_p): Consumed by dephosphorylation at rate V_{dpM} ; generated by phosphorylation of membrane-associated MARCKS, with flux V_{pm} .

$$R_{V,Mp} = -V_{dpM}; \quad R_{S,Mp} = V_{pm}$$

Inactive PKC (C): Binds DAG in an active form with net flux V_{PKC} ; recovered by release of inactive DAG-PKC with flux $V_{off,c}$.

$$R_{V,C} = 0; \quad R_{S,C} = -V_{PKC} + V_{off,c}$$

Active PLC enzyme (e): Recruited with net flux V_{PLC} .

$$r_e = V_{PLC}$$

Total PIP₂ (p_T): Synthesized at a constant rate, $V_{synth,p}$; consumed with basal and active PLC-catalyzed rates ($V_{basal,p}$ and $V_{hyd,PLC}$, respectively).

$$r_{p_T} = V_{synth,p} - V_{basal,p} - V_{hyd,PLC}$$

Total membrane MARCKS (m_T): Recruited to the membrane with the net flux V_{MARCKS} ; released from the membrane through phosphorylation by PKC with flux V_{pm} .

$$r_{m_T} = V_{MARCKS} - V_{pm}$$

Free DAG (d): Produced from PLC-catalyzed hydrolysis of PIP₂ with rate $V_{hyd,PLC}$; consumed via diacylglycerol kinase (DAGK)-mediated phosphorylation with rate V_{DAGK} ; consumed by net binding to PKC with rate V_{PKC} ; recovered by release of inactive DAG-PKC with rate $V_{off,c}$. In addition, the present models include generation of DAG from dephosphorylation of PA by PA phosphatase, with rate V_{PAP} .

$$r_d = V_{hyd,PLC} - V_{DAGK} - V_{PKC} + V_{off,c} + V_{PAP}$$

PA (d_p): Produced via DAGK-catalyzed phosphorylation with rate V_{DAGK} and by phospholipase D (PLD)-catalyzed hydrolysis of phosphatidylcholine with rate V_{PLD} ; consumed with basal rate $V_{basal,dp}$ and conversion of PA to DAG by PA phosphatase with rate V_{PAP} .

$$r_{d_p} = V_{DAGK} + V_{PLD} - V_{basal,dp} - V_{PAP}$$

Active DAG-PKC (c^*): Recruited from the cytosol with net rate, V_{PKC} ; deactivated via dephosphorylation with rate V_{dpc} ; recovered via re-phosphorylation of the inactive form with rate V_{pc} .

$$r_{c^*} = V_{PKC} - V_{dpc} + V_{pc}$$

Inactive DAG-PKC (c): Generated via dephosphorylation of the active form with rate V_{dpc} ; consumed by phosphorylation with rate V_{pc} ; dissociates from DAG with rate $V_{off,c}$.

$$r_c = V_{dpc} - V_{pc} - V_{off,c}$$

B.1.4 Rate law expressions

All rate laws are listed in Table B.2. As explained in Mohan et al. (1), most of them are based on simplified kinetic principles (mass-action binding, pseudo-first-order and pseudo-second-order reactions). For V_{MARCKS} (binding of unphosphorylated MARCKS to the membrane), we assume that MARCKS initially associates with the membrane via reversible insertion of its myristoyl lipid, and is stabilized by quasi-equilibrium binding to PIP_2 ; the polybasic motif of MARCKS is modeled as three equivalent binding sites for PIP_2 . As previously derived (1), these assumptions allow one to calculate p , the density of free (unbound) PIP_2 from p_T , m_T , and the single-site equilibrium constant of MARCKS- PIP_2 binding, K_{PIP_2} .

$$p = \frac{K_{PIP_2}p_T - 3K_{PIP_2}m_T - 1 + [(K_{PIP_2}p_T - 3K_{PIP_2}m_T - 1)^2 + 4K_{PIP_2}p_T]^{1/2}}{2K_{PIP_2}}$$

The rate laws involving p , including V_{MARCKS} , are given in Table B.2.

The net rate of PLC binding to the membrane, V_{PLC} , is also given in Eq. 3.2 of *Chapter 3* and has been modified in the following ways relative to the model presented in Mohan et al. In the association rate, active receptor density, r , is taken as a model input (Eq. 3.1 in *Chapter 3*), and we account for the depletion of free PLC binding sites (density $r-e$). The dissociation rate

accounts for positive feedback loop (PFL) 1 and considers that receptor-bound PLC is in pseudo-equilibrium with the local concentration of PA (d_p). Taking K_{PA} as the associated equilibrium constant, the density of membrane-bound PLC that is bound to PA according to this approximation is $\left(\frac{K_{PA}d_p}{1+K_{PA}d_p}\right)e$, while the density of membrane-bound PLC that is not bound to PA is $\left(\frac{1}{1+K_{PA}d_p}\right)e$. While bound to PA, if PLC dissociates from the active receptor complex, it will either dissociate from PA and join the cytosolic pool or rebind the receptor (by diffusion-controlled capture) before that happens. Taking ε as a (presumably low) constant probability that PLC will dissociate from PA before recapture, we obtained the rate expression given in Table B.2 and in Eq. 3.2 of *Chapter 3*. The rate of PA production by PLD, V_{PLD} , is a new reaction in the present models. It introduces a second route of PA generation and reflects the influence of PFL 2. A Hill function is assumed, as explained in *Chapter 3* (Eq. 3.3).

Table B.2 Reaction rate expressions

Rate	Description	Expression	Base parameters
V_{PLC}	Net PLC binding with enhancement by PA (PFL 1)	$k_{on,e}(r - e)E _S - k_{off,e} \left(\frac{1 + \varepsilon K_{PA} d_p}{1 + K_{PA} d_p} \right) e$	$k_{on,e}$: $0.1 \mu\text{M}^{-1}\text{s}^{-1}$ $k_{off,e}$: 0.1s^{-1} ε : 0.01 K_{PA} : $10 \mu\text{m}^2$
$V_{synth,p}$	Production of free PIP ₂	$V_{synth,p}$	$V_{synth,p}$: $2.5 \mu\text{m}^{-2}\text{s}^{-1}$
$V_{basal,p}$	Basal PIP ₂ consumption	$k_{basal,p}p$	$k_{basal,p}$: 0.005s^{-1}
$V_{hyd,PLC}$	PIP ₂ hydrolysis by PLC	$k_{hyd,PLC}ep$	$k_{hyd,PLC}$: $0.0005 \mu\text{m}^2\text{s}^{-1}$
V_{MARCKS}	Net MARCKS binding to PIP ₂	$k_{on,m}M _S - \frac{k_{off,m}m}{(1 + K_{PIP_2}p)^3}$	$k_{on,m}$: $792 \mu\text{M}^{-1}\mu\text{m}^{-2}\text{s}^{-1}$ $k_{off,m}$: 1s^{-1} K_{PIP_2} : $0.00135 \mu\text{m}^2$
V_{pm}	MARCKS phosphorylation	$k_{pm}c^*m$	k_{pm} : $1 \mu\text{m}^2\text{s}^{-1}$
V_{dpm}	MARCKS dephosphorylation	$k_{dpm}M_p$	k_{dpm} : 0.3s^{-1}
$V_{basal,dp}$	Basal PA consumption	$k_{basal,dp}d_p$	$k_{basal,dp}$: 1s^{-1}
V_{DAGK}	DAG conversion to PA	$k_{DAGK}d$	k_{DAGK} : 1s^{-1}
V_{PAP}	PA conversion to DAG	$k_{PAP}d_p$	k_{PAP} : 1s^{-1}
V_{PKC}	Net PKC binding to DAG	$k_{on,c}dC _S - k_{off,c}c^*$	$k_{on,c}$: $1 \mu\text{M}^{-1}\text{s}^{-1}$ $k_{off,c}$: 0.1s^{-1}
V_{dpc}	Dephosphorylation of PKC	$k_{dpc}c^*$	k_{dpc} : 1s^{-1}
V_{pc}	PKC re-phosphorylation	$k_{pc}c$	k_{pc} : 1s^{-1}
$V_{off,c}$	Dissociation of inactive PKC	$k_{off,c}c$	$k_{off,c}$: 0.1s^{-1}
V_{PLD}	Production of PA with enhancement by active PKC (PFL 2)	$V_{synth,dp} \left(\frac{1 + \gamma(K_{PLD}c^*)^n}{1 + (K_{PLD}c^*)^n} \right)$	$V_{synth,dp}$: $0.0001 \mu\text{m}^{-2}\text{s}^{-1}$ γ : variable K_{PLD} : variable n : 2

B.1.5 Specification of rate parameters

Where reasonable, we kept values of rate constants the same as in the previous modeling study (1). Exceptions and new rate parameters are discussed below.

In the Mohan model, parameters $k_{on,e}$ and $k_{off,e}$ in V_{PLC} were chosen to yield fast kinetics and a dissociation constant ($k_{off,e}/k_{on,e}$) of 10 nM. To achieve that, the previous value of $k_{on,e}$ ($10 \mu\text{M}^{-1}\text{s}^{-1}$, or $10^7 \text{M}^{-1}\text{s}^{-1}$) was at the high end of the observed range for protein-protein interactions. Furthermore, those kinetics did not account for enhancement of PLC recruitment by PA. Therefore, we reduced the value of $k_{on,e}$ by two logs, to $0.1 \mu\text{M}^{-1}\text{s}^{-1}$ ($10^5 \text{M}^{-1}\text{s}^{-1}$), well within the observed range for protein-protein interactions, to offset the effect of PA (characterized by the chosen value of the escape probability, $\varepsilon = 0.01$). The other new parameter associated with V_{PLC} is the PLC-PA equilibrium constant, K_{PA} . For the base case, it was set to an order-of-magnitude value of $10 \mu\text{m}^2$, since the maximum values of d and d_p are $\sim 1 \mu\text{m}^2$. The new way we are handling receptor activation in these models results in a substantially higher magnitude of the active receptor density; even though the characteristic receptor density is the same, the receptor dynamics considered in Mohan et al. resulted in a small fraction of receptors activated, even at saturating [PDGF]. To adjust for that, such that a comparable rate of PIP_2 hydrolysis was achieved, we reduced the initial PLC concentration modestly ($0.02 \mu\text{M}$, from $0.03 \mu\text{M}$) and the value of $k_{hyd,PLC}$ by a factor of 10 ($0.0005 \mu\text{m}^2\text{s}^{-1}$, from $0.005 \mu\text{m}^2\text{s}^{-1}$). The other parameter that was adjusted, modestly, is the pseudo-first-order rate constant characterizing MARCKS dephosphorylation in the cytosol (0.3s^{-1} , reduced from 1s^{-1}). Collectively these changes bring the effects of MARCKS regulation on the PKC pathway in line with those characterized in Mohan et al. (1).

In the modeling by Mohan et al., PA was an implicit variable, as the phosphorylation of DAG by DAGKs was considered irreversible. As stated above, the present models consider the reverse reaction, with rate V_{PAP} and pseudo-first-order rate constant k_{PAP} . As a base case, we chose $k_{PAP} = k_{DAGK} = 1 \text{ s}^{-1}$. The effect of this parameter on the relative densities of DAG and PA are elucidated in the following section. PA is also generated by a newly considered reaction: hydrolysis of phosphatidylcholine catalyzed by PLD. In the associated rate expression, V_{PLD} , the phosphatidylcholine concentration does not appear, as it is assumed relatively abundant and approximately constant. To simplify the analysis, we chose an extremely low value of the basal synthesis rate ($V_{\text{synth},dp}$), such that the effect of this reaction is negligible in the absence of PFL 2. In effect, the rate constant for PLD is the product, $\gamma V_{\text{synth},dp}$, and that is why it is stated that way in the caption of Fig. 3.10. As explained in *Chapter 3*, extensive parameter sweeps of K_{PLD} and γ were run to determine optimal values for amplification by PFL 2 in conjunction with MARCKS, PFL 1, or both MARCKS and PFL 1.

B.1.6 Steady state analysis of DAG and PA levels (no PFL 2)

A steady-state analysis, assuming negligible spatial gradients of the lipid species, predicts a consistent proportional relationship between the concentrations of DAG and PA, dependent on just four parameters (k_{DAGK} , $k_{\text{basal},dp}$, k_{PAP} , and $V_{\text{synth},dp}$). The derivation for this relationship follows, starting with the reaction-diffusion equation for PA:

$$\frac{\partial d_p}{\partial t} = D_i \nabla^2 d_p + r_{dp}$$

Assuming a steady state has been reached and neglecting the diffusion term,

$$\frac{\partial d_p}{\partial t} = 0 \approx r_{dp} = V_{DAGK} + V_{PLD} - V_{basal,dp} - V_{PAP}$$

Substituting in the rate expressions, with no PFL 2 ($V_{PLD} = V_{synth,dp}$) and rearranging,

$$k_{DAGK}d + V_{synth,dp} - k_{basal,dp}d_p - k_{PAP}d_p \approx 0$$

$$k_{DAGK}d + V_{synth,dp} \approx (k_{basal,dp} + k_{PAP})d_p$$

$$d_p \approx \left(\frac{k_{DAGK}}{k_{basal,dp} + k_{PAP}} \right) d + \frac{V_{synth,dp}}{k_{basal,dp} + k_{PAP}}$$

For our set of parameters, the second term is negligible, and therefore

$$d_p \approx \left(\frac{k_{DAGK}}{k_{basal,dp} + k_{PAP}} \right) d$$

Another, related analysis was to plot e - and ‘DAG’-nullclines with free DAG (d) on the abscissa and active PLC (e) on the ordinate. For the e -nullcline,

$$r_e = V_{PLC} = k_{on,e}(r - e)E|_S - k_{off,e} \left(\frac{1 + \varepsilon K_{PA}d_p}{1 + K_{PA}d_p} \right) e = 0;$$

$$e = \frac{k_{on,e}rE|_S}{k_{on,e}E|_S + k_{off,e} \left(\frac{1 + \varepsilon K_{PA}d_p}{1 + K_{PA}d_p} \right)},$$

and the linear relationship between d_p and d derived above, in the absence of PFL 2, is invoked.

The concentration of PLC in the cytosol, E , was approximately uniform at steady state, and its value was obtained from the corresponding simulation. The e -nullcline equation also includes the local density of active receptors, r . For the ‘DAG’-nullcline, we consider both free and bound forms of DAG:

$$r_d + r_{c^*} + r_c = V_{hyd,PLC} - V_{DAGK} + V_{PAP} = k_{hyd,PLC} ep - k_{DAGK}d + k_{PAP}d_p = 0$$

Incorporating the approximately proportional relationship between d_p and d derived above, the DAG-nullcline is, approximately,

$$e = \left(\frac{k_{basal,dp}}{k_{basal,dp} + k_{PAP}} \right) \frac{k_{DAGK}}{k_{hyd,PLC} p} d.$$

The local densities of free PIP₂, p , at the front and back of the cell were obtained from the corresponding simulation.

B.2 References

1. Mohan K, Nosbisch JL, Elston TC, Bear JE, Haugh JM. A reaction-diffusion model explains amplification of the PLC/PKC pathway in fibroblast chemotaxis. *Biophysical Journal*. 2017. July 11;;113(1):185–94. 10.1016/j.bpj.2017.05.035.

Appendix C

C.1 VCell Math Description Code for PLCy1 Activation Model

MathDescription {

```
Constant _F_ 96485.3321;  
Constant _F_nmol_ 9.64853321E-5;  
Constant _K_GHK_ 1.0E-9;  
Constant _N_pmol_ 6.02214179E11;  
Constant _PI_ 3.141592653589793;  
Constant _R_ 8314.46261815;  
Constant _T_ 300.0;  
Constant K_millivolts_per_volt 1000.0;  
Constant KMOLE 0.001660538783162726;
```

```
Constant kact_2_r10_0 10.0;  
Constant kact_2_r10_1 10.0;  
Constant kact_2_r10_2 10.0;  
Constant kact_r11_0 0.01;  
Constant kact_r11_1 0.01;  
Constant kact_r11_2 0.01;  
Constant kbind_c_r07_0 100.0;  
Constant kbind_c_r07_1 100.0;  
Constant kbind_c_r07_2 100.0;  
Constant kbind_c_r07_3 100.0;  
Constant kbind_p_r08_0 100.0;  
Constant kbind_p_r08_1 100.0;  
Constant kbind_p_r08_2 100.0;  
Constant kbind_p_r08_3 100.0;  
Constant kdp_783_r05_0 1.0;  
Constant kdp_783_r05_1 1.0;  
Constant kdp_783_r05_2 1.0;
```

```

Constant kdp_783_r05_3 1.0;
Constant kdp_783_r05_4 1.0;
Constant kdp_783_r05_5 1.0;
Constant kinact_r12_0 0.1;
Constant kinact_r12_1 0.1;
Constant kinact_r12_2 0.1;
Constant kinact_r12_3 0.1;
Constant kinact_r12_4 0.1;
Constant kinact_r12_5 0.1;
Constant koff_nSH2_r03_0 1.0;
Constant koff_nSH2_r03_1 1.0;
Constant koff_nSH2_r03_2 1.0;
Constant koff_nSH2_r03_3 1.0;
Constant koff_nSH2_r03_4 1.0;
Constant koff_nSH2_r03_5 1.0;
Constant koff_nSH2_r03_6 1.0;
Constant koff_nSH2_r03_7 1.0;
Constant kon_nSH2_2_r02_0 1000.0;
Constant kon_nSH2_2_r02_1 1000.0;
Constant kon_nSH2_2_r02_2 1000.0;
Constant kon_nSH2_r01_0 1.0;
Constant kon_nSH2_r01_1 1.0;
Constant kon_nSH2_r01_2 1.0;
Constant kon_nSH2_r01_3 1.0;
Constant kon_nSH2_r01_4 1.0;
Constant kp_783_r04_01.0;
Constant kp_783_r04_11.0;
Constant kp_783_r04_21.0;

```

```

Constant Kr_r01_0 0.0;
Constant Kr_r01_1 0.0;
Constant Kr_r01_2 0.0;
Constant Kr_r01_3 0.0;

```

Constant Kr_r01_4 0.0;
Constant Kr_r02_0 0.0;
Constant Kr_r02_1 0.0;
Constant Kr_r02_2 0.0;
Constant Kr_r03_0 0.0;
Constant Kr_r03_1 0.0;
Constant Kr_r03_2 0.0;
Constant Kr_r03_3 0.0;
Constant Kr_r03_4 0.0;
Constant Kr_r03_5 0.0;
Constant Kr_r03_6 0.0;
Constant Kr_r03_7 0.0;
Constant Kr_r04_0 0.0;
Constant Kr_r04_1 0.0;
Constant Kr_r04_2 0.0;
Constant Kr_r05_0 0.0;
Constant Kr_r05_1 0.0;
Constant Kr_r05_2 0.0;
Constant Kr_r05_3 0.0;
Constant Kr_r05_4 0.0;
Constant Kr_r05_5 0.0;
Constant Kr_r06_0 0.0;
Constant Kr_r06_1 0.0;
Constant Kr_r06_2 0.0;
Constant Kr_r06_3 0.0;
Constant Kr_r07_0 0.0;
Constant Kr_r07_1 0.0;
Constant Kr_r07_2 0.0;
Constant Kr_r07_3 0.0;
Constant Kr_r08_0 0.0;
Constant Kr_r08_1 0.0;
Constant Kr_r08_2 0.0;
Constant Kr_r08_3 0.0;

```

Constant Kr_r09_0  0.0;
Constant Kr_r09_1  0.0;
Constant Kr_r09_2  0.0;
Constant Kr_r09_3  0.0;
Constant Kr_r10_0  0.0;
Constant Kr_r10_1  0.0;
Constant Kr_r10_2  0.0;
Constant Kr_r11_0  0.0;
Constant Kr_r11_1  0.0;
Constant Kr_r11_2  0.0;
Constant Kr_r12_0  0.0;
Constant Kr_r12_1  0.0;
Constant Kr_r12_2  0.0;
Constant Kr_r12_3  0.0;
Constant Kr_r12_4  0.0;
Constant Kr_r12_5  0.0;

```

```

Constant kunbind_c_r06_0  1.0;
Constant kunbind_c_r06_1  1.0;
Constant kunbind_c_r06_2  1.0;
Constant kunbind_c_r06_3  1.0;
Constant kunbind_p_r09_0  1.0;
Constant kunbind_p_r09_1  1.0;
Constant kunbind_p_r09_2  1.0;
Constant kunbind_p_r09_3  1.0;

```

```

Constant Size_cell  5000.0;
Constant PLCgamma1_init_uM  0.02;
Constant RTK_init_uM  0.05;
Constant s10_init_uM  0.0;
Constant s11_init_uM  0.0;
Constant s12_init_uM  0.0;
Constant s13_init_uM  0.0;

```

```

Constant s14_init_uM 0.0;
Constant s15_init_uM 0.0;
Constant s16_init_uM 0.0;
Constant s2_init_uM 0.0;
Constant s3_init_uM 0.0;
Constant s4_init_uM 0.0;
Constant s5_init_uM 0.0;
Constant s6_init_uM 0.0;
Constant s7_init_uM 0.0;
Constant s8_init_uM 0.0;
Constant s9_init_uM 0.0;

```

```

VolumeVariable Compartment::s10
VolumeVariable Compartment::s11
VolumeVariable Compartment::s12
VolumeVariable Compartment::s13
VolumeVariable Compartment::s14
VolumeVariable Compartment::s15
VolumeVariable Compartment::s16
VolumeVariable Compartment::s2
VolumeVariable Compartment::s3
VolumeVariable Compartment::s4
VolumeVariable Compartment::s5
VolumeVariable Compartment::s6
VolumeVariable Compartment::s7
VolumeVariable Compartment::s8
VolumeVariable Compartment::s9

```

```

Function Compartment::J_r01_0 (((kon_nSH2_r01_0 * RTK) * PLCgamma1) - (Kr_r01_0 * s2));
Function Compartment::J_r01_1 (((kon_nSH2_r01_1 * RTK) * s3) - (Kr_r01_1 * s4));
Function Compartment::J_r01_2 (((kon_nSH2_r01_2 * RTK) * s8) - (Kr_r01_2 * s5));
Function Compartment::J_r01_3 (((kon_nSH2_r01_3 * RTK) * s10) - (Kr_r01_3 * s9));
Function Compartment::J_r01_4 (((kon_nSH2_r01_4 * RTK) * s14) - (Kr_r01_4 * s12));

```

Function Compartment::J_r02_0 (((kon_nSH2_2_r02_0 * RTK) * s6) - (Kr_r02_0 * s7));
 Function Compartment::J_r02_1 (((kon_nSH2_2_r02_1 * RTK) * s13) - (Kr_r02_1 * s11));
 Function Compartment::J_r02_2 (((kon_nSH2_2_r02_2 * RTK) * s16) - (Kr_r02_2 * s15));
 Function Compartment::J_r03_0 ((koff_nSH2_r03_0 * s2) - ((Kr_r03_0 * RTK) * PLCgamma1));
 Function Compartment::J_r03_1 ((koff_nSH2_r03_1 * s4) - ((Kr_r03_1 * RTK) * s3));
 Function Compartment::J_r03_2 ((koff_nSH2_r03_2 * s5) - ((Kr_r03_2 * RTK) * s8));
 Function Compartment::J_r03_3 ((koff_nSH2_r03_3 * s7) - ((Kr_r03_3 * RTK) * s6));
 Function Compartment::J_r03_4 ((koff_nSH2_r03_4 * s9) - ((Kr_r03_4 * RTK) * s10));
 Function Compartment::J_r03_5 ((koff_nSH2_r03_5 * s11) - ((Kr_r03_5 * RTK) * s13));
 Function Compartment::J_r03_6 ((koff_nSH2_r03_6 * s12) - ((Kr_r03_6 * RTK) * s14));
 Function Compartment::J_r03_7 ((koff_nSH2_r03_7 * s15) - ((Kr_r03_7 * RTK) * s16));
 Function Compartment::J_r04_0 ((kp_783_r04_0 * s2) - (Kr_r04_0 * s5));
 Function Compartment::J_r04_1 ((kp_783_r04_1 * s4) - (Kr_r04_1 * s9));
 Function Compartment::J_r04_2 ((kp_783_r04_2 * s7) - (Kr_r04_2 * s11));
 Function Compartment::J_r05_0 ((kdp_783_r05_0 * s5) - (Kr_r05_0 * s2));
 Function Compartment::J_r05_1 ((kdp_783_r05_1 * s8) - (Kr_r05_1 * PLCgamma1));
 Function Compartment::J_r05_2 ((kdp_783_r05_2 * s9) - (Kr_r05_2 * s4));
 Function Compartment::J_r05_3 ((kdp_783_r05_3 * s10) - (Kr_r05_3 * s3));
 Function Compartment::J_r05_4 ((kdp_783_r05_4 * s11) - (Kr_r05_4 * s7));
 Function Compartment::J_r05_5 ((kdp_783_r05_5 * s13) - (Kr_r05_5 * s6));
 Function Compartment::J_r06_0 ((kunbind_c_r06_0 * PLCgamma1) - (Kr_r06_0 * s3));
 Function Compartment::J_r06_1 ((kunbind_c_r06_1 * s2) - (Kr_r06_1 * s4));
 Function Compartment::J_r06_2 ((kunbind_c_r06_2 * s5) - (Kr_r06_2 * s9));
 Function Compartment::J_r06_3 ((kunbind_c_r06_3 * s8) - (Kr_r06_3 * s10));
 Function Compartment::J_r07_0 ((kbind_c_r07_0 * s3) - (Kr_r07_0 * PLCgamma1));
 Function Compartment::J_r07_1 ((kbind_c_r07_1 * s4) - (Kr_r07_1 * s2));
 Function Compartment::J_r07_2 ((kbind_c_r07_2 * s9) - (Kr_r07_2 * s5));
 Function Compartment::J_r07_3 ((kbind_c_r07_3 * s10) - (Kr_r07_3 * s8));
 Function Compartment::J_r08_0 ((kbind_p_r08_0 * s9) - (Kr_r08_0 * s12));
 Function Compartment::J_r08_1 ((kbind_p_r08_1 * s10) - (Kr_r08_1 * s14));
 Function Compartment::J_r08_2 ((kbind_p_r08_2 * s11) - (Kr_r08_2 * s15));
 Function Compartment::J_r08_3 ((kbind_p_r08_3 * s13) - (Kr_r08_3 * s16));
 Function Compartment::J_r09_0 ((kunbind_p_r09_0 * s12) - (Kr_r09_0 * s9));

```

Function Compartment::J_r09_1 ((kunbind_p_r09_1 * s14) - (Kr_r09_1 * s10));
Function Compartment::J_r09_2 ((kunbind_p_r09_2 * s15) - (Kr_r09_2 * s11));
Function Compartment::J_r09_3 ((kunbind_p_r09_3 * s16) - (Kr_r09_3 * s13));
Function Compartment::J_r10_0 ((kact_2_r10_0 * s4) - (Kr_r10_0 * s7));
Function Compartment::J_r10_1 ((kact_2_r10_1 * s9) - (Kr_r10_1 * s11));
Function Compartment::J_r10_2 ((kact_2_r10_2 * s12) - (Kr_r10_2 * s15));
Function Compartment::J_r11_0 ((kact_r11_0 * s3) - (Kr_r11_0 * s6));
Function Compartment::J_r11_1 ((kact_r11_1 * s10) - (Kr_r11_1 * s13));
Function Compartment::J_r11_2 ((kact_r11_2 * s14) - (Kr_r11_2 * s16));
Function Compartment::J_r12_0 ((kinact_r12_0 * s6) - (Kr_r12_0 * s3));
Function Compartment::J_r12_1 ((kinact_r12_1 * s7) - (Kr_r12_1 * s4));
Function Compartment::J_r12_2 ((kinact_r12_2 * s11) - (Kr_r12_2 * s9));
Function Compartment::J_r12_3 ((kinact_r12_3 * s13) - (Kr_r12_3 * s10));
Function Compartment::J_r12_4 ((kinact_r12_4 * s15) - (Kr_r12_4 * s12));
Function Compartment::J_r12_5 ((kinact_r12_5 * s16) - (Kr_r12_5 * s14));

```

```

Function Compartment::K_PLCGamma1_total ((Size_cell * PLCgamma1_init_uM) + (Size_cell * s2_init_uM) +
(Size_cell * s3_init_uM) + (Size_cell * s4_init_uM) + (Size_cell * s5_init_uM) + (Size_cell * s6_init_uM) + (Size_cell * s7_init_uM)
+ (Size_cell * s8_init_uM) + (Size_cell * s9_init_uM) + (Size_cell * s10_init_uM) + (Size_cell * s11_init_uM) + (Size_cell *
s12_init_uM) + (Size_cell * s13_init_uM) + (Size_cell * s14_init_uM) + (Size_cell * s15_init_uM) + (Size_cell * s16_init_uM));
Function Compartment::K_RTK_total ((Size_cell * RTK_init_uM) + (Size_cell * s2_init_uM) + (Size_cell * s4_init_uM) +
(Size_cell * s5_init_uM) + (Size_cell * s7_init_uM) + (Size_cell * s9_init_uM) + (Size_cell * s11_init_uM) + (Size_cell *
s12_init_uM) + (Size_cell * s15_init_uM));
Function O0_PLCGamma1_active (s6 + s7 + s11 + s13 + s15 + s16);
Function O0_PLCGamma1_cytosol (PLCGamma1 + s3 + s8 + s10 + s14);
Function O0_PLCGamma1_dpTyr783 (PLCGamma1 + s2 + s3 + s4 + s6 + s7);
Function O0_PLCGamma1_inactive (PLCGamma1 + s2 + s3 + s4 + s5 + s8 + s9 + s10 + s12 + s14);
Function O0_PLCGamma1_pTyr783 (s5 + s8 + s9 + s10 + s11 + s12 + s13 + s14 + s15 + s16);
Function O0_PLCGamma1_RTK_bound (s2 + s4 + s5 + s7 + s9 + s11 + s12 + s15);
Function O0_PLCGamma1_RTK_bound_inactive (s2 + s4 + s5 + s9 + s12);
Function O0_PLCGamma1_tot (PLCGamma1 + s2 + s3 + s4 + s5 + s6 + s7 + s8 + s9 + s10 + s11 + s12 + s13 + s14 +
s15 + s16);

```

```

Function O0_RTK_tot      (RTK + s2 + s4 + s5 + s7 + s9 + s11 + s12 + s15);
Function Compartment::PLCgamma1 ((K_PLCgamma1_total - (Size_cell * s2) - (Size_cell * s3) - (Size_cell * s4) - (Size_cell
* s5) - (Size_cell * s6) - (Size_cell * s7) - (Size_cell * s8) - (Size_cell * s9) - (Size_cell * s10) - (Size_cell * s11) - (Size_cell * s12) -
(Size_cell * s13) - (Size_cell * s14) - (Size_cell * s15) - (Size_cell * s16)) / Size_cell);
Function Compartment::RTK      ((K_RTK_total - (Size_cell * s2) - (Size_cell * s4) - (Size_cell * s5) - (Size_cell * s7) -
(Size_cell * s9) - (Size_cell * s11) - (Size_cell * s12) - (Size_cell * s15)) / Size_cell);

CompartmentSubDomain Compartment {
    OdeEquation s2 {
        Rate      (J_r05_0 + J_r07_1 + J_r01_0 - J_r03_0 - J_r06_1 - J_r04_0);
        Initial    s2_init_uM;
    }
    OdeEquation s3 {
        Rate      (- J_r11_0 + J_r05_3 - J_r07_0 - J_r01_1 + J_r03_1 + J_r12_0 +
J_r06_0);
        Initial    s3_init_uM;
    }
    OdeEquation s4 {
        Rate      (- J_r07_1 + J_r05_2 + J_r01_1 - J_r03_1 + J_r12_1 - J_r10_0 -
J_r04_1 + J_r06_1);
        Initial    s4_init_uM;
    }
    OdeEquation s5 {
        Rate      (J_r07_2 - J_r03_2 - J_r05_0 + J_r01_2 - J_r06_2 + J_r04_0);
        Initial    s5_init_uM;
    }
    OdeEquation s6 {
        Rate      (J_r11_0 + J_r05_5 + J_r03_3 - J_r12_0 - J_r02_0);
        Initial    s6_init_uM;
    }
    OdeEquation s7 {
        Rate      (J_r05_4 - J_r03_3 - J_r12_1 + J_r10_0 - J_r04_2 + J_r02_0);
        Initial    s7_init_uM;
    }
}

```

```

    }
    OdeEquation s8 {
        Rate      (J_r07_3 - J_r05_1 + J_r03_2 - J_r01_2 - J_r06_3);
        Initial    s8_init_uM;
    }
    OdeEquation s9 {
        Rate      ( - J_r07_2 + J_r09_0 - J_r03_4 - J_r05_2 + J_r01_3 + J_r12_2 -
J_r10_1 + J_r04_1 + J_r06_2 - J_r08_0);
        Initial    s9_init_uM;
    }
    OdeEquation s10 {
        Rate      ( - J_r11_1 - J_r07_3 + J_r09_1 - J_r05_3 + J_r03_4 - J_r01_3 +
J_r12_3 + J_r06_3 - J_r08_1);
        Initial    s10_init_uM;
    }
    OdeEquation s11 {
        Rate      ( - J_r05_4 + J_r09_2 - J_r03_5 - J_r12_2 + J_r10_1 - J_r08_2 +
J_r04_2 + J_r02_1);
        Initial    s11_init_uM;
    }
    OdeEquation s12 {
        Rate      ( - J_r03_6 - J_r09_0 + J_r01_4 + J_r12_4 - J_r10_2 + J_r08_0);
        Initial    s12_init_uM;
    }
    OdeEquation s13 {
        Rate      (J_r11_1 - J_r05_5 + J_r09_3 + J_r03_5 - J_r12_3 - J_r08_3 -
J_r02_1);
        Initial    s13_init_uM;
    }
    OdeEquation s14 {
        Rate      ( - J_r11_2 - J_r09_1 + J_r03_6 - J_r01_4 + J_r12_5 + J_r08_1);
        Initial    s14_init_uM;
    }
}

```

```

OdeEquation s15 {
    Rate      ( - J_r03_7 - J_r09_2 - J_r12_4 + J_r10_2 + J_r08_2 + J_r02_2);
    Initial    s15_init_uM;
}
OdeEquation s16 {
    Rate      (J_r11_2 + J_r03_7 - J_r09_3 - J_r12_5 + J_r08_3 - J_r02_2);
    Initial    s16_init_uM;
}
}
}

```

C.2 VCell Math Description Code for Combined PLC γ 1 Activation Model and PLC/PKC Polarization Model

```
MathDescription {  
  
  Constant _F_ 96485.3321;  
  Constant _F_nmol_ 9.64853321E-5;  
  Constant _K_GHK_ 1.0E-9;  
  Constant _N_pmol_ 6.02214179E11;  
  Constant _PI_ 3.141592653589793;  
  Constant _R_ 8314.46261815;  
  Constant _T_ 300.0;  
  Constant AreaPerUnitArea_nuclear_membrane1.0;  
  Constant AreaPerUnitArea_plasma_membrane1.0;  
  
  Constant c_active_diffusionRate 0.5;  
  Constant c_active_init_molecules_um_2 0.0;  
  Constant C_diffusionRate 24.0;  
  Constant c_diffusionRate 0.5;  
  Constant c_init_molecules_um_2 0.0;  
  Constant C_init_uM 0.3;  
  Constant d_diffusionRate 0.5;  
  Constant d_init_molecules_um_2 0.0;  
  Constant d_p_diffusionRate 0.5;  
  Constant d_p_init_molecules_um_2 0.0;  
  Constant gamma 1000000.0;  
  Constant k_basal_dp 1.0;  
  Constant k_basal_p 0.005;  
  Constant k_DAGK 1.0;  
  Constant k_dpc 1.0;  
  Constant k_dpm 0.3;  
  Constant k_hyd_PLC 5.0E-4;  
  Constant K_millivolts_per_volt 1000.0;
```

```

Constant k_PA      10.0;
Constant k_PAP     1.0;
Constant k_pc      1.0;
Constant k_PIP2    0.00135;
Constant k_PLD     1.0;
Constant k_pm      1.0;
Constant kact      0.01;
Constant kact_2    10.0;
Constant kbind_c   100.0;
Constant kbind_p   100.0;
Constant kdp_783   1.0;
Constant kinact    0.1;
Constant KMOLE     0.001660538783162726;
Constant koff_c    0.1;
Constant koff_m    1.0;
Constant koff_nSH2 1.0;
Constant kon_c     1.0;
Constant kon_m     792.0;
Constant kon_nSH2  1.0;
Constant kon_nSH2_2 1000.0;
Constant kp_783    1.0;
Constant kunbind_c 1.0;
Constant kunbind_p 1.0;
Constant M_diffusionRate 32.0;
Constant m_diffusionRate0.5;
Constant m_init_molecules_um_2 3727.0;
Constant M_init_uM 1.0;
Constant M_p_diffusionRate 32.0;
Constant M_p_init_uM 0.0;
Constant n         2.0;
Constant netValence_r01_0 1.0;
Constant netValence_r01_1 1.0;
Constant netValence_r01_2 1.0;

```

Constant netValence_r01_3 1.0;
Constant netValence_r01_4 1.0;
Constant netValence_r02_0 1.0;
Constant netValence_r02_1 1.0;
Constant netValence_r02_2 1.0;
Constant netValence_r03_0 1.0;
Constant netValence_r03_1 1.0;
Constant netValence_r03_2 1.0;
Constant netValence_r03_3 1.0;
Constant netValence_r03_4 1.0;
Constant netValence_r03_5 1.0;
Constant netValence_r03_6 1.0;
Constant netValence_r03_7 1.0;
Constant netValence_r04_0 1.0;
Constant netValence_r04_1 1.0;
Constant netValence_r04_2 1.0;
Constant netValence_r05_0 1.0;
Constant netValence_r05_2 1.0;
Constant netValence_r05_4 1.0;
Constant netValence_r05_5 1.0;
Constant netValence_r06_1 1.0;
Constant netValence_r06_2 1.0;
Constant netValence_r07_1 1.0;
Constant netValence_r07_2 1.0;
Constant netValence_r08_0 1.0;
Constant netValence_r08_2 1.0;
Constant netValence_r08_3 1.0;
Constant netValence_r09_0 1.0;
Constant netValence_r09_2 1.0;
Constant netValence_r09_3 1.0;
Constant netValence_r10_0 1.0;
Constant netValence_r10_1 1.0;
Constant netValence_r10_2 1.0;

```

Constant netValence_r11_0 1.0;
Constant netValence_r11_1 1.0;
Constant netValence_r11_2 1.0;
Constant netValence_r12_0 1.0;
Constant netValence_r12_1 1.0;
Constant netValence_r12_2 1.0;
Constant netValence_r12_3 1.0;
Constant netValence_r12_4 1.0;
Constant netValence_r12_5 1.0;
Constant netValence_V_basal_dp 1.0;
Constant netValence_V_basal_p 1.0;
Constant netValence_V_DAGK 1.0;
Constant netValence_V_dpc 1.0;
Constant netValence_V_hyd_PLC 1.0;
Constant netValence_V_MARCKS 1.0;
Constant netValence_V_off_c 1.0;
Constant netValence_V_PAP 1.0;
Constant netValence_V_pc 1.0;
Constant netValence_V_PKC 1.0;
Constant netValence_V_pm 1.0;
Constant netValence_Vsynth_dp 1.0;
Constant netValence_Vsynth_p 1.0;
Constant PLCgamma1_diffusionRate 19.0;
Constant PLCgamma1_init_uM 0.02;
Constant pT_diffusionRate 0.5;
Constant pT_init_molecules_um 25000.0;
Constant rfrac 0.0;
Constant rsteep1 0.0;
Constant rsteep2 0.0;
Constant s10_diffusionRate 19.0;
Constant s10_init_uM 0.0;
Constant s11_diffusionRate 0.01;
Constant s11_init_molecules_um_2 0.0;

```

```

Constant s12_diffusionRate 0.01;
Constant s12_init_molecules_um_2 0.0;
Constant s13_diffusionRate 0.01;
Constant s13_init_molecules_um_2 0.0;
Constant s14_diffusionRate 19.0;
Constant s14_init_uM 0.0;
Constant s15_diffusionRate 0.01;
Constant s15_init_molecules_um_2 0.0;
Constant s16_diffusionRate 0.01;
Constant s16_init_molecules_um_2 0.0;
Constant s2_diffusionRate 0.01;
Constant s2_init_molecules_um_2 0.0;
Constant s3_diffusionRate 19.0;
Constant s3_init_uM 0.0;
Constant s4_diffusionRate 0.01;
Constant s4_init_molecules_um_2 0.0;
Constant s5_diffusionRate 0.01;
Constant s5_init_molecules_um_2 0.0;
Constant s6_diffusionRate 0.01;
Constant s6_init_molecules_um_2 0.0;
Constant s7_diffusionRate 0.01;
Constant s7_init_molecules_um_2 0.0;
Constant s8_diffusionRate 19.0;
Constant s8_init_uM 0.0;
Constant s9_diffusionRate 0.01;
Constant s9_init_molecules_um_2 0.0;
Constant Voltage_nm 0.0;
Constant Voltage_pm 0.0;
Constant VolumePerUnitVolume_cytosol 1.0;
Constant VolumePerUnitVolume_extracellular 1.0;
Constant VolumePerUnitVolume_nucleus 1.0;
Constant Vsynth_dp 1.0E-4;
Constant Vsynth_p 2.5;

```

VolumeVariable subdomain1::C
 VolumeVariable subdomain1::M
 VolumeVariable subdomain1::M_p
 VolumeVariable subdomain1::PLCgamma1
 VolumeVariable subdomain1::s10
 VolumeVariable subdomain1::s14
 VolumeVariable subdomain1::s3
 VolumeVariable subdomain1::s8

MembraneVariable subdomain0_subdomain1_membrane::c
 MembraneVariable subdomain0_subdomain1_membrane::c_active
 MembraneVariable subdomain0_subdomain1_membrane::d
 MembraneVariable subdomain0_subdomain1_membrane::d_p
 MembraneVariable subdomain0_subdomain1_membrane::m
 MembraneVariable subdomain0_subdomain1_membrane::pT
 MembraneVariable subdomain0_subdomain1_membrane::s11
 MembraneVariable subdomain0_subdomain1_membrane::s12
 MembraneVariable subdomain0_subdomain1_membrane::s13
 MembraneVariable subdomain0_subdomain1_membrane::s15
 MembraneVariable subdomain0_subdomain1_membrane::s16
 MembraneVariable subdomain0_subdomain1_membrane::s2
 MembraneVariable subdomain0_subdomain1_membrane::s4
 MembraneVariable subdomain0_subdomain1_membrane::s5
 MembraneVariable subdomain0_subdomain1_membrane::s6
 MembraneVariable subdomain0_subdomain1_membrane::s7
 MembraneVariable subdomain0_subdomain1_membrane::s9

Function subdomain0_subdomain1_membrane::J_r01_0 (kon_nSH2 * (((130.0 * rfrac * (1.0 + (rsteep1 * x / 40.0)) * ((t > 2000.0) && (t < 20000.0))) + (130.0 * rfrac * (1.0 + (rsteep2 * x / 40.0)) * (t > 20000.0)) - (s2 + s4 + s5 + s7 + s9 + s11 + s12 + s15)) * PLCgamma1));
 Function subdomain0_subdomain1_membrane::J_r01_1 (kon_nSH2 * (((130.0 * rfrac * (1.0 + (rsteep1 * x / 40.0)) * ((t > 2000.0) && (t < 20000.0))) + (130.0 * rfrac * (1.0 + (rsteep2 * x / 40.0)) * (t > 20000.0)) - (s2 + s4 + s5 + s7 + s9 + s11 + s12 + s15)) * s3));

```

Function subdomain0_subdomain1_membrane::J_r01_2      (kon_nSH2 * (((130.0 * rfrac * (1.0 + (rsteep1 * x / 40.0)) * ((t >
2000.0) && (t < 20000.0))) + (130.0 * rfrac * (1.0 + (rsteep2 * x / 40.0)) * (t > 20000.0)) - (s2 + s4 + s5 + s7 + s9 + s11 + s12 + s15))
* s8));
Function subdomain0_subdomain1_membrane::J_r01_3      (kon_nSH2 * (((130.0 * rfrac * (1.0 + (rsteep1 * x / 40.0)) * ((t >
2000.0) && (t < 20000.0))) + (130.0 * rfrac * (1.0 + (rsteep2 * x / 40.0)) * (t > 20000.0)) - (s2 + s4 + s5 + s7 + s9 + s11 + s12 + s15))
* s10));
Function subdomain0_subdomain1_membrane::J_r01_4      (kon_nSH2 * (((130.0 * rfrac * (1.0 + (rsteep1 * x / 40.0)) * ((t >
2000.0) && (t < 20000.0))) + (130.0 * rfrac * (1.0 + (rsteep2 * x / 40.0)) * (t > 20000.0)) - (s2 + s4 + s5 + s7 + s9 + s11 + s12 + s15))
* s14));
Function subdomain0_subdomain1_membrane::J_r02_0      (kon_nSH2_2 * (((130.0 * rfrac * (1.0 + (rsteep1 * x / 40.0)) *
((t > 2000.0) && (t < 20000.0))) + (130.0 * rfrac * (1.0 + (rsteep2 * x / 40.0)) * (t > 20000.0)) - (s2 + s4 + s5 + s7 + s9 + s11 + s12 +
s15)) * s6));
Function subdomain0_subdomain1_membrane::J_r02_1      (kon_nSH2_2 * (((130.0 * rfrac * (1.0 + (rsteep1 * x / 40.0)) *
((t > 2000.0) && (t < 20000.0))) + (130.0 * rfrac * (1.0 + (rsteep2 * x / 40.0)) * (t > 20000.0)) - (s2 + s4 + s5 + s7 + s9 + s11 + s12 +
s15)) * s13));
Function subdomain0_subdomain1_membrane::J_r02_2      (kon_nSH2_2 * (((130.0 * rfrac * (1.0 + (rsteep1 * x / 40.0)) *
((t > 2000.0) && (t < 20000.0))) + (130.0 * rfrac * (1.0 + (rsteep2 * x / 40.0)) * (t > 20000.0)) - (s2 + s4 + s5 + s7 + s9 + s11 + s12 +
s15)) * s16));
Function subdomain0_subdomain1_membrane::J_r03_0      (koff_nSH2 * s2);
Function subdomain0_subdomain1_membrane::J_r03_1      (koff_nSH2 * s4);
Function subdomain0_subdomain1_membrane::J_r03_2      (koff_nSH2 * s5);
Function subdomain0_subdomain1_membrane::J_r03_3      (koff_nSH2 * s7);
Function subdomain0_subdomain1_membrane::J_r03_4      (koff_nSH2 * s9);
Function subdomain0_subdomain1_membrane::J_r03_5      (koff_nSH2 * s11);
Function subdomain0_subdomain1_membrane::J_r03_6      (koff_nSH2 * s12);
Function subdomain0_subdomain1_membrane::J_r03_7      (koff_nSH2 * s15);
Function subdomain0_subdomain1_membrane::J_r04_0      (kp_783 * s2);
Function subdomain0_subdomain1_membrane::J_r04_1      (kp_783 * s4);
Function subdomain0_subdomain1_membrane::J_r04_2      (kp_783 * s7);
Function subdomain0_subdomain1_membrane::J_r05_0      (kdp_783 * s5);
Function subdomain1::J_r05_1      (kdp_783 * s8);
Function subdomain0_subdomain1_membrane::J_r05_2      (kdp_783 * s9);
Function subdomain1::J_r05_3      (kdp_783 * s10);

```

Function subdomain0_subdomain1_membrane::J_r05_4	(kdp_783 * s11);
Function subdomain0_subdomain1_membrane::J_r05_5	(kdp_783 * s13);
Function subdomain1::J_r06_0	(kunbind_c * PLCgamma1);
Function subdomain0_subdomain1_membrane::J_r06_1	(kunbind_c * s2);
Function subdomain0_subdomain1_membrane::J_r06_2	(kunbind_c * s5);
Function subdomain1::J_r06_3	(kunbind_c * s8);
Function subdomain1::J_r07_0	(kbind_c * s3);
Function subdomain0_subdomain1_membrane::J_r07_1	(kbind_c * s4);
Function subdomain0_subdomain1_membrane::J_r07_2	(kbind_c * s9);
Function subdomain1::J_r07_3	(kbind_c * s10);
Function subdomain0_subdomain1_membrane::J_r08_0	(kbind_p * s9);
Function subdomain1::J_r08_1	(kbind_p * s10);
Function subdomain0_subdomain1_membrane::J_r08_2	(kbind_p * s11);
Function subdomain0_subdomain1_membrane::J_r08_3	(kbind_p * s13);
Function subdomain0_subdomain1_membrane::J_r09_0	(kunbind_p * s12);
Function subdomain1::J_r09_1	(kunbind_p * s14);
Function subdomain0_subdomain1_membrane::J_r09_2	(kunbind_p * s15);
Function subdomain0_subdomain1_membrane::J_r09_3	(kunbind_p * s16);
Function subdomain0_subdomain1_membrane::J_r10_0	((kact_2 * (1.0 + (k_PA * d_p))) * s4);
Function subdomain0_subdomain1_membrane::J_r10_1	((kact_2 * (1.0 + (k_PA * d_p))) * s9);
Function subdomain0_subdomain1_membrane::J_r10_2	((kact_2 * (1.0 + (k_PA * d_p))) * s12);
Function subdomain0_subdomain1_membrane::J_r11_0	((kact * (1.0 + (k_PA * d_p))) * s3);
Function subdomain0_subdomain1_membrane::J_r11_1	((kact * (1.0 + (k_PA * d_p))) * s10);
Function subdomain0_subdomain1_membrane::J_r11_2	((kact * (1.0 + (k_PA * d_p))) * s14);
Function subdomain0_subdomain1_membrane::J_r12_0	(kinact * s6);
Function subdomain0_subdomain1_membrane::J_r12_1	(kinact * s7);
Function subdomain0_subdomain1_membrane::J_r12_2	(kinact * s11);
Function subdomain0_subdomain1_membrane::J_r12_3	(kinact * s13);
Function subdomain0_subdomain1_membrane::J_r12_4	(kinact * s15);
Function subdomain0_subdomain1_membrane::J_r12_5	(kinact * s16);
Function subdomain0_subdomain1_membrane::J_V_basal_dp	(k_basal_dp * d_p);

```

Function subdomain0_subdomain1_membrane::J_V_basal_p      (k_basal_p * ( - (1.0 / 2.0) * ((3.0 * k_PIP2 * m) - (k_PIP2 * pT) -
sqrt(((9.0 * (k_PIP2 ^ 2.0) * (m ^ 2.0)) - (6.0 * (k_PIP2 ^ 2.0) * m * pT) + ((k_PIP2 ^ 2.0) * (pT ^ 2.0)) + (6.0 * k_PIP2 * m) + (2.0 *
k_PIP2 * pT) + 1.0)) + 1.0) / k_PIP2));
Function subdomain0_subdomain1_membrane::J_V_DAGK          (k_DAGK * d);
Function subdomain0_subdomain1_membrane::J_V_dpc            (k_dpc * c_active);
Function subdomain1::J_V_dpm                                (k_dpm * M_p);
Function subdomain0_subdomain1_membrane::J_V_hyd_PLC        (k_hyd_PLC * (s6 + s7 + s11 + s13 + s15 + s16) * ( - (1.0 / 2.0) *
((3.0 * k_PIP2 * m) - (k_PIP2 * pT) - sqrt(((9.0 * (k_PIP2 ^ 2.0) * (m ^ 2.0)) - (6.0 * (k_PIP2 ^ 2.0) * m * pT) + ((k_PIP2 ^ 2.0) *
(pT ^ 2.0)) + (6.0 * k_PIP2 * m) + (2.0 * k_PIP2 * pT) + 1.0)) + 1.0) / k_PIP2));
Function subdomain0_subdomain1_membrane::J_V_MARCKS         ((kon_m * M) - ((koff_m * m) / (1.0 - ((1.0 / 2.0 * ((3.0 * k_PIP2 *
m) - (k_PIP2 * pT) - sqrt(((9.0 * (k_PIP2 ^ 2.0) * (m ^ 2.0)) - (6.0 * (k_PIP2 ^ 2.0) * m * pT) + ((k_PIP2 ^ 2.0) * (pT ^ 2.0)) + (6.0 *
k_PIP2 * m) + (2.0 * k_PIP2 * pT) + 1.0)) + 1.0)) * (3.0 - ((1.0 / 2.0 * ((3.0 * k_PIP2 * m) - (k_PIP2 * pT) - sqrt(((9.0 * (k_PIP2 ^
2.0) * (m ^ 2.0)) - (6.0 * (k_PIP2 ^ 2.0) * m * pT) + ((k_PIP2 ^ 2.0) * (pT ^ 2.0)) + (6.0 * k_PIP2 * m) + (2.0 * k_PIP2 * pT) + 1.0))
+ 1.0)) * (( - (3.0 / 2.0) * k_PIP2 * m) + ((1.0 / 2.0) * k_PIP2 * pT) + ((1.0 / 2.0) * sqrt(((9.0 * (k_PIP2 ^ 2.0) * (m ^ 2.0)) - (6.0 *
(k_PIP2 ^ 2.0) * m * pT) + ((k_PIP2 ^ 2.0) * (pT ^ 2.0)) + (6.0 * k_PIP2 * m) + (2.0 * k_PIP2 * pT) + 1.0))) + (5.0 / 2.0))))));
Function subdomain0_subdomain1_membrane::J_V_off_c          (koff_c * c);
Function subdomain0_subdomain1_membrane::J_V_PAP            (k_PAP * d_p);
Function subdomain0_subdomain1_membrane::J_V_pc             (k_pc * c);
Function subdomain0_subdomain1_membrane::J_V_PKC            ((kon_c * d * C) - (koff_c * c_active));
Function subdomain0_subdomain1_membrane::J_V_pm             (k_pm * c_active * m);
Function subdomain0_subdomain1_membrane::J_Vsynth_dp         (Vsynth_dp * (1.0 + (gamma * ((k_PLD * c_active) ^ n))) / (1.0 +
((k_PLD * c_active) ^ n)));
Function subdomain0_subdomain1_membrane::J_Vsynth_p         Vsynth_p;
Function subdomain0_subdomain1_membrane::KFlux_plasma_membrane_cytosol (AreaPerUnitArea_plasma_membrane /
VolumePerUnitVolume_cytosol);
Function subdomain1::Size_cytosol (VolumePerUnitVolume_cytosol * vcRegionVolume('subdomain1'));
Function subdomain0::Size_extracellular (VolumePerUnitVolume_extracellular * vcRegionVolume('subdomain0'));
Function subdomain1_subdomain2_membrane::Size_nuclear_membrane (AreaPerUnitArea_nuclear_membrane *
vcRegionArea('subdomain1_subdomain2_membrane'));
Function subdomain2::Size_nucleus (VolumePerUnitVolume_nucleus * vcRegionVolume('subdomain2'));
Function subdomain0_subdomain1_membrane::Size_plasma_membrane (AreaPerUnitArea_plasma_membrane *
vcRegionArea('subdomain0_subdomain1_membrane'));

```

```

Function subdomain0_subdomain1_membrane::sobj_subdomain11_subdomain00_size
vcRegionArea('subdomain0_subdomain1_membrane');
Function subdomain1_subdomain2_membrane::sobj_subdomain22_subdomain11_size
vcRegionArea('subdomain1_subdomain2_membrane');
Function UnitFactor_uM_um3_molecules_neg_1 (1000000.0 / 6.02214179E8);
Function subdomain0::vobj_subdomain00_size vcRegionVolume('subdomain0');
Function subdomain1::vobj_subdomain11_size vcRegionVolume('subdomain1');
Function subdomain2::vobj_subdomain22_size vcRegionVolume('subdomain2');

```

```

CompartmentSubDomain subdomain2 {
    BoundaryXm      Flux
    BoundaryXp      Flux
    BoundaryYm      Flux
    BoundaryYp      Flux
}

```

```

CompartmentSubDomain subdomain1 {
    BoundaryXm      Flux
    BoundaryXp      Flux
    BoundaryYm      Flux
    BoundaryYp      Flux
    PdeEquation M {
        Rate          J_V_dpm;
        Diffusion      M_diffusionRate;
        Initial        M_init_uM;
    }
    PdeEquation M_p {
        Rate          - J_V_dpm;
        Diffusion      M_p_diffusionRate;
        Initial        M_p_init_uM;
    }
    PdeEquation C {
        Rate          0.0;
    }
}

```

```

        Diffusion      C_diffusionRate;
        Initial        C_init_uM;
    }
    PdeEquation PLCgamma1 {
        Rate            (J_r05_1 - J_r06_0 + J_r07_0);
        Diffusion       PLCgamma1_diffusionRate;
        Initial         PLCgamma1_init_uM;
    }
    PdeEquation s3 {
        Rate            (J_r05_3 + J_r06_0 - J_r07_0);
        Diffusion       s3_diffusionRate;
        Initial         s3_init_uM;
    }
    PdeEquation s8 {
        Rate            (- J_r05_1 - J_r06_3 + J_r07_3);
        Diffusion       s8_diffusionRate;
        Initial         s8_init_uM;
    }
    PdeEquation s10 {
        Rate            (- J_r05_3 + J_r06_3 - J_r07_3 - J_r08_1 + J_r09_1);
        Diffusion       s10_diffusionRate;
        Initial         s10_init_uM;
    }
    PdeEquation s14 {
        Rate            (J_r08_1 - J_r09_1);
        Diffusion       s14_diffusionRate;
        Initial         s14_init_uM;
    }
}

CompartmentSubDomain subdomain0 {
    BoundaryXm          Flux
    BoundaryXp          Flux

```

```

        BoundaryYm      Flux
        BoundaryYp      Flux
    }

MembraneSubDomain subdomain1 subdomain0 {
    Name                subdomain0_subdomain1_membrane
    BoundaryXm          Value
    BoundaryXp          Value
    BoundaryYm          Value
    BoundaryYp          Value
    PdeEquation pT {
        Rate            (- J_V_basal_p + J_Vsynth_p - J_V_hyd_PLC);
        Diffusion        pT_diffusionRate;
        Initial          pT_init_molecules_um_2;
    }
    PdeEquation d {
        Rate            (- J_V_PKC + J_V_hyd_PLC + J_V_off_c + J_V_PAP -
J_V_DAGK);
        Diffusion        d_diffusionRate;
        Initial          d_init_molecules_um_2;
    }
    PdeEquation c_active {
        Rate            (J_V_PKC - J_V_dpc + J_V_pc);
        Diffusion        c_active_diffusionRate;
        Initial          c_active_init_molecules_um_2;
    }
    PdeEquation c {
        Rate            (J_V_dpc - J_V_pc - J_V_off_c);
        Diffusion        c_diffusionRate;
        Initial          c_init_molecules_um_2;
    }
    PdeEquation m {
        Rate            (J_V_MARCKS - J_V_pm);

```

	Diffusion	m_diffusionRate;
	Initial	m_init_molecules_um_2;
}		
PdeEquation d_p {		
	Rate	(J_Vsynth_dp - J_V_basal_dp - J_V_PAP + J_V_DAGK);
	Diffusion	d_p_diffusionRate;
	Initial	d_p_init_molecules_um_2;
}		
PdeEquation s2 {		
	Rate	(- J_r03_0 - J_r04_0 + J_r05_0 - J_r06_1 + J_r07_1 + J_r01_0);
	Diffusion	s2_diffusionRate;
	Initial	s2_init_molecules_um_2;
}		
PdeEquation s4 {		
	Rate	(J_r01_1 - J_r03_1 - J_r04_1 + J_r05_2 + J_r06_1 - J_r07_1 -
J_r10_0 + J_r12_1);		
	Diffusion	s4_diffusionRate;
	Initial	s4_init_molecules_um_2;
}		
PdeEquation s5 {		
	Rate	(J_r01_2 - J_r03_2 + J_r04_0 - J_r05_0 - J_r06_2 + J_r07_2);
	Diffusion	s5_diffusionRate;
	Initial	s5_init_molecules_um_2;
}		
PdeEquation s6 {		
	Rate	(- J_r02_0 + J_r03_3 + J_r05_5 + J_r11_0 - J_r12_0);
	Diffusion	s6_diffusionRate;
	Initial	s6_init_molecules_um_2;
}		
PdeEquation s7 {		
	Rate	(J_r02_0 - J_r03_3 - J_r04_2 + J_r05_4 + J_r10_0 - J_r12_1);
	Diffusion	s7_diffusionRate;
	Initial	s7_init_molecules_um_2;

<pre> } PdeEquation s9 { J_r08_0 + J_r09_0 - J_r10_1 + J_r12_2); </pre>	<pre> Rate Diffusion Initial </pre>	<pre> (J_r01_3 - J_r03_4 + J_r04_1 - J_r05_2 + J_r06_2 - J_r07_2 - s9_diffusionRate; s9_init_molecules_um_2; </pre>
<pre> } PdeEquation s11 { J_r10_1 - J_r12_2); </pre>	<pre> Rate Diffusion Initial </pre>	<pre> (J_r02_1 - J_r03_5 + J_r04_2 - J_r05_4 - J_r08_2 + J_r09_2 + s11_diffusionRate; s11_init_molecules_um_2; </pre>
<pre> } PdeEquation s12 { </pre>	<pre> Rate Diffusion Initial </pre>	<pre> (J_r01_4 - J_r03_6 + J_r08_0 - J_r09_0 - J_r10_2 + J_r12_4); s12_diffusionRate; s12_init_molecules_um_2; </pre>
<pre> } PdeEquation s13 { J_r12_3); </pre>	<pre> Rate Diffusion Initial </pre>	<pre> (- J_r02_1 + J_r03_5 - J_r05_5 - J_r08_3 + J_r09_3 + J_r11_1 - s13_diffusionRate; s13_init_molecules_um_2; </pre>
<pre> } PdeEquation s15 { </pre>	<pre> Rate Diffusion Initial </pre>	<pre> (J_r02_2 - J_r03_7 + J_r08_2 - J_r09_2 + J_r10_2 - J_r12_4); s15_diffusionRate; s15_init_molecules_um_2; </pre>
<pre> } PdeEquation s16 { </pre>	<pre> Rate Diffusion Initial </pre>	<pre> (- J_r02_2 + J_r03_7 + J_r08_3 - J_r09_3 + J_r11_2 - J_r12_5); s16_diffusionRate; s16_init_molecules_um_2; </pre>

```

    }
    JumpCondition M {
        InFlux      - (UnitFactor_uM_um3_molecules_neg_1 *
KFlux_plasma_membrane_cytosol * J_V_MARCKS);
        OutFlux      0.0;
    }
    JumpCondition M_p {
        InFlux      (UnitFactor_uM_um3_molecules_neg_1 *
KFlux_plasma_membrane_cytosol * J_V_pm);
        OutFlux      0.0;
    }
    JumpCondition C {
        InFlux      ( - (UnitFactor_uM_um3_molecules_neg_1 *
KFlux_plasma_membrane_cytosol * J_V_PKC) + (UnitFactor_uM_um3_molecules_neg_1 * KFlux_plasma_membrane_cytosol *
J_V_off_c));
        OutFlux      0.0;
    }
    JumpCondition PLCgamma1 {
        InFlux      ((UnitFactor_uM_um3_molecules_neg_1 *
KFlux_plasma_membrane_cytosol * J_r03_0) - (UnitFactor_uM_um3_molecules_neg_1 * KFlux_plasma_membrane_cytosol *
J_r01_0));
        OutFlux      0.0;
    }
    JumpCondition s3 {
        InFlux      ((( - (UnitFactor_uM_um3_molecules_neg_1 *
KFlux_plasma_membrane_cytosol * J_r01_1) + (UnitFactor_uM_um3_molecules_neg_1 * KFlux_plasma_membrane_cytosol *
J_r03_1)) - (UnitFactor_uM_um3_molecules_neg_1 * KFlux_plasma_membrane_cytosol * J_r11_0)) +
(UnitFactor_uM_um3_molecules_neg_1 * KFlux_plasma_membrane_cytosol * J_r12_0));
        OutFlux      0.0;
    }
    JumpCondition s8 {

```

```

                                InFlux          ( - (UnitFactor_uM_um3_molecules_neg_1 *
KFlux_plasma_membrane_cytosol * J_r01_2) + (UnitFactor_uM_um3_molecules_neg_1 * KFlux_plasma_membrane_cytosol *
J_r03_2));
                                OutFlux          0.0;
                                }
                                JumpCondition s10 {
                                InFlux          ((( - (UnitFactor_uM_um3_molecules_neg_1 *
KFlux_plasma_membrane_cytosol * J_r01_3) + (UnitFactor_uM_um3_molecules_neg_1 * KFlux_plasma_membrane_cytosol *
J_r03_4)) - (UnitFactor_uM_um3_molecules_neg_1 * KFlux_plasma_membrane_cytosol * J_r11_1)) +
(UnitFactor_uM_um3_molecules_neg_1 * KFlux_plasma_membrane_cytosol * J_r12_3));
                                OutFlux          0.0;
                                }
                                JumpCondition s14 {
                                InFlux          ((( - (UnitFactor_uM_um3_molecules_neg_1 *
KFlux_plasma_membrane_cytosol * J_r01_4) + (UnitFactor_uM_um3_molecules_neg_1 * KFlux_plasma_membrane_cytosol *
J_r03_6)) - (UnitFactor_uM_um3_molecules_neg_1 * KFlux_plasma_membrane_cytosol * J_r11_2)) +
(UnitFactor_uM_um3_molecules_neg_1 * KFlux_plasma_membrane_cytosol * J_r12_5));
                                OutFlux          0.0;
                                }
                                }
                                }

MembraneSubDomain subdomain2 subdomain1 {
    Name                                subdomain1_subdomain2_membrane
    BoundaryXm                          Value
    BoundaryXp                          Value
    BoundaryYm                          Value
    BoundaryYp Value
    JumpCondition M {
                                InFlux          0.0;
                                OutFlux          0.0;
                                }
    JumpCondition M_p {
                                InFlux          0.0;

```

```

    OutFlux      0.0;
}
JumpCondition C {
    InFlux      0.0;
    OutFlux     0.0;
}
JumpCondition PLCgamma1 {
    InFlux      0.0;
    OutFlux     0.0;
}
JumpCondition s3 {
    InFlux      0.0;
    OutFlux     0.0;
}
JumpCondition s8 {
    InFlux      0.0;
    OutFlux     0.0;
}
JumpCondition s10 {
    InFlux      0.0;
    OutFlux     0.0;
}
JumpCondition s14 {
    InFlux      0.0;
    OutFlux     0.0;
}
}
}

```